University of Southampton
School of Civil Engineering and the Environment

The influence of fine platy particles on the behaviour of a rotund sand

by
Michelle Theron

A Thesis Submitted in Fulfillment of the Degree of Doctor of Philosophy
in the School of Civil Engineering and the Environment of the
University of Southampton

April 2004

UNIVERSITY OF SOUTHAMPTON

ABSTRACT

FACULTY OF ENGINEERING
CIVIL AND ENVIRONMENTAL ENGINEERING

THE INFLUENCE OF FINE PLATY PARTICLES ON THE BEHAVIOUR OF A ROTUND SAND

by Michelle Theron

The behaviour of mine tailings displays characteristics of both sand and clay. It is widely recognised that the behaviour of the tailings is governed by the fines content i.e. the greater the fines content the more clay-like the behaviour. Analytic analysis of tailings has revealed that some clay minerals are present. However, Olsen and Mesri (1970) proved that the behaviour of these clay minerals are controlled by mechanical forces rather than electro-chemical forces as initially thought. The clay-like behaviour of the tailings could thus not be attributed to the electro-chemical forces acting on fine particles, implying that some other mechanism must be at work.

A recent investigation into the behaviour of gold mine tailings (Vermeulen, 2001) showed that the particle shape of the fines tailings is predominantly platy whilst that of the coarse particles are angular. Various researchers have demonstrated that platy particles markedly influence the behaviour of sand. Consequently, research has been undertaken to establish whether the platy fines might govern the behaviour of the mine tailings. A laboratory investigation was conducted on an artificial soil namely Soton Soil, of which the particle shape and relative particle sizes were similar to those investigated by Vermeulen (2001). The Soton Soil consisted of coarse rotund particles containing various amounts of platy fines in the form of mica.

The compressibility, stiffness and shear behaviour of the Soton Soil were measured in the laboratory. Stiffness measurements included both small strain shear stiffness and Young's modulus. Although the former are commonly

measured in the laboratory using bender elements, several uncertainties are associated with the technique. Consequently a bender element new configuration and novel interpretation technique was developed that yielded repeatable results.

The observed behaviour of the Soton Soil was compared with the characteristic behaviour of mine tailings as documented in the literature, especially that by Vermeulen (2001). The mean diameter of the coarse rotund sand employed in the research was 1mm whilst that of the mica 0.1mm. The relative sizes of the Soton Soil particles compared well with the gold tailings tested by Vermeulen (2001). The percentage of platy fine particles (mica) (by weight) present in the Soton Soil varied between 5% and 20% which falls within the typical range found in mine tailings. A good correlation was found between the mechanical behaviour of mine tailings and Soton Soil. The unique behaviour of the mine tailings might thus be attributed to the particle shape of the fines.

Contents

Abstract i

List of tables vii

List of figures ix

List of Symbols xvii

Acknowledgements xxi

1 INTRODUCTION 1

1.1 Background 1

1.2 Objective 2

1.3 Scope 2

1.4 Methodology 3

1.5 Organisation of the thesis 3

2 LITERATURE REVIEW 5

2.1 Introduction 5

2.2 Description of tailings behaviour 5

2.2.1 *Composition of tailings* 6

2.2.2 *Index parameters and particle size distribution* 7

2.2.3 *Compressibility and consolidation* 9

2.2.4 *Stiffness* 11

2.2.5 *Shear strength* 11

2.3 Behaviour of geomaterials containing platy particles 14
2.3.1 *Behaviour of rotund particles compared to platy particles* 15
2.3.2 *Addition of platy particles to rotund particles* 21

3 DEVELOPMENT OF A BENDER ELEMENT TECHNIQUE 50
3.1 Bender element uncertainties 52
3.1.1 *Dispersion* 52
3.1.2 *Near field effects* 55
3.1.3 *Effective travel length* 58
3.1.4 *Travel time* 59
3.2 Bender element techniques 59
3.2.1 *Time-of-flight techniques* 61
3.2.2 *Phase sensitive technique* 61
3.3 New bender element technique: Two side bender receiver elements 63
3.3.1 *Specimen preparation* 64
3.3.2 *Time-of-flight technique* 65
3.3.3 *Phase sensitive technique* 66
3.4 Three side bender element probes 67

4 LABORATORY TESTING OF SOTON SOIL 93
4.1 Experimental set-up 93
4.1.1 *Triaxial apparatus* 93
4.1.2 *Instrumentation* 94
4.1.3 *Calibration* 96
4.2 Laboratory Testing 98
4.2.1 *Description of materials* 98
4.2.2 *Preparation of undrained isotropic triaxial specimens* . 99
4.2.3 *Description of test procedure and results* 105
4.3 Microscopic investigation of Soton Soil specimens 111
4.3.1 *Specimen preparation for thin sections* 112

5 DISCUSSION **141**

5.1 Introduction 141

5.2 Influence of platy fines on the behaviour of rotund coarse particles 142

5.2.1 *Fabric* 142

5.2.2 *Compressibility* 147

5.2.3 *Small strain stiffness* 148

5.2.4 *Shear strength* 154

5.3 Influence of platy fines on the behaviour of mine tailings . . . 160

5.3.1 *Compressibility* 161

5.3.2 *Small strain stiffness* 163

5.3.3 *Shear strength* 163

6 CONCLUSIONS AND RECOMMENDATIONS **193**

6.1 Bender elements 193

6.1.1 *Interpretation of bender element results* 193

6.1.2 *Development of a new bender element configuration and novel interpretation technique* 194

6.2 Influence of platy particles on the behaviour of rotund sand . . 194

6.2.1 *Fabric* 194

6.2.2 *Compressibility* 195

6.2.3 *Limitations of the new bender element technique and Soton Soil results* 196

6.2.4 *Small strain stiffness* (G_{max}) 196

6.2.5 *Shear strength* 197

6.3 Influence of platy fines on the behaviour of gold mine tailings . 199

6.3.1 *Comparison between gold mine tailings and Soton Soil characteristics* 199

6.3.2 *Compressibility* 199

6.3.3 *Small strain stiffness* 199

6.3.4 *Shear strength* 200

6.4 RECOMMENDATIONS 200

A Cross Correlation program for analysing bender element results 216

List of Tables

2.1 Summary of the grading properties of dispersed gold tailings from Vaal River operations (after Vermeulen (2001)) 26
2.2 Typical values for the coefficient of compressibility and consolidation 27
2.3 Summary of shear strength parameters of mine tailings 28
2.4 Critical state properties derived from undrained triaxial shear (after Vermeulen (2001)) 29
2.5 Selected definitions of Sphericity (after Santamarina et al. (2001)) 30

3.1 Summary of bender element interpretation techniques 71
3.2 Time delay and shear wave velocity obtained from time-of-flight techniques using a sinusoidal and square pulse for an input frequency of 15kHz 72
3.3 Time delay and shear wave velocity obtained from cross correlation interpretation 73
3.4 Influence of time range on the travel time obtained from cross correlation for an input frequency of 12kHz 74

4.1 Summary of instrumentation and calibration 115
4.2 Leighton Buzzard sand and mica properties 116
4.3 Summary of isotropic undrained triaxial tests 117
4.4 Shear wave velocity calculations for sand samples 118

4.5 Shear wave velocity calculations for Soton Soil containing 10% mica 119
4.6 Shear wave velocity calculations for Soton Soil containing 15% mica 120
4.7 Shear wave velocity calculations for Soton Soil containing 20% mica 121

5.1 Classification of sands according to their relative density (after Terzaghi and Peck (1948)) 167
5.2 Initial bulk and relative densities of Soton Soil and rotund sand specimens 167
5.3 Calculated and measured equivalent void ratios 168
5.4 Measured radial and average axial strain for an effective consolidation pressure of 400kPa 169
5.5 Travel time obtained from cross correlation and characteristic peak 170
5.6 Comparison between predicted and observed shear behaviour at large strains 171
5.7 Summary of critical state parameters of Soton Soil 172
5.8 Estimate of dilatancy obtained from effective friction angles of Soton Soil 172

List of Figures

2.1 Particle size sorting of diamond tailings 31
2.2 Layout of typical South African gold tailings dam showing (a) plan view and (b) cross section 32
2.3 Vertical layering in a gold tailings dam noticeable from piezo-cone results 33
2.4 Scanning electron micrograph of the (a) coarsest and (b) finest fraction of gold tailings delivery at Mizpah Dam 34
2.5 Flocculation of flaky slimes onto (a) coarser sand particles and (b) into flocs of slimes 35
2.6 Influence of dispersant on the hydrometer results of Boddington gold mine slimes 36
2.7 Influence of dispersant on grading analysis of Mizpah pond fine tailings 37
2.8 Summary of grading analysis of dispersed gold tailings 37
2.9 Compressibility of different fractions of Mizpah tailings delivery slurry 38
2.10 Variation of compressibility index with void ratio 38
2.11 Compressibility relationship between D_{50}, σ'_v and e 39
2.12 Small strain shear stiffness of silty sand tailings, with distance from dam crest and sample preparation 39
2.13 Shear strength data for sand and silt tailings 40
2.14 Particle dimension 40
2.15 Classifying particle shape according to elongation and flatness 41

2.16 Illustration of Wadell's procedure for evaluating particle Roundness 42
2.17 Definition of Angularity 42
2.18 Minimum void ratios obtained for binary mixtures of round steel shot having different grain size ratios 43
2.19 Schematic diagram of particle structure of silty sand following (a) low energy deposition and (b) isotropic compression and shear 44
2.20 Effects of fines content and relative density on volume compressibility 44
2.21 Influence of mica, silt and kaolin content on the void ratio of an uniform sand 45
2.22 Importance of shape and location of additives in sand 45
2.23 Variation in effective friction angle with mica content and (a) relative and (b) dry density at 69kPa (10psi) confining stress . 46
2.24 Influence of mica content on the undrained behaviour of sand in simple shear 47
2.25 Effect of mica and void ratio on the undrained behaviour of sand in simple shear 48
2.26 Undrained triaxial compression and extension of air pluviated sand and mica mixes 49

3.1 Schematic representation of ceramic bender element with a) composition and b) cantilever action 75
3.2 Forced harmonic response with regards to a) phase and velocity and b) amplitude (resonant frequency at 3500Hz and width 200Hz) 76
3.3 Velocity and amplitude response of a Biot medium 77
3.4 Velocity-frequency profile for a) forced harmonic response followed by a Biot response (sender) and b) Biot response followed by a forced harmonic response (receiver) 78

3.5 Typical oscilloscope signals from bender element test with square pulse excitation 79
3.6 Schematic layout of bender elements and instrumentation . . . 79
3.7 Reversed signals of receiver element, transmitter element excited with a 15kHz square pulse 80
3.8 Recorded transmitted (15kHz square pulse) and received signals 80
3.9 Recorded transmitted (15kHz sinusoidal pulse) and received signals 81
3.10 Phase angle and amplitude measurements obtained from a phase sensitive technique, using a conventional bender element configuration 81
3.11 Derived relationship between cumulative phase difference and input frequency obtained from a conventional bender element configuration 82
3.12 Schematic layout of side mounted bender elements and instrumentation 82
3.13 Equipment used for inserting bender element probes 83
3.14 Dimensions of a two-side bender configuration 83
3.15 Received signal of receiver elements R1 and R2 when transmitter excited with 15kHz sine pulse 84
3.16 Examples of reversed signals received by side bender element probes with (a) 7kHz and (b) 15kHz input frequencies 85
3.17 Frequency spectrum of receiver probes R1 and R2 for (a) 6kHz and (b) 15kHz input frequencies 86
3.18 Group velocities measured between side bender elements (R1 and R2) for a range of single sinusoidal input frequencies . . . 87
3.19 Phase sensitive technique results, considering two side bender probes (R1 and R2) 87
3.20 Comparison between measured and calculated phase angle with frequency, measured between R1 and R2 88

3.21 Cumulative phase angle as a function of input frequency, measured between side two bender probes (R1 and R2) 88
3.22 Schematic layout of three side mounted bender elements and instrumentation 89
3.23 Picking positions used to derive group velocity 90
3.24 Group velocity as a function of input frequency derived from the first 6 picks of received signals 90
3.25 Group velocities measured between side-mounted receiver probes when transmitter probe excited by a range of input sine pulse frequencies 91
3.26 An example of a cross correlation between two side receiver probes for an input frequency of 12kHz 91
3.27 Measured group velocities using hand picking on the second peak and cross correlation for input frequencies between 6kHz and 30kHz 92
3.28 Box showing which part of the recorded signals were used for cross correlation analysis 92

4.1 The triaxial equipment used during the experimental program 122
4.2 Design drawings of LVDT brackets 123
4.3 Typical calibration graph for a Druck PDCR810 pressure transducer 124
4.4 Calibration graph for 10kN load cell 124
4.5 Typical calibration graph for a LVDT 125
4.6 Calibration graph for the LDS 125
4.7 Microscope picture showing particle shape of platy and rotund sand particles 126
4.8 Pictures of specimen preparation showing (a) completed bender element configuration, (b) specimen with bender elements and LVDT and (c) specimen with complete instrumentation . 127
4.9 Schematic presentation of enlarged funnel used for preparing loose rotund sand specimens 128

4.10 Comparison of external and local volumetric strain for (a) 15% mica specimen, (b) dense rotund sand specimen 129
4.11 Example of an "easily interpreted" bender element result showing (a) recorded traces (b) cross correlation for 15% soton soil specimen at an effective consolidation pressure and input frequency of 200kPa and 15kHz respectively 130
4.12 Example of a "complicated interpreted" bender element result showing (a) recorded traces (b) cross correlation for 15% soton soil specimen at an effective consolidation pressure and input frequency of 50kPa and 30kHz respectively 131
4.13 Influence of effective consolidation pressure on the repeatability of the travel time for a Soton Soil containing 10% mica . . 132
4.14 Influence of frequency on the travel distance between the transmitter and first receiver in terms of wavelength of a 10% Soton SOil specimen for an effective consolidation pressure of 200kPa 133
4.15 Influence of mica content on the travel distance between the transmitter and first receiver in terms of wavelength for an effective consolidation pressure and input frequency of 200kPa and 15kHz respectively 133
4.16 Influence of effective consolidation pressure on the travel distance between the transmitter and first receiver in terms of wavelength of a 10% Soton SOil specimen for an input frequency of 15kHz 134
4.17 Example of bottom receiver signal of 15% Soton Soil for input frequency and effective consolidation pressure of 30kHz and 400kPa respectively, showing the "apparent compression wave" 134
4.18 Local and external axial strain measurement for 15% Soton Soil specimen at 200kPa effective consolidation pressure showing (a) small strain and (b) large strain behaviour 135

4.19 Example of stress vs strain and pore water curves for a Soton Soil specimen containing 15% mica, isotropically consolidated to 200kPa effective consolidation pressure 136
4.20 Example of stress vs strain and pore water curves for loose rotund sand specimen isotropically consolidated to 200kPa effective consolidation pressure 137
4.21 Undrained secant Young's modulus as a function of local axial strain of loose rotund sand and 15% Soton Soil specimens isotropically consolidated to 200kPa effective consolidation pressure 138
4.22 Horisontal section of Soton Soil containing 20% mica for (a) polarized and (b) cross polarized light at 22.5 magnification . 139
4.23 Horisontal section of Soton Soil containing 20% mica for (a) polarized and (b) cross polarized light at 47.5 magnification . 140

5.1 Influence of mica content on the equivalent void ratio of Soton Soil 173
5.2 Horizontal section of Soton Soil containing 5% mica at a magnification of 22.5 for (a) polarization and (b) cross polarization 174
5.3 Horizontal section of Soton Soil containing 10% mica at a magnification of 22.5 for (a) polarization and (b) cross polarization 175
5.4 Horizontal section of Soton Soil containing 15% mica at a magnification of 22.5 for (a) polarization and (b) cross polarization 176
5.5 Horizontal section of Soton Soil containing 20% mica at a magnification of 22.5 for (a) polarization and (b) cross polarization 177
5.6 Horizontal section cross polarized photograph of Soton Soil containing 10% mica at 47.5 magnification, highlighting location and orientation of mica particles 178
5.7 Void ratio vs. mean effective stress for isotropically consolidated rotund sand and Soton Soil specimens containing various percentages of mica 178

5.8 Cross correlation of (a) 20% Soton Soil and (b) dense rotund sand specimen at an effective consolidation pressure of 250kPa 179
5.9 Recorded traces of 20% Soton Soil specimen at 250kPa effective consolidation pressure 180
5.10 Recorded bottom receiver signal and noise amplitudes employed for calculating the signal-to-noise ratio 180
5.11 Influence of effective consolidation pressure on the signal-to-noise ratio of the recorded bottom receiver for input frequency of 15kHz and 20% mica content 181
5.12 Signal-to-noise ratio degradation with mica content of recorded bottom receiver for an effective consolidation pressure of 250kPa and input frequency of 15kHz 181
5.13 Small strain shear stiffness derived from bender element results for Soton Soil and rotund sand specimens 182
5.14 Comparison of bender element and local axial strain results for an effective consolidation pressure of 100kPa 183
5.15 Comparison of bender element and local axial strain results for an effective consolidation pressure of 200kPa 184
5.16 Comparison of bender element and local axial strain results for an effective consolidation pressure of 400kPa 185
5.17 Undrained stress-strain behaviour 186
5.18 Stress-strain and pore water vs strain curve for rotund sand and Soton Soil at 400kPa effective consolidation pressure . . . 187
5.19 Stress-strain and pore water vs strain curve for rotund sand and Soton Soil at 100kPa effective consolidation pressure . . . 188
5.20 Stress-strain and pore water vs strain curve for rotund sand and Soton Soil at 200kPa effective consolidation pressure . . . 189
5.21 Effect of mica content on stress paths of rotund sand and Soton Soil specimens isotropically consolidated to (a) 100kPa, (b) 200kPa and (c) 400kPa effective consolidation pressure . . 190

5.22 Effective internal friction angle of Soton Soil and rotund sand specimens 191
5.23 Influence of mica content and internal deformation on the shear behaviour of Soton Soil at an effective consolidation pressure of 400kPa 192

List of Symbols

Roman symbols

A	angularity
A	receiver amplitude
a	corner angle
B	intermediate grain dimension
$1/A$	threshold coefficient
$^{\circ}C$	intrinsic compression index
C_c^*	intrinsic compression index
C_c	coefficient of gradation
C_u	uniformity coefficient
c_v	coefficient of consolidation
$CVSS$	constant volume simple shear apparatus
D	diameter of smallest circle circumscribing projected area
D_e	equivalent grain diameter
D_x	grain diameter corresponding to x% finer
E	aspect ratio
E	Young's modulus
E_{usec}	undrained secant Young's modulus
e	void ratio
e^*	equivalent void ratio
e_{fine}	void ratio of fine tailings
e_{coarse}	void ratio of coarse tailings
e_{max}	maximum void ratio of specimen

e_{min}	minimum void ratio of specimen
F	flatness
f	driving frequency of transmitter
f_c	proportion of coarse particles by weight
G	shear modulus
G_{max}	small strain shear modulus
$G_{s-r}(f)$	cross power spectrum
H	minimum grain dimension
i	direction of wave propagation
j	direction of wave polarization
K_0	coefficient of earth pressure at rest
LL	liquid limit
L	maximum dimension of grain
$L(f)$	linear spectrum
$L_s^*(f)$	complex conjugate of L_s
l	maximum transmitter length
l_b	bender element length
L_{tt}	travel distance
M	constraint modulus
M	slope of the critical state line
N	specific volume of isotropic normally consolidated at p'=1.0kPa
$n(t)$	noise
p'	mean effective stress
p'_0	initial mean effective pressure
p_1	pressure constant
PL	plastic limit
PI	plasticity index
q	deviator stress
R	radius of transmitter
R	roundness
R_d	ratio of distance between bender elements and wave length

RF	surface roughness
r	radium of inscribed circle of grain projection
$r(t)$	receiver signal
S	transverse motion of wave
$s(t)$	transmitter signal
V	grain volume
v_p	compression wave velocity
v_s	shear wave velocity
X	distance from source to observational point
x	distance measured from inscribed circle centre to corner
Y	difference between roughness line and length of a 32cm cord

Greek symbols

δ	small increment of
Δ	large increment of
ε_a	axial strain
ε_{aL}	local axial strain
ε_r	radial strain
ε_{rL}	local radial strain
ε_v	volumetric strain
ε_{vL}	local volumetric strain
ε_{vE}	external volumetric strain
ζ	geometric attenuation constant
λ	wave length
ν	Poisson's ratio
Γ	specific volume of soil at critical state with p'=1.0kPa
Γ	coupling
ρ	sample density
ϕ'	effective internal angle of friction
ϕ_f'	effective internal angle of friction at failure

ϕ_r'	residual effective internal angle of friction
ω	phase angle
σ'_{vo}	effective overburden pressure
σ'_v	vertical effective stress
σ'_p	effective pre-consolidation pressure
χ	sphericity

Prefixes

m	milli ($\times 10^{-3}$)
μ	micro ($\times 10^{-6}$)
k	kilo ($\times 10^{3}$)
M	mega ($\times 10^{6}$)

Acknowledgements

I would like to thank my supervisor, Chris Clayton, for all the technical support during the three years, but also to make sure that I had all the financial back-up to complete it.

My father in law and Wendy for proof reading my thesis. Harvey and Dave Smallman for helping me when things go wrong which meant taking some punishment for the poor performance of the South African rugby and cricket teams.

Special thanks to Martin for the moral support and giving me a hand when things simply won't come right. Thanks also for motivating me to run.

Jo and John for being good friends and putting up with us during the last three months of our stay. Also Jo, thanks for introducing me to veggie food. Michelle (my imaginary friend) for having fun with and lending a listening ear. Irene and Morgan for the beer and evenings out. Andy Cresswell for the hikes in the lake and peak districst and the lesson in making the squidgy bits. Ming for our talks about the weather. Skevi and Andy, Jeff, Geoff, Hannes, Yann, Yelena, Chris, Dominique, Siavash Kiriaki and Nikos for making life fun.

Chapter 1

INTRODUCTION

1.1 Background

The behaviour of mine tailings is currently described by means of classical soil models and theories. Predicted and observed behaviour often differ, as tailings are a man made material and thus do not always fit within the framework of natural soil (Martin and Roberts, 1998). It has been recognised by several researchers such as Pettibone and Kealy (1971); Mittal and Morgenstern (1975); Vick (1990) and Stone, Randolph, Toh and Sales (1994) that the behaviour of mine tailings could be described as somewhere between that of sand and clay, with the fines controlling the mass. Consequently, assumptions made in the classical soil models and theories often do not apply. Although much has been done in recent years to quantify the soil properties of tailings, governing mechanisms are still not fully identified and understood.

Vermeulen (2001) has investigated the composition and state of gold tailings. Very little clay minerals with colloidal activities were found in the tailings and hence clay-like behaviour could not be attributed to electro-static forces. Microscope analysis of the gold mine tailings revealed that the particle shape of the fine tailings differs from that of the coarse. The particle shape of the fine tailings was found to be predominantly platy while that of the coarse angular. Similar observations were made by Colin (1980). Following

this research it was decided to investigate the influence of fabric and more specifically, particle shape on the behaviour of mine tailings. The behaviour of mine tailings in general was investigated with the emphasis placed on gold mine tailings. It was anticipated that the results of this thesis would put forward a governing mechanism which explains the behaviour of mine tailings, more specifically that of gold mine tailings.

1.2 Objective

The objective of this research is to identify a possible mechanism that controls the behaviour of mine tailings, namely the particle shape of the fines. "Soton soil", in this thesis, was defined as the combination of platy fine and rotund coarse sand particles. The Soton Soil consisted of platy particles in the form of mica and coarse rotund particles (Leighton Buzzard sand). The term "rotund sand" was used for equidimensional particles which was representative of the coarse tailings particles. The influence of particle shape on the compressibility, small strain stiffness (both shear and elastic) and shear behaviour of Soton Soil, having similar particle shape to the mine tailings, was investigated. In doing so, a new bender element configuration and novel interpretation technique was developed which improved the repeatability of bender element results. Observed behaviour was then compared against that of mine tailings, as documented in the literature with special reference to the work carried out by Vermeulen (2001).

1.3 Scope

The influence of particle shape on the mechanical behaviour of mine tailings was investigated within a laboratory environment by using Soton Soil. The small strain stiffness, compressibility and shear strength behaviour of the Soton Soil specimens were assessed. The results were then compared with that of rotund sand specimens and mine tailings. The small strain stiffness

of the material was obtained from bender element measurements as well as local deformation devices such as linear variable differential transformers. In order to do so, a literature review was conducted on the current practices of bender elements. A new bender element configuration and novel interpretation technique was developed, with the aim of improving the repeatability of results.

1.4 Methodology

The aims of the research were achieved by adopting the following methodology:

- literature review focussing on the mechanical behaviour of mine tailings and other geomaterials of similar particle shape,
- literature review on current bender element practices followed by the development of a bender element configuration and interpretation technique that yields repeatable results,
- a series of comparative isotropic normally consolidation tests and undrained triaxial shear tests to assess the influence of particle shape of the fines,
- microscopic investigation of the particle alignment of the various Soton Soil specimens and
- analysis and interpretation of the results to establish the influence of particle shape on the mechanical behaviour of Soton Soil as well as to compare the behaviour of mine tailings and Soton Soil.

1.5 Organisation of the thesis

The thesis consists of the following chapters:

- *Chapter 1* serves as an introduction to the research.

- *Chapter 2* reviews the literature with regards to the composition, compressibility and state of tailings and the influence of particle shape on other geomaterials having similar particle shape.
- *Chapter 3* reviews current bender element practices and as a result develop a bender element technique that yields repeatable results.
- *Chapter 4* outlines the laboratory testing program, specimen preparation as well as preliminary test results.
- *Chapter 5* discusses the results of the experimental work so as to establish whether the behaviour of tailings could be contributed to particle shape.
- *Chapter 6* draws conclusions from the results.
- *Appendix A* Visual Basic program for calculating the cross correlation between two bender element signals.

Chapter 2

LITERATURE REVIEW

2.1 Introduction

The mechanisms controlling the behaviour of mine tailings dams are not yet fully understood. Tailings behaviour may be classified as somewhere between that of sand and clay with the material becoming more clay-like closer to the pond of the tailings dam. It is unclear as to what causes the tailings to behave in such a manner, as very little clay is present. The literature, with regards to the composition and mechanical behaviour of mine tailings have been reviewed with the emphasis placed on gold mine tailings. Geomaterials with similar fabric have also been studied to determine whether fabric might influence the behaviour of the material.

2.2 Description of tailings behaviour

Central to the understanding of tailings behaviour, is the nature of depositional processes that tailings undergo. Tailings are placed hydraulically by means of a peripheral discharge method such as spigotting which produces a highly heterogenous material in both horizontal and vertical direction. A full description of current practices may be found in Robertson (1987), Vick (1990) and Vermeulen (2001).

Hydraulic segregation of the particles occurs as they move away from the deposition point towards the pond (Figure 2.1). As a result the material towards the pond becomes progressively finer (Blight and Bentel, 1983; Matyas, Welch and Reades, 1984; Rassam, 2002). The material in the day wall is termed whole tailings, the transitional zone sand and slimes and pond, slimes (Figure 2.2). As the coarse particles settle out, the moisture content of the remaining slurry increases whilst the pulp density decreases. This reduces the slope of the beach which in turn increases deposition of particles (Blight, 1987; Robertson, 1987; Wates, Stevenson and Purchase, 1987). The shape of the hydraulic fill beach is thus governed by the particle size sorting process, strength of the settled slurry and conservation of energy. The degree of grain segregation depends on the slurry density and flow concentrations (Robertson, 1987).

In the vertical direction, the material is highly layered owing to these depositional practices (movement of the discharge point and penstock (Höeg, Dyvik and Sandbaekken, 2000)), soil forming processes and variation in milling consistencies. Figure 2.3 is an example of normalised piezocone results from a gold tailings dam. The variation of the material with depth can clearly be seen. If the discharge point or spigots are widely spaced, the variation in fines content increases and could be as much as 50% over short vertical distances (Vick, 1990).

The in situ properties of the tailings such as permeability, compressibility and strength are related to the beach profile. This will be illustrated in the remainder of this section.

2.2.1 *Composition of tailings*

Pettibone and Kealy (1971) investigated the backfill material of several mine tailings under a microscope. The data were collected from the Spokane Mining Research Centre. The material was found to be angular. On the other hand, Hamel and Gunderson (1973) found the particle shape of Homestead gold slimes to consist of both angular and needle shaped particles with the

latter being predominant. Colin (1980) also noted the angularity of the large grains (sand) and significant proportions of needle shaped particles present in the slimes.

Vermeulen (2001) investigated the composition of gold tailings on a micro scale. A scanning electron micrograph (SEM) was employed to investigate the particle shape of the respective particle fractions as well as to visually grade the tailings. In addition, undisturbed samples obtained from block samples were studied to investigate the structure of the sample in its undisturbed state. It was found that the coarse fraction was sub-angular with either smooth or rough surfaces while the particles of the fine fraction were platy with smooth and flat surfaces (Figure 2.4). The fine fraction appears to not only attach itself onto the coarser sand grains but also to form flocs of fine particles (Figure 2.5).

2.2.2 *Index parameters and particle size distribution*

Matyas et al. (1984) investigated the behaviour of uranium tailings and found tailings sand to be non-plastic, while the slimes had a plasticity index ranging between 0 and 10% and a liquid limit between 25-40%. Aubertin, Bussière and Chapuis (1996) described the tailings of four different hard rocks as slightly plastic with a liquid limit of 17.5% and plastic limit of zero. According to Wagener, Craig, Blight, McPhail, Williams and Strydom (1998) the Atterberg limits of gold tailings generally fall within the following ranges:

$$\begin{aligned} \text{Liquid Limit (LL)} &= 23\text{-}43 \\ \text{Plastic Limit (PL)} &= 22\text{-}35 \\ \text{Plasticity Index (PI)} &= 1\text{-}8 \\ \text{Linear Shrinkage} &= 2.7\text{-}4.7 \end{aligned}$$

Qiu and Sego (2001) investigated samples of three different mine tailings i.e. copper, gold and coal wash in the laboratory. They found that with the

exception of the coal wash tailings, all of the tailings could be regarded as non-plastic according to the Atterberg limit tests (BS1377, 1990). Vermeulen (2001) investigated the properties of gold mine tailings and found that the material had a very low plasticity. Depending on the grading of the material, and hence their location in the tailings dam relative to the discharge point, the classification varied between low to high plasticity silt on the Casagrande A-line or standard plasticity chart (BS1377, 1990).

Stone et al. (1994) investigated the properties of the fine grained residue produced at the Boddington gold mine in Western Australia. The particle size distribution of the tailings were assessed by means of two hydrometer tests. The first test followed the procedure as outlined in BS1377 whilst the second test was conducted with decanted pore fluid without the addition of dispersant. Figure 2.6 shows that the coarser fraction is essentially similar for both tests. Flocculation of the residue in the second test however, resulted in a much coarser apparent particle size distribution. Vermeulen (2001) investigated the particle size distribution of two gold tailings using standard wet-sieve and hydrometer methods as well as "visual" grading from electron micrographs. The tailings were pre-treated to remove calcareous compounds and organic matter but also to ensure they were in a dispersed state. Parallel tests were performed on non-treated material for reference. No carbonate compounds were detected, suggesting that carbonate bonding had not occurred in these tailing deposits. Pre-treatment of organic compounds made very little difference to the tailings particle size distribution. Treatment with a dispersant however, altered the measured grading from medium silt sized ($> 10\mu$m) to a relatively uniform distribution in the fine sand and silt size ranges (10% finer than 2μm) (Figure 2.7). This difference in particle distribution might be attributed to:

- Tailings being deposited in a flocculated state. Without dispersant, the finer material aggregates into flocs with a diameter greater than 10μm.
- The fine flaky tailings attaching themselves to the sand and coarse silt particles in the flocculated state and settling out together. The dis-

persant detached these fine particles from the coarser particle allowing them to settle out separately.

Table 2.1 and Figure 2.8 summarize the grading properties of the dispersed gold tailings. Visual interpretation of the grading was conducted on representative dispersed samples of the sieve and hydrometer analysis (Vermeulen, 2001). Each sample (representative of a size fraction) was investigated under a scanning electron microscope (SEM) and the average diameter of the particle measured. This measurement was then applied to the mass fraction represented by the micrograph. It was found that the visual grading resulted in a coarser grading than obtained by the sieve and hydrometer analysis. The reason for this is that the particle shape of the fine fraction is platy whilst both the sieve and hydrometer analysis is based on the assumption of a round particle shape. Terzaghi (1925) also identified the fact that soil classification by means of grading analysis assumes round particle shape while most soil particles have a different shape, thus resulting in an inaccurate assessment of particle size.

In conclusion it may be said that tailings and gold tailings in particular are granular materials consisting mainly of silt and sand sized particles with very few clay particles present. The grading of the material depends on the location of the tailings relative to the discharge point. Tailings appear to exhibit very little plasticity, and based on this, it might be assumed that the behaviour of the tailings would follow that of a granular material such as sand.

2.2.3 *Compressibility and consolidation*

"Because of their loose depositional state, high angularity and grading characteristics, both sand and slimes tailings are more compressible than most natural soils of similar type.", Vick (1990).

It is generally assumed that tailings are in a normally consolidated state owing to their recent stress history, although over-consolidation could be

found in cases where the tailings are deposited in a sub-aerial fashion[1]. Primary and secondary consolidation occurs simultaneously in the tailings (Vick, 1990).

Matyas et al. (1984) conducted conventional oedometer tests on undisturbed and reconstituted uranium tailing samples obtained from below the water table. The fine tailings appeared to be more compressible than the coarse tailings (Figures 2.10 and 2.11), which was also noted by Robertson (1987). It is interesting to note that the compressibility of the undisturbed silt (fine) sample was higher than its reconstituted version. Vermeulen (2001) investigated the isotropic compressibility of undisturbed and reconstituted gold tailing samples (Figure 2.9). The fine tailings appeared more compressible than the coarse tailings. If the void ratio of the fine and coarse reconstituted tailing samples were compared with each other for the stress range of 20kPa to 500kPa in virgin compression, it would be seen that:

$$\begin{aligned} \text{Mizpah pond tailings} &= e_{fine} \approx 1.5 e_{coarse} \\ \text{Pay dam penstock tailings} &= e_{fine} \approx 2 e_{coarse} \end{aligned}$$

Additionally Matyas et al. (1984) constructed a 5m high test embankment consisting of sand tailings on top of the 11m high tailings dam to monitor the corresponding settlement and excess pore pressure generation. The excess pore pressures dissipated relatively quickly from the sand tailings, but at a much-reduced rate in the silt tailings.

Table 2.2 summarizes the coefficients of compressibility and consolidation for mine tailings as measured by several researchers such as Blight and Steffen (1979), Matyas et al. (1984), Stone et al. (1994), Aubertin et al. (1996) and Trojcek (2002). It is evident from the Table that both the compressibility and consolidation of the tailings are affected by the grading. The tailings slimes appear to be three times more compressible and up to six orders of

[1] achieved through open ended pipe discharge, spigotting or cycloning

magnitude slower to consolidate than the tailings sand.

2.2.4 *Stiffness*

Höeg et al. (2000) assessed the small strain shear stiffness (G_{max}) of fine tailings collected from the Polish Zelazny tailings dam. The dam was built by the upstream construction method, which is commonly used for tailings dams in South Africa. Undisturbed tube samples were collected at 40m, 120m and 200m from the dam crest in the direction of the pond. Reconstituted specimens were also prepared by means of moist tamping to bulk densities equal to that of the undisturbed specimens. The samples were anisotropically consolidated ($K_o = 0.5$) to confining pressures of 50kPa, 250kPa and 500kPa after which G_{max} was measured using bender elements. It was found that G_{max} increased with increasing confining pressure (Figure 2.12). Apart from the initial stiffness measurement of the specimen collected at 40m from the dam crest, the recorded G_{max} value of the undisturbed specimens were 20% to 30% higher than their reconstituted counterparts, despite similar void ratios. No evidence of cementation could be found and consequently this was ascribed to differences in soil fabric. G_{max} also seemed to decrease with increasing distance from the dam crest, i.e. increasing fines content. The literature review with regards to the small strain shear stiffness of tailings were restricted to a single case study due to limited information on the topic.

2.2.5 *Shear strength*

As noted in the previous sections, mine tailings are predominantly granular materials with low plasticity, despite the fact that their coefficient of compressibility can be surprisingly high. It might thus be reasonable to expect the shear strength behaviour of tailings to follow that of a granular material such as sand. The effective internal friction angle (ϕ') of a sand is greatly influenced by its density, particle size distribution and particle shape and typically ranges from 27° to 50° (Terzaghi, Peck and Mesri, 1996). Bolton

(1986) investigated the published data of several sands at different densities and confining pressures in terms of their strength and dilatancy. It was found that the critical state angle of shearing resistance is a function of mineralogy with that of quartz and feldspar typically in the order of 33° and 40° respectively. The extra angle of shearing of dense soil is correlated with its rate of dilation and falls within a margin of about 2°. Literature on the subject however suggests that the ϕ' value of tailings are independent of the above factors.

Matyas et al. (1984) found the ϕ' of uranium tailings to be highly dependent on the void ratio prior to shearing. The silt fraction exhibited higher friction angles than the sand tailing at equal void ratios. This was attributed to the higher percentage of needle shaped particles present in the silt. Kuerbis, Negussey and Vaid (1988) investigated the phenomenon of nearly constant friction angles of the tailings sands and slimes by adding natural silt fines to the tailings sands. The effective friction angle at phase transformation for undrained compression and extension remained constant and proved to be independent of both silt content and mode of deformation. It was thought that the silt fines simply occupied the voids while the sand skeleton still controlled the shear behaviour. The addition of silt fines did however result in higher densities following sample preparation and increased dilatancy under shear. This demonstrated that contrary to their initial belief, the addition of silt particles did influence the shear behaviour of the tailings sand despite ϕ' remaining constant. Kuerbis et al. (1988) results were in direct contrast with those of Matyas et al. (1984) who found ϕ' to be dependent on the fines content. A possible explanation for this is the difference in particle shape of the fines. Kuerbis et al. (1988) results however, is supported by both Vermeulen (2001) and Rassam (2002) (the effective friction angle to be independent of particle size).

Vick (1990) investigated the shear strength behaviour of tailings by means of undrained triaxial compression tests and found them to be cohesionless, with typical effective friction angles (ϕ') ranging between 30° and 37°. The

effective friction angle was found to be relatively unaffected by particle size distribution, over consolidation ratio and density of the tailings. The effective stress level on the other hand, seemed to be the controlling factor, i.e. an increase in effective stress results in an increase in effective friction angle. Vermeulen (2001) conducted consolidated undrained triaxial compression tests on both reconstituted and undisturbed samples of whole, coarse and fine tailings. All of the samples with the exception of the Pay Dam fine tailings showed phase transfer dilation at failure followed by strain hardening. Dilatancy was more pronounced with the coarser grades. In terms of the Cam-Clay theory, it was found that the state boundary surface and critical state line of the fine and coarse tailings in the stress plane (q, p') were close to each other (Table 2.4). On the other hand, major differences exist in the compression plane (e, p') between the fine and coarse tailings owing to differences in density and hence void ratio.

A summary of the shear strength parameters as measured by several researchers such as Mittal and Morgenstern (1975), Qiu and Sego (2001) and Byrne and Seid-Karbasi (2003) can be found in Table 2.3.

The stability of mine tailing dams is evaluated using slope stability analysis based on constant effective friction angle. Although the literature suggests that ϕ' remains constant irrespective of the particle size and density, caution should be exercised as the post failure stress paths of the fine and coarse tailings differ. As noted, fine tailings compress whilst the coarse tailings dilate (Vermeulen, 2001). Furthermore, idealised laboratory conditions (undrained and drained) do not model field-loading conditions correctly. The higher permeability of the coarse layers mobilises greater partially drained shear strength. Ultimately, layers of coarse tailings on a tailings dam will dissipate excess pore pressures more rapidly than layers of fine tailings. Depending on the rate of shear, coarse tailings will show a drained response whilst fine tailings an undrained response when sheared. Vermeulen (2001) showed that the drained shear strength of the coarse gold tailings were almost three times that of the undrained shear strength of the fine tailings under

similar initial isotropic confinement stress conditions. It should however be noted that as the material is highly layered, a weighted permeability might be more applicable and hence the mobilised shear strength would actually lie somewhere between drained and undrained.

Following the above it can be concluded that:

- Tailings predominantly consist of quartz with very few clay particle minerals.
- The behaviour of tailings is dependent on the content of fine particles, which in gold tailings appear to be flat and platy.
- The void ratio of the slimes is higher than that of the sand tailings.
- "Tailings are more compressible than most natural soils of similar type" (Vick, 1990).
- Tailings slimes appear to be three times more compressible and consolidate at a rate of up to six orders of magnitude slower than the tailings sand.
- The material is cohesionless with an effective angle of friction that appears to be largely unaffected by the particle size or density.
- Fine tailings reach failure at constant volume and shear strength. Coarse tailings on the other hand, undergo phase transformation followed by dilation and therefore strain hardening under undrained conditions.

2.3 Behaviour of geomaterials containing platy particles

A number of researchers e.g. Vermeulen (2001), Vick (1990) and Matyas et al. (1984) have recognized that the behaviour of mine tailings are governed by the fine fraction. Several researchers such as Hamel and Gunderson (1973),

Colin (1980) and Vermeulen (2001) noted that this fraction contains very little colloidal clay minerals, but that they have a platy particle shape. The mechanical behaviour of other geomaterials having similar particle shape will now be investigated to establish their characteristic behaviour. This will then be compared with that of mine tailings, previously described, to determine whether any similarities exist.

2.3.1 *Behaviour of rotund particles compared to platy particles*

The particle shape of the fine and coarse tailings have previously been described as angular, sub-angular, platy and needle shaped. Particle characterisation is thus addressed followed by a description of platy and rotund particle behaviour.

Particle characterisation

Terzaghi and Peck (1948), Mitchell (1976), Bolton (1986), Terzaghi et al. (1996) and Craig (1997) postulated that the behaviour of granular soil is influenced by the inherent characteristics of the material such as :

- *Particle size* which is the size of the individual particles.
- *Particle size distribution* gives an indication of the distribution of the particle sizes within a representative specimen of soil. This can be determined from sieve and hydrometer analysis. Some discontinuity exist where the two ranges overlap as the former presents the intermediate particle dimension whereas the latter presents the diameter of a sphere that would settle at the same rate as the soil particle.
- *Particle shape* describes the general shape of the particle in three dimensions (Yudhbir and Abedinzadeh, 1991). It is independent of angularity and surface roughness of the particle (Sukumaran and Ashmawy,

2001). Two parameters namely elongation (aspect ratio) (E) and flatness (F) (Figure 2.14) are required for particle shape classification (Figure 2.15) which are defined as follows:

$$E = L/B \tag{2.1}$$

$$F = B/H \tag{2.2}$$

where

$$\begin{aligned} L &= \text{maximum dimension of particle} \\ B &= \text{intermediate particle dimension} \\ H &= \text{minimum dimension of a particle} \end{aligned}$$

Although characterisation in three dimensions is more representative of the particle shape, it is often difficult to perform these measurements, especially on fine particles. As a two dimensional approximation, Wadell (1932) introduced the term Sphericity (χ) which is defined as:

$$\chi = D_e/D \tag{2.3}$$

$$0 \leq \chi \leq 1 \tag{2.4}$$

$$\begin{aligned} \chi &\sim 0 \text{ flaky grains} \\ \chi &\sim 1 \text{ bulky, spherical grains} \end{aligned}$$

where

$$D = \text{diameter of smallest circle circumscribing projected area}$$

D_e = $(\frac{6V}{\pi})^{1/3}$ equivalent diameter of grain

V = volume of grain

- *Roundness (R)* is defined as ratio of the curvature of the corners and edges of particles to that of the overall particle (Figure 2.16) (Wadell, 1932). It is most sensitive to the sharpness of angular protrusions (Bowman, Soga and Drummond, 2000). Krumbein (1941) developed a two dimensional equivalent where:

$$R = N/\sum_{I=1}^{N} D/d_i \tag{2.5}$$

R > 0.6 high roundness

R = 0.4 to 0.6 medium roundness

R < 0.4 low roundness

Lees (1963) proposed an alternative concept namely Angularity (A) since Roundness was inadequate to describe particles with sharp corners. Angularity is calculated (Equation 2.17) from the projections of the particle (Figure 2.17) (Miura, Maeda, Furukawa and Toki, 1997).

$$A = \sum (180 - a) * X/r \tag{2.6}$$

a = corner angle

r = radius of inscribed circle of grain projection

X = distance measured from the inscribed circle centre O to the corner

- *Surface roughness* express the surface topography of particles. Wright (1955) introduced a Roughness Factor (RF) that varies between 0 (smooth) and 20 (extremely rough) and is calculated as follows:

$$RF = 100Y/32 \tag{2.7}$$

$$\begin{aligned} RF &> 10 \text{ rough texture} \\ RF &= 7 \text{ to } 10 \text{ medium texture} \\ RF &< 7 \text{ smooth texture} \end{aligned}$$

where

Y = difference between the roughness line and a 32cm cord

According to BS812 (1975), surface roughness can be categorised in six broad qualitative classes namely glassy, smooth, granular, rough crystalline, honeycomb and porous.

- *Specific gravity* is the ratio of the unit weight of a given material to the unit weight of water at 4°C.

Some of these inherent characteristics can be quantified using standard techniques such as particle size analysis and specific gravity (Sukumaran and Ashmawy, 2001). Such techniques however, do not provide enough information regarding the shape of the particles (Barrett, 1980).

Rotund particles

Lade and Overton (1989) investigated the influence of non-plastic fines on the maximum and minimum void ratio of sand. Spheres of two different

grain sizes were used to model the behaviour of sand, with the diameter of the one being much smaller than the other. The larger diameter spheres present the primary fabric of the soil. The addition of smaller spheres to the primary fabric increased the total mass whilst the overall volume remained constant. A minimum void ratio was reached once the voids of the primary fabric were completely filled with the smaller spheres. Beyond this point, the large particles were being pushed apart and the void ratio increased. The authors found that an optimum grain size ratio exists for rotund particles of different sizes that result in the lowest voids ratio. Figure 2.18 illustrates the relationship between void ratio to particle diameter ratio (large to small). There is a sharp decrease in the minimum void ratio with increasing diameter ratio up to 7, after which this relationship stabilises. A transition in packing efficiency occurs at a diameter ratio of about 7. At about this value, finer particles can migrate and fit through the pore paths formed between the larger particles. At smaller diameter ratios, the finer grains push the larger grains apart and hence increase the minimum void ratio.

Thevanayagam (1999) postulated that the undrained response of granular mixes (i.e. equi-dimensional particles but of different particle diameter) is governed by intergrain contacts and friction. The role of the finer grains during undrained shear depends on the quantity of the finer grains present in the granular mix. At high coarse grain content, the fines are inactive in the transfer of inter particle forces. Once the fine grains are dominant so that the coarse grains are fully dispersed in the fine matrix, the contact and shear forces are carried by the fines.

Yamamuro and Lade (1997) investigated the stability of binary rotund particles in terms of grain contacts. Three different grain contacts namely "unstable", "stable" and "passive" were identified (Figure 2.19). Upon low energy deposition, the larger load bearing grains of the sand skeleton are held apart by the smaller fine grains (Figure 2.19(a)) resulting in an unstable configuration. When sheared, the initial volumetric compressibility is high resulting in the generation of excess pore pressures. With continued shear the

larger grains move closer together and a more dilatant or stable material is formed (Figure 2.19(b)). The fine particles resting on the sand within the void spaces (passive contacts) do not contribute to the compressibility of the material but do increase its density. Wood and Yamamuro (2000) investigated the particle contacts developed in Nevada sand containing various percentages of non-plastic silt under a scanning electron microscope. Specimens were prepared by means of dry pluviation and water sedimentation to equal void ratios and an isotropic consolidation pressure of 25kPa. It was found that the dominating grain contact changed from largely stable at 10% silt to mostly passive contacts at 40% silt.

Platy particles

Olsen and Mesri (1970) investigated the mechanisms that control the compressibility of clay minerals. Both mechanical and physio-chemical models were evaluated for this purpose. According to the physio-chemical model, the position of the swelling curve is greatly affected by pore water electrolyte concentration. The mechanical model on the other hand predicts either no change or a very small change, depending on whether it is assumed that the electrolyte concentration influences the surface friction of the particles. One-dimensional consolidation tests were conducted on kaolinite, illite and smectite where the pore water was changed. These results were contrasted against that of ground muscovite, a soil composed of platy particles, where mechanical effects dominate. It was found that with the exception of smectite, mechanical effects dominated the compressibility of the clay minerals and muscovite.

Special reference should be made to the compressibility behaviour of the ground muscovite as it has commonly been used in the research discussed in the remainder of this chapter. Olsen and Mesri (1970) postulated that at low consolidation pressures, the angle between particles is a maximum and surface friction stabilizes the loose soil structure. At high consolidation pressures, compressibility and swelling is controlled by the flexure of the

plates due to the orientation of the plates being near parallel. As the aspect ratio increases, the energy stored in the soil by particle bending and the slope of the plates increases (Olsen and Mesri, 1970). This results in an increase in the slope of the swelling curve. The aspect ratio[2] of muscovite varies between 20 and 50 and consequently it could be expected to have a steep swelling line as confirmed by experimental data obtained by Olsen and Mesri (1970).

2.3.2 *Addition of platy particles to rotund particles*

The behaviour of a combination of platy and rotund particles will now be considered.

Void ratio and density

Hammond and Hardcastle (1987) investigated the influence of mica (i.e. platy particles) on the density of a micaceous sand. Model sand consisting of Ottawa silica sand and muscovite particles of equal particle size (grain sizes varying between 0.1mm and 0.7mm with median of 0.42mm) as well as natural micaceous sand found in the national forests of northern Idaho, was used. Various percentages of mica by weight were investigated namely 0%, 5%, 10%, 25%, 50%, 75% and 100%. Model sand containing more than 5% of mica resulted in lower limiting dry densities (i.e. both maximum and minimum dry density) than that obtainable by sand particles of equal particle dimension. This was attributed to the platy mica particles bridging the equi-dimensional sand grains (Audibert, Ismael and Clough, 1976). A similar result was obtained for natural micaceous sand.

Hight, Georgiannou, Martin and Mundegar (1999) investigated the influence of mica content on the void ratio of micaceous sand. This was done by increasing the mica (MF 60) content of a fine dumped silica sand from 0% to 20% by weight and noting the difference in void ratio (Figure 2.21). As previously demonstrated by Gilboy (1928), the addition of mica to equally sized

[2]the aspect ratios for clay minerals are typically in the order of 3 to 100

quartz sand, increased the void ratio of the material dramatically. The importance of particle shape and position of the fines was illustrated by adding an angular silt and clay (kaolin) to the sand (Figures 2.21 and 2.22). Both of these had a very small influence on the void ratio of the sand and in fact, slightly reduced the void ratio (Hight and Leroueil, 2003; Mundegar, 1997). This supports the conclusions of Miura et al. (1997) who found that the void ratio extent (e_{min} and e_{max}) is a function of the grain shape and grading i.e. the void ratio extent is indirectly proportional to the mean diameter and directly proportional to angularity.

Compressibility and stiffness

Terzaghi (1925) postulated that the compressibility of cohesionless material is governed by the grain size, uniformity, volume of voids and mica content. This was supported by laboratory test results in which the compressibility of sand samples of different particle shape and surface condition were evaluated. Following this research, Gilboy (1928) investigated the influence of mica content on the compressibility of sand. Mixtures of smooth round quartz sand and mica particles were prepared by pouring them into a compression apparatus. The sand and mica were uniformly graded (particle size ranging between 0.417mm and 0.589mm) and of equal particle size. An increase in mica content resulted in an increase in void ratio of the uncompressed material as well as an increase in compressibility (both positive and negative compression) until ultimately it approached that of clay. It was also found that at low percentages of mica, a slight variation in mica content resulted in a substantial variation in compressibility. Moore (1971) added mica particles to Chattahoochee sand (described as medium, uniform, sub-angular) and measured the compressibility of the material. Each sample was consolidated anisotropically in a triaxial apparatus fitted with lateral deformation sensors to 345kPa (50psi). It was found that the compressibility is directly proportional to mica content. The rate of increase in compressibility however, reducing with mica content. This confirmed Gilboy (1928)'s results which in-

dicated that the compressibility of sand is most influenced by low percentages of mica.

Shear strength

Hammond and Hardcastle (1987) assessed the influence of platy particles on the shear behaviour of sand. This was done by conducting isotropically consolidated drained triaxial compression tests on the model sand consisting of Ottawa sand with varying amounts of mica as well as natural micaceous soil found in the forests of northern Idaho. The Ottawa sand and mica particles were of equal particle size. Comparing equal relative density model sand specimens with each other, it was found that an increase in mica content results in a decrease in the effective friction angle (Figure 2.23(a)). The opposite effect was noted when comparing specimens of equal absolute density (Figure 2.23(b)). The addition of mica in excess of 5% increased the dilative nature of the material. Confining pressure had a greater influence on the effective friction angle than mica content. Audibert et al. (1976) conducted a series of triaxial and plane strain tests on Chattahoochee sand, a uniform slightly alluvial micaceous sand. Small amounts of crushed mica of similar particle size (2% and 10% by weight) were added to the sand so as to establish its influence on the friction angle. It was found that the mica had very little influence on the friction angle, if any. This was contrary to the results of Hammond and Hardcastle (1987).

Differing from the above investigations where the shear behaviour of micaceous soil were evaluated on the basis of a change in friction angle with mica content, Hight et al. (1999) investigated the effect of mica content on the stress strain relationship of the material. Fine silica sand with various percentages of mica by weight (0%, 1%, 2.5%, 5%, 10%, 20% and 40%) was tested in a constant volume simple shear (CVSS) apparatus. It was found that small percentages of mica had the greatest influence. The addition of 1% mica altered the sand from a dilative to a brittle material with collapse potential. It should however be noted that due to the aspect ratio of the

mica (50:1), the addition of 1% mica by weight is equal to 25% by number of grains. A further increase in mica content increased the stability of the sand (Figure 2.24). In order to prove that the influence of mica on the sand is not purely related to a change in void ratio, three samples were prepared: two samples with 5% mica at different void ratios (0.7 and 0.91) and a pure sand sample with a void ratio of 0.7. The two mica samples behaved similarly, despite differences in void ratio (Figure 2.25).

Undrained triaxial compression and extension tests were conducted on air-pluviated sand specimens with increasing mica content as well as natural micaceous sand from the Bangabandhu bridge site in Bangladesh. The specimens were subjected to anisotropic normal consolidation prior to undrained shearing. In compression, the addition of mica increased the initial stability of the specimen and decreased the undrained brittleness, whilst in extension a greater collapse potential was noted with increased brittleness (Figure 2.26). The natural material behaved in a similar fashion with the undrained shear strength in compression and extension being 180kPa and 10kPa respectively. This extreme weakness of the micaceous sand in extension loading was found to be the cause of several flow slides.

Lupini, Skinner and Vaughan (1981) found that the residual shear strength behaviour of a soil mass is governed by the proportion of platy particles to rotund particles present in the soil mass. Three different types of residual shear strength behaviour were identified namely:

- *Turbulent shear* occurs when the behaviour of the soil is dominated by the rotund particles or when platy particles with a high coefficient of interparticle friction are dominant. Residual strength is high with no preferred particle orientation and brittleness is the result of dilation. The mobilized friction angle is equal to or slightly smaller than the critical friction angle (Leroueil, Guerriero, Picarelli and Saihi, 1997).

- *Sliding shear* occurs when the behaviour is dominated by low friction platy particles. The particles orientate themselves in the direction of

shear and a progressive decrease in shear strength towards residual shear strength occurs (Leroueil et al., 1997).

- *A transitional shear mode* occurs when there is no dominant particle shape. Turbulent and sliding shear occur in different parts of a shear zone.

The soil discussed in this section consists of platy particles in the form of mica and round to sub-rounded sand particles, be it natural or artificially prepared. Most of the research conducted on this material was concerned with assessing the influence of the platy particles on the behaviour of sand by varying the mica content of the material. It was found that the addition of mica particles altered the void ratio (and hence density), compressibility and shear behaviour of the sand so that it approaches that of clay at large percentages. The change in soil behaviour was greatest at small mica percentages. It should be noted that the particle size of the rotund and platy particles was similar in all of the cases reported above. The change in soil behaviour could thus only be attributed to particle shape of the mica and not particle size.

As already mentioned, the behaviour of the tailings change with distance from the discharge, becoming more clay-like towards the pond. The tailings physically change in particle size and shape becoming platier towards the pond. A similar change in behaviour was noted for the micaceous sand. This change however, was only brought about by particle shape. It may thus be true that the platy particle shape of the fines and not the particle size as previously believed governs the behaviour of tailings.

This research project aims to investigate this hypothesis by conducting a series of isotropic consolidation and triaxial compression tests on micaceous sand of which the particle size is representative of mine tailings. The small strain shear and elastic stiffness of the micaceous sand were also measured. Prior to doing so, bender elements which measures the small strain shear stiffness of the soil, was investigated (Chapter 3).

Table 2.1: Summary of the grading properties of dispersed gold tailings from Vaal River operations (after Vermeulen (2001))

Tailings dam	Description	D_{10} (μm)	D_{30} (μm)	D_{60} (μm)	D_{90} (μm)	C_u ($\frac{D_{60}}{D_{10}}$)	CC ($\frac{D_{30}^2}{D_{10}D_{160}}$)
Mizpah	Whole tailings	2.0	10.0	55.0	125.0	27.5	0.91
	Pond fines	1.5	4.5	16.0	55.0	10.7	0.84
	Pond coarse	3.0	25.0	75.0	145.0	25.0	2.78
Pay dam	Penstock fines	1.7	3.2	8.3	41.0	4.9	0.75
	Penstock coarse	2.0	9.0	43.0	115.0	21.5	0.94

Table 2.2: Typical values for the coefficient of compressibility and consolidation

Reference	Tailing description	Coefficient of compressibility (C_c)		Coefficient of consolidation (c_v) m^2yr^{-1}	
		Fine	Coarse	Fine	Coarse
Vick (1990)	Gold	0.23 - 0.3	0.05 - 0.1	0.3 to 30	$1.6 * 10^3$ to $0.3 * 10^6$
Blight and Steffen (1979)	Gold	0.35		198	
Stone et al. (1994)	Gold	0.75 (centrifuge) 0.35 (Rowe cell)		15 - 26	
Vermeulen (2001)	Gold			210 - 1200	800-6900
Qiu and Sego (2001)	Gold Copper Coal	0.083-0.156 0.056 - 0.094 0.37-0.396		13.58 - 80.07 22.32 - 104.23 1.48 - 17.26	
Matyas et al. (1984)	Uranium	0.2 - 0.48	0.05 - 0.1		
Trojcek (2002)	Uranium	0.6 - 0.79	0.04 - 0.08		
Aubertin et al. (1996)	Hard rock tailings	0.046 - 0.13		15.8 - 8830	

Table 2.3: Summary of shear strength parameters of mine tailings

Reference	Tailings Description	Test	Cohesion (kPa)	Effective internal angle of friction (degree)
Vick (1990)	General		0	30 - 37
Mittal and Morgenstern (1975)	Copper sands	Direct shear		
Rassam (2002)	Gold	Drained compression		41.7 - 40.7
Vermeulen (2001)	Gold, undisturbed and reconstituted	Undrained compression and extension	0	31.5-36
Byrne and Seid-Karbasi (2003)	Gold	Triaxial test	0	30 - 39
Qiu and Sego (2001)	Gold, reconstituted	Undrained compression	0	33
Qiu and Sego (2001)	Copper, reconstituted	Undrained compression	0	34
Qiu and Sego (2001)	Coal, reconstituted	Undrained compression	10	32

Table 2.4: Critical state properties derived from undrained triaxial shear (after Vermeulen (2001))

Dam	Description	λ	N	Γ	M
Mizpah	Reconstituted (whole tailings, delivery pulp)	0.066	2.082	1.025	1.4
	Pond fines (reconstituted)	0.105	2.512	1.442	1.4
	Pond coarse (reconstituted)	0.045	1.856	0.826	1.35
Pay Dam	Penstock fines (reconstituted)	0.176	3.126	1.99	1.27
	Penstock coarse (reconstituted)	0.068	2.040	0.980	1.27
	Penstock fines (undisturbed)	0.162	3.053	1.935	1.37
	Penstock coarse (undisturbed)	0.080	2.134	1.07	1.46

Table 2.5: Selected definitions of Sphericity (after Santamarina et al. (2001))

Definition	Value	Relative to
Sphericity	surface area of a sphere with the same volume as the particle	actual surface area of the particle
True sphericity	diameter of a sphere with the same volume as the particle	diameter of circumscribing sphere
Projection sphericity	area of the particle projection	area of the circle with diameter equal to the longest length of projection
Inscribed circle sphericity	diameter of the largest inscribed circle	diameter of the smallest circumscribed circle

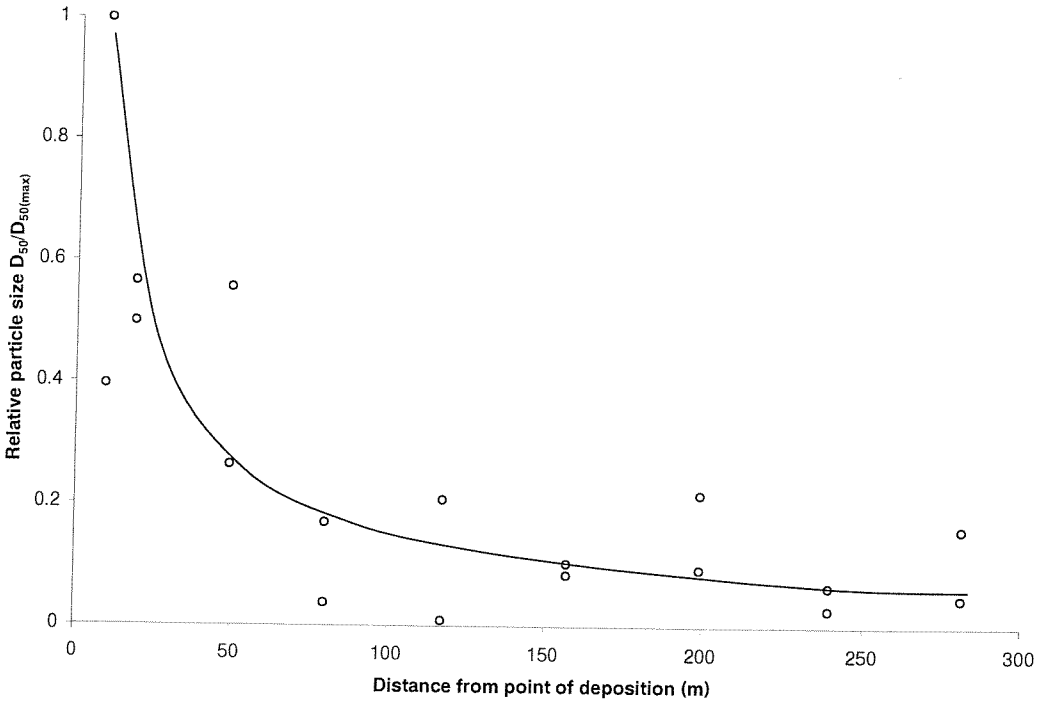

Figure 2.1: Particle size sorting of diamond tailings (after Blight and Bentel (1983))

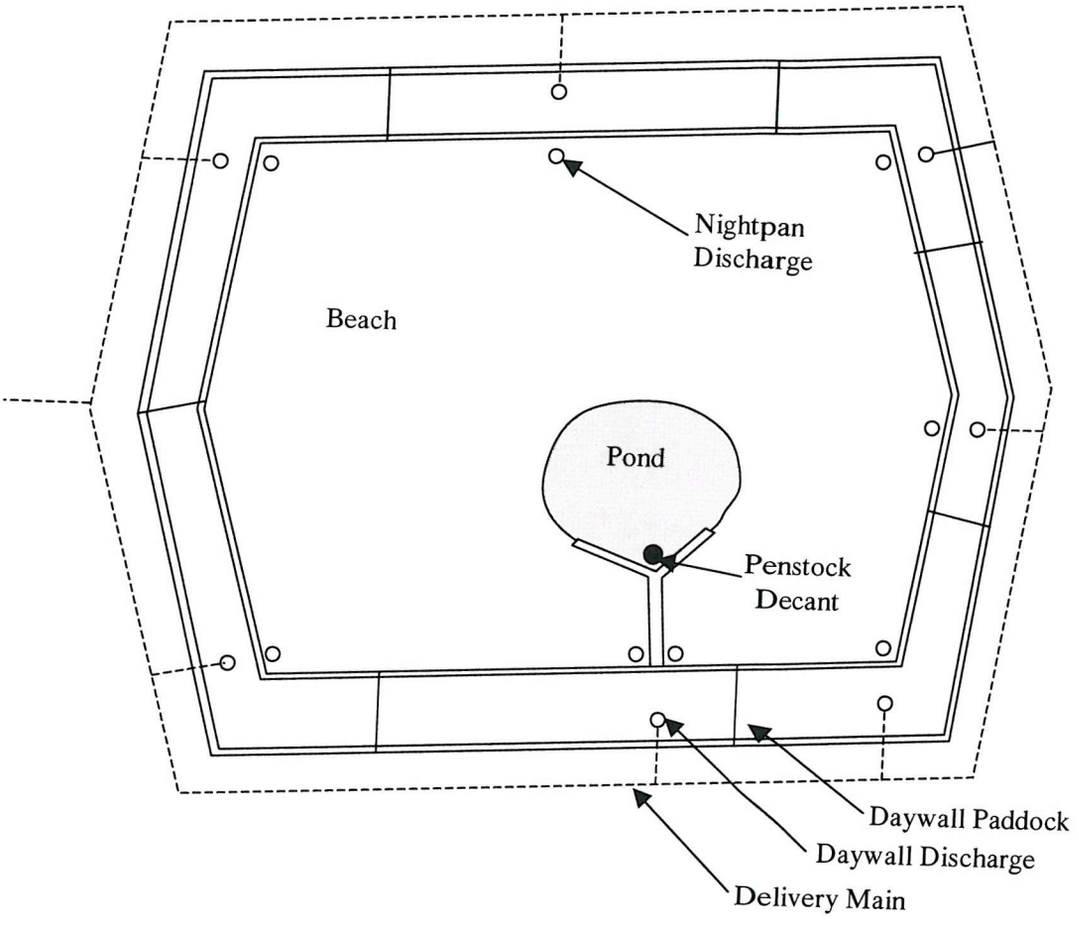

(a)

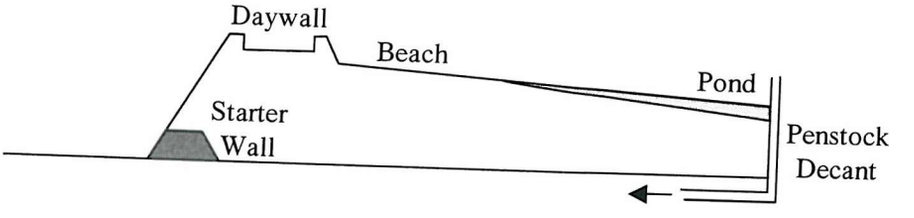

(b)

Figure 2.2: Layout of typical South African gold tailings dam showing (a) plan view and (b) cross section (after McPhail and Wagner (1989))

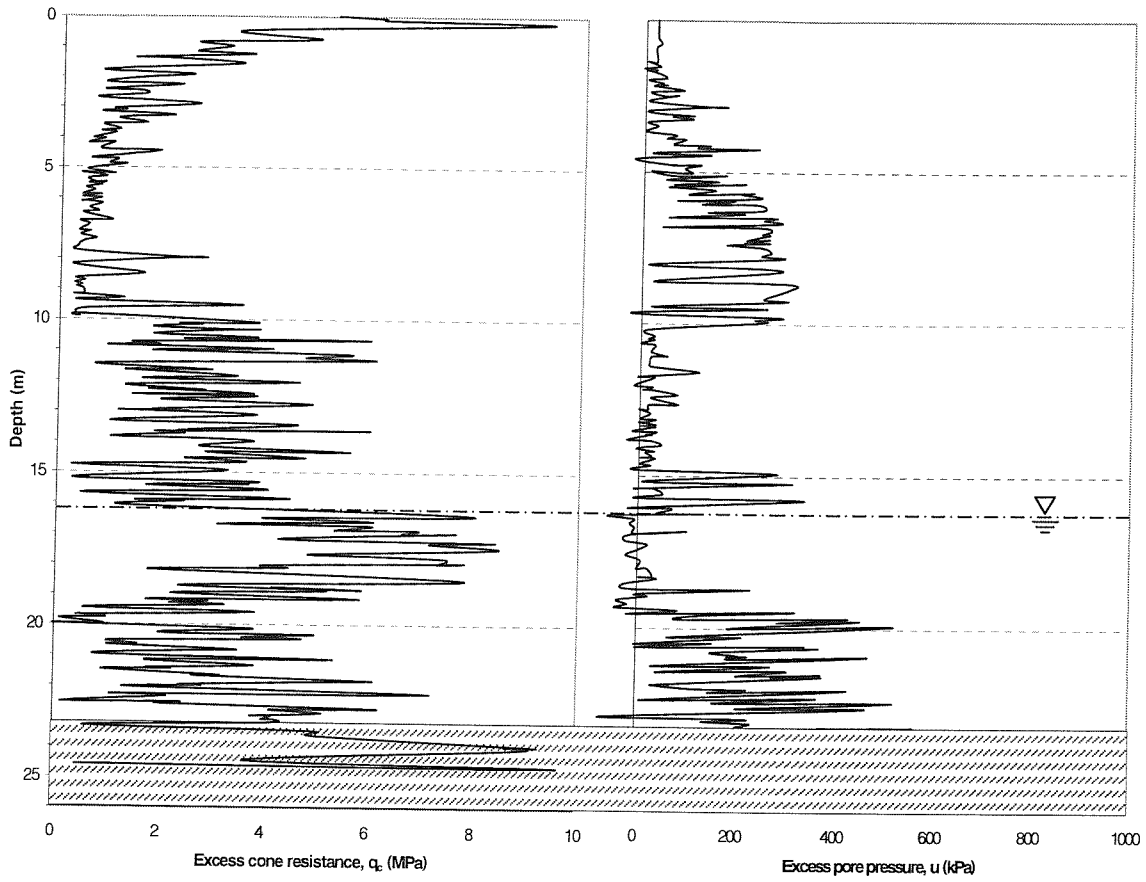

Figure 2.3: Vertical layering in a gold tailings dam noticeable from piezocone results (after Vermeulen (2001))

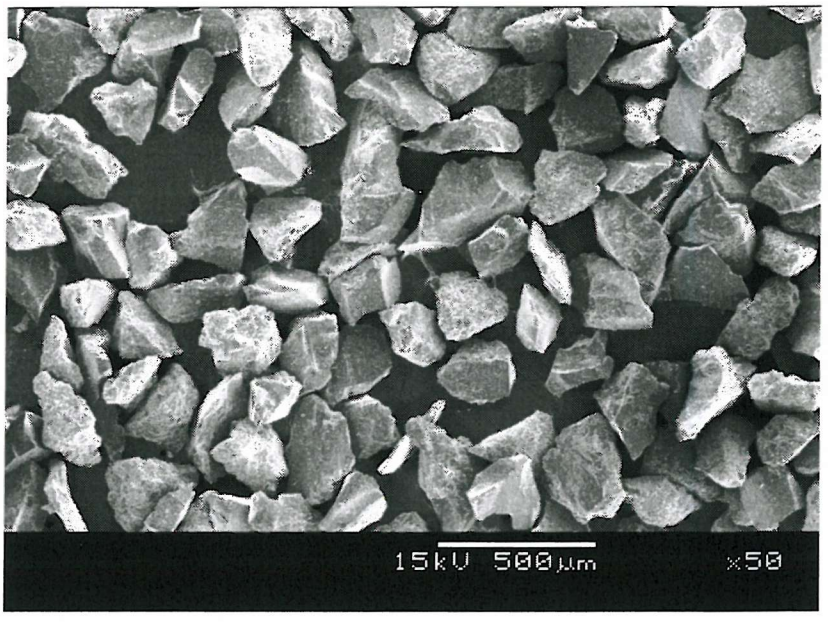

(a)

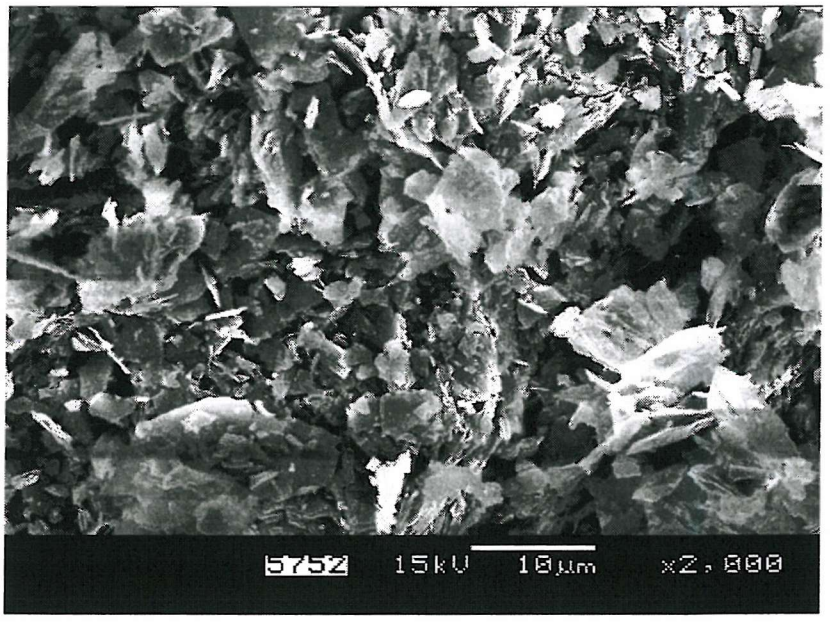

(b)

Figure 2.4: Scanning electron micrograph of the (a) coarsest and (b) finest fraction of gold tailings delivery at Mizpah Dam (after Vermeulen (2001))

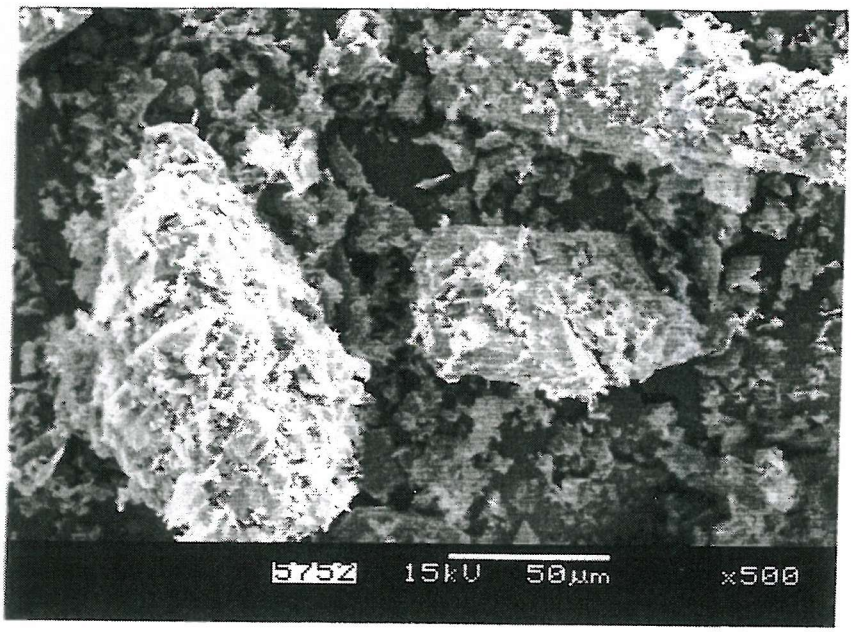

(a)

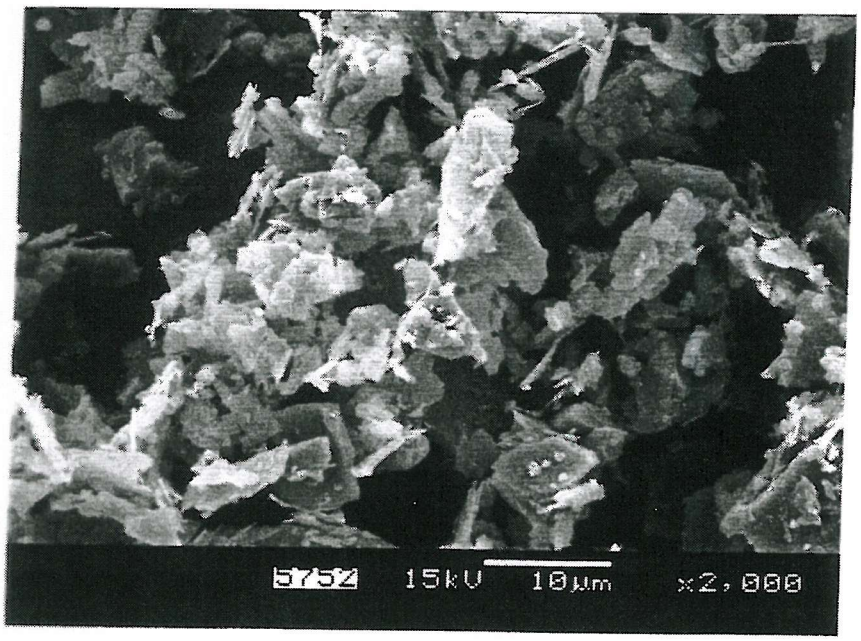

(b)

Figure 2.5: Flocculation of flaky slimes onto (a) coarser sand particles and (b) into flocs of slimes (after Vermeulen (2001))

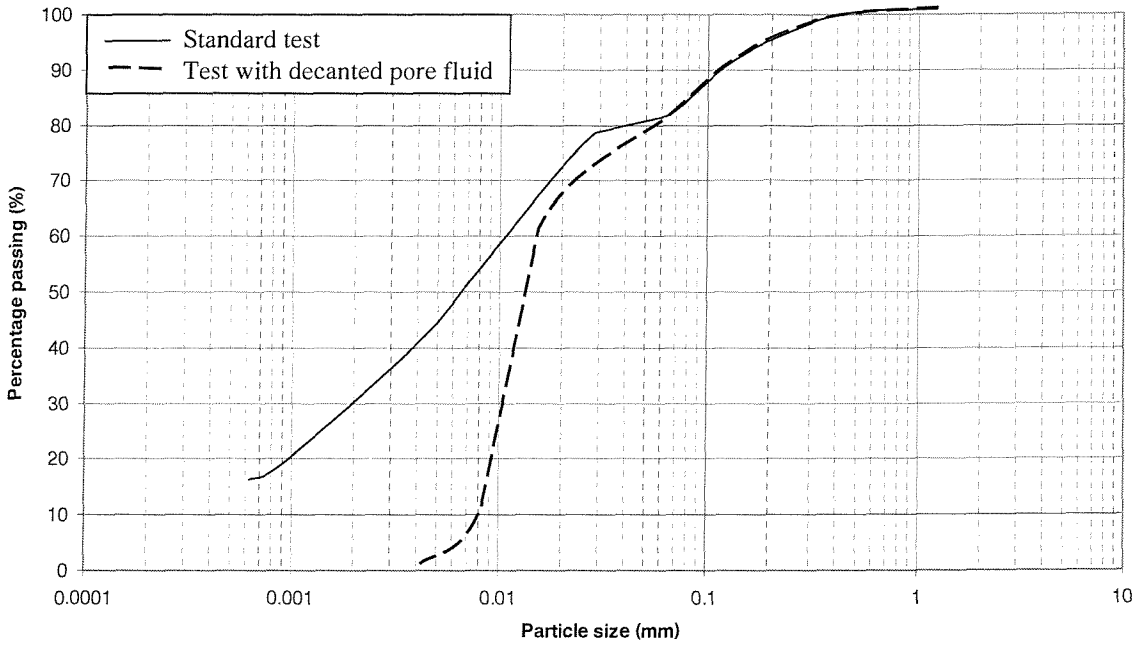

Figure 2.6: Influence of dispersant on the hydrometer results of Boddington gold mine slimes (after Stone et al. (1994))

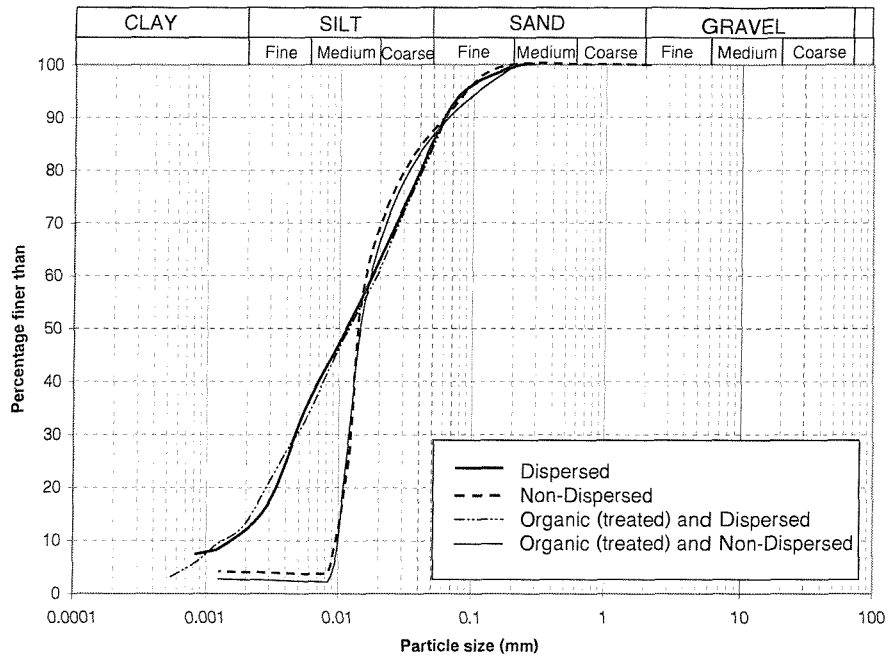

Figure 2.7: Influence of dispersant on grading analysis of Mizpah pond fine tailings (after Vermeulen (2001))

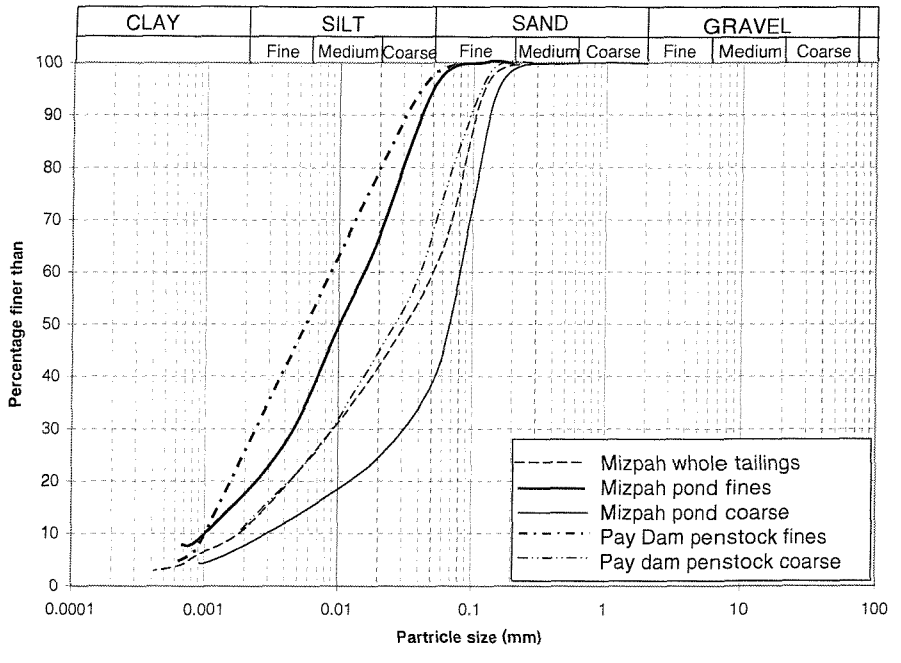

Figure 2.8: Summary of grading analysis of dispersed gold tailings (after Vermeulen (2001))

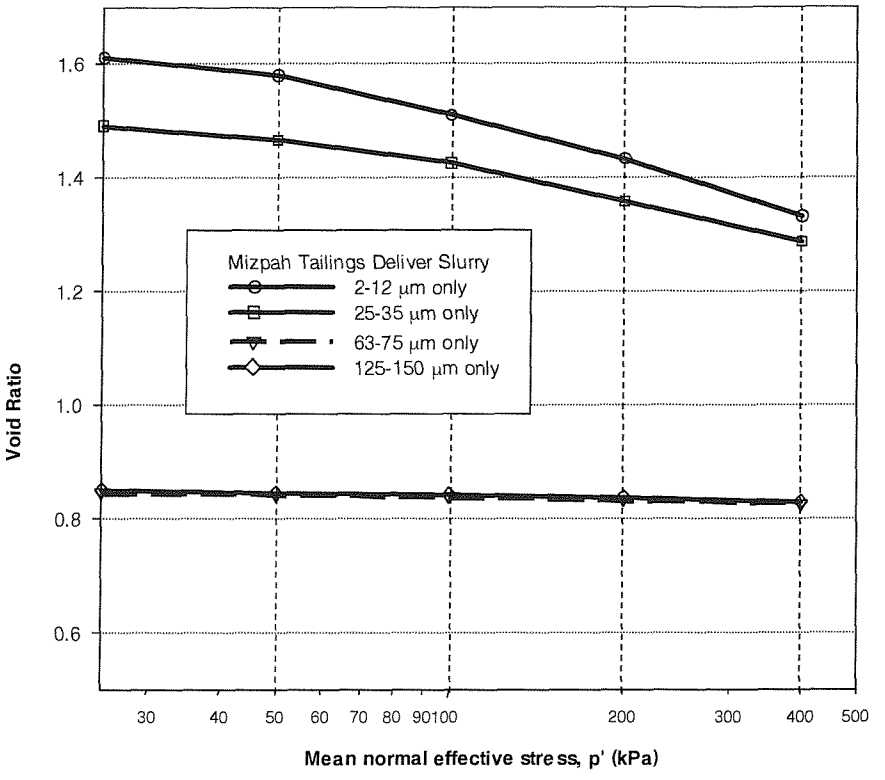

Figure 2.9: Compressibility of different fractions of Mizpah tailings delivery slurry (after Vermeulen (2001))

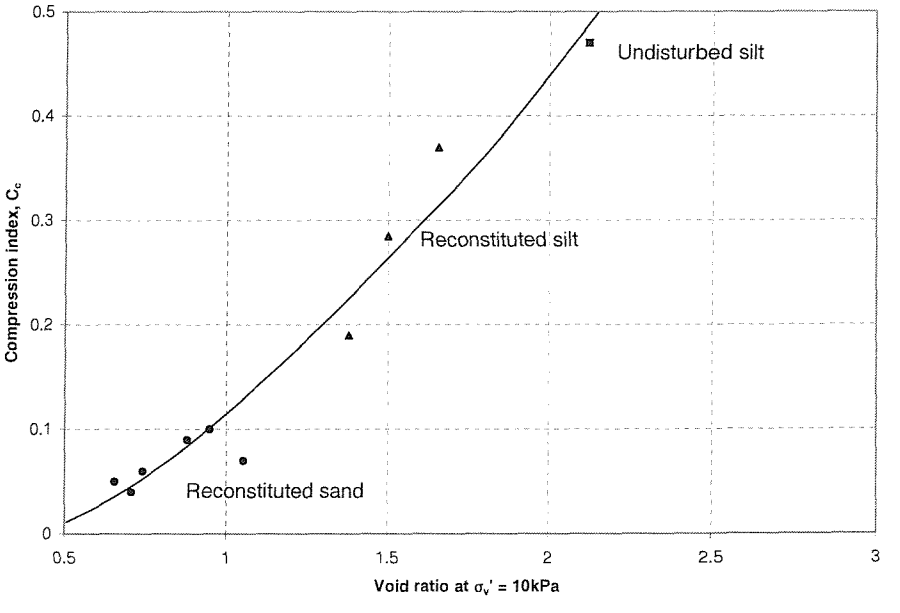

Figure 2.10: Variation of compressibility index with void ratio (after Matyas et al. (1984))

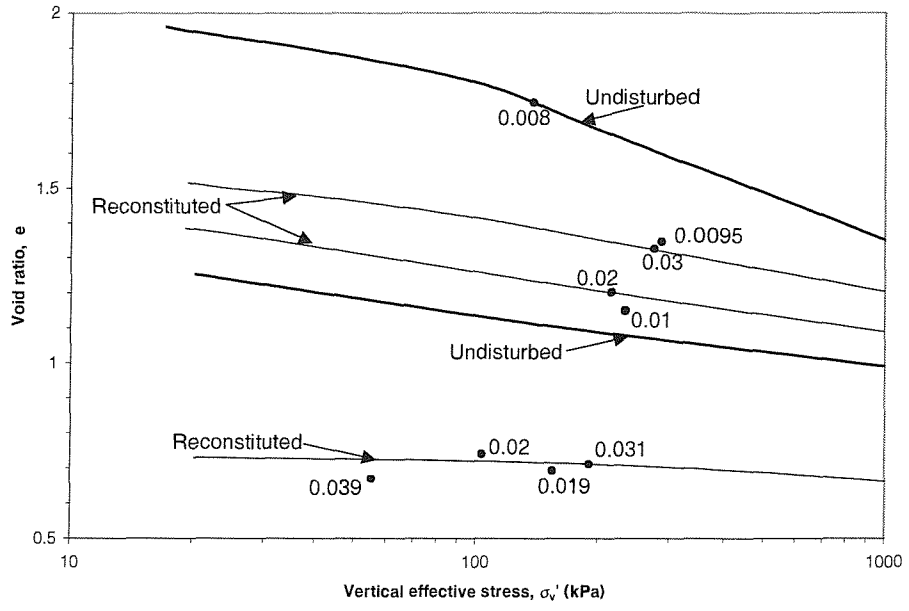

Figure 2.11: Compressibility relationship between D_{50}, σ'_v and e (after Matyas et al. (1984))

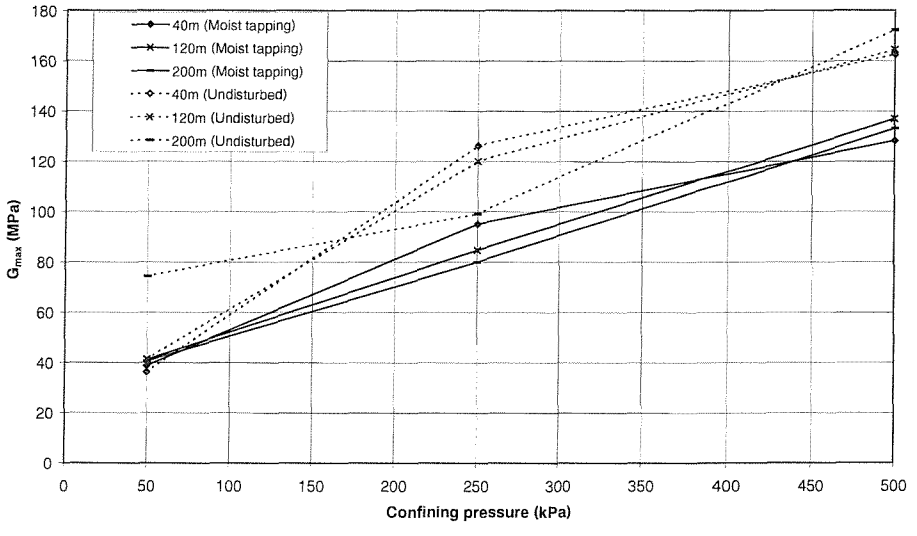

Figure 2.12: Small strain shear stiffness of silty sand tailings, with distance from dam crest and sample preparation (after Höeg et al. (2000))

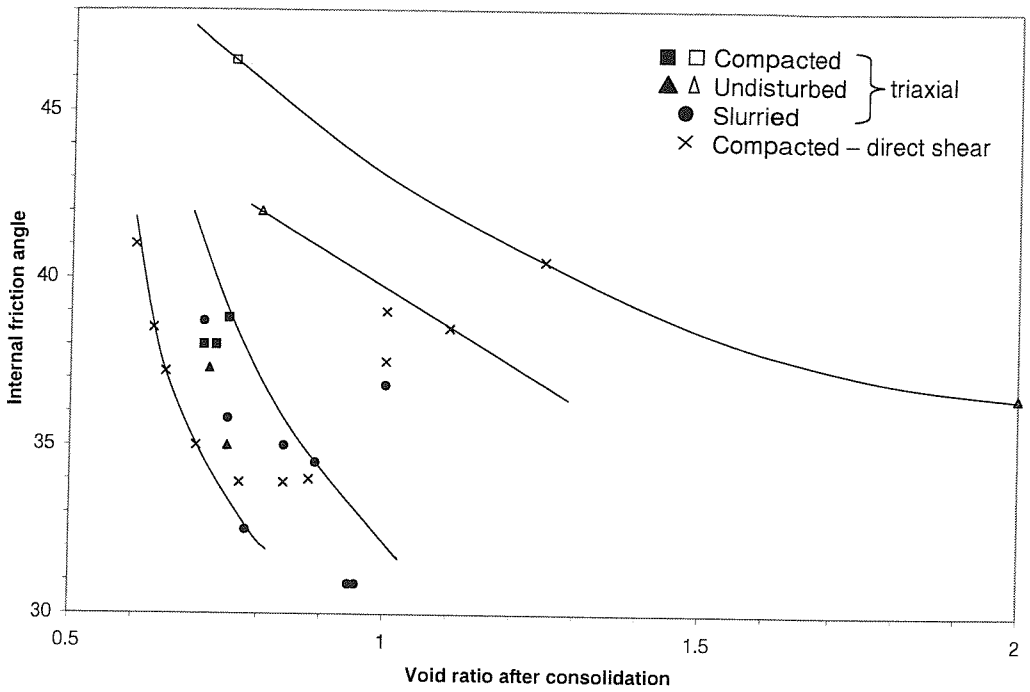

Figure 2.13: Shear strength data for sand and silt tailings (after Matyas et al. (1984))

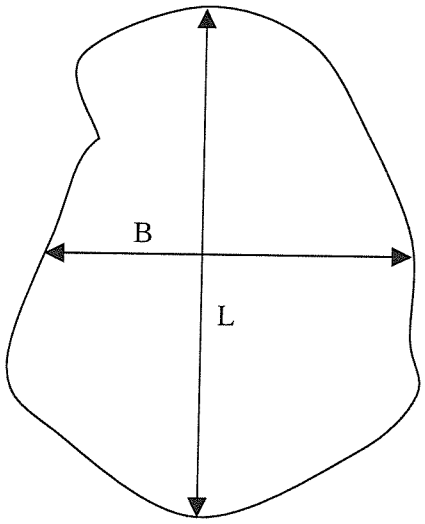

Figure 2.14: Particle dimension (after Santamarina, Klein and Fam (2001))

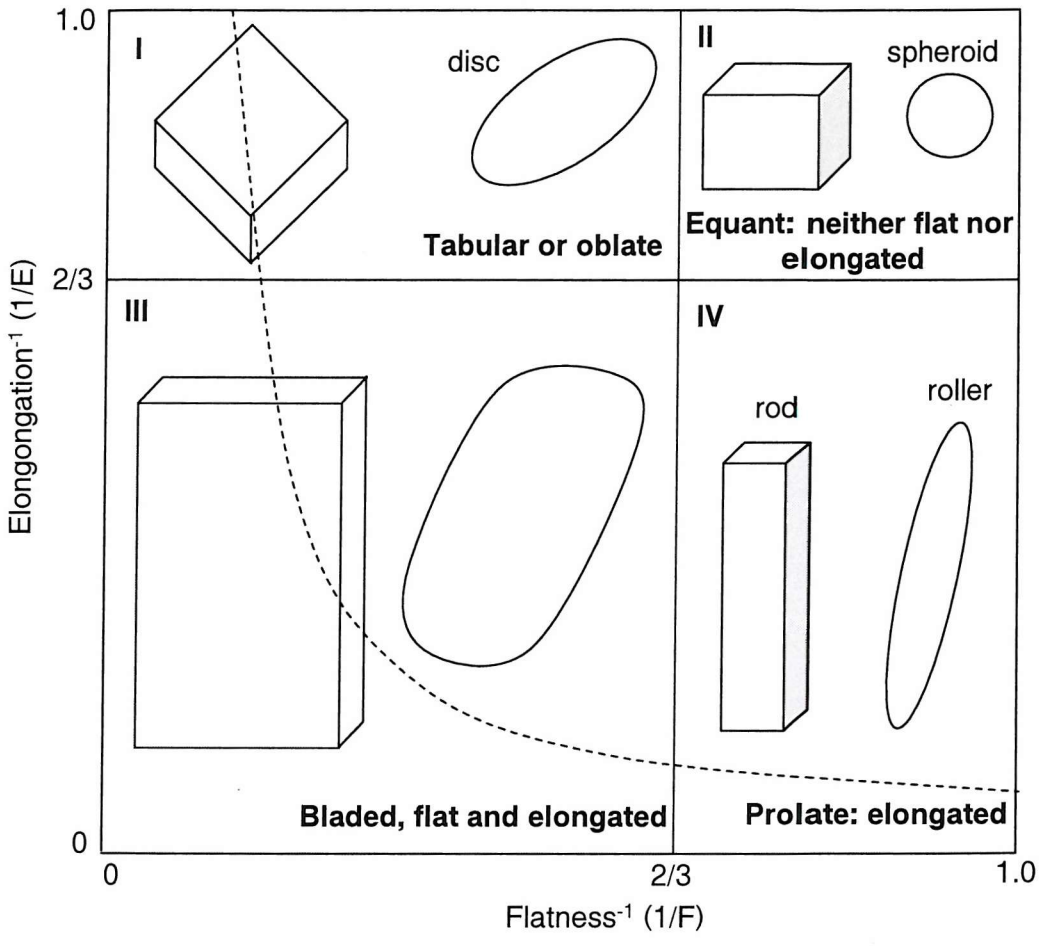

Figure 2.15: Classifying particle shape according to elongation and flatness (after Santamarina et al. (2001))

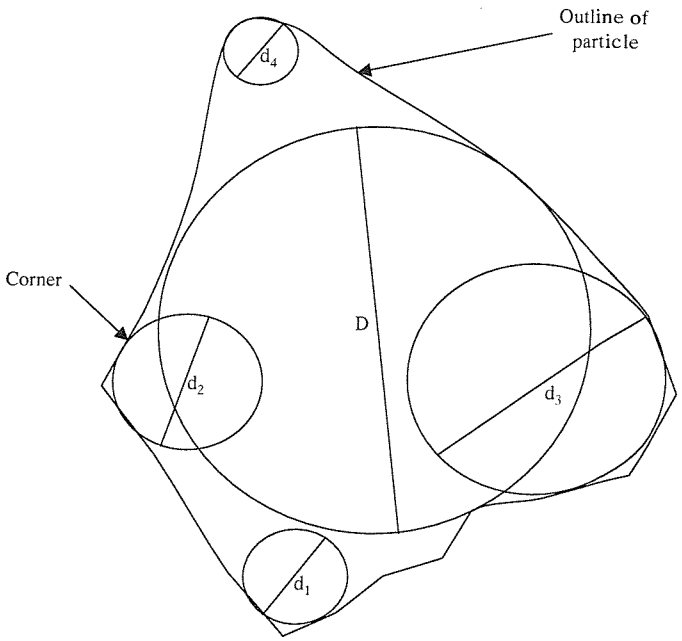

Figure 2.16: Illustration of Wadell's procedure for evaluating particle Roundness (after Sukumaran and Ashmawy (2001))

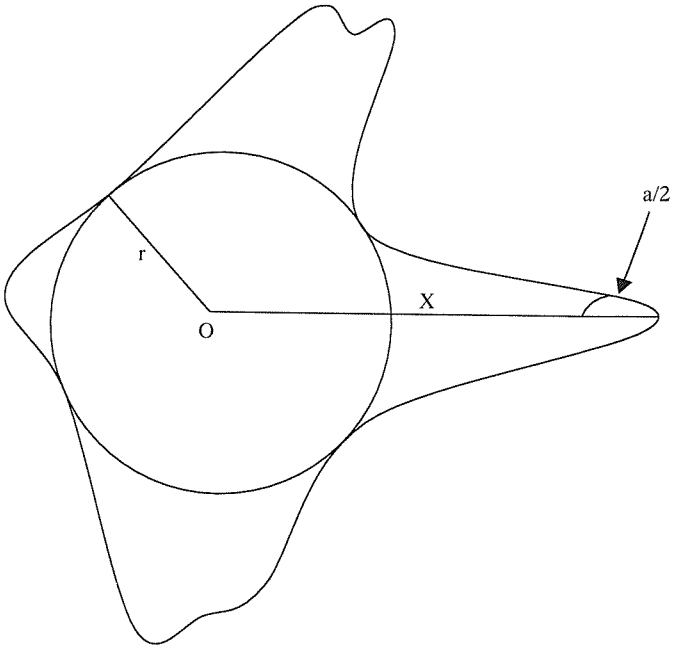

Figure 2.17: Definition of Angularity (after Miura et al. (1997))

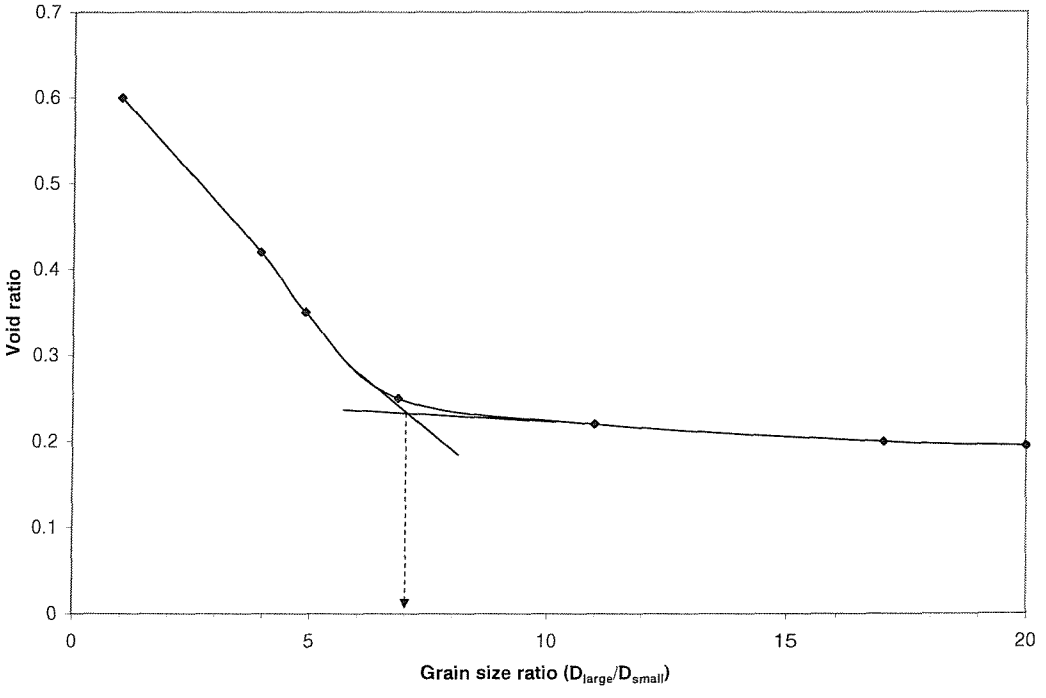

Figure 2.18: Minimum void ratios obtained for binary mixtures of round steel shot having different grain size ratios (after Lade et al. (1998))

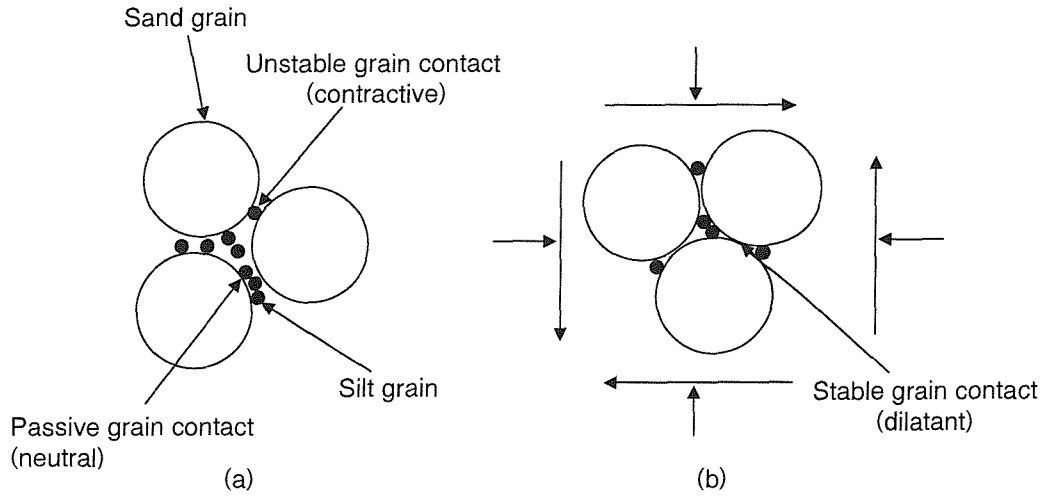

Figure 2.19: Schematic diagram of particle structure of silty sand following (a) low energy deposition and (b) isotropic compression and shear (after Yamamuro and Lade (1997))

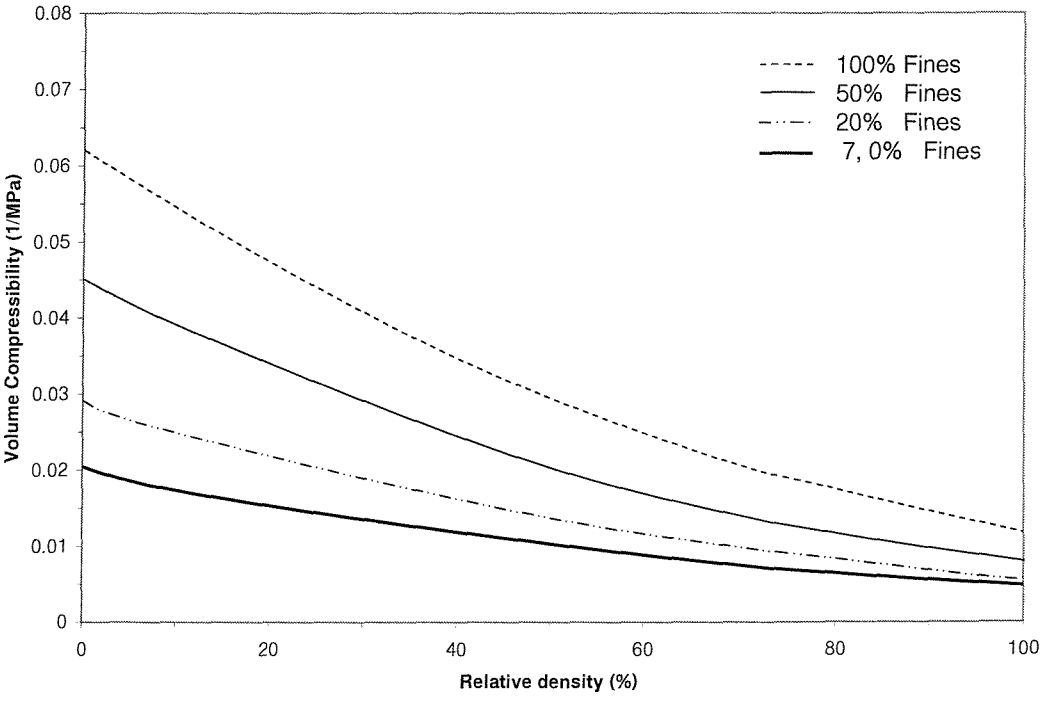

Figure 2.20: Effects of fines content and relative density on volume compressibility (after Lade et al. (1998))

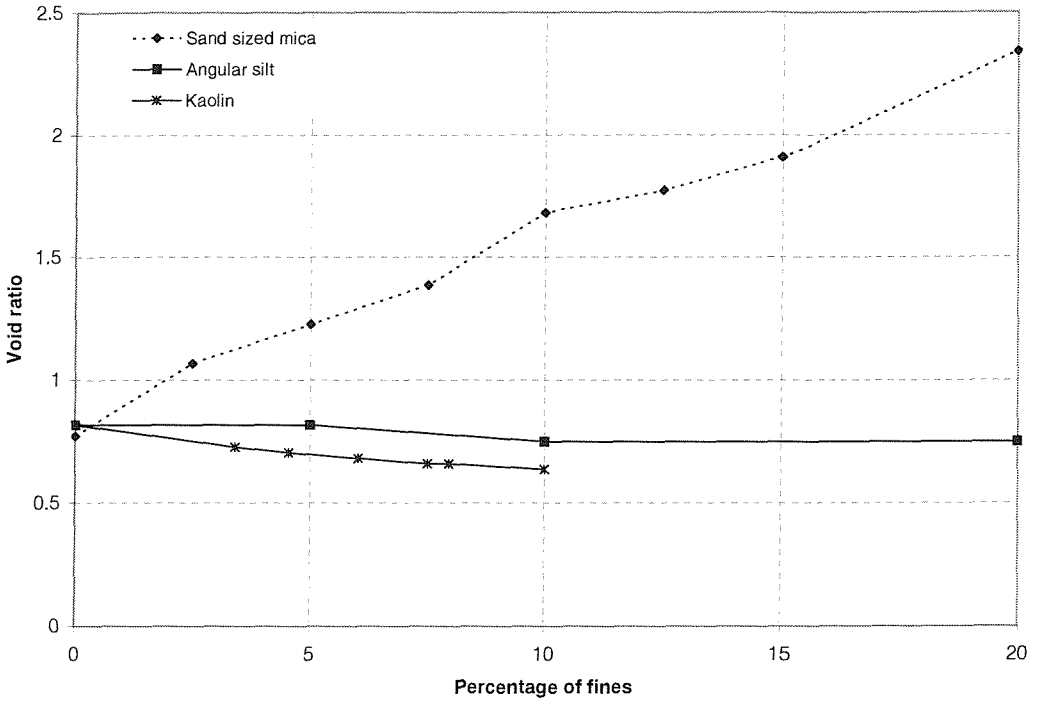

Figure 2.21: Influence of mica, silt and kaolin content on the void ratio of an uniform sand (after Hight and Leroueil (2003))

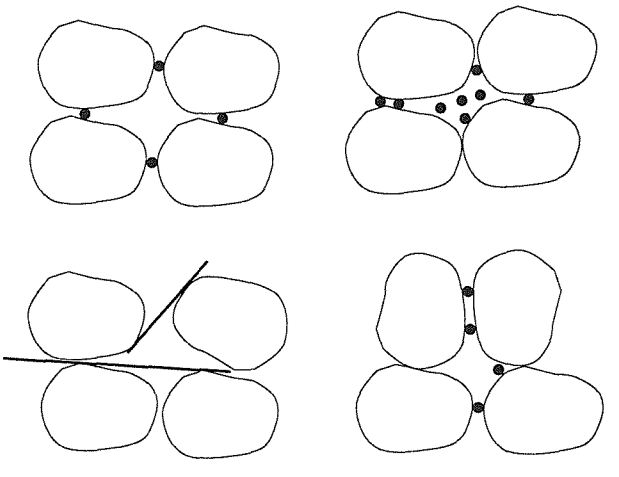

Figure 2.22: Importance of shape and location of additives in sand (after Hight and Leroueil (2003))

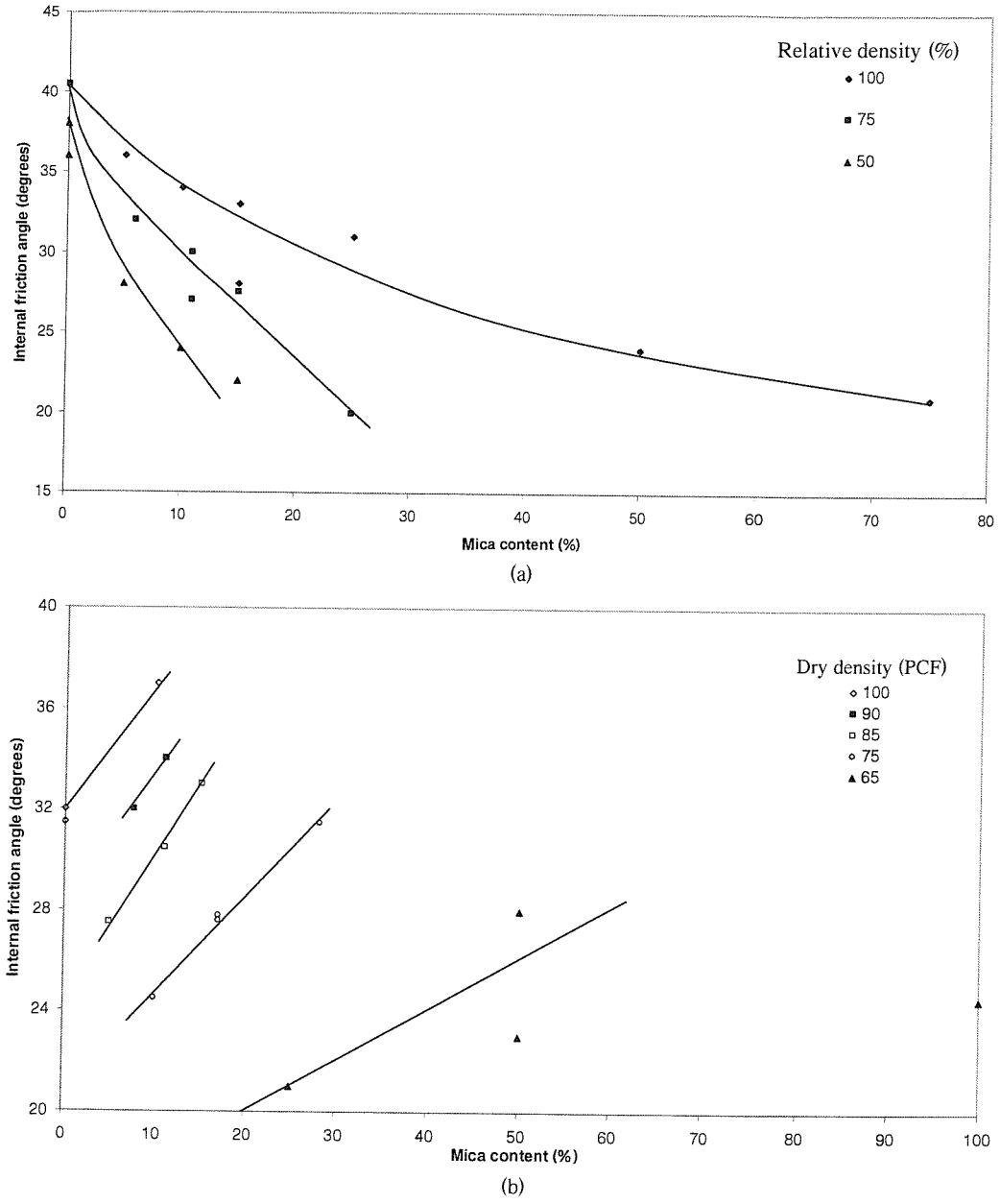

Figure 2.23: Variation in effective friction angle with mica content and (a) relative and (b) dry density at 69kPa (10psi) confining stress (after Hammond and Hardcastle (1987))

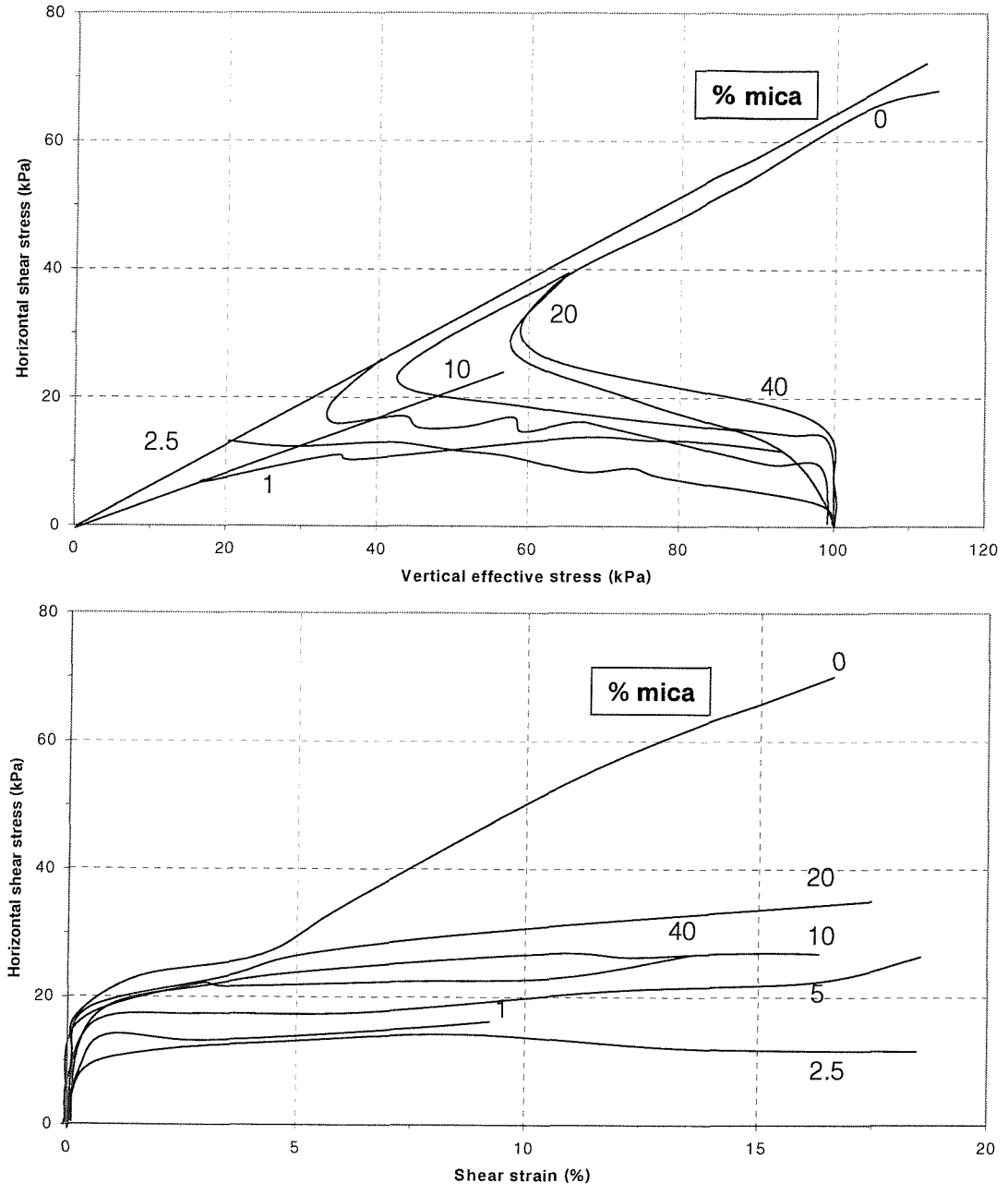

Figure 2.24: Influence of mica content on the undrained behaviour of sand in simple shear (after Hight and Leroueil (2003))

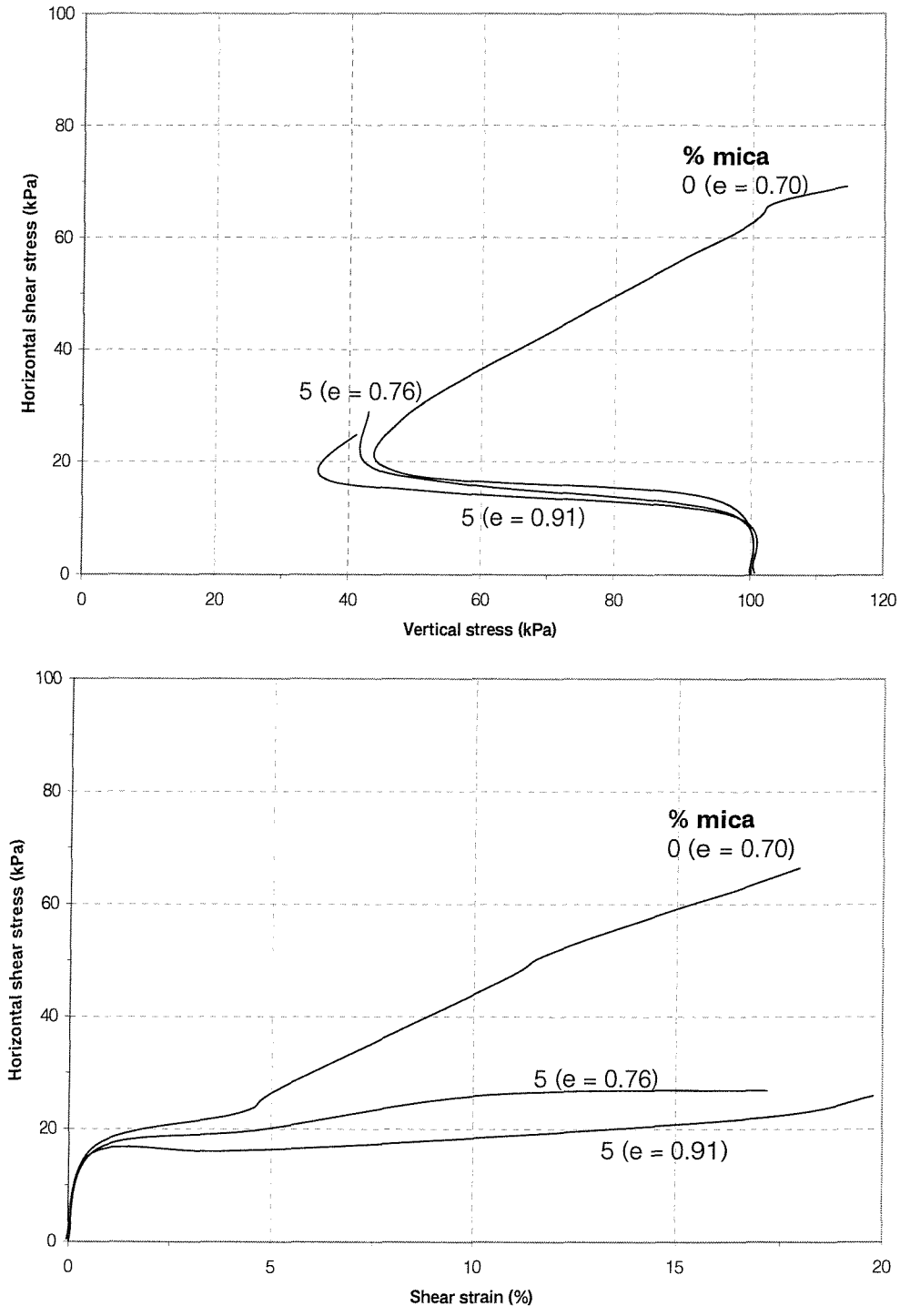

Figure 2.25: Effect of mica and void ratio on the undrained behaviour of sand in simple shear (after Hight and Leroueil (2003))

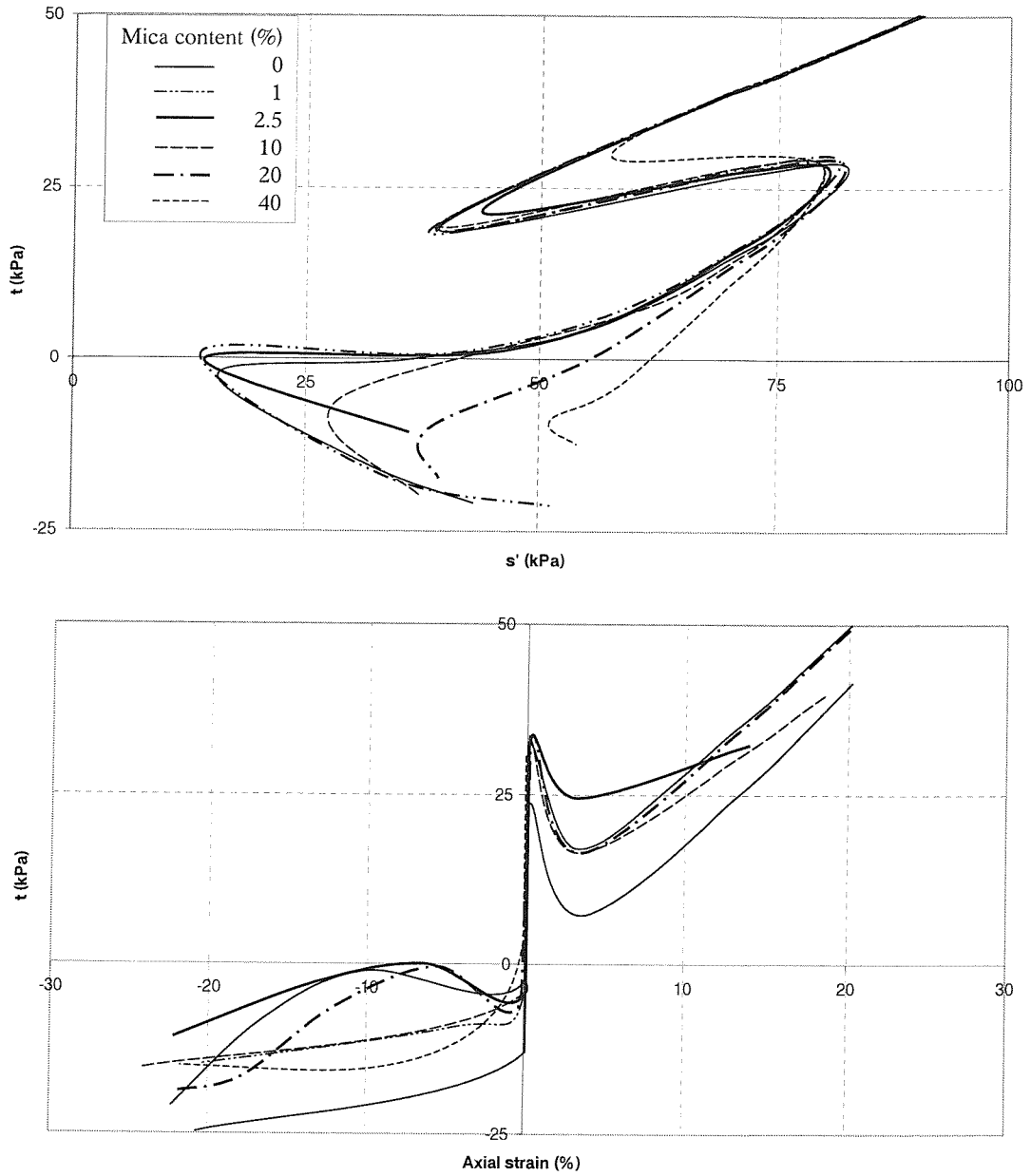

Figure 2.26: Undrained triaxial compression and extension of air pluviated sand and mica mixes (after Hight and Leroueil (2003))

Chapter 3

DEVELOPMENT OF A BENDER ELEMENT TECHNIQUE

The influence of particle shape on the compressibility, stiffness and state of gold mine tailings have been investigated by considering laboratory model tailing specimens made up of sand particles consisting of two different particle shapes i.e. platy and rotund. The instrumentation required to measure compressibility and state are well developed and details of these will follow in the next chapter. The emphasis of this chapter will be placed on work carried out to develop bender elements as a means of assessing shear stiffness. A further literature review was therefore conducted to identify possible problems that might arise. Experiments using different bender element configurations and interpretation techniques were set-up in an attempt to improve the reliability of the technique.

Bender elements are piezoelectric transducers that transform electrical energy into mechanical energy and vice versa. They consist of piezo-ceramic plates (bimorph elements) that are separated by a layer of high compliance material (Shirley, 1978) (Figure 3.1a). As the one plate contracts, the other expands under an applied voltage causing the element to bend. Bender el-

ements are normally embedded in the end plate of a triaxial testing cell or other soil testing apparatus and act as a cantilever system (Figure 3.1b). Shear and compressive stresses are induced in the surrounding soil, propagating mainly in a direction normal to the end face of the benders (Brignoli, Gotti and Stokoe, 1996). Elastic shear waves travel through the sample and force the receiver element on the opposite side of the sample to bend. An electrical current is then produced by the receiver element. The function of the bender element i.e. transmitter or receiver governs the electrical connection between the two piezoceramic plates. A parallel connection results in a maximum displacement as the voltage is applied to each plate and is normally used for the transmitter element. The receiver element is connected in series as this doubles the voltage output since this then becomes the sum of the potentials available to each of the plates.

If isotropic soil conditions are assumed, the very small strain shear modulus (G_{max}) is a function of shear wave velocity and bulk density (Equation 3.1) (Shirley and Hampton, 1978). The shear wave velocity is the ratio of the travelled distance to the time required to travel this distance. In principle, the latter can be obtained from the time lag between the transmitted and received signal, displayed on a digital oscilloscope.

$$G_{max} = \rho v_s^2 = \rho(d/t)^2 \tag{3.1}$$

where

ρ = mass density of the sample

v_s = shear wave velocity

d = distance between bender elements

t = travel time

It should be noted that errors in distance and travel time are squared when obtaining the shear modulus.

3.1 Bender element uncertainties

Bender elements have been incorporated in many laboratory apparatuses such as the triaxial cell, oedometer and simple shear (Kuwano, Connolly and Kuwano, 1999). The configuration of bender elements in an experimental set-up creates various uncertainties. These uncertainties stem from inaccuracies in the determination of wave travel time due to mechanical and electrical phenomena (Phillips, 1998). Electrical phenomena can be compensated for by placing the bender elements in direct contact with each other and measuring the response time (Brignoli et al., 1996; Gajo, Fedel and Mongiovi, 1997). Mechanical phenomena on the other hand are difficult to quantify, as they are concerned with the energy absorbing nature of soil and the damped movement of the elements due to the higher stiffness of the soil (Shirley and Hampton, 1978; Arulnathan, Boulanger and Riemer, 1998; Brocanelli and Rinaldi, 1998).

3.1.1 *Dispersion*

The dynamic interaction between the transducer and the soil causes the signal frequency of the transmitter to be lower than the electrical input frequency (Brignoli et al., 1996; Brocanelli and Rinaldi, 1998). Propagation of a shear wave through the soil appears to follow Biot's theory (Santamarina et al., 2001). According to Biot (1956) the soil response lags the induced oscillation due to frame losses (movement of particles against each other) and viscous effects (movement of pore fluid relative to soil particles). This phase delay causes the shear waves to propagate faster at higher frequencies than at lower frequencies, despite the fact that they travel in the same medium. The shear wave energy then drives the receiver element as a harmonic oscillator, although once again its movement is damped by the soil (Blewett, Blewett and Woodwards, 2000).

Figure 3.2a illustrates the phase lag (solid line) and relative velocity (dotted line) with frequency response of a theoretical forced harmonic oscillator.

It can be seen that as the resonant frequency is approached from a lower frequency, the phase lag between the drive and response increases. The amplitude response has a similar behaviour (Figure 3.2b). Once the driving and resonant frequencies are equal, the amplitude reaches a maximum and the phase delay changes rapidly. Beyond resonance, the amplitude response decreases and the phase lag changes to being out of phase. The width of the resonant region is governed by the damping of the subsystem, i.e. heavy damping results in a wider resonant region while light damping results in a narrow but high resonance.

Figure 3.3 illustrates the velocity (solid line) and relative amplitude (dotted line) response with frequency for a Biot medium. Dispersion causes the shear wave velocity to increase with frequency which is opposite to the forced harmonic oscillator behaviour where the velocity decreases as resonance is approached. The amplitude response of the medium is similar to that of the forced harmonic response although the resonant region is large when compared with a heavily damped harmonic oscillator response.

Figure 3.4 illustrates a velocity-frequency profile as a shear wave is firstly induced in a soil sample (Figure 3.4a) and secondly received by the opposite bender (Figure 3.4b). The soil behaviour is modelled by Biot's theory whilst the bender element by forced harmonic oscillation. Considering the bender element-soil response (Figure 3.4a), it can be seen that the bender element (forced harmonic oscillation) response initially dominates. The velocity decreases at resonance (approximately 1kHz in this example) followed by an increase in velocity at higher frequencies as the soil response becomes active. In the second case (Figure 3.4b), the velocity is initially governed by the Biot response (soil) and increases until resonance (3.5kHz in this example). The forced harmonic response then becomes active and the velocity decreases. Consequently, the measured response is not a true measure of the soil characteristics as was initially postulated. Blewett et al. (2000) investigated the phase and amplitude response of sand using bender elements. Experiments were carried out simulating the response in both finite and infinite sand lay-

ers. The experiments confirmed the combined theoretical behaviour.

"The relation between attenuation[1] and dispersion can be generalized: in a linear, casual system attenuation implies dispersion." Santamarina et al. (2001). Although bender elements are not traditionally employed for assessing the attenuation characteristics of soil, some estimate could be obtained. The attenuation of a soil can be estimated from a combination of its geometric, apparent attenuation as well as material losses. According to Santamarina et al. (2001), the last two contribute very little to the total attenuation of the soil and can thus be ignored. Geometric attenuation can be estimated from:

$$\frac{A_2}{A_1} = (\frac{r_1}{r_2})^{\varsigma} \tag{3.2}$$

where

A_1 = amplitude of first receiver

A_2 = amplitude of second receiver

r_1 = location of first receiver relative to transmitter

r_2 = location of second receiver relative to transmitter

ς = constant

The following values can be assumed for ς, depending on the shape of the wavefront:

0 = plane waves in infinite media

0.5 = cylindrical fronts

1 = spherical fronts

[1] amplitude decay as a function of time and distance due to geometric spreading, material losses and partial transmission and scattering (Fratta and Santamarina, 1996)

In decibel notation, attenuation can be expressed as:

$$dB = 20\log(\frac{A_2}{A_1}) \tag{3.3}$$

3.1.2 *Near field effects*

Detection of the shear wave arrival is complicated by what is called the near field effect (Santamarina et al., 2001). The near field effect is the result of coupled waves that have similar particle motion but different propagation velocities and attenuation rates. Reflective body energy is created at the interface between soil layers and boundaries (Zywicki, 1991) and has the following properties:

- the type and amount of energy reflected is governed by the elastic parameters, mass density and angle of incidence (Zywicki, 1991),
- the reflected waves travel at a velocity equal to that of the compression waves (induced by the bender oscillation, but to a lesser extent than the shear wave) (Sanches-Salinero, Roesset and Stokoe, 1986) and
- once the energy is reflected, it propagates cylindrically at a decaying rate equal to $\sqrt{x}$, where x is the radial distance from the source (Zywicki, 1991).

These additional waves created by the near field effect arrive as an apparent compression wave prior to the actual shear wave but with a smaller amplitude (Gordon and Clayton, 1997). The influence of the near field effect on the measured travel time can be minimized by separating the source and receiver element by an adequate distance (Stokoe and Santamarina, 2000). The exact distance by which to separate the transmitter and receiver is unclear as the extent of the near field or Fresnel zone (Santamarina et al., 2001) is unknown.

Various empirical relationships exist that attempt to define the boundary between near and far field. The 'field' around a point source could be described by means of a two-region model i.e. the near field (Fresnel zone)

and the far field (Fraunhofer zone) or a three-region model namely Fresnel, transitional and Fraunhofer zone (Capps, 2001). Depending on the model adopted, the boundary between the near and far field varies from a clear boundary to a zone.

Sanches-Salinero et al. (1986) evaluated the assumptions made by the different methods for interpreting the travel time from methods such as the down-hole or cross-hole tests. An analytic solution for body waves generated by point sources in a 3-D elastic space was used to illustrate that wave fronts spread in a spherical manner and involved coupling. It was shown that cross correlation could be used to derive the shear wave velocity provided that the distance (d_1) between the source and first receiver was greater that one wavelength (λ) and the distance between the source and second receiver was twice d_1. The transverse motion (S) of waves through an infinite isotropic elastic medium following a sinusiodal pulse transmitted from a point source could be represented by the following equation:

$$S = \frac{\Gamma}{4\pi\rho v_s^2} \tag{3.4}$$

where

$$\begin{aligned} v_s &= \text{shear wave velocity} \\ \rho &= \text{density of the medium} \\ \Gamma &= \text{coupling} \end{aligned}$$

It was found that the shear wave has three coupled components namely:

$$\Gamma = \Gamma_1 + \Gamma_2 - \Gamma_3 \tag{3.5}$$

These three terms represent transverse motion, but with different propagation velocities. The first two terms (Γ_1 and Γ_2) propagate with the velocity of a shear wave while the last with the velocity of a compression wave. Attenuation due to geometrical damping occurs at different rates for the three

components with the last two terms attenuating an order of magnitude faster than the first term. The first term (Γ_1) presents the far field shear wave. A travel distance/wave length (d/λ) ratio was defined and results were presented accordingly. It was noted that the shape of the received signal is controlled by this ratio through the degree of attenuation. Consequently it was recommended to separate the receiver and transmitter by at least 2 to 4 wavelengths (Sanches-Salinero et al., 1986; De Alba and Baldwin, 1991; Gohl and Finn, 1991; Stokoe and Santamarina, 2000). Care should be taken when applying this approximation to a laboratory bender element configuration as it was developed for field conditions employing multi receivers (Arroyo, Wood and Greening, 2003), a transmitter that acts as a point source and the propagation of planar waves. Brignoli et al. (1996) demonstrated the existence of near field effects in bender element tests. Near field effects are potentially more complicated in a triaxial specimen (Arulnathan et al., 1998) as:

- Interpretation techniques that use the input signal, correspond to a d/λ of zero. Consequently, near field waves will be stronger than were considered in Sanches-Salinero et al. (1986) analysis.

- The spherical spreading of the wave front generated by the transmitter element can reflect from boundaries and thus travel between benders by indirect paths (Rio, Greening and Medina, 2003).

- The transmitting element is not a point source and hence the assumption of planar waves moving one dimensionally between caps will introduce errors.

Arulnathan et al. (1998) investigated the influence of bender element length (i.e. bender element protrusion) (l_b), travel distance (L) and wavelength (λ) on the derived shear wave velocity within a conventional bender element configuration. Following tests on a variety of soils, they suggested that the optimum input frequency range for these instruments often correspond to a λ/l_b of 8 to 16. This range of input frequencies seems to balance the following competing factors:

- the transmitting element appears as a "point source" at the receiver element for values of $\lambda/l_b \gg 4$,
- waves generated by the transmitting element can become more complex at λ/l_b values close to 4 due to resonance of the bender element,
- the output signal is strongest for λ/l_b near 4 and decreases with increasing λ/l_b,
- theoretically, distortion of the output signal increases with increasing λ/l_b and
- in order to reduce the influence of near field effect, L/λ needs to be a maximum and λ/l_b minimum.

Following the discussion above it can be concluded that the extent of the near field is unknown. It is not clear which ratio would yield the most reliable results. The approximation of Sanches-Salinero et al. (1986) is widely adopted by other researchers such as Viggiani and Atkinson (1995), Jovičič, Coop and Simic (1996), Brignoli et al. (1996) and Arulnathan et al. (1998).

3.1.3 *Effective travel length*

The effective travel length of the shear wave presents some uncertainty as bender elements protrude some distance into the sample. Dyvik and Olsen (1989) investigated the possibility of incorporating bender elements into oedometer and simple shear apparatuses. The results were compared with those obtained from triaxial and resonant column apparatuses. Comparable results were only obtained if a tip-to-tip travel distance was used. In order to determine what the effective sample length should be, Gordon and Clayton (1997) and Viggiani and Atkinson (1995) experimented with sample height. The effective stress of a sample was varied and the corresponding travel time was noted. A linear regression analysis of the travel time and sample height indicated that the effective travel distance of the shear wave was equal to the

distance between the bender tips. Similar results were obtained if the bender protrusion height as opposed to the sample height was varied (Brignoli et al., 1996). As all of the above experiments yield similar results, it seems reasonable to use a tip-to-tip travel distance in calculations.

3.1.4 *Travel time*

The accuracy of measured shear stiffness using bender elements is governed mostly by the accurate measurement of the arrival time. The literature suggests that this is not a simple matter as the driving signal separates into several frequency components, distorting the received signal. It is then up to the experimentalist to decide which part of the distorted signal best represents the arrival of the shear wave. Figure 3.5 illustrates this phenomenon. The transmission of the input wave is clearly defined, but some doubt exists about the shear wave arrival time, it being point 0, 1 or 2 (Viggiani and Atkinson, 1995). Abbiss (1981) proposed that the first deflection of the received wave (Point 0) should be adopted as the arrival of the signal. This proposal was based on an investigation where the polarity of the received signal was reversed and compared. Viggiani and Atkinson (1995) measured the shear stiffness of an over consolidated clay using bender elements. The aim of the investigation was to determine the correct point at which the shear wave arrives. The results of a numerical analysis indicated that shear wave arrival should be taken as the first point of inversion, i.e. Point 1 in Figure 3.5.

3.2 Bender element techniques

Interpretation of bender element results is not as simple as initially suggested in the literature. As noted in the above discussion, complicated interference patterns are established within the sample due to, among other things, the sample geometry (Rio et al., 2003). The quality of the received signals are governed by a combination of these patterns, the resonant frequency of the

bender elements itself and the dispersive nature of the material (Brocanelli and Rinaldi, 1998). Researchers such as Dyvik and Madshus (1985), Viggiani and Atkinson (1995), Jovičič et al. (1996), Blewett, Blewett and Woodwards (1999) and Airey (2003) have developed alternative techniques for determining the shear wave velocity to reduce the influence of these. These techniques can be divided into two categories namely time-of-flight and phase sensitive techniques. The former determines the group velocity by considering the travel time of a shear pulse. Phase sensitive techniques on the other hand are based on the phase velocity of a shear wave (i.e. the phase shift between the transmitted and received waves at a given frequency). Table 3.1 summarises the various bender element interpretation techniques as adopted by the various researchers.

As already mentioned, interpretation of bender element results is complicated with the result that the reliability of these instruments is unknown. The reliability of an instrument is normally evaluated in terms of its uncertainty in measurement. This is quantified in terms of its conformance, noise, accuracy, precision (repeatability), resolution and sensitivity (Dunnicliff, 1988). Only two of these namely accuracy and precision is affected by bender element interpretation technique. Few instruments are currently available that can measure the small strain shear modulus of soil. The accuracy of these measurements is also unknown so that the accuracy of bender element results is difficult to quantify. It is however, possible to determine the repeatability (precision) of the bender element results and this will thus be used to evaluate the reliability of the various techniques.

In order to simplify comparison between bender element interpretation techniques, a material with a low intrinsic attenuation was selected. The group and phase velocity of a Leighton Buzzard sand specimen (particle size 300μm to 600μm, silver in colour) was measured by exciting the transmitter with a single pulse and continuous wave respectively. A conventional bender element configuration, i.e. bender elements embedded in the end platens of a triaxial apparatus, was adopted (Figure 3.6). The sample was prepared using

wet pluviation to a bulk density of $1977kgm^{-3}$ (relative density 68%) and consolidated to an isotropic effective stress of 305kPa.

3.2.1 *Time-of-flight techniques*

Several group velocity techniques (Table 3.1) were investigated. The transmitter element was excited with a 20V peak-to-peak square or sinusoidal pulse, generated by a TTi (Thurlby Thandar Instruments) TG1010 function generator. An input frequency of 15kHz was adopted for comparative reasons. The internal trigger of the function generator was set to generate a single pulse every 5ms. The transmitted and received signals were monitored and logged by a LeCroy 9314 AM Quad 400MHz digital storage oscilloscope. Arrival of the shear wave was taken as the first peak, obtained from hand picking. In order to simplify the picking process, the input signal was reversed (Figure 3.7). Typical recorded signals are shown in Figures 3.8 and 3.9. A shear wave velocity of between $348ms^{-1}$ and $358ms^{-1}$ and corresponding shear modulus of 240MPa and 254MPa was measured (Table 3.2).

3.2.2 *Phase sensitive technique*

The transmitter element was excited with a 20V peak-to-peak continuous sinusoidal wave, generated by the function generator. The phase velocity of the specimen was measured using a low frequency spectrum analyser (Hewlett Packard 3582S) which recorded the transmitted and received amplitudes as well as the phase angle and coherence between the two signals. The coherence of two waves provides a measure of the extent that the output signal is the result of the input signal (Fratta and Santamarina, 1996). Only phase angles with a coherence of 0.98 or greater were considered. This implied that only the frequency range common to both signals was processed, thus minimizing the influence of noise and allowing for the correct interpretation by averaged data (Mancusco, Simonelli and Vinale, 1989). The recorded results in this research were averaged to a RMS (root-mean-square) of 16.

Figure 3.10 shows the recorded results in the frequency domain. The change in phase angle and relative amplitude with frequency are represented by the solid and broken lines respectively. The data was obtained by sweeping the input frequency between 5.4kHz and 15kHz at 0.2kHz intervals. The shear wave velocity is related to frequency and wavelength through the fundamental equation:

$$v_s = \frac{L}{t} = f\lambda \tag{3.6}$$

At any given input frequency, the wavelength can be determined from the phase lag in measurement made between two points

$$\lambda = \frac{2\pi}{\Phi} L \tag{3.7}$$

From this it follows that the slope of the phase difference/frequency curve is inversely proportional to the shear wave velocity, since

$$\frac{\delta\Phi}{\delta f} = \frac{2\pi L}{v_s} \tag{3.8}$$

where

$$\begin{aligned} L &= \text{travel distance (m)} \\ t &= \text{travel time (s)} \\ \delta\Phi &= \text{change in phase angle (radians)} \\ f &= \text{frequency of the driving wave (Hz)} \end{aligned}$$

A linear regression (between phase angle and frequency) was fitted to each cycle (180° to −180°) to determine the travel time of the shear wave (Equations 3.6 to 3.8). It can be seen from Figure 3.10 that this relationship is frequency dependent, as suggested by Blewett et al. (2000). The highest correlation factor ($R^2 = 0.9996$) was obtained between input frequencies of 11.4kHz and 12.4kHz. The output amplitude also varied with frequency. Three peaks were found at 9.6kHz, 11.8kHz and 14.7kHz respectively with

the last being the maximum. The correlation factor obtained over the input frequency range of 12.6kHz to 15kHz however, proved to be the lowest for the data set (0.6824), indicating that some other mechanism may be at work. Depending on which frequency range was considered, the wave velocity was found to vary between $216ms^{-1}$ and $575ms^{-1}$ (giving a shear modulus between 92MPa and 651MPa).

Initially it was expected that it might be possible to derive a single shear wave velocity from the data set. It was soon realized that the measured velocity incorporated the effects of interference as well as Biot coupling (dispersion). According to Santamarina and Aloufi (1999), Biot dispersion can lose its relevance in soil due to scattering effects. This however, will only happen when the wavelength approaches the grain size which was not the case. In order to isolate the true phase velocity from these effects, the bender element configuration was changed. This will be considered in Section 3.3. A preliminary estimate of the phase velocity using the current bender element configuration was obtained from the relationship between the cumulative phase angle and frequency (Figure 3.11) over the entire frequency range. This resulted in a shear wave velocity of $215.54ms^{-1}$ and shear modulus of 92MPa. This differs from the previous (Figure 3.10) results as an average shear wave velocity was obtained from the input frequency range of 5kHz to 15kHz whereas the previous results were based on the shear wave velocity for a phase shift of 2π.

3.3 New bender element technique: Two side bender receiver elements

It was noted in Section 3.2 that several factors noticeably influenced the measured shear wave velocity when employing a phase sensitive technique. In order to measure the shear wave velocity more reliably, these factors should be avoided. It was considered that this could be achieved by measuring the change in phase velocity between two side bender receiver probes (R1 and

R2) as opposed to the phase shift between a transmitter and receiver (Figure 3.12). The two receiver elements are subjected to similar interference patterns, resonant frequency, coupling effects and dispersion and would hence contain more similarities. The dispersion results partly from forced harmonic oscillation (Blewett et al., 2000) and relatively high strains induced in the vicinity of the transmitter by its movement. This configuration would also hopefully simplify the determination of the group velocity from time-of-flight techniques, as the recorded signals would closely resemble each other, perhaps with differences in amplitude and frequency due to attenuation.

Although this configuration has been in use for several years in the geophysical discipline (for example in parallel cross hole testing (Hope, Clayton and Butcher, 1999)), it is considered to be the first laboratory application.

3.3.1 *Specimen preparation*

The conventional wet sand pluviation technique was slightly modified to allow for bender element probes to be inserted along side of the specimen. A three-part split mould was modified to incorporate the side bender element probes at third height intervals. Small holes were cut into the membrane at predetermined locations and the probes were inserted using a technique similar to that used for mid-plane pore pressure measurement (Hight, 1982). Figure 3.13 shows the equipment used for this task. The inside of the membrane was filled with de-aired water to three quarters of the height of the mould after which Leighton Buzzard sand (size 300μm to 600μm) was pluvated into the mould to a similar density as before. Once the top-cap was in place, a suction of 20kPa was applied to the specimen. The mould was removed and the cell filled with de-aired water. An effective effective consolidation pressure of 305kPa was applied to the specimen.

3.3.2 *Time-of-flight technique*

In this experiment, the shear wave velocity of the specimen was derived from the travel distance and time required for a pulse to travel between the two receiver element probes. The distance used to calculate the group velocity was taken as the difference in distance between the centre of the transmitter and centre of each of the receivers ($r_1 - r_2 = 57.6mm$, Figure 3.14). This is less than the tip-to-tip distance (66.1mm). Figure 3.15 is an example of the recorded signals measured by each of the receiver element probes (R1 and R2) when the transmitter was excited with a single sinusoidal pulse at a frequency of 15kHz. The received signals were once again reversed to assist in picking of the first peak (Figure 3.16). The use of the square input pulse was abandoned due to its high frequency content. It can be seen from Figure 3.16 that the frequency content varied significantly with the input frequency of a single sinusoidal pulse. In order to investigate the extent of this, the frequency content of the received signals was measured with the spectrum analyser (Figure 3.17). As expected, a wide range of frequencies was generated. It should however, be noted that the measured amplitude is displayed on a logarithmic scale and that the dominant frequencies follow that of the input frequency.

In order to establish whether the group velocity was also frequency dependent, the transmitter element was excited with a range of frequencies (3kHz to 30kHz) (Figure 3.18). The average velocity over this frequency range was calculated as $355ms^{-1}$ with a standard deviation of $11ms^{-1}$ (i.e. measurements are within 3.1% of the average measurement). The measured shear wave velocity below 8kHz appeared to be more scattered than above this value. This may be attributed to the influence of near field effects. As mentioned in Section 3.2.1, the extent of the near field is unknown and consequently various equations exist to obtain some approximation (Section 3.1.2). Sanches-Salinero et al. (1986) approximation was adopted as multi receivers were used which is similar to the configuration employed by them. The distance between the transmitter and first receiver (R1) in this experiment was

78.4mm. If the wavelength were calculated from the average measured shear wave velocity divided by the frequency, two wavelengths would only be obtained at an input frequency of 9kHz. The average shear wave velocity and standard deviation calculated from 9kHz and beyond equates to $351.5ms^{-1}$ and $5ms^{-1}$ respectively (i.e. a coefficient of variation of 1.4%).

3.3.3 *Phase sensitive technique*

The shear wave velocity of the specimen was then derived from the change in phase angle with frequency between the transmitter and Receiver 1 ($\Delta\Phi_1$), transmitter and Receiver 2 ($\Delta\Phi_2$) as well as between the two bender receivers ($\Delta\Phi_3$). Figure 3.19 shows the change of phase angle ($\Delta\Phi_3$) between the two receiver elements and relative amplitudes with input frequency of the two receivers. It can be seen that the ratio of phase angle to frequency varies with input frequency and does not bear any resemblance to that measured in Section 3.2.2. Considering the relative amplitude of the two side benders, it can be seen that both reach a maximum at 14kHz (possibly implying resonance at this point). In order to establish whether the unanticipated results which could not be interpreted were due to an experimental error or an inherent problem, the phase difference between the two receivers was calculated from independent data. This was done by subtracting $\Delta\Phi_2$ from $\Delta\Phi_1$. Figure 3.20 shows the measured (solid line) and calculated (broken line) change in phase angle with input frequency. It is evident that the two are similar, implying that the measured results were indeed correct and thus not caused by an experimental error.

Whilst the measurement of the shear wave velocity using a phase sensitive technique showed that the phase velocity is frequency dependent, the measured group velocity did not suffer from the same problem. In order to understand why this difference arises, the two cases need to be addressed separately.

In the case of a single input pulse, a wave front is generated that initially propagates through the sample in a spherical pattern. Once a boundary is

encountered, it is reflected back and an interference pattern is established. It is of short duration as the reflected wave front decays and is thus strongest in the vicinity of the induced wave front. On the other hand, if the transmitter element is excited with a continuous wave, energy is continuously put into the system, implying that the amplitude remains constant. In this case a complex interference pattern is set up. The complexity of the pattern is a function of the geometry of the sample and is frequency dependent.

Figure 3.21 considers the cumulative phase angle as a function of input frequency. The relationship between the two is clearly not as consistent as previously (Figure 3.11) and also differs quite significantly from the previous correlation factors. If the calculated correlation was adopted, a shear wave velocity of $168ms^{-1}$ and shear stiffness of 56MPa would be obtained which greatly differs from the previous results. A possible explanation for this is that due to radiation and reflection, interference patterns are established in the specimen.

The position of the receiver elements for the two configurations differ, which implies that the amplitude and phase angle varies, depending on whether constructive of destructive interference occurs. The time-of-flight technique would thus be considered henceforth.

3.4 Three side bender element probes

On the basis of the previous results, it was concluded that shear wave velocity measurement using a time-of-flight technique would provide more repeatable results. As a final refinement, the bottom transmitter was replaced with a side bender transmitter, thereby reducing reflection from the base pedestal (Figure 3.22).

A Leighton Buzzard sand specimen was prepared (using a similar technique as before) to a bulk density of $1961kgm^{-3}$. The mould used for doing so was modified to incorporate the three bender element probes. The sample was consolidated to a confining pressure of 300kPa prior to shear stiffness

measurements.

In order to compare the results with those obtained in Section 3.3.2, the transmitter probe was excited with a sinusoidal pulse over a range of frequencies (6kHz to 30kHz). The influence of attenuation and pulse broadening on the travel time was investigated by considering the first 6 peaks of the received signals (Figure 3.23). It could be seen from this Figure that the amplitude of the first peak is fairly low in comparison with the rest. The group velocities derived from these 6 peaks are shown in Figure 3.24. The group velocity obtained from the first peak is more scattered than those of the second and third peak. The group velocities derived from Peaks 5 and 6 appear to be lower than the rest, implying an overestimation in the travel time. This may be the result of pulse broadening caused by attenuation of the higher frequencies. Based on these observations it was decided to derive the travel time from the time difference between second peaks of the two receiver signals.

The group velocity derived in this fashion is shown in Figure 3.25. The average shear wave velocity was calculated as $339.4ms^{-1}$ with a standard deviation of $5.4ms^{-1}$ (i.e. coefficient of variation of 1.6%), resulting in an average shear stiffness of 225.9MPa. The transmitter and first receiver (66.8mm apart) were two wavelengths removed from each other at an input frequency somewhere between 9kHz (1.8 wavelengths) and 12kHz (2.4 wavelengths). If the measured result between 12kHz and 30kHz is considered, a shear wave velocity and standard deviation of $337.2ms^{-1}$ and $3.6ms^{-1}$ respectively are obtained.

The laboratory investigation indicated that shear wave velocity obtained from time-of-flight techniques is more repeatable than that of a phase sensitive technique. The bender element configuration was altered to two side bender receiver probes as it was anticipated that they would be subjected to similar interference patterns, resonant frequency, coupling effects and dispersion. The travel time of the shear wave was derived from the time lag between the two received signals and since these two contained more simi-

larities, this configuration greatly simplified interpretation of bender element results. It should be noted that near field effects could not be eliminated by the change in configuration. Shear wave velocity measurements employing a time-of-flight technique, appeared to be repeatable. The use of a third side bender element (transmitter) slightly improves the standard deviation of the results by 0.4%. This may be attributed to the reduced reflection from the base pedestal. This improvement in standard deviation however, is so small that it probably falls within the experimental error. The advantage that this configuration has over the previous two is its simplicity. Very little modification to the triaxial apparatus is required for small strain shear modulus measurement. Interpretation of bender element results using a time-of-flight technique and the current configuration however, still had some element of operator dependency.

In order to reduce operator dependency, cross correlation was investigated as an alternative. It was anticipated that cross correlation would suppress the effects of noise on the signal to some extent and can be automated. Cross correlation has been employed by other researchers such as Viggiani and Atkinson (1995) and Airey (2003) to determine the travel time between the transmitter and receiver elements. It should be noted that cross correlation should be applied to the transmitted signal and not to the actual shape of the of pulse generated by the bender element (Gajo et al., 1997). Cross correlation between the received signals of the two bender element receivers eliminates this problem. A Visual Basic program was written by the author for this purpose (Appendix A).

In order to assess the repeatability and reliability of the technique, the shear wave velocity derived from cross correlation was compared with that obtained from hand picking for input frequencies ranging between 6kHz and 30kHz. Both the normal and reversed signals were considered. Figure 3.26 is an example of a cross correlation function obtained from the recorded signals of the two bender receiver probes for an input frequency of 12kHz. It can be seen from Figure 3.27 and Table 3.3 that the results of the two techniques

compare well. The average group velocity, derived from cross correlation is $338.6ms^{-1}$ with a standard deviation of $1.8ms^{-1}$ as opposed to the $339.4ms^{-1}$ and $5.4ms^{-1}$ obtained from hand picking. Clearly the standard deviation obtained from the cross correlation is less than that obtained by the hand picking. In fact the travel time derived from the normal and reversed signals using cross correlation differed by only 0.2μs to 0.5μs.

The results obtained using the authors cross correlation program were further compared with that of an independently written program. Small differences in the travel time were found. The reason for this was that the program written by the author only considered that part of the recorded signal that is concerned with the arrival of the shear wave (Figure 3.28) hence ignoring the noise preceding and following the received shear wave. In order to illustrate the influence of the selected time base on the derived travel time, the time base of the received signals were varied. Table 3.4 illustrates the influence of noise on the results. The independent program on the other hand, considered all of the recorded data. The program written by the author would be used for further analysis of the results.

As mentioned in Chapter 2, bender elements would be employed to assess the influence of particle shape on the small strain shear stiffness of a micaceous sand. A bender that appears to measure the small strain stiffness more reliably. The final phase of the experimental program, namely assessing the influence of particle shape on the consolidation, stiffness and shear strength behaviour of artificial micaceous sand (soton soil) would thus now follow.

Table 3.1: Summary of bender element interpretation techniques

References	Interpretation technique	Wave form
Shirley and Hampton (1978)	Time-of-flight	sine and square pulse
Dyvik and Madshus (1985)	Time-of-flight	sine and square pulse
Dyvik and Olsen (1989)	Time-of-flight	sine and square pulse
Mancusco et al. (1989)	Time-of-flight and cross correlation	sine pulse
Viggiani and Atkinson (1995)	Time-of-flight and cross correlation	sine and square pulse
Jovičič et al. (1996), Jovičič (1997)	Time-of-flight, pulse train, distorting the amplitude of first half cycle	sine pulse
Arulnathan et al. (1998)	Time-of-flight and cross correlation	sine pulse
Blewett et al. (1999), Blewett et al. (2000)	Phase sensitive technique	continuous sine wave
Karl, Haegeman, Pyl and Degrande (2003)	Phase sensitive technique	continuous sine wave
Mohsin and Airey (2003)	Cross correlation	sine pulse
Rio et al. (2003)	Phase sensitive technique and numerical analysis	sine pulse

Table 3.2: Time delay and shear wave velocity obtained from time-of-flight techniques using a sinusoidal and square pulse for an input frequency of 15kHz

Input pulse	Time of input pulse	Time of received signal	Travel time	Shear wave velocity	Small strain shear modulus
	ms	ms	ms	ms^{-1}	MPa
Sinusiodal	0.02	0.543	0.523	358	253
Sinusiodal reversed	0.023	0.545	0.522	358	254
Square	0.011	0.548	0.537	348	240
Square reversed	0.011	0.546	0.535	350	242

Table 3.3: Time delay and shear wave velocity obtained from cross correlation interpretation

Input frequency	Normal signal (first beak)			Reversed signal (first beak)		
	Cross correlation factor	Time delay	Group velocity	Cross correlation factor	Time delay	Group velocity
kHz		μs	ms^{-1}		μs	ms^{-1}
6	0.968	197.4	338.4	0.972	197.8	337.7
9	0.969	195.8	341.2	0.958	196.2	340.5
12	0.953	195.9	341.0	0.902	195.7	341.3
15	0.777	197.8	337.7	0.876	196.4	340.1
18	0.842	196.2	340.5	0.727	197.1	338.9
21	0.796	197.0	339.1	0.677	198.2	337.0
24	0.751	197.5	338.2	0.652	198.7	336.2
27	0.695	197.8	337.7	0.638	198.8	336.0
30	0.657	198.2	337.0	0.622	198.9	335.8

Table 3.4: Influence of time range on the travel time obtained from cross correlation for an input frequency of 12kHz

Time range		Cross correlation factor	Travel time
Start time	End time	Cross correlation factor	Travel time
ms	ms		ms
0	1	0.6555	0.2
0	0.8	0.6914	0.2
0	0.5	0.9530	0.195
0.1	0.5	0.9534	0.195

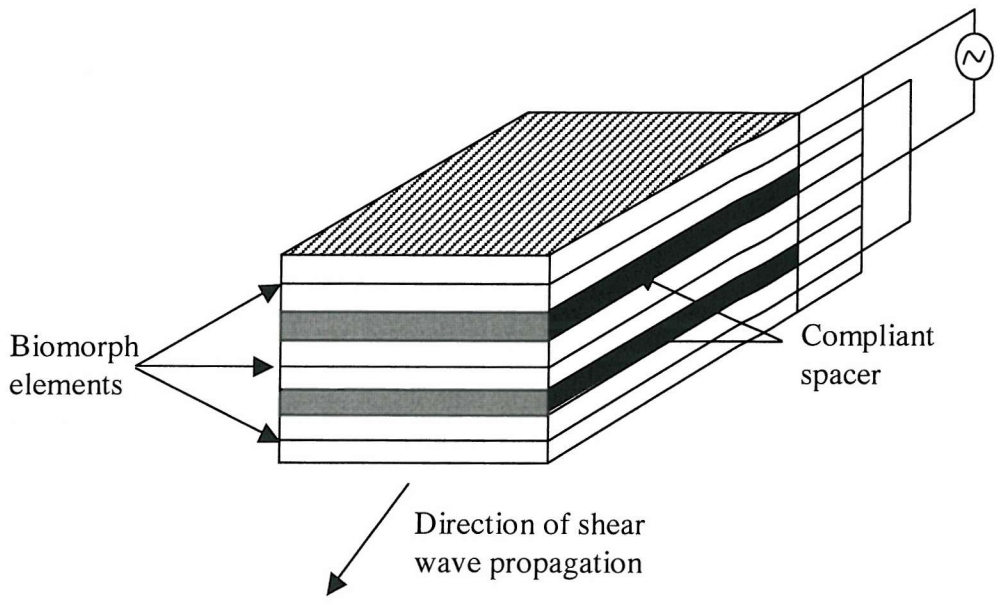

(a)

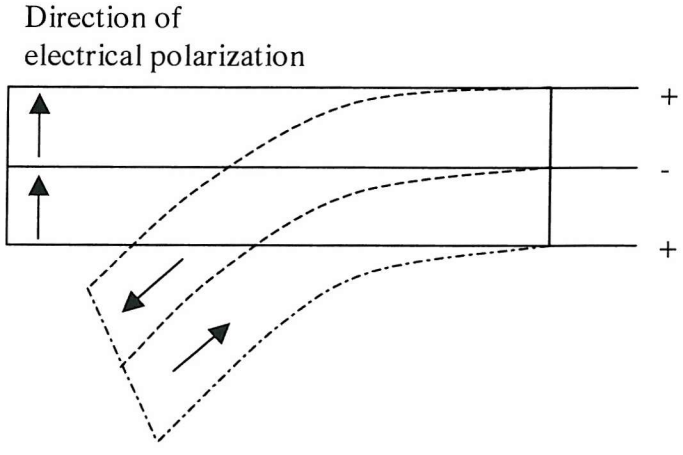

(b)

Figure 3.1: Schematic representation of ceramic bender element with a) composition and b) cantilever action (after Shirley and Hampton (1978))

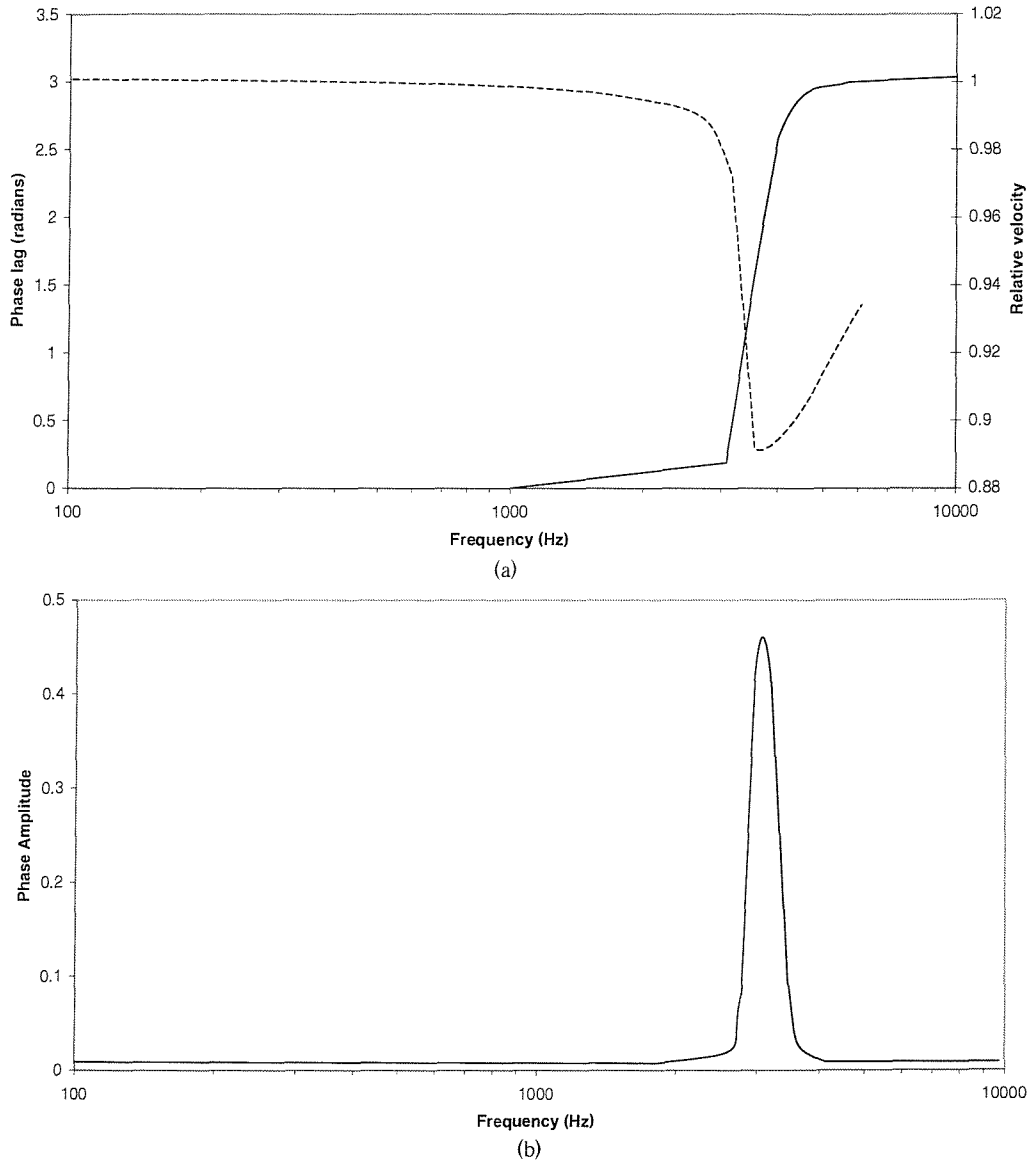

Figure 3.2: Forced harmonic response with regards to a) phase and velocity and b) amplitude (resonant frequency at 3500Hz and width 200Hz) (after Blewett et al. (2000))

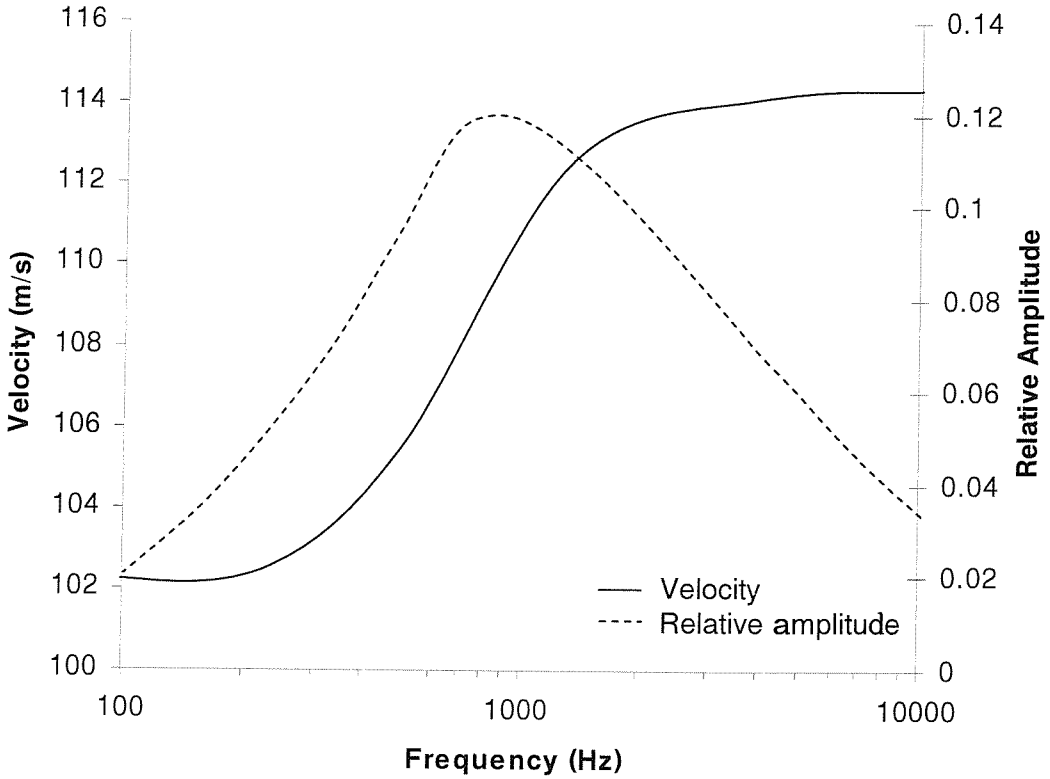

Figure 3.3: Velocity and amplitude response of a Biot medium (after Blewett et al. (2000))

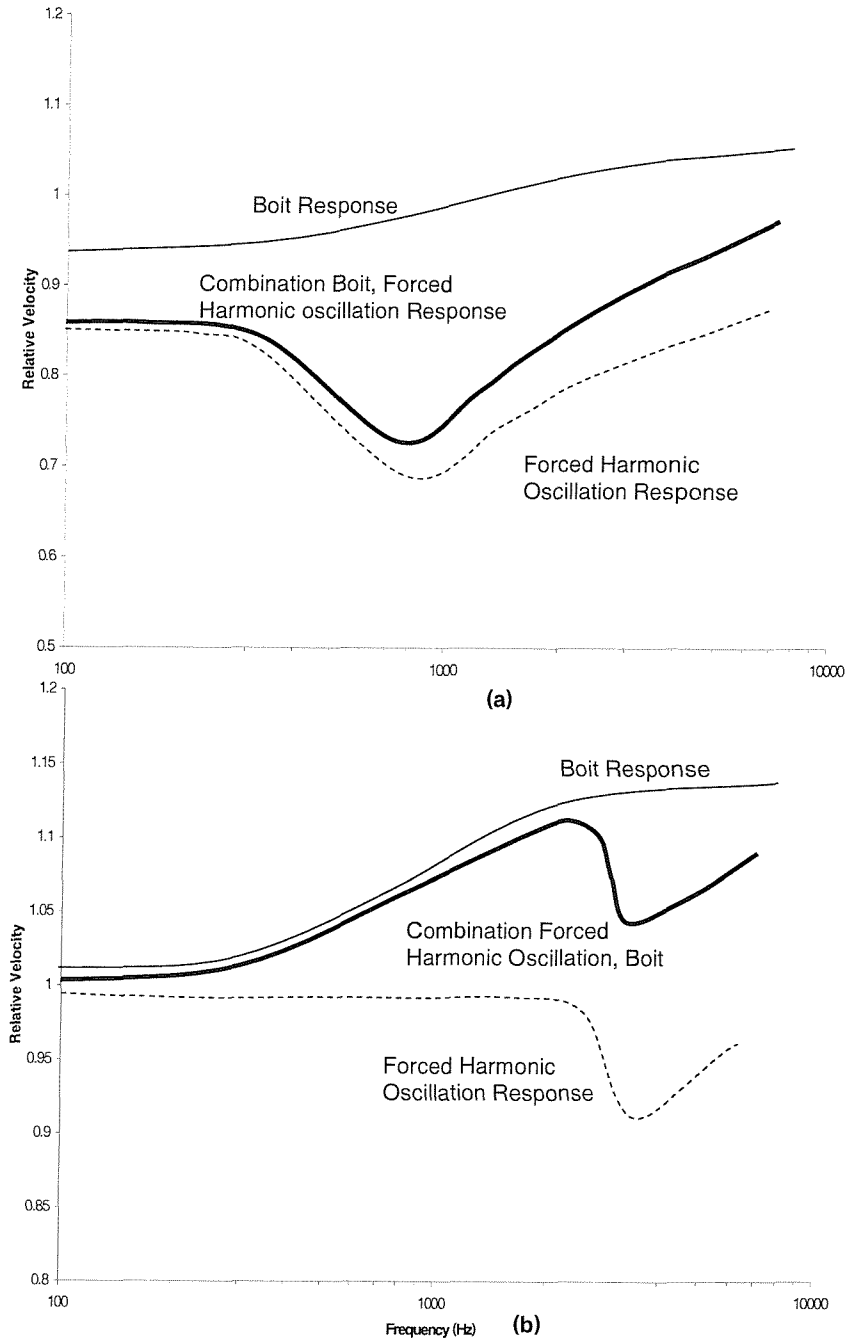

Figure 3.4: Velocity-frequency profile for a) forced harmonic response followed by a Biot response (sender) and b) Biot response followed by a forced harmonic response (receiver) (after Blewett et al. (2000))

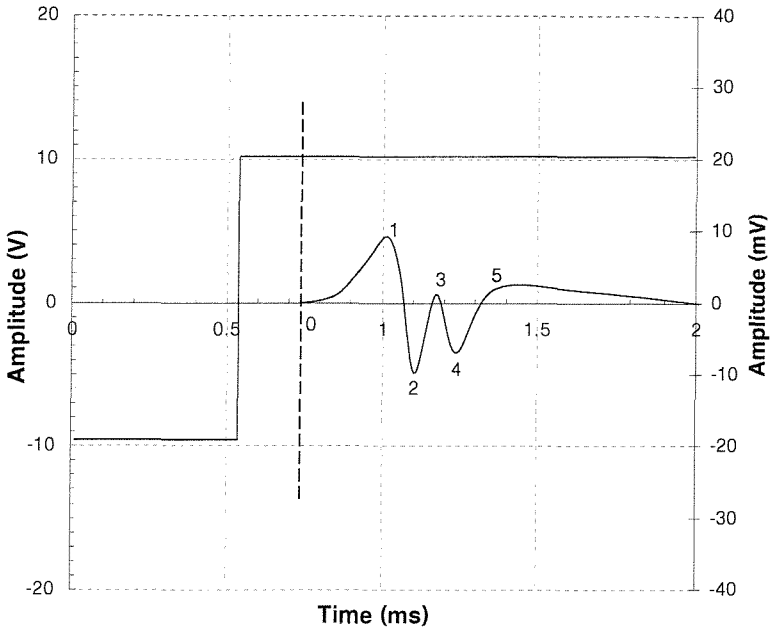

Figure 3.5: Typical oscilloscope signals from bender element test with square pulse excitation (after Viggiani and Atkinson (1995))

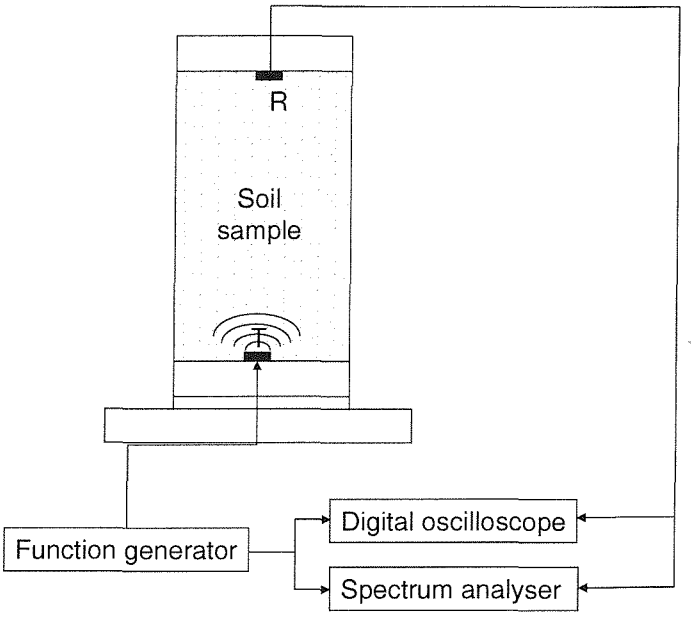

Figure 3.6: Schematic layout of bender elements and instrumentation

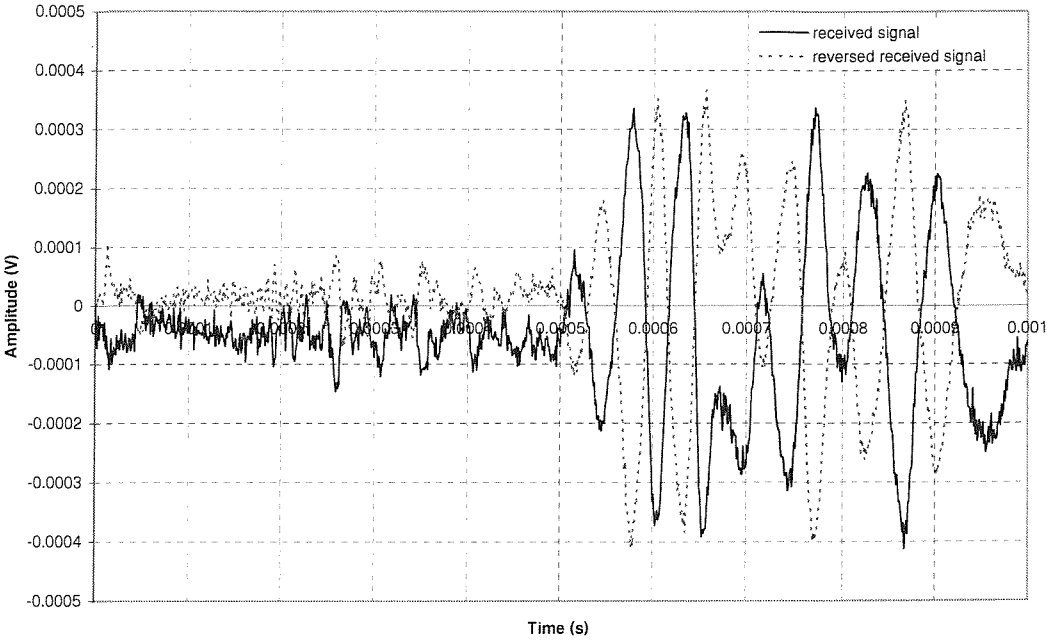

Figure 3.7: Reversed signals of receiver element, transmitter element excited with a 15kHz square pulse

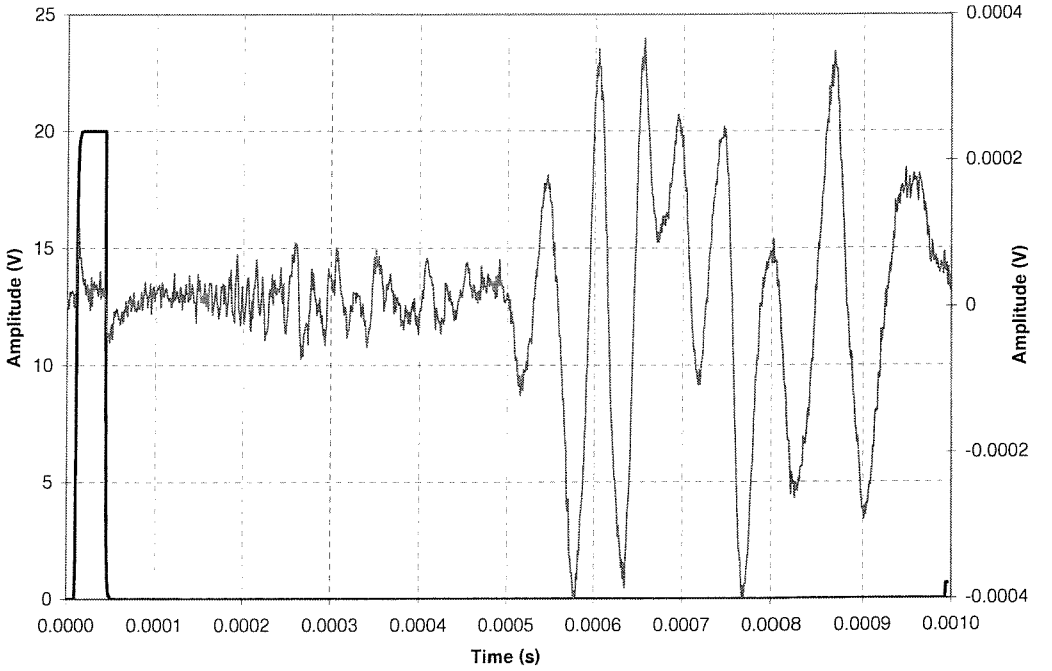

Figure 3.8: Recorded transmitted (15kHz square pulse) and received signals

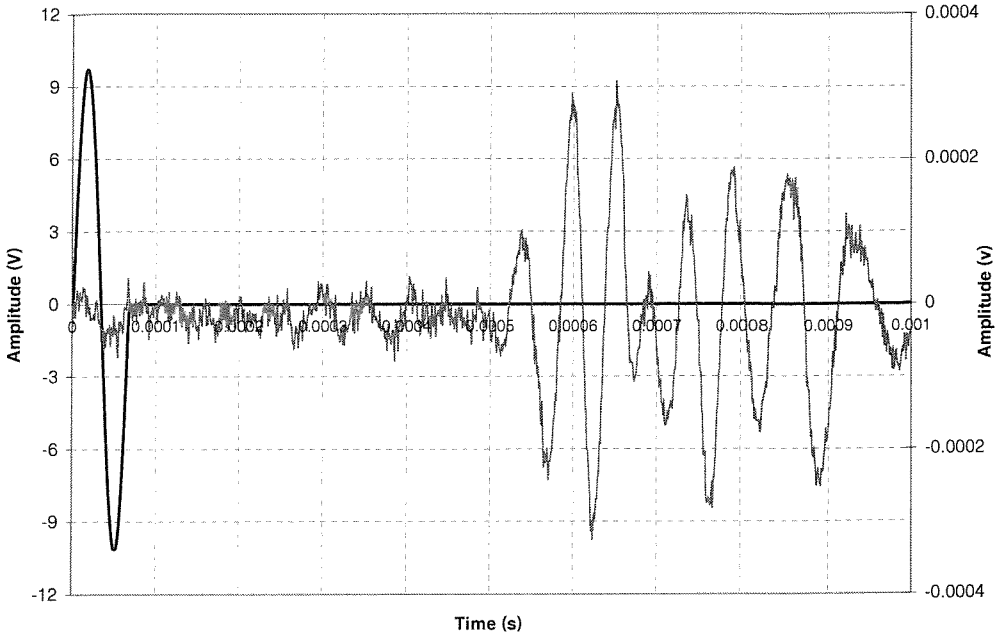

Figure 3.9: Recorded transmitted (15kHz sinusoidal pulse) and received signals

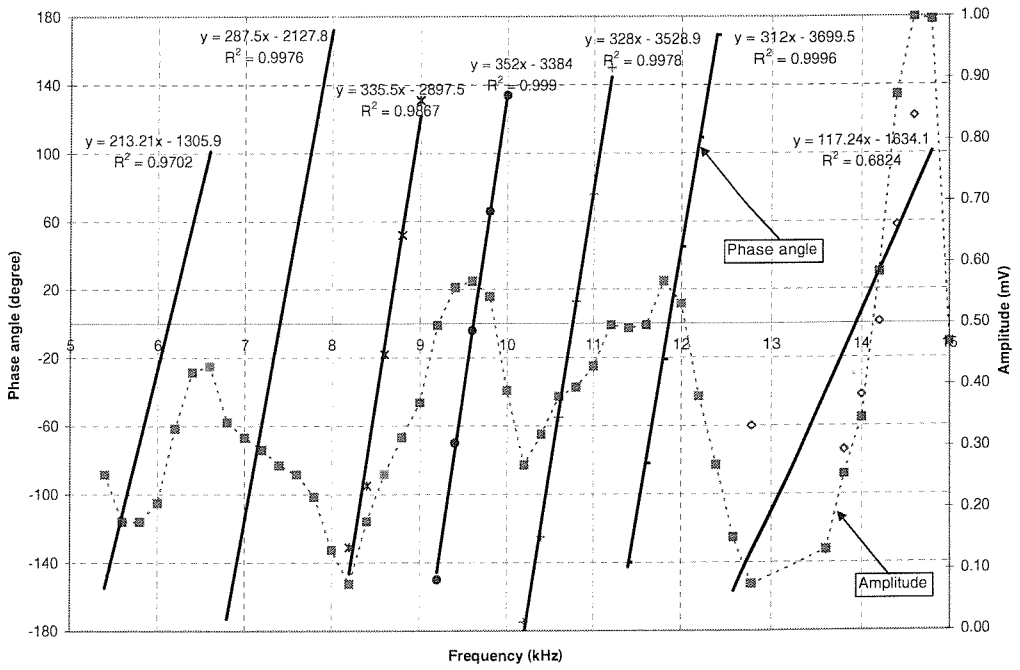

Figure 3.10: Phase angle and amplitude measurements obtained from a phase sensitive technique, using a conventional bender element configuration

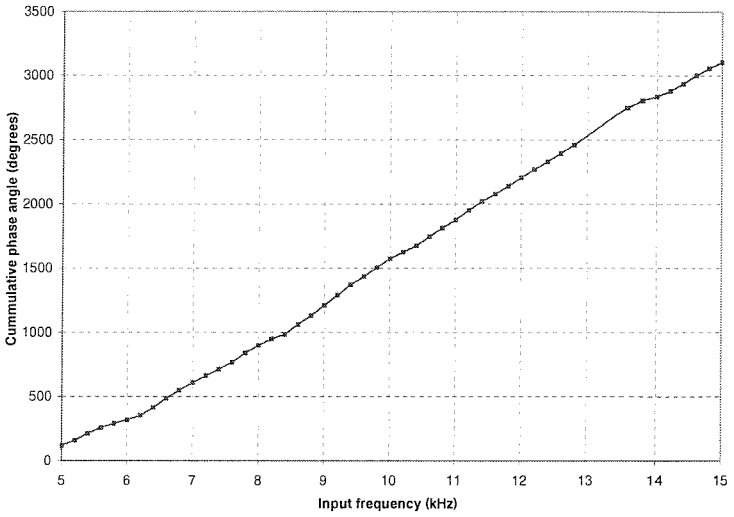

Figure 3.11: Derived relationship between cumulative phase difference and input frequency obtained from a conventional bender element configuration

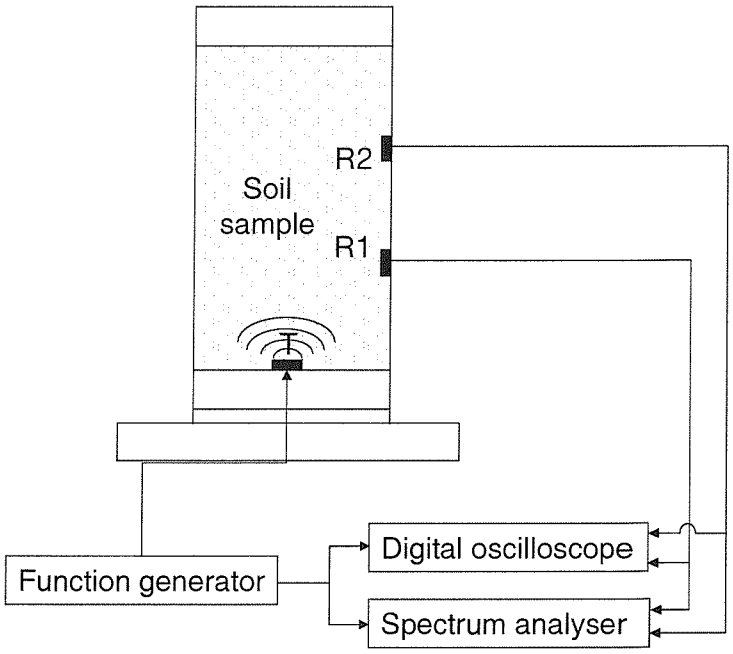

Figure 3.12: Schematic layout of side mounted bender elements and instrumentation

Figure 3.13: Equipment used for inserting bender element probes

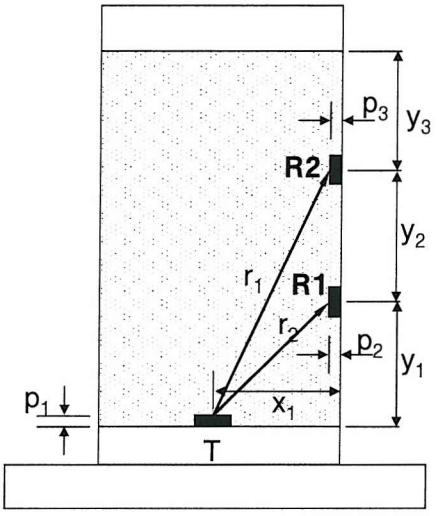

Description	Symbol	Dimension (mm)
Diameter of sample	d	101.9
Height of sample	H	195.5
Distance between centre of transmitter element and side of sample	x_1	51
Protrusion of transmitter element into sample	p_1	4.3
Distance between centre of R1 and top of base pedestal	y_1	64.7
Protrusion of R1 into sample	p_2	1.09
Distance between centre of R1 and R2	y_2	66.1
Protrusion of R2 into sample	p_3	1.24

Figure 3.14: Dimensions of a two-side bender configuration

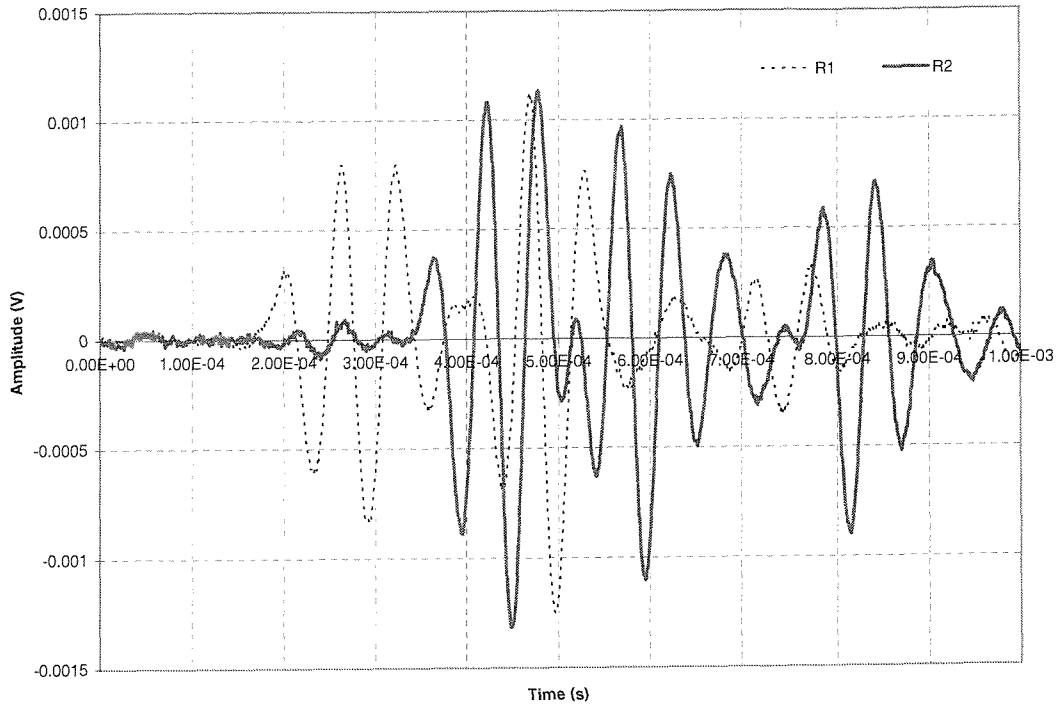

Figure 3.15: Received signal of receiver elements R1 and R2 when transmitter excited with 15kHz sine pulse

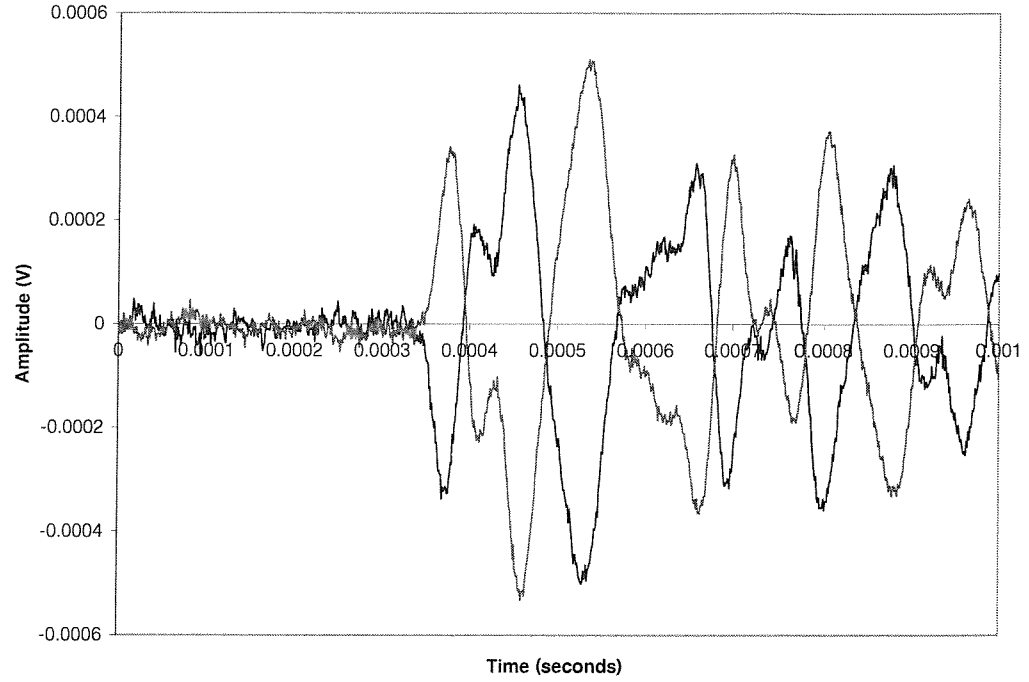

(a)

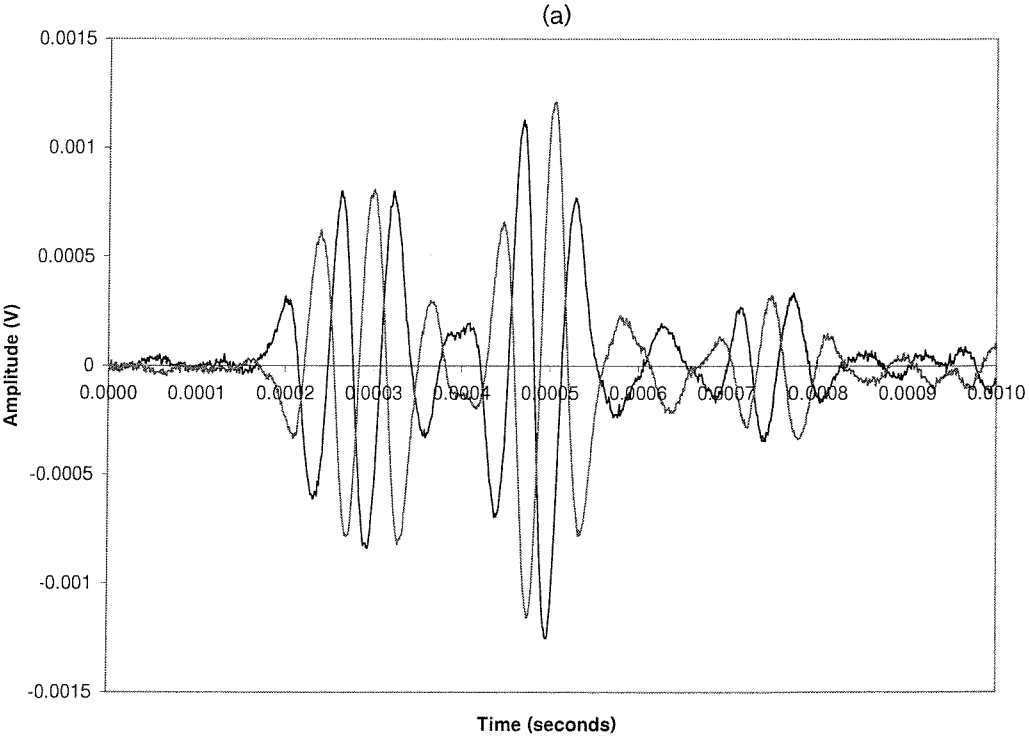

(b)

Figure 3.16: Examples of reversed signals received by side bender element probes with (a) 7kHz and (b) 15kHz input frequencies

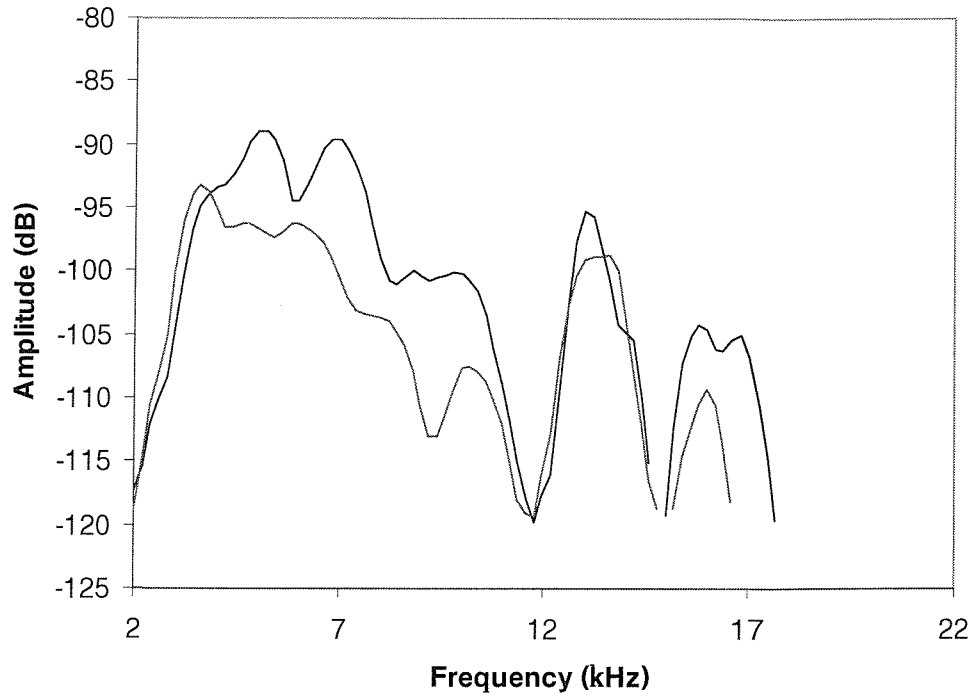

(a)

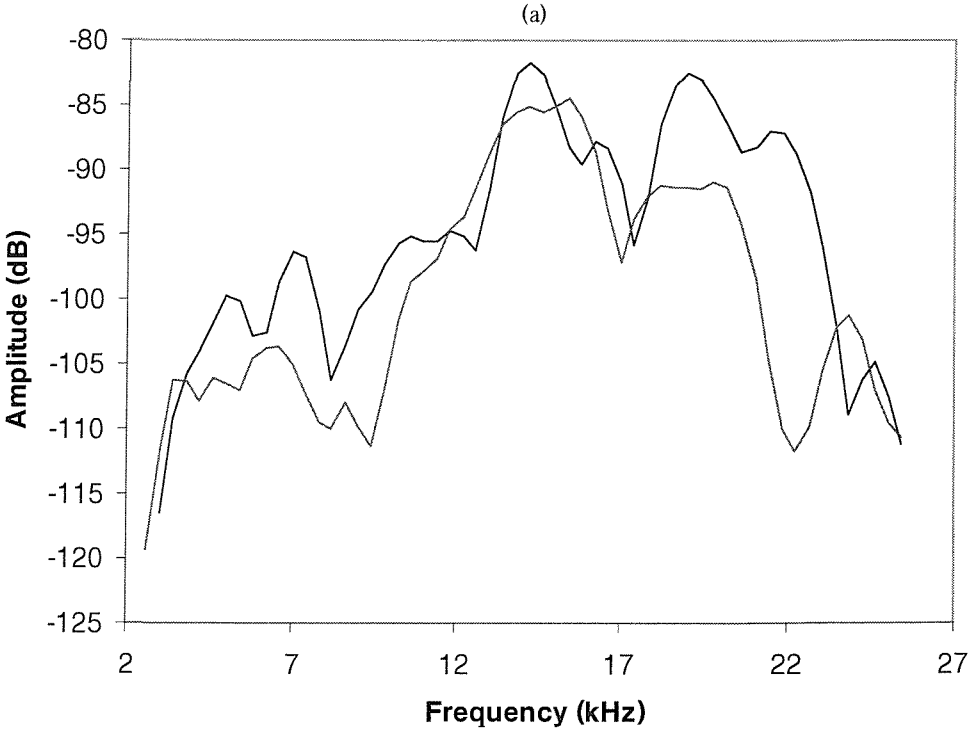

(b)

Figure 3.17: Frequency spectrum of receiver probes R1 and R2 for (a) 6kHz and (b) 15kHz input frequencies

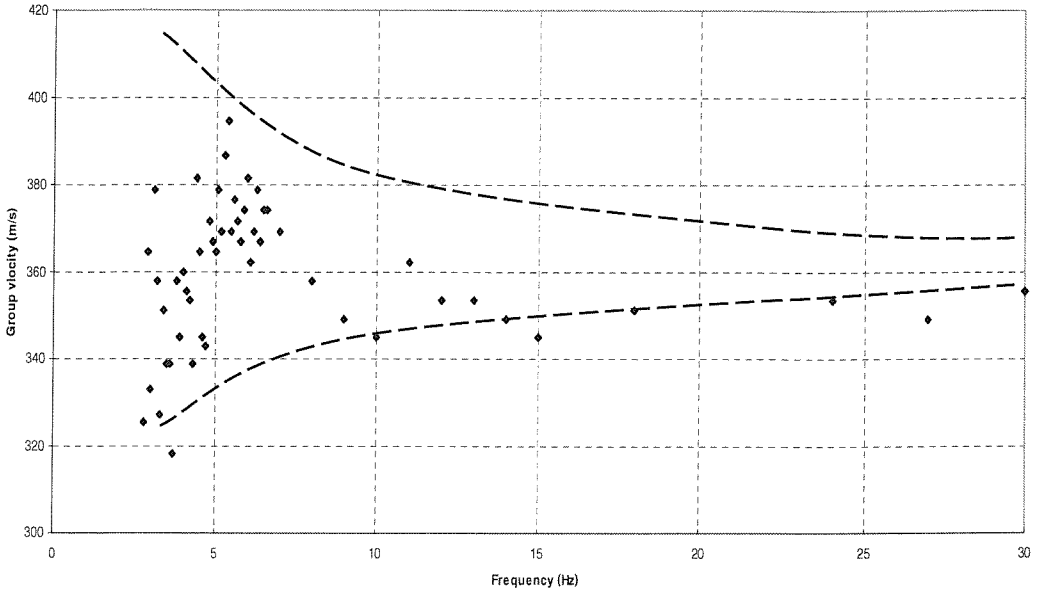

Figure 3.18: Group velocities measured between side bender elements (R1 and R2) for a range of single sinusoidal input frequencies

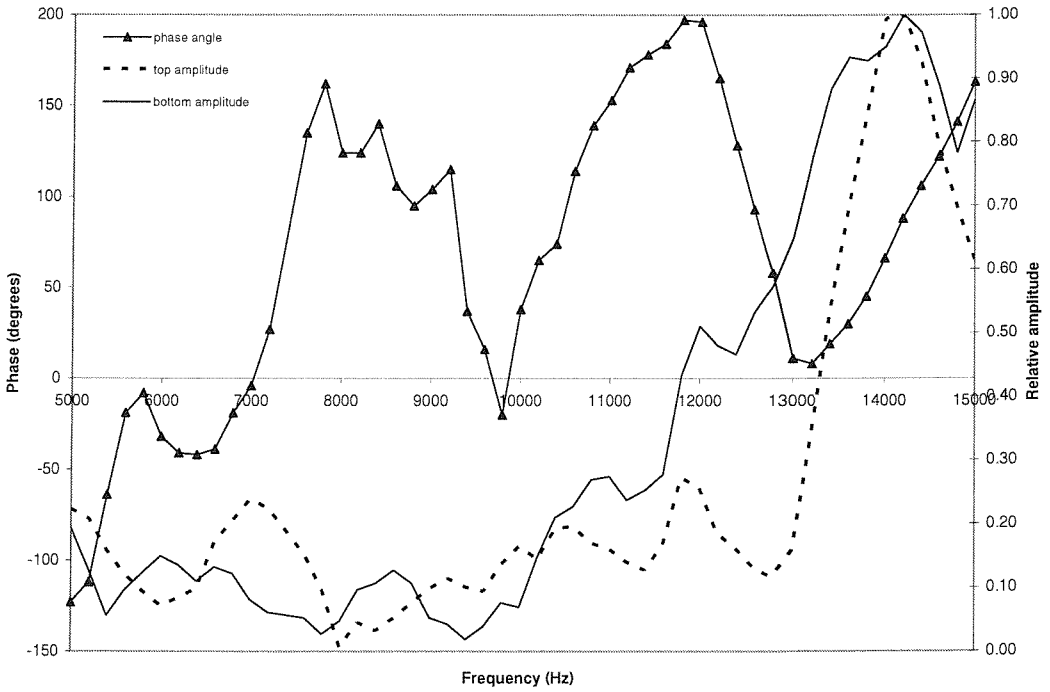

Figure 3.19: Phase sensitive technique results, considering two side bender probes (R1 and R2)

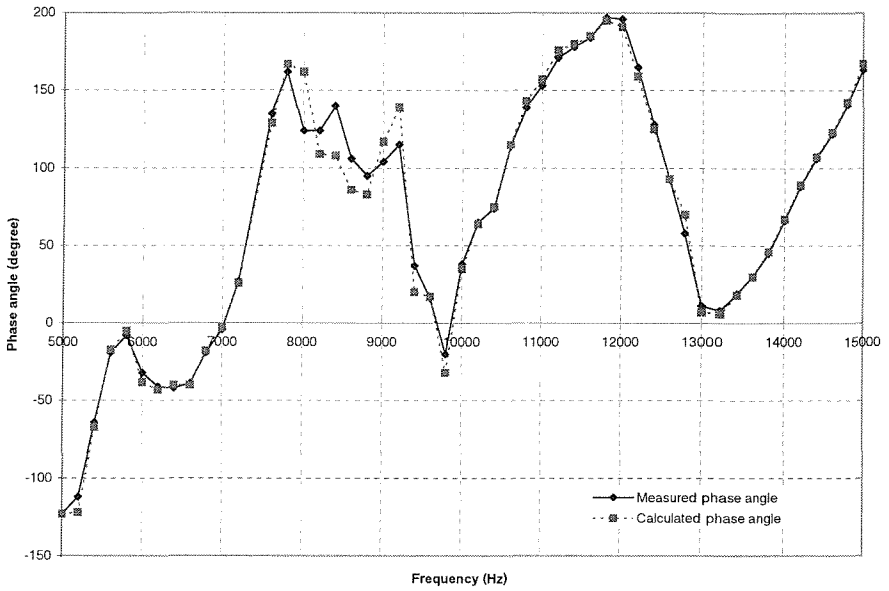

Figure 3.20: Comparison between measured and calculated phase angle with frequency, measured between R1 and R2

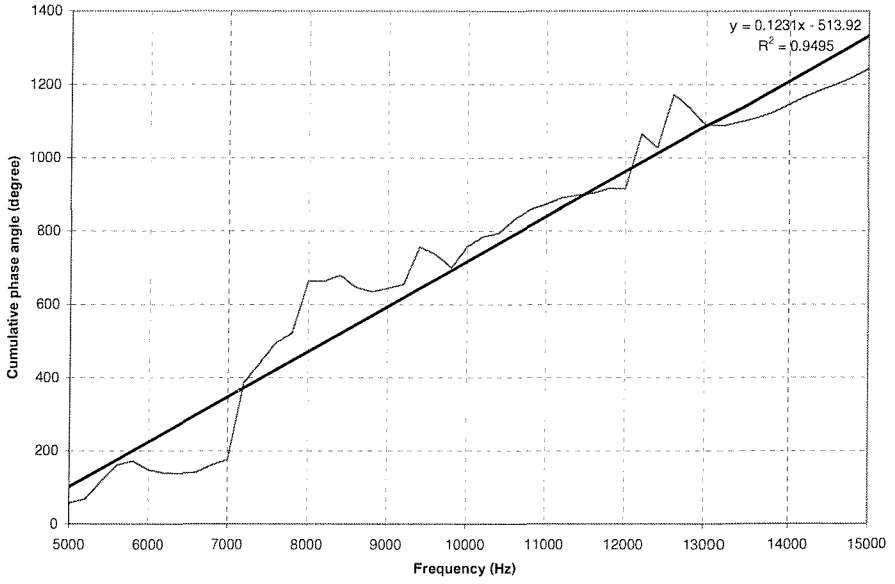

Figure 3.21: Cumulative phase angle as a function of input frequency, measured between side two bender probes (R1 and R2)

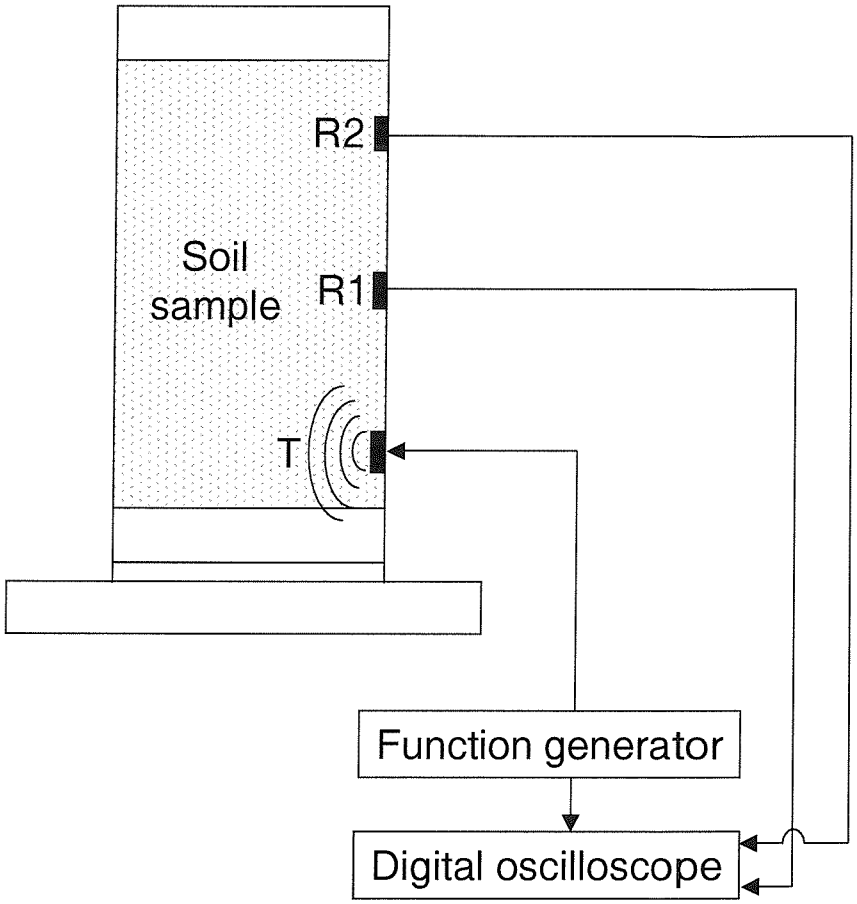

Figure 3.22: Schematic layout of three side mounted bender elements and instrumentation

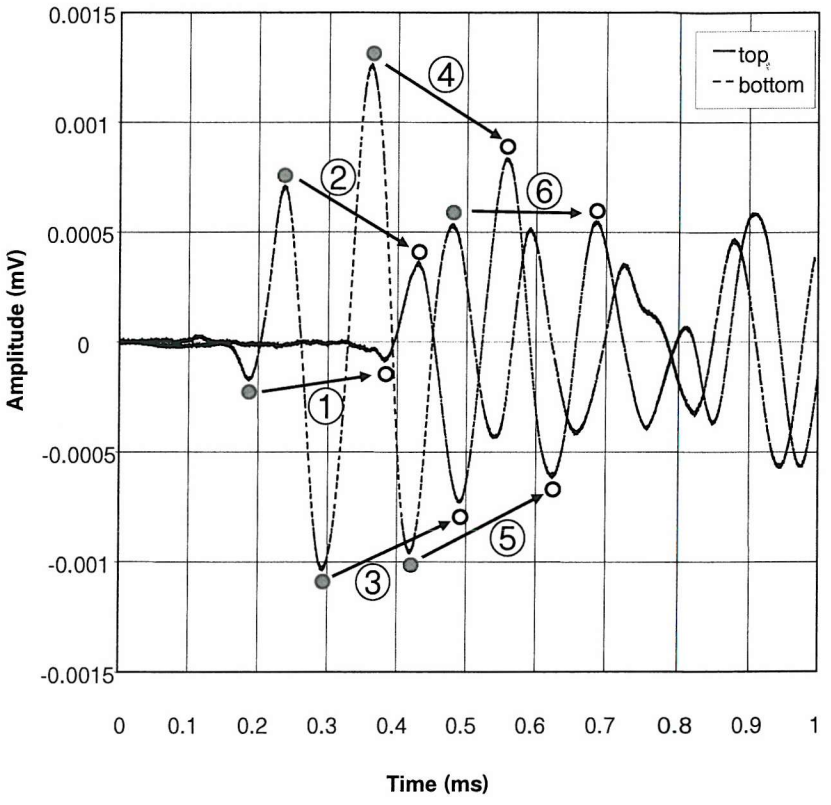

Figure 3.23: Picking positions used to derive group velocity

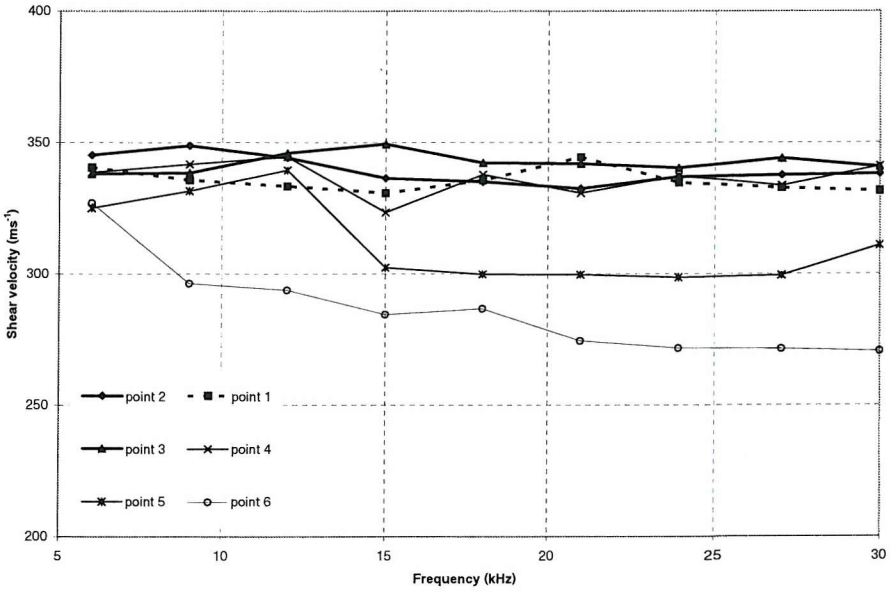

Figure 3.24: Group velocity as a function of input frequency derived from the first 6 picks of received signals

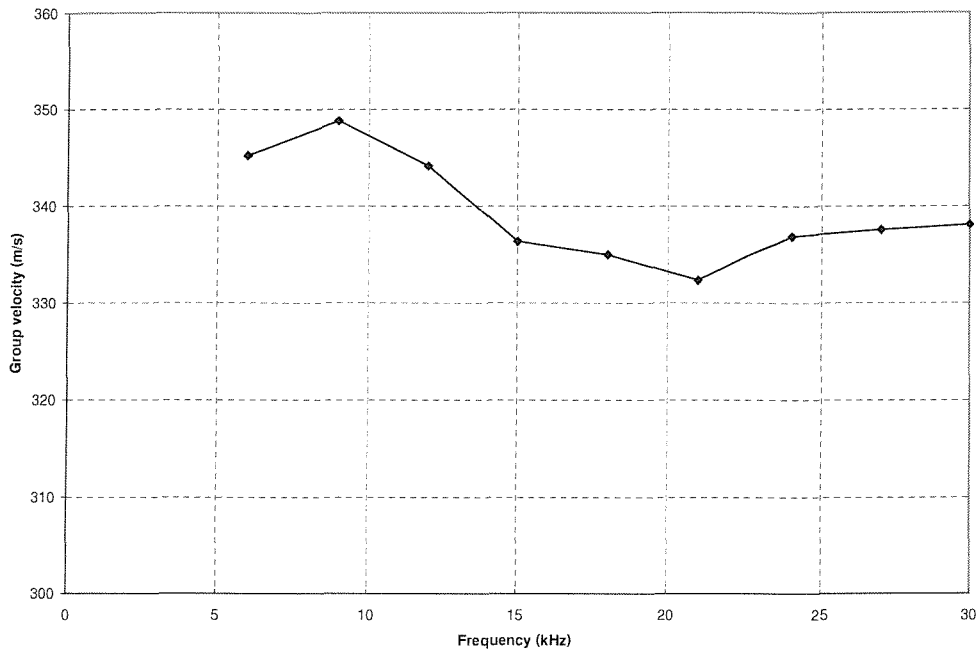

Figure 3.25: Group velocities measured between side-mounted receiver probes when transmitter probe excited by a range of input sine pulse frequencies

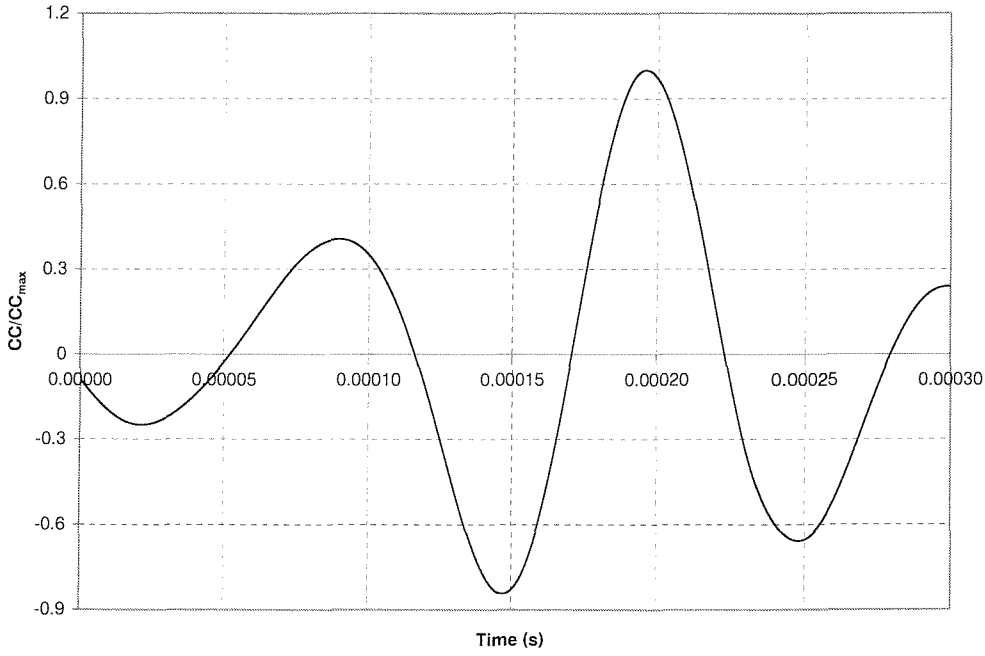

Figure 3.26: An example of a cross correlation between two side receiver probes for an input frequency of 12kHz

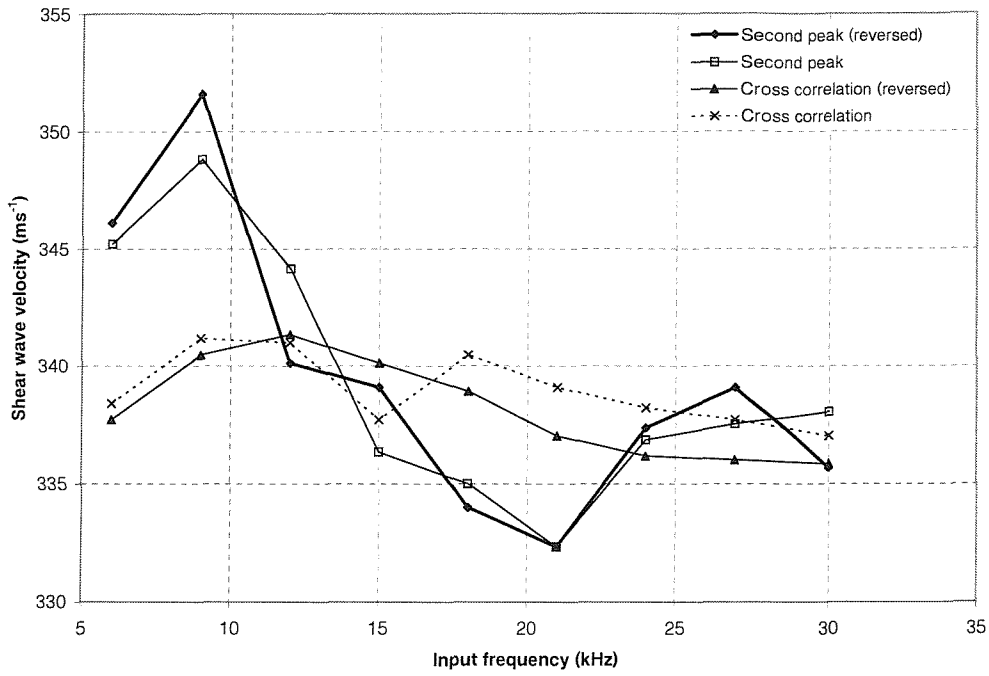

Figure 3.27: Measured group velocities using hand picking on the second peak and cross correlation for input frequencies between 6kHz and 30kHz

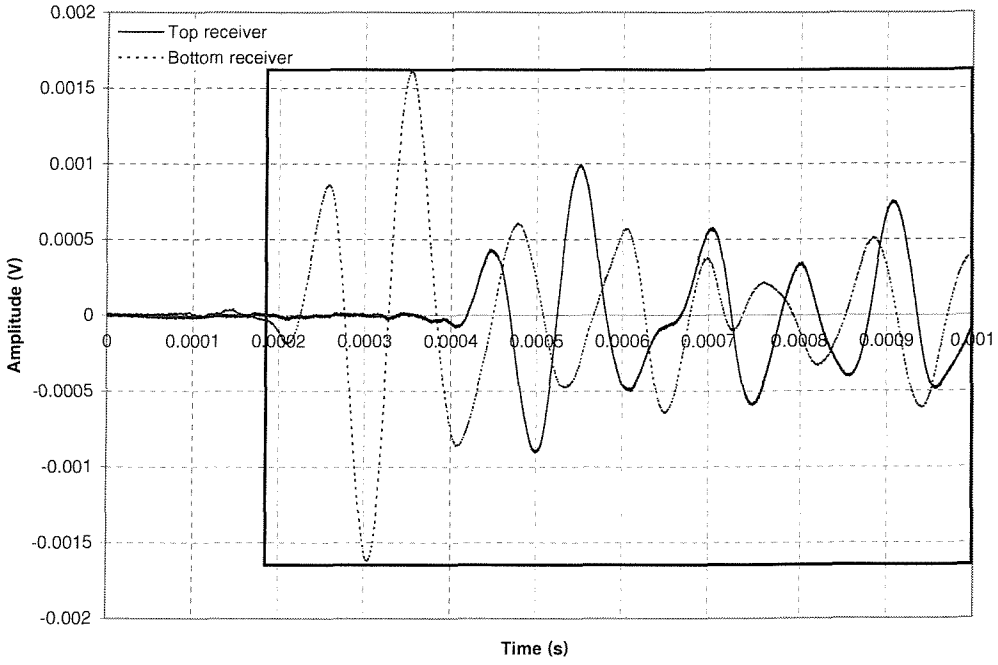

Figure 3.28: Box showing which part of the recorded signals were used for cross correlation analysis

Chapter 4

LABORATORY TESTING OF SOTON SOIL

The influence of platy particles on the behaviour of gold tailings in terms of its compressibility, stiffness and state was assessed by testing mixes of rotund and platy sands i.e.Soton Soil. The fabric of the material was also investigated using thin sections viewed under an optical microscope. Typical test results are given in this chapter. Further analysis, interpretation and discussion of the results will follow Chapter 5.

4.1 Experimental set-up

A description of the laboratory equipment employed for the experimental program is given.

4.1.1 *Triaxial apparatus*

Experiments were conducted in a conventional 100mm diameter Wykeham Farrance triaxial apparatus (Figure 4.1). An instrumentation access ring was added between the base and cell top of the apparatus to provide additional ports for the instrumentation cabling. GDS Instruments Ltd. pressure and

volume controllers were used to control the cell and back pressure. Deviatoric load was applied by a Wykeham Farrance 50kN loading frame.

4.1.2 *Instrumentation*

Pressure transducers

The applied pressure to the base, top-cap and cell was measured with Druck PDCR 810 pressure transducers (10 bar pressure rating) connected to de-airing blocks. Valves were placed on both sides of the de-airing block to assist in the de-airing process and to simplify calibration of the pressure transducers.

Load cell

A Wykeham Farrance STALC 13073 internal submersible load cell was used to measure the applied load. A load cell with adequate range capabilities and high sensitivity was required. It was decided to employ a 10kN load cell, as it would be sufficient in terms of range and resolution for all materials tested.

Local strain devices

Displacement of the sample was measured locally by three submersible LVDTs (linear variable differential transformers) (RDP D5/40W/745) manufactured by RDP Electronics Ltd. UK. The signal from the LVDTs was amplified by alternating current amplifiers (RDP Type S7AC). Two LVDTs were employed to measure the axial displacement over the middle third of the specimen while a third measured radial displacement in a radial calliper. The design of the radial calliper was similar to that of Bishop and Henkel (1962). Each of the LVDTs had a linear range of $\pm$1mm.

The axial displacement LVDTs were held in position on the sample by means of specially designed brackets (Figures 4.2). The LVDT fitted through a hole in the top bracket and was kept in place by a plastic screw. The diameter of the hole was only slightly greater than the outside diameter

of the LVDT to improve alignment. The bottom bracket contained a finely threaded screw that could move vertically to adjust the gauge length of the LVDT to ensure that it was within its linear range.

External strain device

Strain was measured externally partly because the local strain devices were expected to run out of range at large strains, but also to provide redundancy. A single linear displacement sensor (HS25MG0163), manufactured by Measurement Group Ltd. UK, was used. The instrument was capable of measuring axial displacements of up to 25mm. The linear displacement sensor (LDS) was fastened to the load cell with a standard fitting supplied by Wykeham Farrance.

Bender elements

The bender element configuration was based on the results of Chapter 3. Three side bender element probes were used, one acting as the transmitter and the other two as receivers. Great care was taken to improve the signal to noise ratio. This was achieved by the following actions:

- shielding around all bender element cables,
- power supply cables were separated from bender element cables and
- the triaxial apparatus and cable shielding had a common earth provided by the oscilloscope.

The transmitter element probe was excited with a single sinusoidal pulse, generated by a Thurlby Thandar Instruments (TTi) TG1010 programmable function generator. Both the transmitted and received signals were measured and displayed by a digital storage oscilloscope (Gould Integra 20).

Data acquisition

The output from the instrumentation measurements during calibration, consolidation and shearing, with the exception of the bender elements, was logged using the software package GDSLAB developed by GDS Instruments Ltd. The logging system consisted of a GDS 4 channel RS232 Multiplexer, 8 channel interface and GDSLAB modular system. Bender element signals were logged with the Gould Integra 20 digital oscilloscope.

4.1.3 *Calibration*

Transducers were calibrated to assess their accuracy of measurement. Calibration of the transducers were conducted using the following procedure:

- Calibration of the transducer system (i.e. transducer with amplifier) was conducted against a suitably accurate reference.
- The straight line relationship between engineering units and milli Volts was derived using a least square linear fit.
- A calibration graph was produced, showing the above relationship as well as that of the error (taken as the difference between the calculated and measured value).
- The accuracy of each transducer was quoted as twice the standard deviation of the error. Assuming a Gaussian distribution of errors, this implies that 95% of the measured values would fall within the stated accuracy.

Table 4.1 summarises the instrumentation used as well as its calibration characteristics.

Dead-weight calibration system

The load cell and pressure transducers were calibrated using a 580 Series hydraulic dead-weight calibration system manufactured by Budenberg Gauge

Co. Ltd. The system operates on the principle of pressure balance between a piston loaded by dead weights and the pressure at the outlet port.

Pressure transducer calibration

The pressure transducers were calibrated within their fitted positions in the triaxial cell. The pressure outlet of the Budenburg was connected to the de-airing block of the corresponding pressure transducer. The valve nearest to the cell was closed to isolate the pressure to the pressure transducer. The applied pressure was increased in increments of 50kPa starting from 100kPa to a maximum of 900kPa followed by a decrease in pressure again, in 50kPa pressure increments to 100kPa. This provided information about the hysteresis of the instrument. Calibration of the pressure transducers was done relative to atmospheric pressure. Figure 4.3 presents a typical calibration result, obtained using the following procedures.

Load cell

The load cell was calibrated against the dead weight calibration system for compressive loads only. This was done by following a similar procedure as described for the pressure transducer calibration.

The sensing element of the load cell is situated in the middle of the main body. In order to determine the zero readout value, the weight suspended below the sensing element had to be calculated. This was done by averaging the milli Volt reading when suspended under it own weight and when turned upside down. As mentioned, the range of the load cell was selected on the basis of its range and resolution. Figure 4.4 confirmed that this was the case. An accuracy of 15.8N was obtained which is equal to a diviatoric stress of 2.0kPa (considering a 100mm diameter sample).

LVDT

The three submersible LVDTs were calibrated against a micrometer (Mitutoyo Series 152 – 348). The micrometer had a 25mm range with a quoted

accuracy of $\pm 1\mu m$. A purpose built calibration frame was used to position both the micrometer and LVDT.

The LVDTs were calibrated in two stages. The first stage entailed a rough calibration of the LVDT to establish its linear range. The gain setting of the AC RDP amplifier was then set to achieve the highest possible resolution. This process was repeated until the gain was such that only the linear portion of the instrument was covered. The second calibration stage consisted of a precise calibration where the output was noted every $100\mu m$. Figure 4.5 shows the calibration of one of the two axial deformation LVDTs.

Linear displacement sensor

The linear displacement sensor was calibrated using a similar device as that used for calibrating the LVDTs. Measurements were taken every 0.5mm for the full range of the instrument (25mm). Figure 4.6 displays the resulting calibration graph.

4.2 Laboratory Testing

The aim of the experimental program was to assess the influence of different proportions of platy fines on the behaviour of rotund particles.

4.2.1 *Description of materials*

"Soton soil", in this thesis, is defined as the combination of platy fine and rotund coarse sand particles. Classification of this material as a sand was based purely on the particle size of the material. The term "rotund sand" is used for equidimensional rotund particles. The behaviour of the Soton Soil, containing various percentages of platy particles in the form of mica, was contrasted with that of loose and dense rotund sand. The percentage of mica quoted in this thesis refers to the dry weight of mica relative to the total dry weight of the specimen. Four mica percentages were considered namely: 5%,

10%, 15% and 20%.

Microscope pictures were taken of the platy and rotund particles (Figure 4.7) to classify the particles according to the criteria outlined in Section 2.3.1. A summary of these together with some basic properties of the material are found in Table 4.2. Soton Soil consisting of 1mm Leighton Buzzard sand and 52μm to 105μm mica powder were used for this laboratory investigation. Minimum and maximum dry densities of the Leighton Buzzard sand were determined by adopting procedures as outlined in BS1377 (1990) and Cresswell, Barton and Brown (1999). Estimating that of the mica on the other hand was not as straightforward. Due to the particle shape of the mica particles, particle orientation changed when falling through the air and consequently standard techniques did not yield the desired results. A series of techniques such as pluviation using different funnel apertures and a pluviation tube as well as vibration were thus employed and the values cited in Table 4.2 should be viewed in that context. Determination of the minimum and maximum dry densities of mica is a possible avenue for future research.

4.2.2 *Preparation of undrained isotropic triaxial specimens*

Various reconstituted specimen preparation techniques were investigated to determine which technique would produce the most uniform specimen. It should be reiterated that the aim of this research was not to reproduce field conditions, but to illustrate a mechanism that prevails in mine tailings by simulating it on Soton Soil.

Mulilis, Seed, Chan, Mitchell and Arulanandan (1977) investigated the influence of specimen preparation technique on the uniformity of Dover 40-50 sand specimens. It was found that specimens prepared by means of dry pluviation and low frequency vibrations in the horizontal direction were relatively uniform. Following the results of Mulilis et al. (1977), De Alba, Baldwin, Janoo, Roe and Celikkol (1984) assessed the influence of specimen preparation technique on the shear wave velocity of uniform sand. Dover sand

specimens were prepared by means of dry pluviation and moist tamping and their shear wave velocity measured with bender elements at various relative densities. The shear wave velocity of the moist tamped specimen was on average $25ms^{-1}$ higher than that of the dry pluviated sample. Vaid, Sivathayalan and Stedman (1999) prepared uniform, medium graded sand specimens by means of moist tamping and water pluviation to similar global relative densities. Specimen preparation by means of moist tamping produced highly non-uniform specimens with the local relative density differing as much as 10% from the average value over the height of the specimen. In contrast to this, the local relative density of the water pluviated specimens differed by only 2% from the average value. Frost and Yang (2002) conducted a similar experiment on well graded, sub-rounded quartz sand. Specimens were prepared by means of air and water pluviation as well as moist tamping. The water pluviated specimen obtained the greatest uniformity.

Hight et al. (1999) prepared sand specimens consisting of 1mm quartz and mica particles by means of air pluviation, dry spooning and moist tamping. The first two techniques produced a relatively uniform distribution of mica particles with the particles aligning themselves horizontally. The distribution of mica in a specimen prepared by moist tamping, on the other hand was less uniform and particle orientation was random. According to Fourie and Papageorgiou (2003), wet pluviation of silty sand or mine tailings results in a non-uniform specimen. Segregation of the fines occurs, which results in some layering.

Oda (1972a) found that the orientation of the interparticle contact planes is governed by the compaction method employed for preparing sand specimens. Following this discovery, Mulilis et al. (1977) investigated the interparticle contact planes of uniformly graded fine sand prepared by dry pluviation, moist tamping and high frequency vibrations applied horizontally to dry sand. Specimens prepared by means of dry pluviation had the highest distribution of particles aligned parallel to the loading axis whilst the moist tamped specimen had the lowest. A good correlation was found between the

dynamic strength of the specimens and the orientation of the interparticle contact plane. Specimens with the highest distribution of particle contacts, whose normals were parallel to the direction of axial load, exhibited the highest dynamic strength. This confirmed observations made by Oda (1972b) regarding static strength and particle orientation.

It is evident that all of the above mentioned specimen preparation techniques suffered from some limitation and consequently a new technique was designed for preparing soton soil specimens. The technique aimed to limit the falling height of the material to minimize segregation of platy and rotund particles, but at the same time produce relatively uniform specimens. A description of the techniques employed for preparing the dense and loose rotund sand as well as the soton soil specimens is given below.

Preparation of dense rotund sand specimens

1. The required amount of dry sand was weighed and placed in a desiccator. It was then submerged in de-aired water and subjected to a vacuum for at least one hour.

2. Preparation of the apparatus and instrumentation was carried out whilst de-airing the sand. This included:

   - testing the membrane for leaks,
   - de-airing the top-cap and base by flushing it with de-aired water,
   - de-airing the GDS pressure controllers,
   - cleaning the surface of the LVDT brackets to ensure good contact with the rubber membrane,
   - cutting the radial calliper pads and
   - marking the LVDT bracket positions on the membrane using a marker pen at mid-height. Where bender elements were used, these were also marked on the membrane and the holes were cut at the allocated positions.

3. The circumference of the base pedestal was coated with a thin layer of silicon grease to ensure a watertight connection between the membrane and O-rings. The membrane was then slipped over the base pedestal and two 100mm diameter O-rings were pushed into place using an O-ring stretcher. Where bender elements were used, these were inserted using a similar technique as that adopted for a mid-plane pore water probe (Figure 4.8(a)). Details of these could be found in Hight (1982).

4. A modified three-part split mould was used firstly to retain the shape of the specimen during construction and secondly to support the specimen until an effective pressure was applied to it. The modified mould had three holes cut into it along one of the contact seams. The diameter of these holes was 2mm greater than the outer diameter of a bender element probe and their centre points were located at 24mm, 100mm and 167mm from the base of the mould. Great care was taken to ensure that the electrical cables of the bender element probes were in the correct position before slipping the mould ring into position. A cable tie was placed around the base of the mould for additional support.

5. The top of the membrane was then folded back over the mould (resulting in a relatively tight fit between the membrane and mould) and filled 3/4 with de-aired water which pushed the membrane tightly against the inside of the mould.

6. A wet 100mm diameter filter paper was placed on top of the base pedestal to prevent any material from entering the base port.

7. The vacuum was removed from the desiccator and the sand was pluviated into the mould in thin layers. After each consecutive layer (approximately 3cm), the mould was tapped 25 times to increase the density of the specimen. Great care was taken to ensure that the sand remained submerged in the de-aired water. This procedure was repeated until the mould was filled. The top of the specimen was flattened by gently

sliding the sand particles from the centre of the specimen to its side, using the tip of a small screwdriver.

8. The O-ring stretcher with two O-rings was slipped over the top-cap which was placed on top of the specimen. The membrane was slipped over the top-cap, ensuring that no material was trapped between the two before creating a seal using the O-rings.

9. A suction of 20kPa was applied to the top of the specimen. The suction was maintained by specifying a target pressure of -20kPa to the GDS pressure controller, connected to the top-cap. Once the pore pressure (measured at the bottom of the specimen) stabilized at this pressure, the mould was removed. The specimen dimensions (i.e. height and diameter) were measured as well as the exact distance between bender element probes, when used.

10. The LVDT brackets were glued to the membrane using impact adhesive (Loctite) at the allocated positions. The distance between the top surfaces of each bracket pair was measured as well as the distance between the top surfaces of the top bracket to the top of the specimen. Elastic bands were placed around the brackets for extra support. The LVDTs were then inserted and secured in place with the screw on the side of the top bracket (Figure 4.8(b)).

11. The position of the radial calliper was marked on the membrane, taking care to ensure that it was horizontal. In order to reduce the effects of membrane penetration on the radial displacement measurements, the radial calliper was glued to the calliper pads and membrane. The calliper pads consisted of thin rectangular plastic pads, but of which the edges were round. This was done to prevent the pads from puncturing the membrane during glueing. Once the glue had dried, the position of the radial calliper relative to the top of the specimen was measured and the radial LVDT was inserted (Figure 4.8(c)).

12. The gauge length of the LVDTs was adjusted to ensure a maximum linear range during testing. This was achieved either by adjusting the screw in the bottom axial LVDT bracket or by moving the radial LVDT up and down of its bracket.

13. The cell was then sealed, filled with de-aired water and a cell pressure applied to it. The specimen was left overnight to ensure that any air trapped in the specimen would dissolve into the high quality de-aired water. Sand remaining in the dessicator was washed into a metal container and oven dried. The dry weight of the specimen was calculated by subtracting the dry weight of the sand retained in the dessicator from the original dry weight. Dry density was calculated using the dry weight of the specimen, specific gravity and initial dimensions of the specimen.

Preparation of loose rotund sand specimens

1. The procedure followed Steps 1 to 6 for the preparation of the dense rotund sand specimens.

2. A funnel with an enlarged base (Figure 4.9) was used to prepare the loose specimens. The funnel was placed inside the mould and filled with saturated sand. The volume of the enlarged funnel was equal to that of the completed specimen. Care was taken to ensure that the sand remained submerged in de-aired water at all times. Excess water was retained in the base of the pedestal. The funnel was then slowly lifted clear from the mould. Once again the top of the specimen was flattened by gently sliding particles towards the side of the specimen, using the tip of a small screwdriver.

3. Steps 8 to 13 of the procedure for preparing dense rotund sand specimens were then repeated.

Preparation of Soton Soil specimens

1. A sufficient amount of platy and rotund sand particles were weighed out and transferred to the desiccator. The specimen was submerged in de-aired water and stirred to obtain a uniform mixture. The mixture was then placed under a vacuum for at least one hour.

2. Steps 2 to 6 of the procedure for preparing dense rotund sand specimens were repeated.

3. During this period some of the mica particles came out of suspension and formed a layer on top of the other material. Careful mixing was therefore required before making the actual specimen. The Soton Soil was spooned into the mould in thin layers, stirring after each layer to prevent segregation of the platy and rotund particles. Once the platy particles had settled out, excess water was drawn off using a syringe. Care was taken to ensure that the Soton Soil remained saturated at all times. The Soton Soil was stirred a second time before placing the next layer. The process was repeated until the mould was filled.

4. Steps 8 to 13 of the procedure for preparing dense rotund sand specimens were then completed.

4.2.3 *Description of test procedure and results*

Isotropic consolidation tests with shear stiffness measurements, followed by undrained triaxial compression tests were conducted on specimens prepared according to the procedures outlined in the previous section. Table 4.3 contains a list of all the tests that were carried out. With the exception of the Soton Soil containing 5% mica, each material type was subjected to three triaxial tests, with effective consolidation pressures of 100kPa, 200kPa and 400kPa. Only the specimen with the highest maximum effective isotropic consolidation pressure (400kPa) had bender elements installed.

Isotropic consolidation

Isotropic consolidation tests were conducted on each of the material types on the specimen subjected to 400kPa isotropic consolidation pressure. The tests were carried out in eight effective consolidation pressure stages namely 25kPa, 50kPa, 100kPa, 150kPa, 200kPa, 250kPa, 300kPa and 400kPa. The first effective consolidation pressure (25kPa) was applied by raising the back and cell pressure in increments to final pressures of 200kPa and 225kPa respectively. Care was taken to ensure that the applied effective pressure remained below 25kPa at all times. The following effective consolidation pressures were achieved by raising the cell pressure whilst keeping the back pressure constant. Pore pressure coefficients (B) obtained for the Soton Soil were typically in the order of 0.98 whilst those of the rotund sand were 0.95. Pore pressures were measured at the base of the specimen and drainage allowed through the top-cap.

The volumetric strain of the specimen was measured using two independent methods. External volumetric strains (ε_{vE}) were based on the volume change of the GDS controller connected to the drainage port on the top-cap of the specimen, whilst local volumetric strains (ε_{vL}) were calculated from the measured LVDT displacements using Equation 4.1.

$$\varepsilon_v = \varepsilon_{aL} + 2 * \varepsilon_{rL} \tag{4.1}$$

where

$$\begin{aligned} \varepsilon_{vL} &= \text{local volumetric strain} \\ \varepsilon_{aL} &= \text{axial strain} \\ \varepsilon_{rL} &= \text{radial strain} \end{aligned}$$

It can be seen from Figure 4.10(a) that the external volumetric strains (ε_{vE}) of the Soton Soil containing 15% mica particles are similar to the local volumetric strains with a difference of approximately 1%. However, this was

not the case for the dense rotund sand specimen (Figure 4.10(b)). The very large difference in volumetric strains between that measured locally and externally in this case is probably due to membrane penetration. Consolidation results were thus based on ε_{vL}.

Development of shear stiffness during isotropic consolidation

The shear stiffness of the Soton Soil containing various percentages of platy particles was assessed during isotropic consolidation. The measured shear wave travel time was obtained from cross correlation analysis of bender element results, as described in Chapter 3. Travel distances used for calculating the shear wave velocity of the Soton Soil took the axial deformation of the specimen into account. Specimen densities were also adjusted using measured volumetric strains. Figures 4.11 and 4.12 show typical recorded signals (of different quality) as well as the cross correlation function derived from these signals. Note the decrease in amplitude with distance from the receiver (Figure 4.11(a)).

In Chapter 3 it was shown that the shear wave velocity of a Leighton Buzzard sand specimen could be assessed using three side bender element probes. The results were relatively repeatable for input frequencies ranging between 12kHz and 30kHz. Based on the repeatability of the results it was assumed that the receivers were in the far field and wave attenuation acceptably low. The rotund sand tested here is similar to that employed for the preliminary tests discussed in Chapter 3. The bender element configuration and the relative positions of the bender elements in the specimen remained unchanged. It thus seemed reasonable to assume that the material properties would remain similar, as would the input frequencies applicable to the far field and low attenuation. An input frequency of 15kHz was thus adopted for measuring the small strain shear stiffness of the loose and dense rotund sand. Table 4.4 summarizes the shear wave velocity results of the loose and dense rotund sand specimens. The normalised cross correlation of two data sets is the ratio between the cross correlation obtained at some point to the

maximum cross correlation value. A normalised cross correlation value of one implies a perfect fit between two data sets.

The addition of mica to the Leighton Buzzard sand increased compressibility and damping and changed the dynamic response of the bender element-soil system:

- It was therefore necessary to re-evaluate the frequency range to ensure that the receivers were in the far field.
- Attenuation reduced the signal-to-noise-ratio and affected the repeatability of the travel time determination for some specimens.
- At high frequencies the identification of the first array shear wave became problematic.

The addition of platy mica to the Leighton Buzzard sand changed the compressibility and density of the sand. It was thus anticipated that the dispersion and attenuation characteristics of the material would also change. In order to determine the repeatability of bender element tests on the Soton Soil, the shear modulus of the 10% mica specimen was measured for input frequencies of 10kHz, 15kHz, 20kHz, 25kHz and 30kHz (Table 4.5). Figure 4.13 illustrates the relationship between measured travel time and effective consolidation pressure. Note that the repeatability of the measurements improved with effective consolidation pressure. At low effective consolidation pressures, the attenuation of the Soton Soil is relatively high, resulting in a low signal-to-noise ratio and hence low repeatability. Interpretation of the bender element results of the Soton Soil became more complicated as the mica content increased, especially for the lower effective consolidation pressures. This could be attributed to the decrease in stiffness of the Soton Soil with increasing mica content and hence a decrease in the signal-to-noise ratio.

Calculating the wavelength of the shear wave from the average shear wave velocity and input frequency, it was found that the first receiver probe was in the far field (i.e. the distance between the two bender elements were greater than two wave lengths) at input frequencies of more than 15kHz

(Figure 4.14). Measurements below this value should thus best be ignored. Consequently the shear stiffness of the remaining specimens was assessed for input frequencies of 15kHz, 20kHz and 30kHz (Tables 4.6 and 4.7). Figure 4.15 shows the influence of mica content on the travel distance between the transmitter and first receiver in terms of the wavelength. The travel distance of the dense and loose rotund sand specimens are also shown. A reference effective consolidation pressure of 200kPa and input frequency of 15kHz was adopted. Considering both the rotund sand and Soton Soil specimens, it should be noted that:

- the travel distance of the dense rotund specimen is lower than that of the loose specimen and
- the travel distance increases with increasing mica content.

Following these observations it could be concluded that the travel distance in terms of wavelength decreases with density. In order to confirm this, the relationship between travel distance in terms of wavelength and effective consolidation pressure of the 10% mica specimen was investigated (Figure 4.16). A reference input frequency of 15kHz was used. Apart from the data point at 50kPa, the travel distance decreases with increasing effective consolidation pressure, hence confirming the above conclusion.

Figure 4.17 shows the bottom receiver signal of a 15% mica specimen for an effective consolidation pressure and input frequency of 400kPa and 30kHz respectively. Initially the period of the received signal was very short but increased at approximately 0.0004 seconds. The same trend was noted for the top receiver signal. The travel time obtained from the first part of the two received signals (i.e. below 0.0004 seconds) was equal to 0.000077s. This results in a shear wave velocity of $901ms^{-1}$ and shear stiffness of 1576MPa. The obtained "shear wave" velocity is in the same order of magnitude as that of a compression wave which suggests that a compression wave precedes the shear wave. It was uncertain what the cause of this was. This behaviour seemed characteristic for the Soton Soil when excited with an input frequency

of 30kHz. The shear wave velocity of the Soton Soil was thus derived from averaged travel times obtained from input frequencies of 15kHz and 20kHz.

The geometric attenuation of the Soton Soil and rotund sand specimens was estimated using Equations 3.2 and 3.3. It was assumed that the waves spread in a planar fashion and consequently a value of 0 was adopted for ς resulting in a geometric attenuation of 1. Several researchers such as Brocanelli and Rinaldi (1997) and Karl et al. (2003) employed bender elements to determine material attenuation or damping. The specimen however, was excited with a continuous sinusoidal wave of which the frequency was varied to obtain the resonant frequency. Following the discussion in Chapter 4, it was decided not to employ a phase sensitive technique as it was found that the shear wave velocity is frequency dependent. The material damping of the sand specimens could thus not be determined as a time-of-flight technique was employed.

Triaxial compression

Isotropically consolidated undrained triaxial compression tests with pore pressure and local strain measurement were conducted under isotropic effective consolidation pressures of 100kPa, 200kPa and 400kPa to determine the shear behaviour of the various Soton Soils. Following consolidation, the drainage valves to the specimen were closed and an axial compressive load was applied using the loading frame. The strain rate (2% per day) at which the tests were conducted was governed by the maximum logging rate of the GDSLAB system. A flat top-cap was used to reduce sample disturbance caused by misalignment of the loading ram (Baldi, Hight and Thomas, 1988).

A combination of local and external strain measurements was adopted. In order to establish at which point the transition from the local to the external strain measurements should be made, the change in deviator stress with axial strain was compared (Figure 4.18). At lower axial strain ranges (0% to 0.3%) the global strain measurements exceeded that of the local strain which may be attributed to bedding errors and system compliance. Beyond this value,

the two measurements coincided up to an axial strain of 1%. This procedure was applied to all of the specimens to establish the strain level at which external strain measurements should be applied.

The gauge length of the local strain devices (LVDT's) was of the order of 35mm, which is approximately half of that normally employed. The reason for this is that part of the research was concerned with the compressibility of the material at small strains. The reduced gauge length provided greater sensitivity at these strains, although at the expense of accuracy. If the full linear range of these instruments were employed (2mm), an axial strain of 5.7% could be measured. Local strain however, was typically measured only to an axial strain of 4.3% since a proportion of the linear range was employed during consolidation.

Figures 4.20 and 4.19 illustrate the development of deviatoric stress and excess pore pressure with axial strain for the loose rotund and Soton Soil containing 15% mica specimens respectively. The displayed axial strain is based on a combination of local and external axial strain measurements.

The undrained secant Young's modulus of the rotund sand and Soton Soil specimens was derived from the effective pressure and local as well as external displacement measurements. Figure 4.21 shows the relationship between undrained secant Young's modulus and axial strain of a 15% Soton Soil and loose rotund sand specimens isotropically consolidated to 200kPa effective consolidation pressure.

4.3 Microscopic investigation of Soton Soil specimens

Thin sections of Soton Soil specimens containing 0%, 5%, 10%, 15% and 20% mica were examined under a microscope. This was done to investigate the fabric and structure of the specimens. According to Rowe (1972), fabric refers to the "size, shape and arrangement of the solid particles, the organic inclusions and the associated voids" whilst structure is defined as that "ele-

ment of fabric which deals with the arrangement of a particular size range." Burland (1990) defined structure as the combination of bonding and fabric. The latter is described as the arrangement and distribution of the particles comprising the soil (Cuccovillo and Coop, 1997).

4.3.1 *Specimen preparation for thin sections*

Preparation of the thin section specimens was carries out in two phases. The first phase consisted of preparing a representative specimen in the laboratory that had some strength once dried. This phase was carried out by the author. The second phase entailed the actual making of the thin section. This was done by the School of Ocean and Earth Science at the University of Southampton.

Representative specimens were prepared using a 100mm diameter triaxial base pedestal, top-cap and mould. Specimens were prepared in accordance with the procedure outlined in Section 4.2.2. The mould supported the specimens so that no cell pressure need be applied. It should be noted that the soil structure of the specimens might influenced by the lack of effective stress. In order to ensure that the specimens retained their shape once dried, they were saturated with diluted PVA glue (Cresswell, n.d.). The concentration of the PVA glue was 7.5% by weight which resulted in a milky fluid with the viscosity close to that of water. PVA glue was introduced from the bottom of the specimen under a pressure head. Once the colour of the fluid exiting the top-cap turned milky, the pipe connected to the base port was removed from the glue and the PVA was drained from the specimen using a vacuum. The suction was then removed and the specimen left to dry. Drying of the specimen was carried out in three stages namely:

- The specimen ports (top and bottom) were left open to the atmosphere for a period of 24 hours.
- Thereafter the top-cap was removed to expose a larger surface to the atmosphere. The specimen was left for another 48 hours.

- Finally, the membrane was gently removed, and the specimen was left for another 36 hours to dry before cutting into smaller sections for preparation of the thin sections.

Sub-samples for thin sectioning were prepared from vertical and horizontal sections of each specimen. This was done by cutting the representative specimens into two smaller sections, with the length of the sides approximately 6cm. Only the middle third of each specimen was considered as it was assumed that fabric disturbances in this part of the specimen would be minimal. The sections were then impregnated with an epoxy resin. A blue dye was added to the epoxy resin to simplify identification of the voids. The sections were left to cure. The impregnated section was then mounted onto a glass plate and sanded to a thickness of 0.3mm. It was then polished and covered with the resin to protect it.

Photographs were taken of each thin section under polarized and cross-polarized light. These two were adopted as the former gives an indication of the pore spaces, shape and orientation of the particles whilst the latter is more suited to distinguish between the different minerals as well as particle orientation. Two magnifications (22.5 and 47.5 times) were used to obtain an overview of the composition of the material and closely inspect the shape and contacts between the particles.

Figure 5.5 is an example of a photograph taken of Soton Soil containing 20% mica particles at a magnification of 22.5 under polarized and cross-polarized light. Under polarized light the quartz particles (Leighton Buzzard sand) appear colourless with their shape being rounded to sub-rounded. The mica particles are light brown and platy. A feldspar particle could be seen in the top left corner. The feldspar could be distinguished from the quartz particles by the inclusions on its surface so that it almost appears dirty (Erricson, n.d.). The small black dots could indicate the presence of some iron in the sand. Under cross-polarized light, the quartz particles change colour as their polarization changes. Their birefringence is weak (0.009) so that they have first order white interference colour with a slight tingle of yellow (Rogers

and Kerr, 1942). In the right hand corner a quartz particle could be noted of which the colour varies over its surface. According to Erricson (n.d.), this is an indication that the particle has been subjected to high pressure during its formation. It is difficult to distinguish feldspar under cross-polarized light, as its colour is similar to that of the quartz. The interference colour of the mica particles is second order and varies between red, orange and yellow. Figure 4.23 shows the same specimen under 47.5 magnification. In the top left hand corner one of the quartz particles is coloured by some iron oxide and appears darker (brown) than the rest in polarized light. Some air bubbles, trapped during the preparation of the thin section, were noted. The multi-crystalline quartz particles were identified by their two to three distinctive colours under cross polarization. The shape and orientation of the mica particles are easily distinguished at this magnification.

Table 4.1: Summary of instrumentation and calibration

Transducer	Measurement	Manufacturer and type	Design range	Calibration range	Resolution	Accuracy (95% confidence)
Load cell	Axial load	Applied Measurements Ltd., UK, STALC 13073	10kN	10kN	2.1N/bit	15.81N
Pressure transducer	Cell pressure	Druck PDCR810	1000kPa	900kPa	0.10kPa/bit	0.67kPa
Pressure transducer	Back pressure (top)	Druck PDCR810	1000kPa	900kPa	0.10kPa/bit	1.26kPa
Pressure transducer	Back pressure (bottom)	Druck PDCR810	1000kPa	900kPa	0.10kPa/bit	1.08kPa
LVDT	Axial local displacement	RDP Electronics Ltd., RDP D5/40W/745	± 1mm	± 1mm	0.2μm/bit	7.6 μm
LVDT	Axial local displacement	RDP Electronics Ltd., RDP D5/40W/745	± 1mm	± 1mm	0.2μm/bit	7.8μm
LVDT	Radial local displacement	RDP Electronics Ltd., RDP D5/40W/745	± 1mm	± 1mm	0.2μm/bit	6.8μm
LDS	Axial global displacement	Measurement Group Ltd, HS25MG	25mm	25mm	1μm/bit	30μm
Bender elements	Shear wave velocity	SGC				

Table 4.2: Leighton Buzzard sand and mica properties

	Leighton Buzzard sand	Mica
Supplier	Dawid Ball Group plc.	Dean and Tranter Ltd.
Particle size	Fraction B (1.18mm-600μm)	100 Mesh (52-105μm)
Description	Natural uncrushed silica sand, washed, dried and graded. Free from silt, clay or organic matter	Dry ground muscovite mica powder
Geological classification	Lower Greensand, Leighton Buzzard, Beds, UK	Muscovite
Particle shape	rounded to sub-rounded	Flat, platy
Sphericity	fairly spherical	flaky
Roundness	medium to high	low
Colour	Pale silver to brown	White
Specific gravity	2.65	2.9
Maximum dry density (kgm^{-3})	1752	916
Minimum dry density (kgm^{-3})	1496	728

Table 4.3: Summary of isotropic undrained triaxial tests

Test number	Specimen description	Isotropic consolidation test with bender element measurement of G_{max}		Undrained triaxial compression with pore pressure and local strain measurement
		Effective consolidation pressure	Excitation frequencies	Effective isotropic consolidation pressure
		kPa	kHz	kPa
1	Dense sand	n.a.		100
2		n.a.		200
3		25, 50, 100, 150, 200, 250, 300, 400	15	400
4	Loose sand	n.a.		100
5		n.a.		200
6		25, 50, 100, 150, 200, 250, 300, 400	15	400
7	5% mica	25, 50, 100, 150, 200, 250, 300, 400		400
8	10% mica	n.a.		100
9		n.a.		200
10		25, 50, 100, 150, 200, 250, 300, 400	10, 15, 20, 25, 30	400
11	15% mica	n.a.		100
12		n.a.		200
13		25, 50, 100, 150, 200, 250, 300, 400	15, 20, 30	400
14	20% mica	n.a.		100
15		n.a.		200
16		25, 50, 100, 150, 200, 250, 300, 400	15, 20, 30	400

Table 4.4: Shear wave velocity calculations for sand samples

Sample description	Isotropic effective consolidation pressure	Input frequency	Travel distance	Normalised cross correlation	Travel time	Shear wave velocity
	kPa	kHz	mm		ms	ms^{-1}
Dense sand	25	15	68.10	1.00	0.19	358.4
	50	15	68.09	1.00	0.16	425.6
	100	15	68.07	1.00	0.14	504.3
	150	15	68.06	1.00	0.12	555.6
	200	15	68.06	1.00	0.12	579.2
	250	15	68.05	1.00	0.11	604.9
	300	15	68.05	1.00	0.11	618.6
	400	15	68.04	1.00	0.10	663.8
Loose sand	25	15	68.70	1.00	0.26	264.2
	50	15	68.69	1.00	0.21	327.1
	100	15	68.68	1.00	0.17	404.0
	150	15	68.67	1.00	0.2	440.1
	200	15	68.66	1.00	0.15	467.1
	250	15	68.65	1.00	0.13	497.6
	300	15	68.65	1.00	0.12	525.7
	400	15	68.63	1.00	0.12	571.9

Table 4.5: Shear wave velocity calculations for Soton Soil containing 10% mica

Isotropic consolidation pressure	Input frequency	Travel distance	Normalised cross correlation	Travel time	Average travel time	Shear wave velocity
kPa	kHz	mm		ms	ms	ms^{-1}
25	10	66.78	1.00	0.70	0.28	236.4
	15		1.00	0.63		
	20		1.00	0.11		
	25		1.00	0.11		
	30		1.00	0.63		
50	10	66.72	1.00	0.13	0.16	406.8
	15		0.64	0.16		
	20		0.73	0.17		
	25		0.72	0.17		
	30		1.00	0.16		
100	10	66.62	1.00	0.24	0.24	281.1
	15		0.88	0.24		
	20		0.73	0.24		
	25		0.63	0.24		
	30		0.53	0.24		
150	10	66.57	1.00	0.21	0.21	316.0
	15		1.00	0.21		
	20		1.00	0.021		
	25		1.00	0.21		
	30		1.00	0.11		
200	10	66.53	1.00	0.19	0.19	351.4
	15		1.00	0.19		
	20		0.96	0.19		
	25		0.98	0.19		
	30		1.00	0.11		
250	10	66.44	1.00	0.18	0.18	367.8
	15		1.00	0.18		
	20		1.00	0.18		
	25		1.00	0.18		
	30		1.00	0.19		
300	10	66.50	1.00	0.18	0.17	394.9
	15		1.00	0.17		
	20		1.00	0.17		
	25		1.00	0.12		
	30		1.00	0.17		
400	10	66.44	1.00	0.17	0.16	413.6
	15		1.00	0.16		
	20		1.00	0.16		
	25		1.00	0.16		
	30		1.00	0.16		

Table 4.6: Shear wave velocity calculations for Soton Soil containing 15% mica

Isotropic consolidation pressure	Input frequency	Travel distance	Normalised cross correlation	Travel time	Average travel time	Shear wave velocity
kPa	kHz	mm	ms	ms	ms^{-1}	ms^{-1}
25	15 20 30	68.2	1.00 1.00 1.00	0.10 0.20 0.16	0.15	446.4
50	15 20 30	67.9	1.00 1.00 1.00	0.16 0.16 0.19	0.16	433.9
100	15 20 30	67.6	1.00 1.00 1.00	0.25 0.25 0.11	0.25	271.6
150	15 20 30	67.6	1.00 1.00 1.00	0.21 0.21 0.21	0.00021	316.9
200	15 20 30	67.2	1.00 1.00 1.00	0.19 0.19 0.19	0.19	351.2
250	15 20 30	67.0	1.00 1.00 1.00	0.18 0.18 0.18	0.18	377.7
300	15 20 30	66.93	1.00 1.00 1.00	0.17 0.17 0.16	0.17	396.7
400	15 20 30	66.76	1.00 1.00 1.00	0.16 0.16 0.16	0.16	423.9

Table 4.7: Shear wave velocity calculations for Soton Soil containing 20% mica

Isotropic consolidation pressure	Input frequency	Travel distance	Normalised cross correlation	Travel time	Average travel time	Shear wave velocity
kPa	kHz	mm	ms	ms	ms^{-1}	ms^{-1}
25	15 20 30	67.52	1.00 1.00 1.00	0.12 0.12 0.11	0.12	579.6
50	15 20 30	66.98	1.00 1.00 1.00	0.37 0.37 0.16	0.37	181.0
100	15 20 30	66.13	0.63 0.69 0.7	0.28 0.27 0.27	0.27	241.4
150	15 20 30	65.52	0.49 0.5 0.43	0.23 0.23 0.23	0.23	281.2
200	15 20 30	65.11	0.63 0.69 0.8	0.21 0.21 0.22	0.21	307.1
250	15 20 30	64.78	1.00 1 1.00	0.19 0.19 0.19	0.00019	342.8
300	15 20 30	64.61	1.00 1 1.00	0.18 0.18 0.18	0.18	367.1
400	15 20 30	64.44	1.00 1 1.00	0.17 0.17 0.16	0.17	390.6

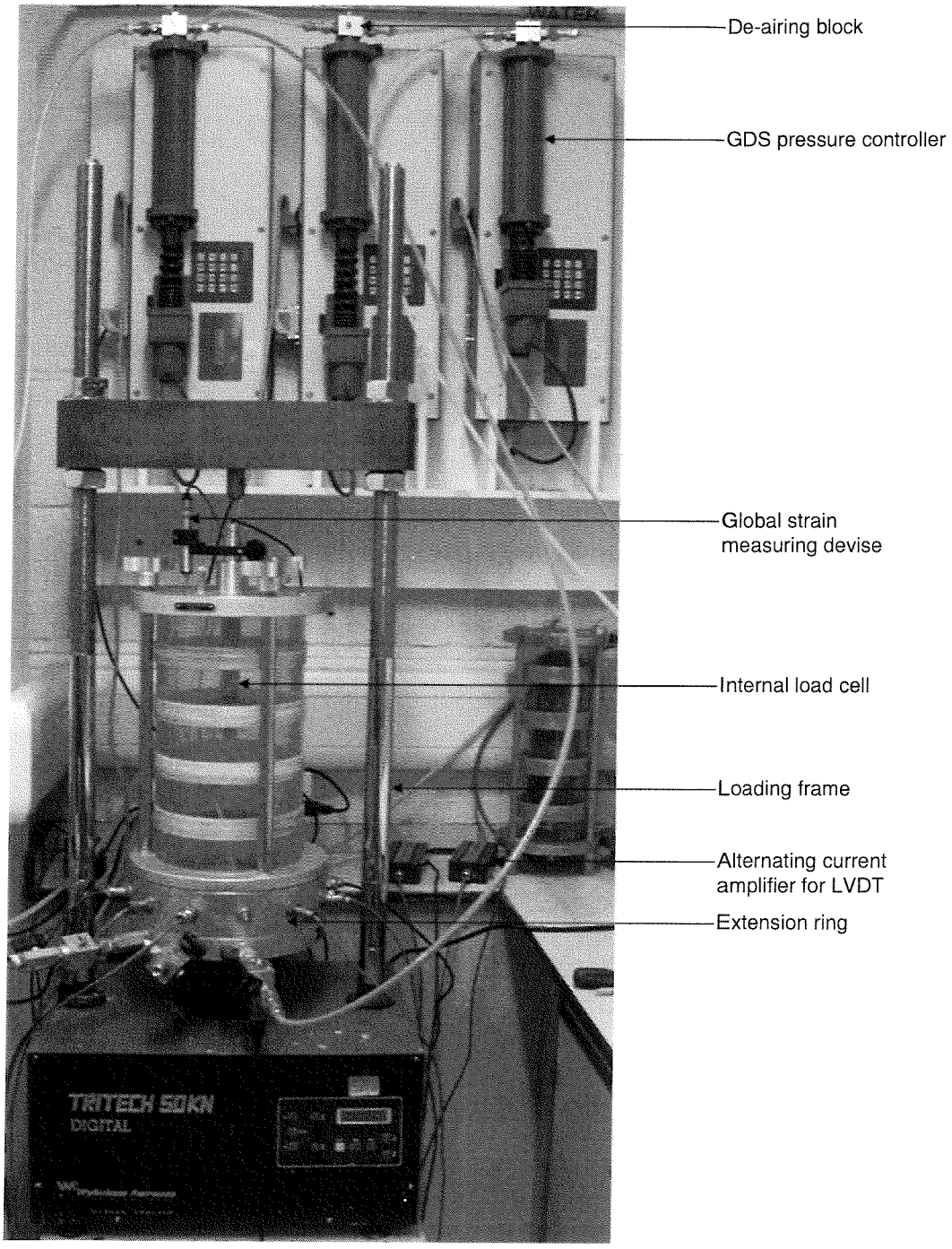

Figure 4.1: The triaxial equipment used during the experimental program

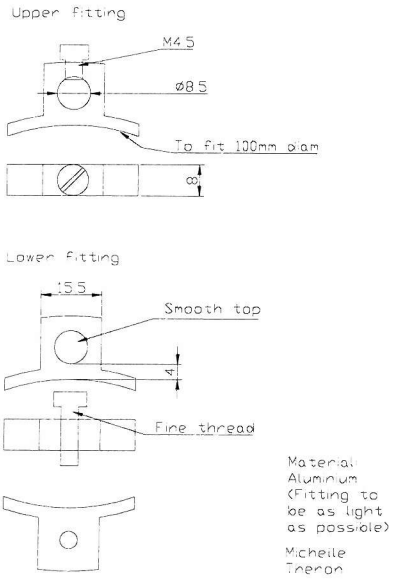

Figure 4.2: Design drawings of LVDT brackets

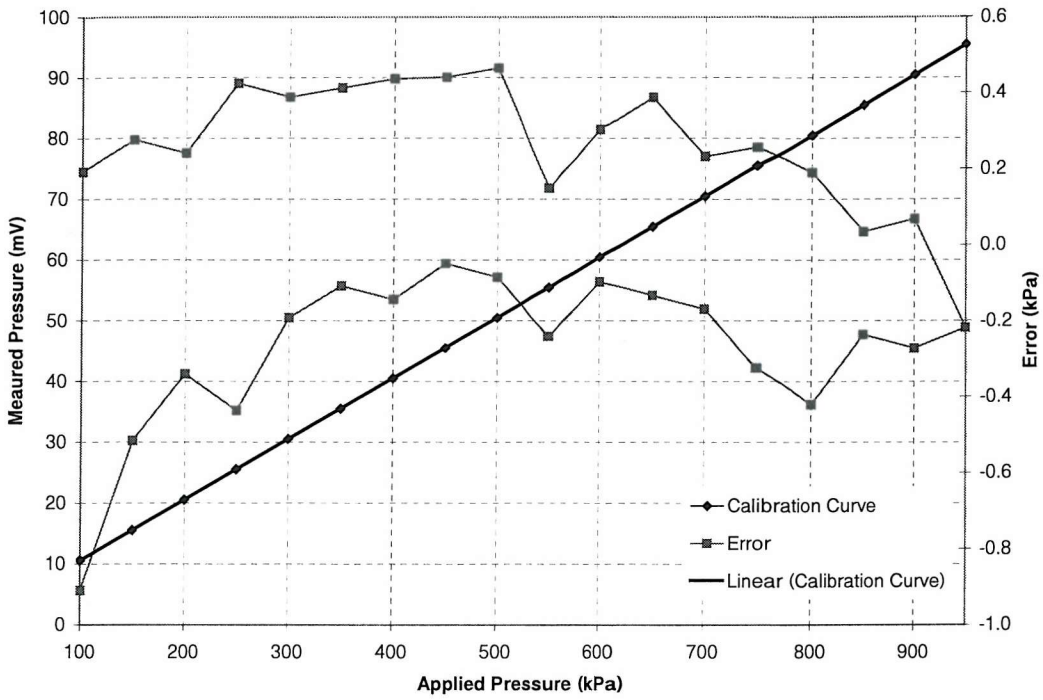

Figure 4.3: Typical calibration graph for a Druck PDCR810 pressure transducer

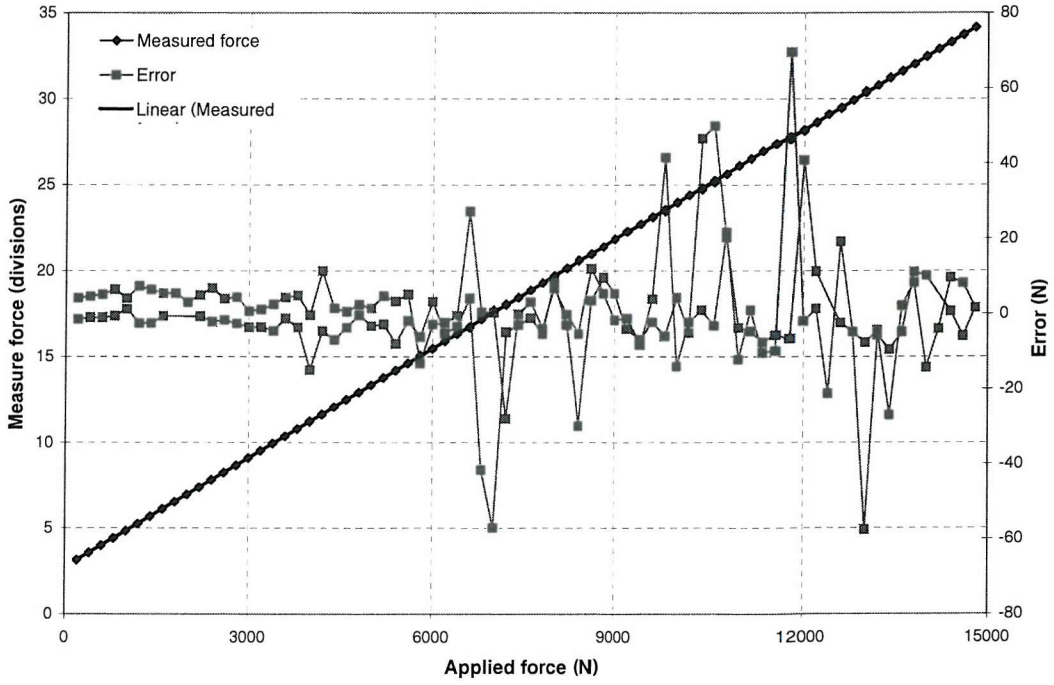

Figure 4.4: Calibration graph for 10kN load cell

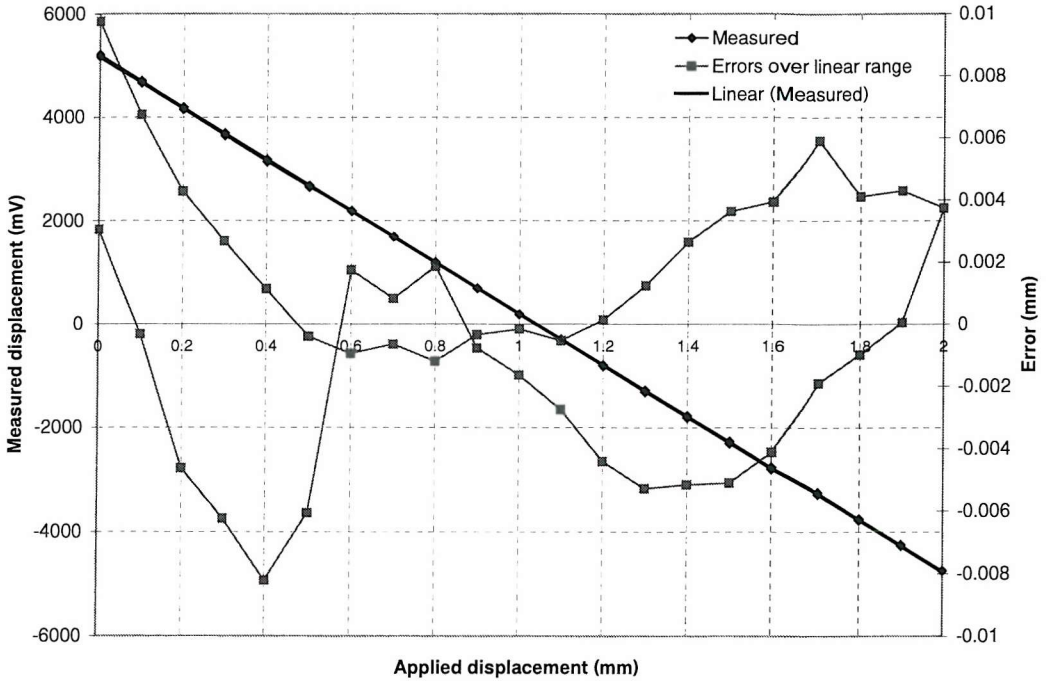

Figure 4.5: Typical calibration graph for a LVDT

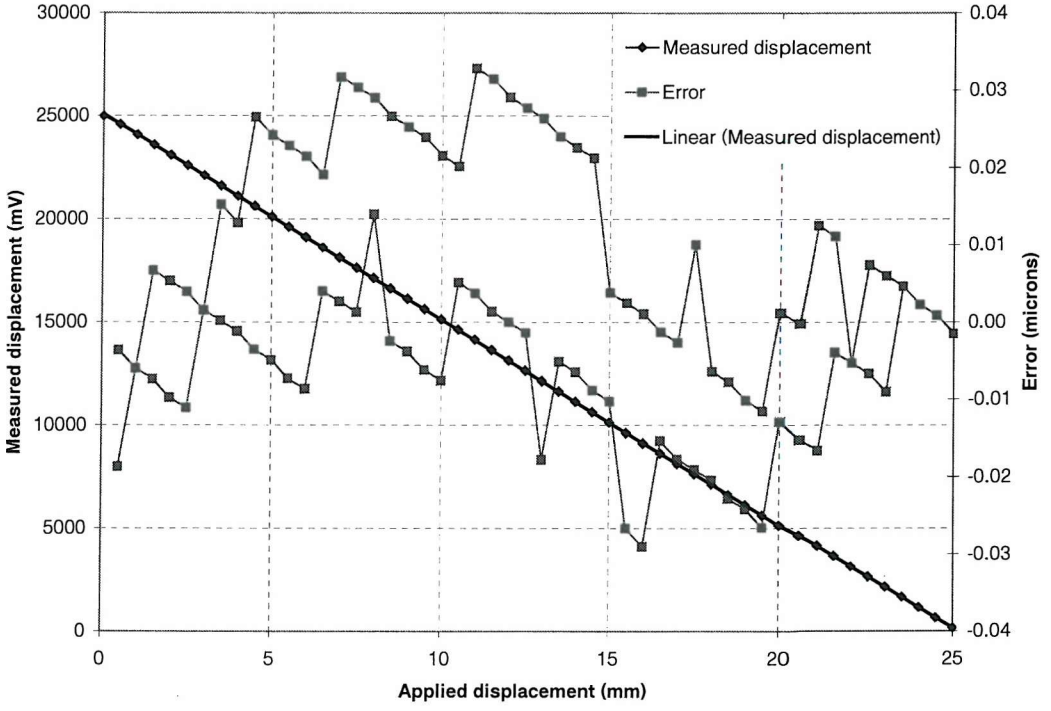

Figure 4.6: Calibration graph for the LDS

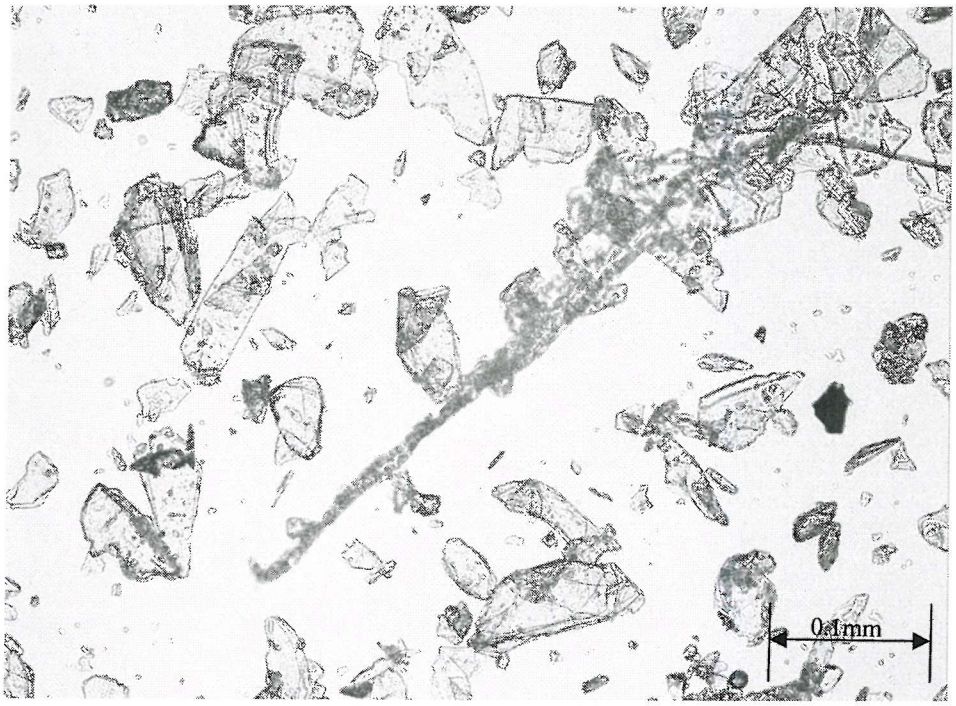

(a)

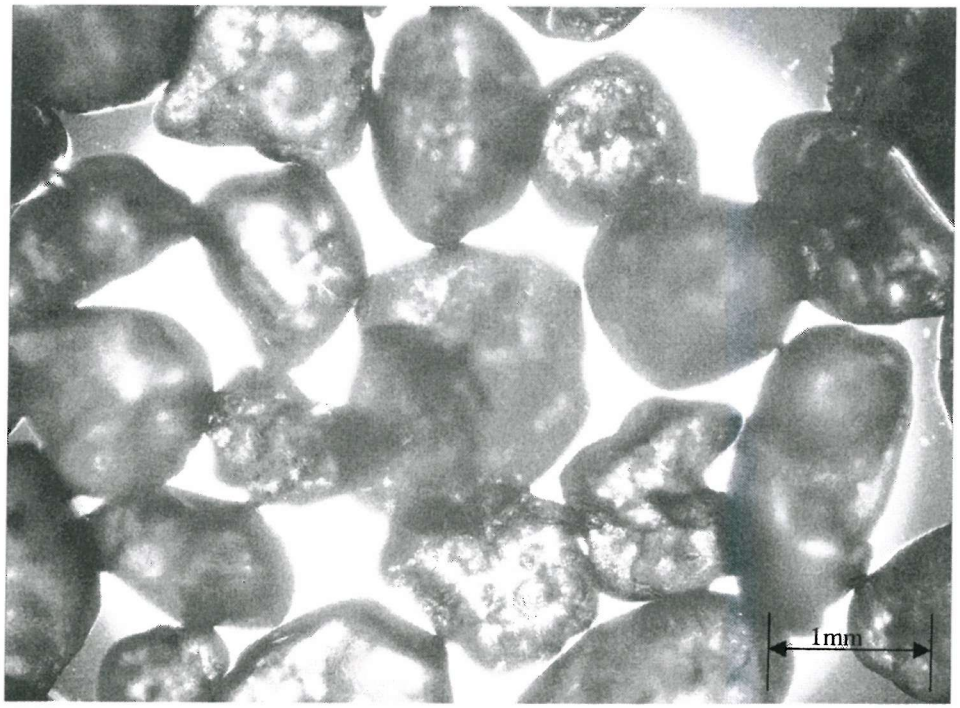

(b)

Figure 4.7: Microscope picture showing particle shape of platy and rotund sand particles

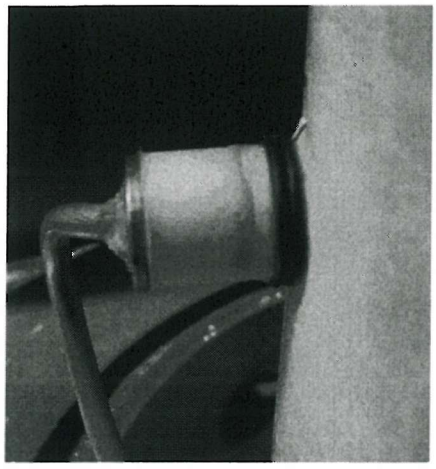

(a)

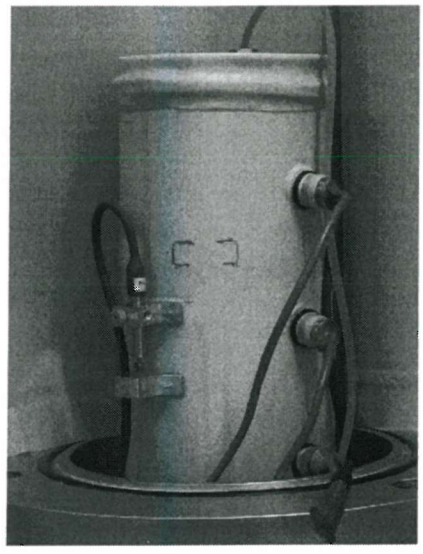

(b)

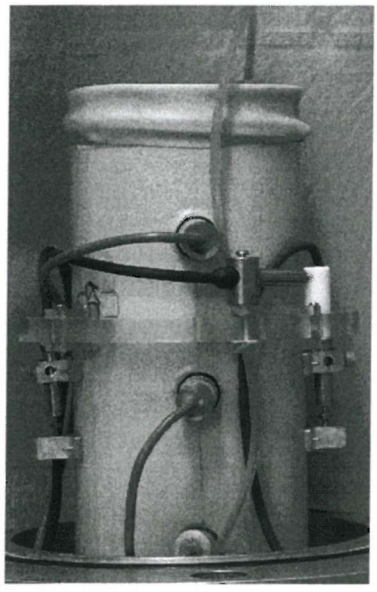

(c)

Figure 4.8: Pictures of specimen preparation showing (a) completed bender element configuration, (b) specimen with bender elements and LVDT and (c) specimen with complete instrumentation

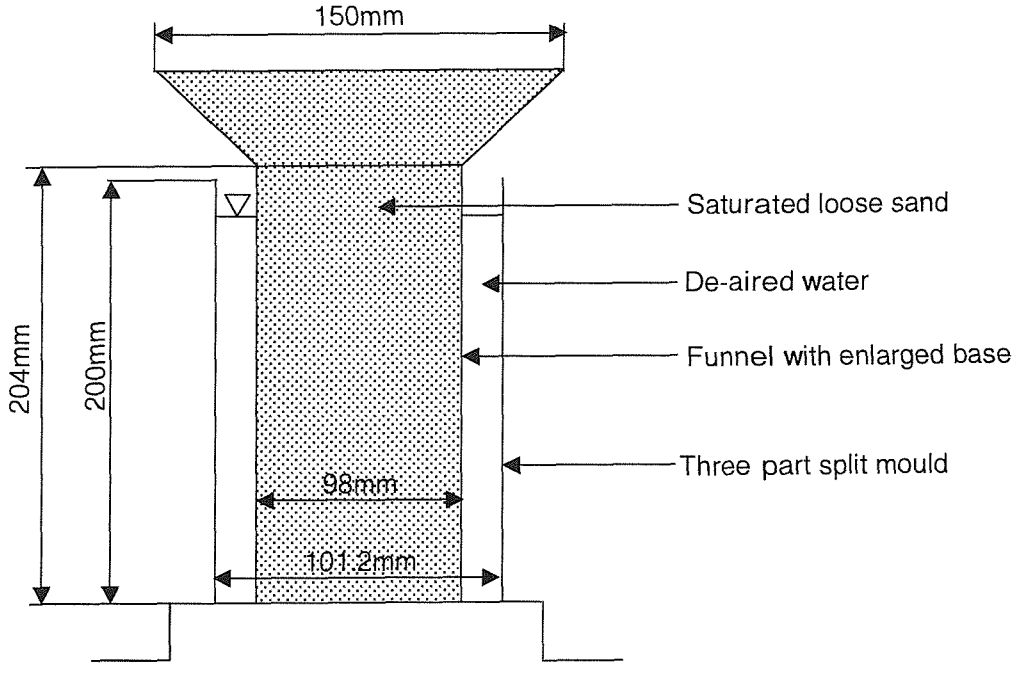

Figure 4.9: Schematic presentation of enlarged funnel used for preparing loose rotund sand specimens

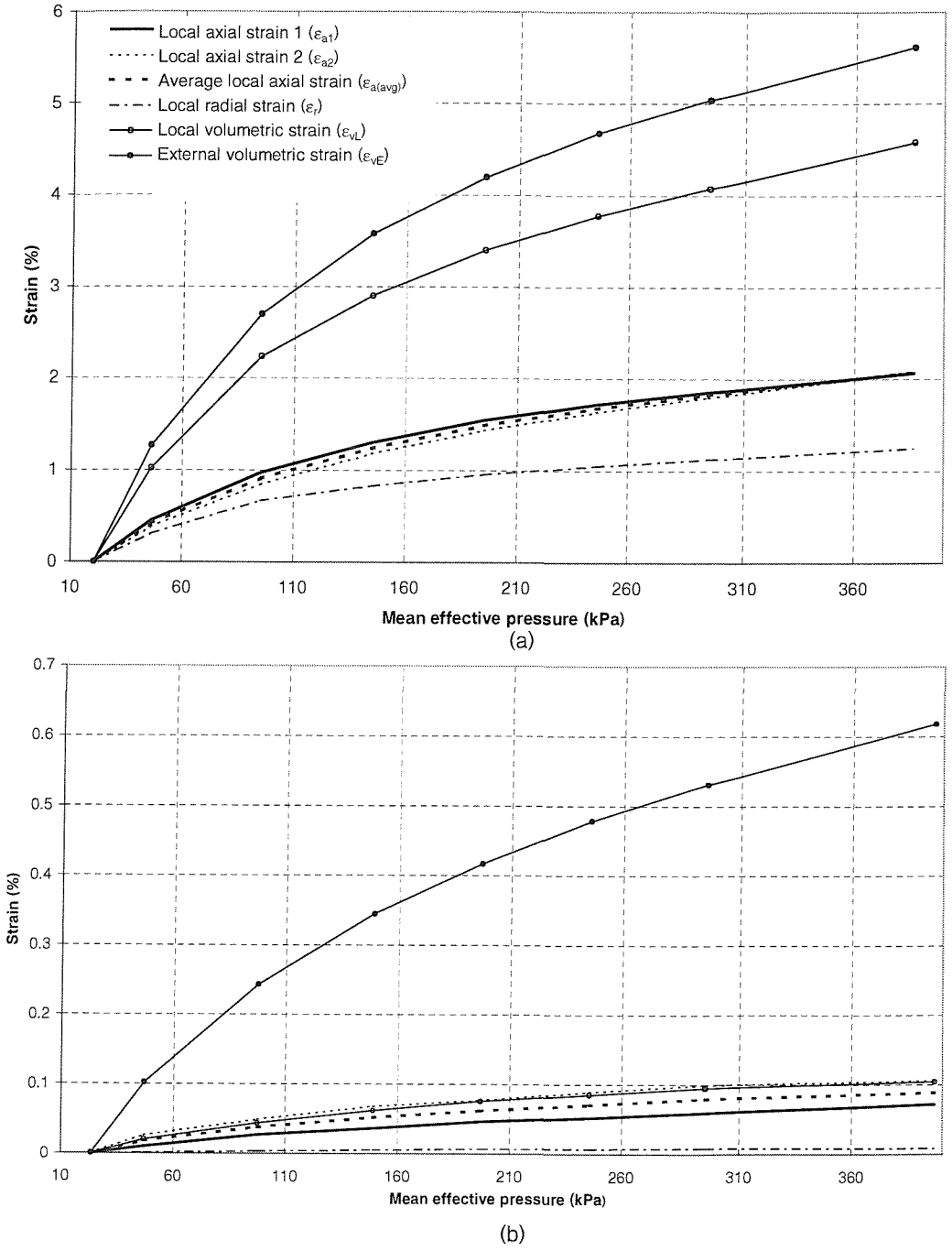

Figure 4.10: Comparison of external and local volumetric strain for (a) 15% mica specimen, (b) dense rotund sand specimen

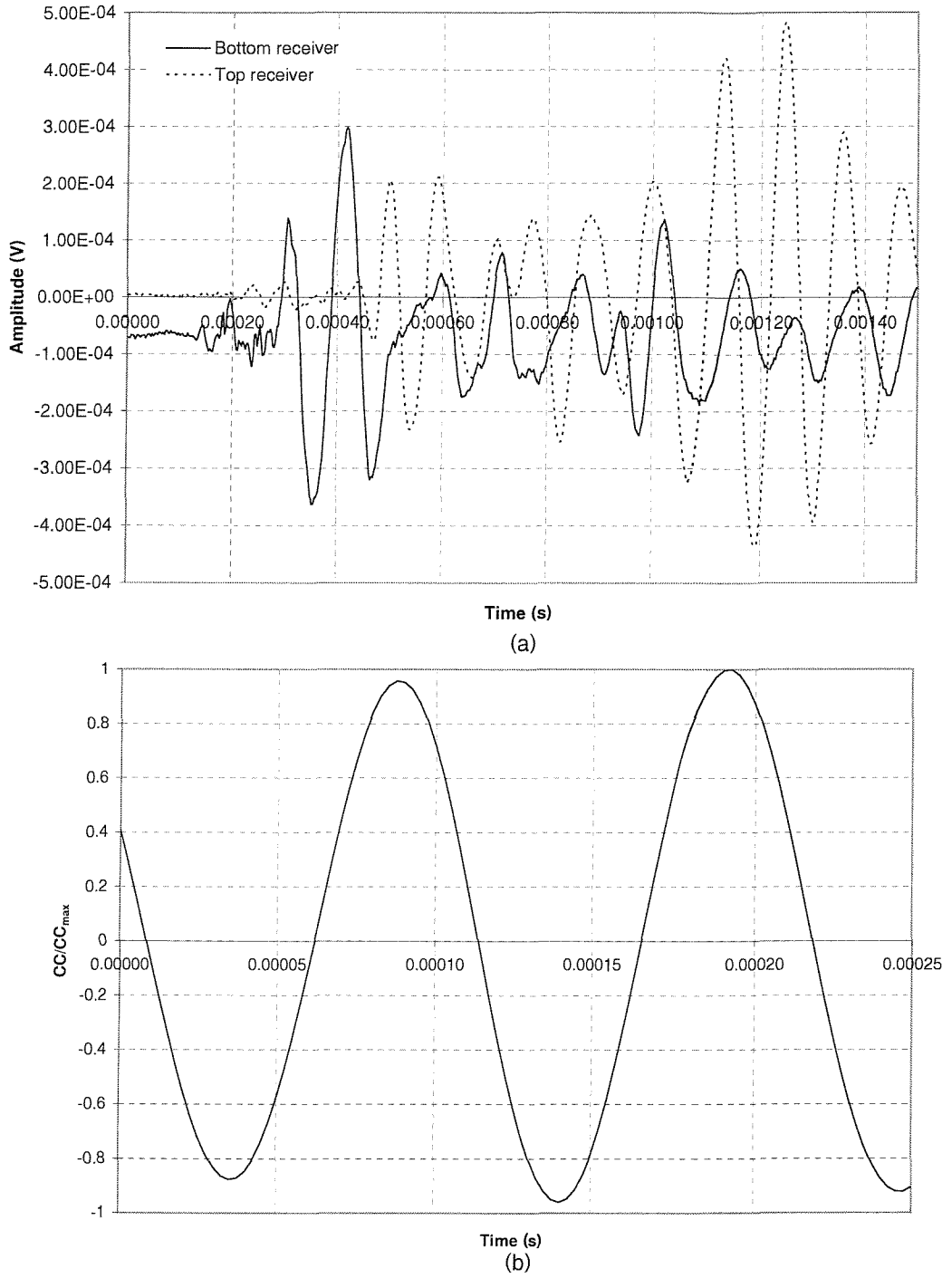

Figure 4.11: Example of an "easily interpreted" bender element result showing (a) recorded traces (b) cross correlation for 15% soton soil specimen at an effective consolidation pressure and input frequency of 200kPa and 15kHz respectively

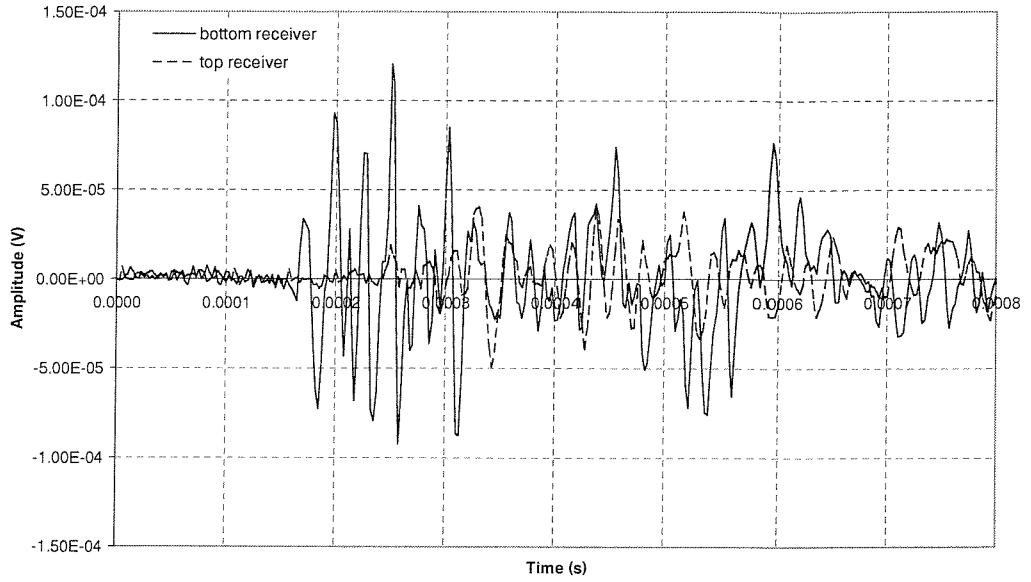

(a)

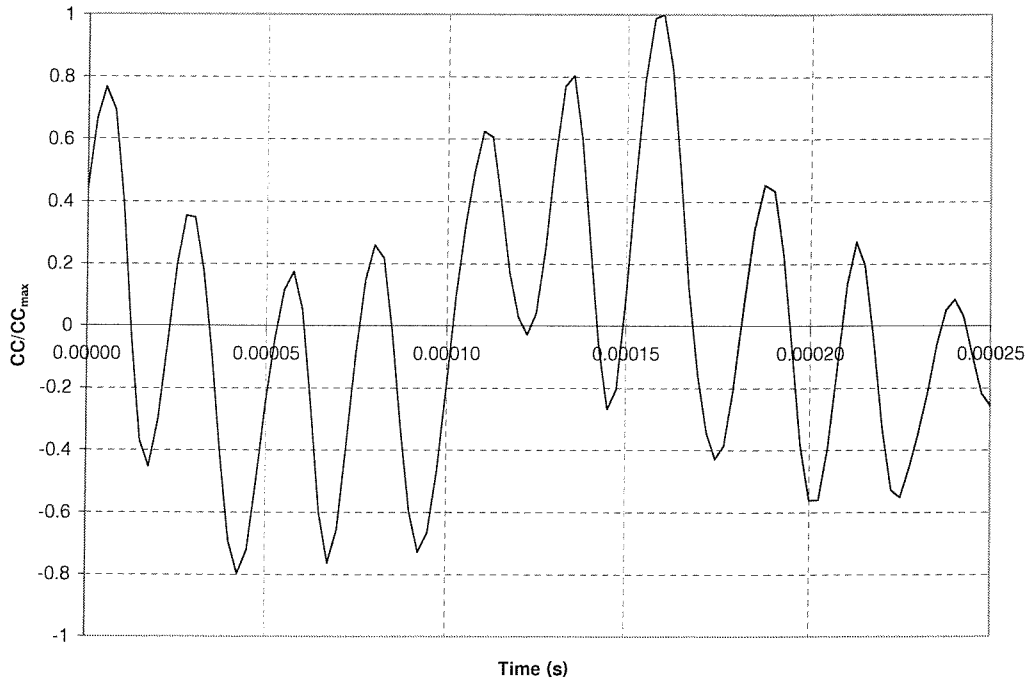

(b)

Figure 4.12: Example of a "complicated interpreted" bender element result showing (a) recorded traces (b) cross correlation for 15% soton soil specimen at an effective consolidation pressure and input frequency of 50kPa and 30kHz respectively

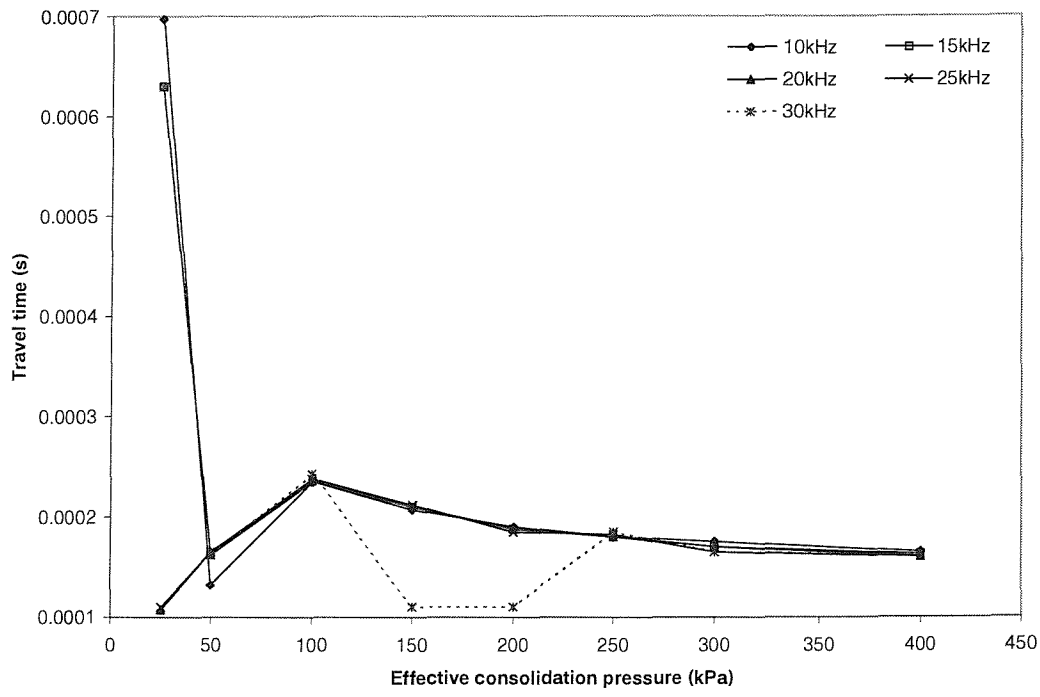

Figure 4.13: Influence of effective consolidation pressure on the repeatability of the travel time for a Soton Soil containing 10% mica

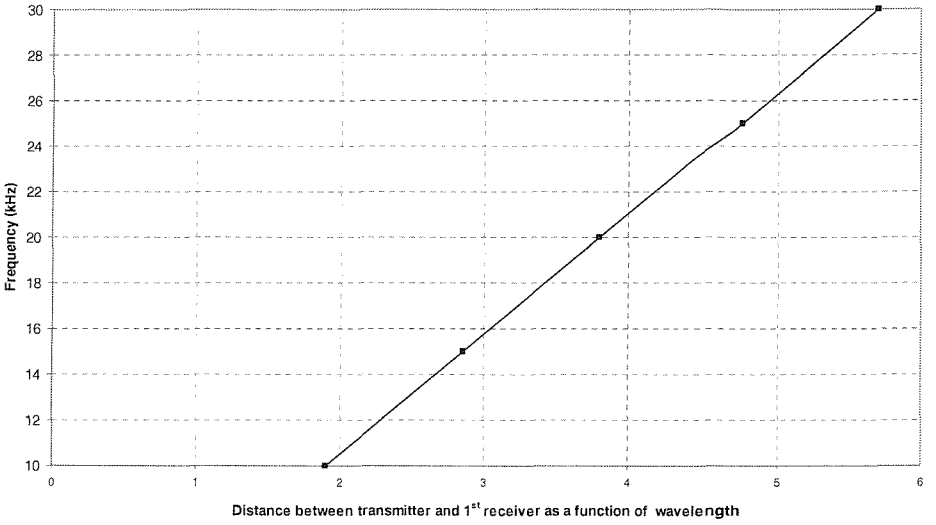

Figure 4.14: Influence of frequency on the travel distance between the transmitter and first receiver in terms of wavelength of a 10% Soton SOil specimen for an effective consolidation pressure of 200kPa

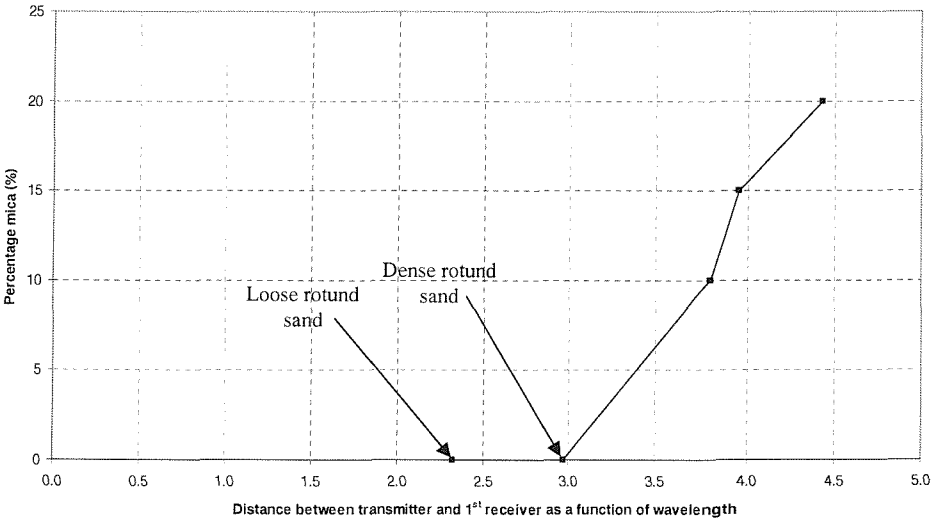

Figure 4.15: Influence of mica content on the travel distance between the transmitter and first receiver in terms of wavelength for an effective consolidation pressure and input frequency of 200kPa and 15kHz respectively

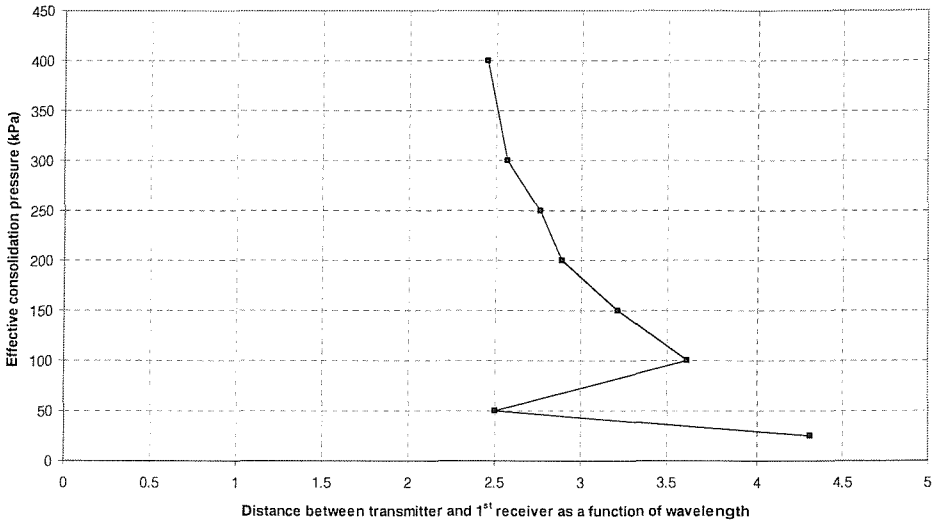

Figure 4.16: Influence of effective consolidation pressure on the travel distance between the transmitter and first receiver in terms of wavelength of a 10% Soton SOil specimen for an input frequency of 15kHz

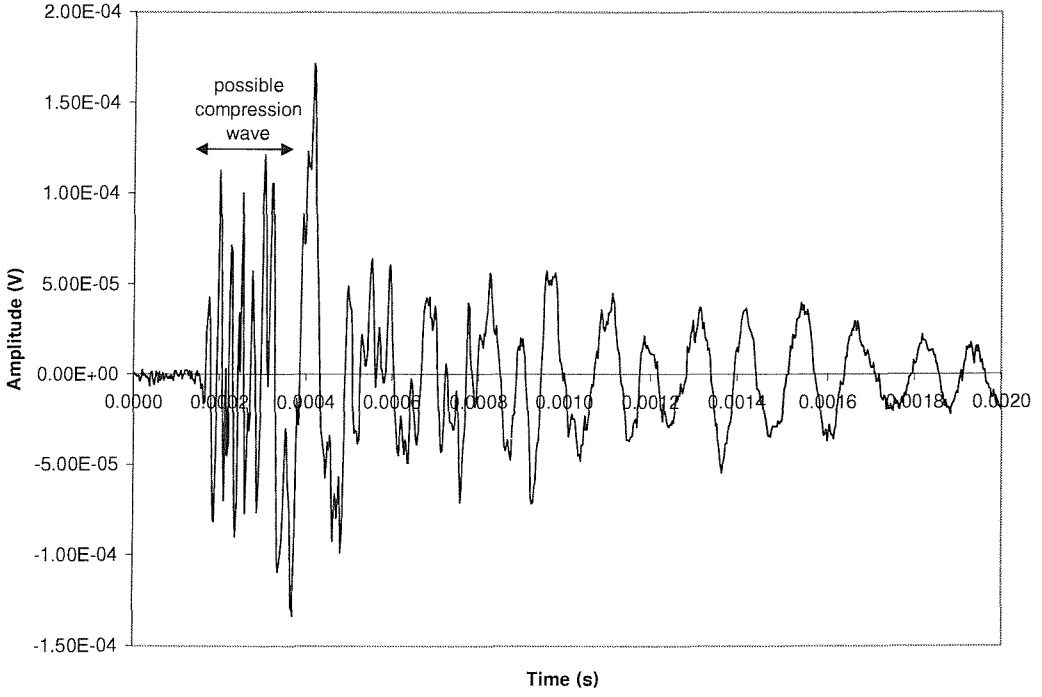

Figure 4.17: Example of bottom receiver signal of 15% Soton Soil for input frequency and effective consolidation pressure of 30kHz and 400kPa respectively, showing the "apparent compression wave"

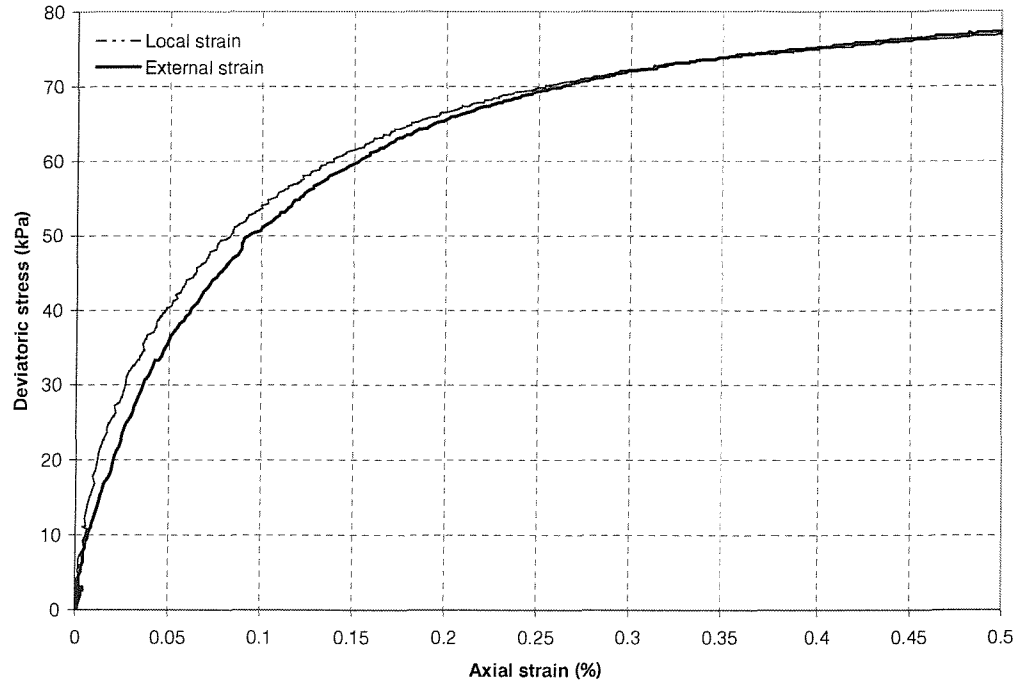

(a)

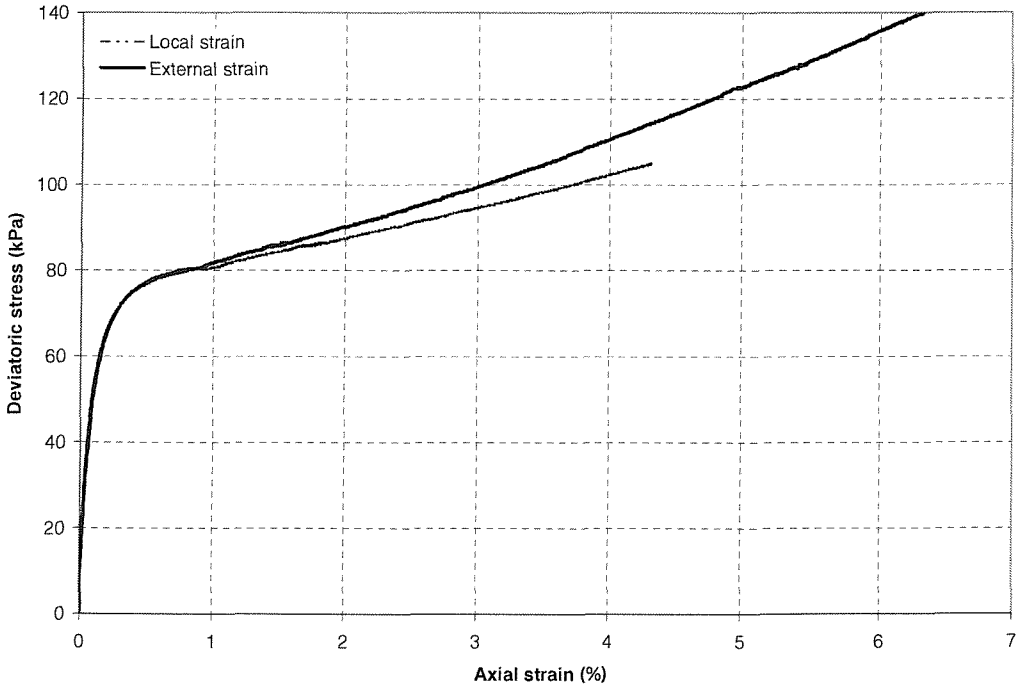

(b)

Figure 4.18: Local and external axial strain measurement for 15% Soton Soil specimen at 200kPa effective consolidation pressure showing (a) small strain and (b) large strain behaviour

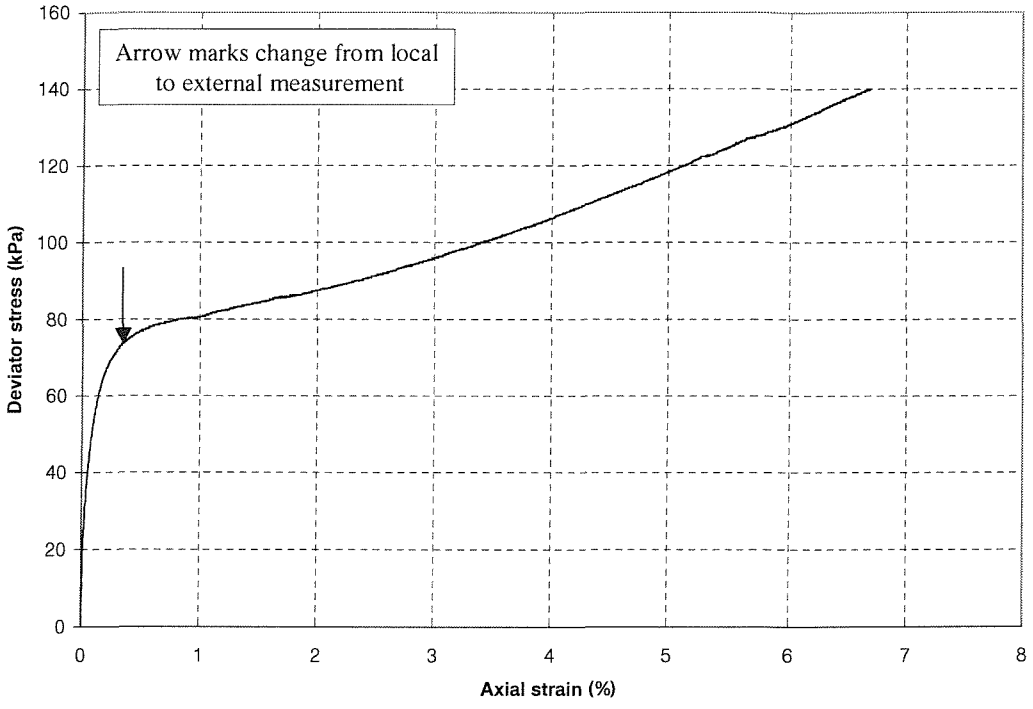

(a)

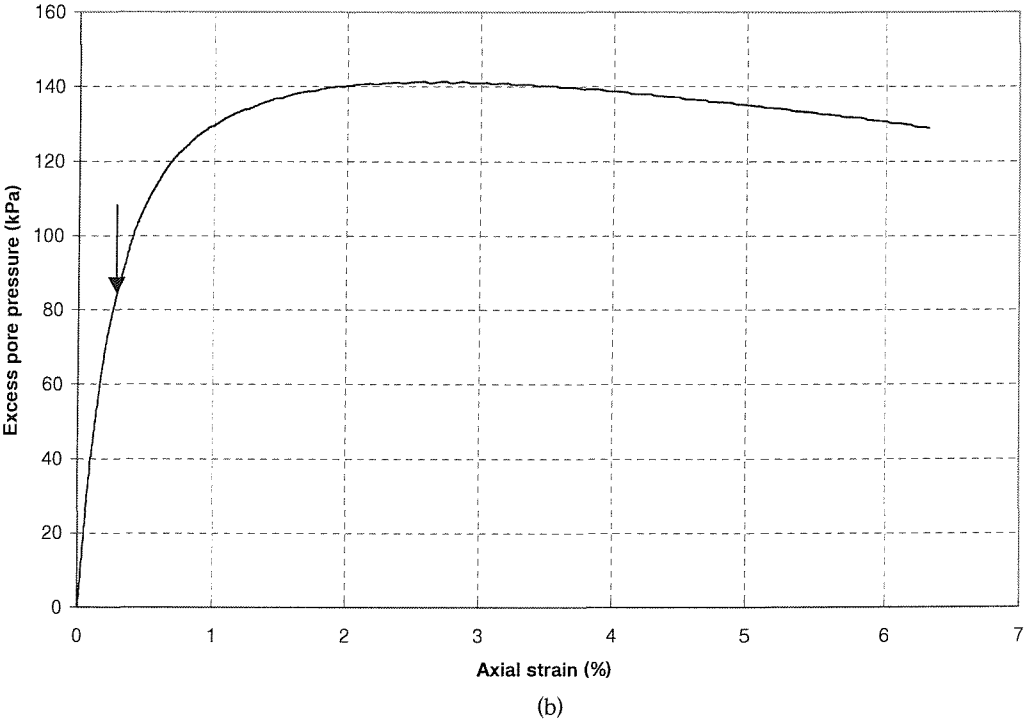

(b)

Figure 4.19: Example of stress vs strain and pore water curves for a Soton Soil specimen containing 15% mica, isotropically consolidated to 200kPa effective consolidation pressure

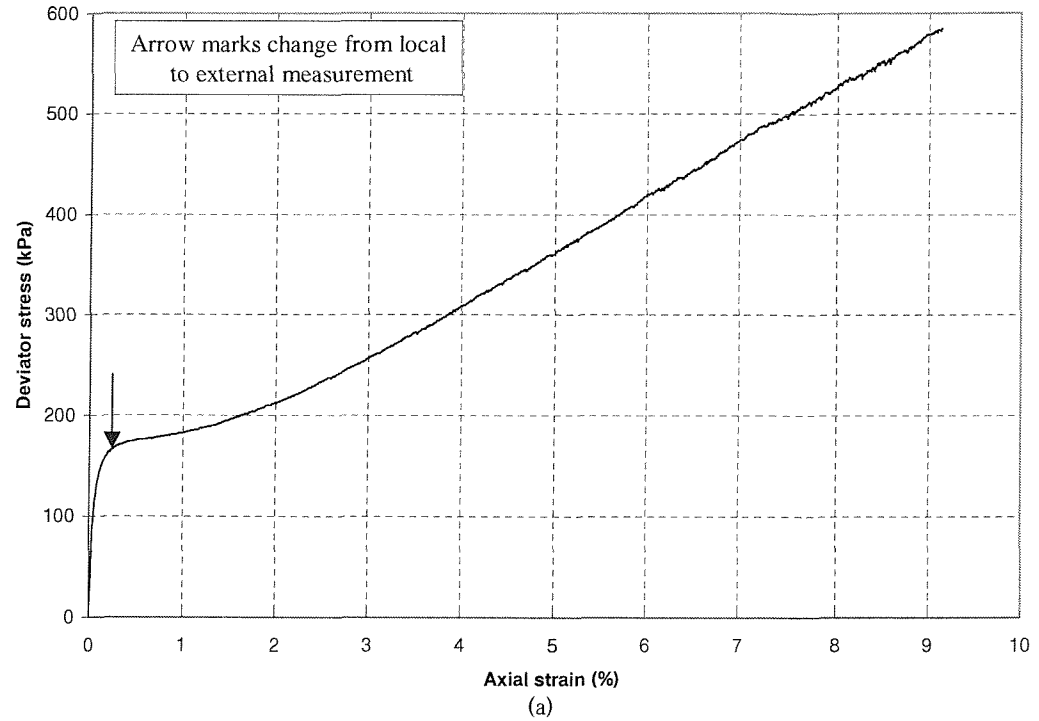

(a)

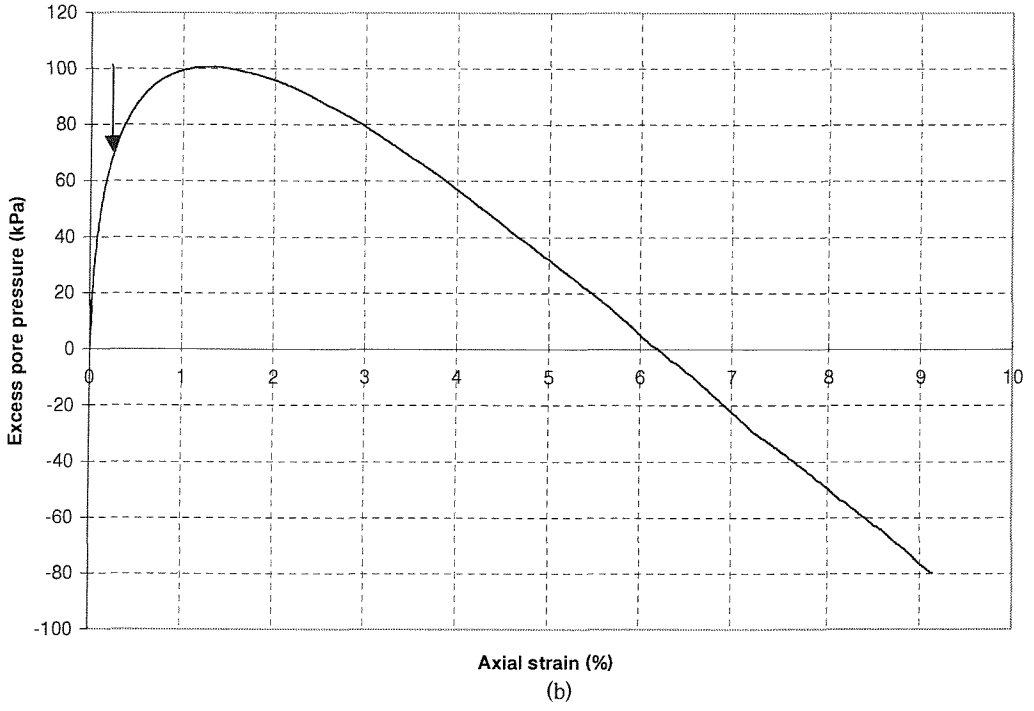

(b)

Figure 4.20: Example of stress vs strain and pore water curves for loose rotund sand specimen isotropically consolidated to 200kPa effective consolidation pressure

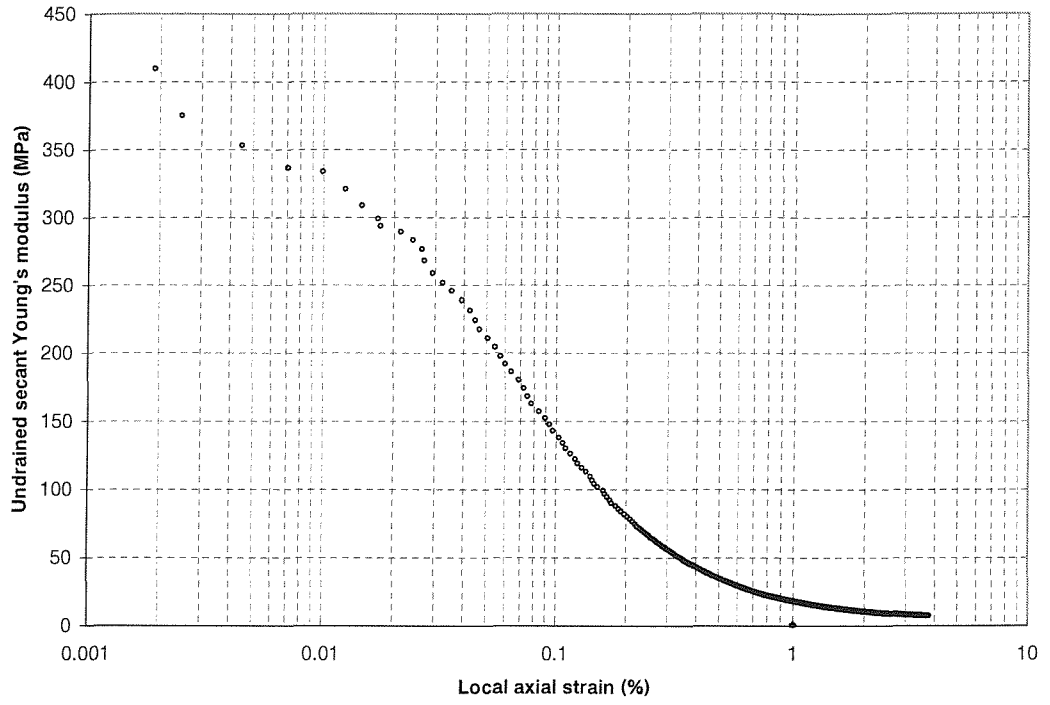

(a)

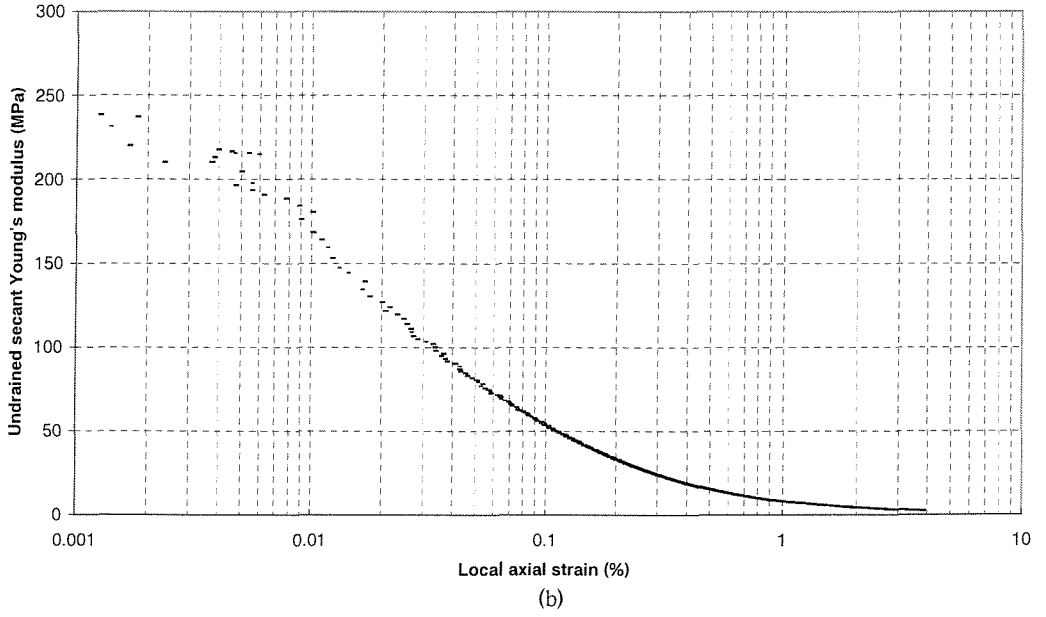

(b)

Figure 4.21: Undrained secant Young's modulus as a function of local axial strain of loose rotund sand and 15% Soton Soil specimens isotropically consolidated to 200kPa effective consolidation pressure

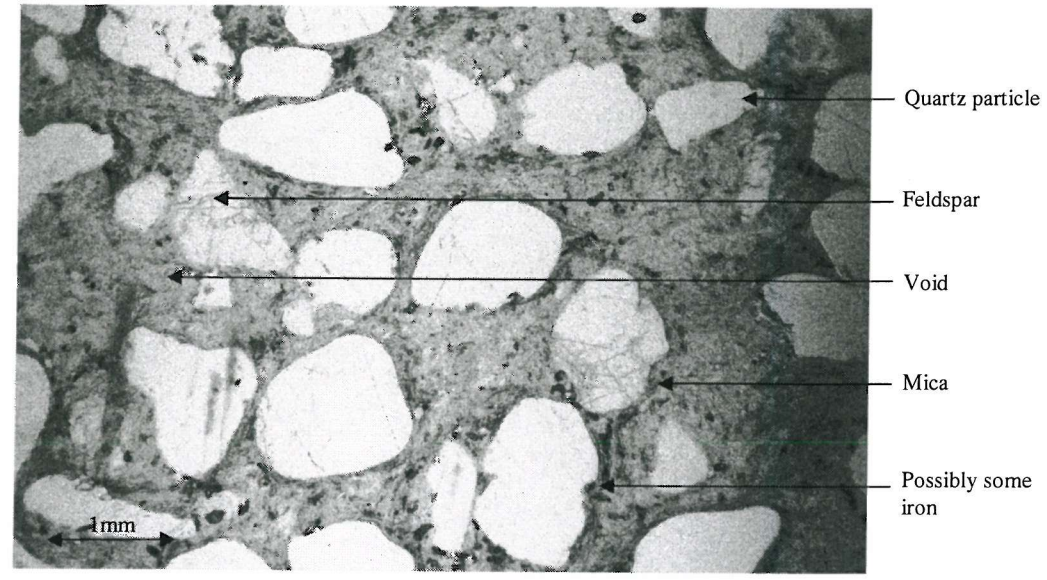

(a)

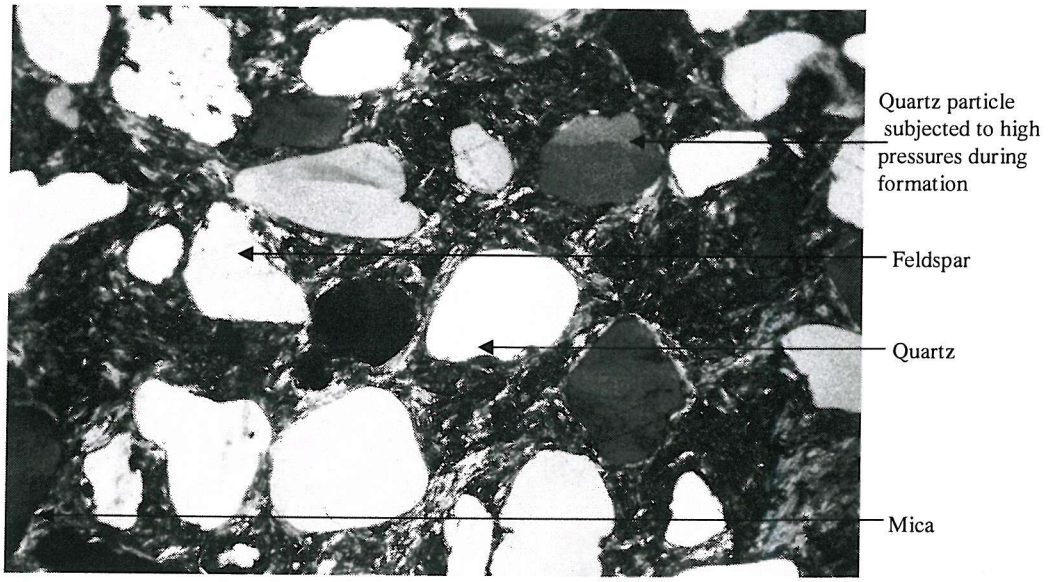

(b)

Figure 4.22: Horisontal section of Soton Soil containing 20% mica for (a) polarized and (b) cross polarized light at 22.5 magnification

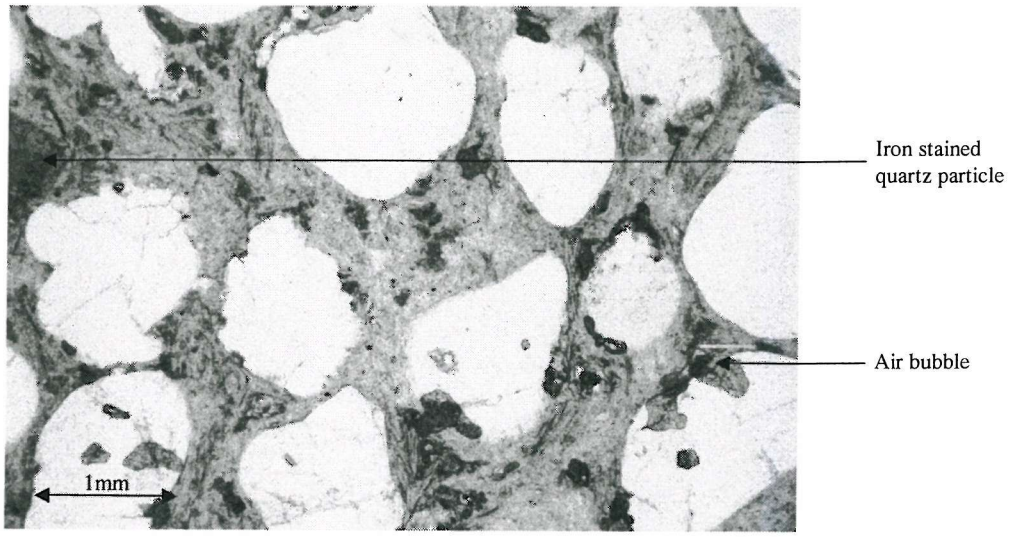

(a)

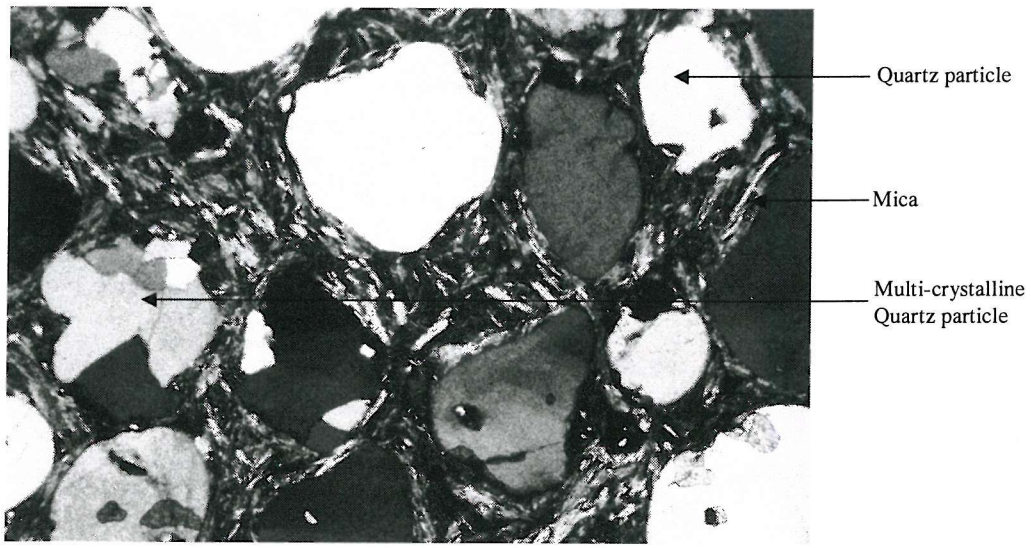

(b)

Figure 4.23: Horisontal section of Soton Soil containing 20% mica for (a) polarized and (b) cross polarized light at 47.5 magnification

Chapter 5

DISCUSSION

5.1 Introduction

A literature review was conducted to develop a framework for the mechanical behaviour of mine tailings as well as to investigate the behaviour of other geomaterials containing similar particle shapes (Chapter 2). The influence of platy fines on the behaviour of rotund coarse particles was assessed by means of a laboratory investigation on Soton Soil (Chapter 4). The Soton Soil consisted of coarse rotund particles containing various amounts of platy fines in the form of mica. The particle shape of the fine and coarse particles employed in this study was similar to gold mine tailings investigated by Vermeulen (2001). The intention was to draw a parallel between the behaviour of the Soton Soil and gold mine tailings. A new bender element configuration and novel interpretation technique was developed to measure the small strain shear stiffness of the Soton Soil. This was discussed in detail in Chapter 3 and will thus not be included in this chapter.

5.2 Influence of platy fines on the behaviour of rotund coarse particles

The influence of platy particles on the behaviour of rotund particles has been investigated by other researchers such as Gilboy (1928), Moore (1971), Audibert et al. (1976), Hammond and Hardcastle (1987) and Hight et al. (1999). In all of these studies, particles of equal diameter were used. Several researchers such as Miura et al. (1997), Zlatovic and Ishihara (1997), Thevanayagam (1998), Thevanayagam (1999) and Yamamuro, Covert and Lade (1999) investigated the influence of silt sized particles on the behaviour of sand. These investigations however, were limited to equi-dimensional particles (i.e. non-platy particles). The research in both fields of interest indicated that both particle size and shape influence the mechanical behaviour of sand. The combination, to the knowledge of the author, however has not been addressed.

Natural soil and mine tailings incorporate both of these particle characteristics (shape and size). It is hypothesized that the platy fines govern the mechanical behaviour of mine tailings, especially that of gold tailings. As the combination of particle shape and size has not yet been investigated, this could not be confirmed from the literature.

This research project investigates the influence of platy fines on the behaviour of coarse rotund particles by means of an experimental program. The diameter of the platy fines was a tenth of the coarse rotund particles. The observed behaviour was then compared with that of gold mine tailings.

5.2.1 *Fabric*

The influence of platy fines on the mechanical behaviour of coarse rotund particles was firstly assessed in terms of fabric[1]. This was achieved by studying the change in density and void ratio with a range of platy fines content.

[1] definition of fabric is found in Chapter 4

Photographs taken of magnified thin sections were also used.

Terzaghi and Peck (1948) developed a classification system for sands based on their standard penetration resistance. Numerical values for the relative densities corresponding to these descriptions were later added by Gibbs and Holtz (1957) (Table 5.1). Table 5.2 summarizes the global bulk and relative densities of the Soton Soil and rotund sand specimens at an effective consolidation pressure of 400kPa. Global densities were calculated from the measured specimen weight and dimensions. The relative densities cited in this table refer to the coarse rotund particles only. Comparing the relative density of the Soton Soil containing 5% platy particles with those proposed by Gibbs and Holtz (1957), it could be seen that the material could be classified as a loose sand. The measured density (bulk and relative) should thus be viewed in the light of this description.

The addition of 5% platy fines to the rotund coarse particles increased the bulk density of the sand. This was due to the fact that the platy fines partially fill the voids between the rotund particles without changing the volume of the specimen. The addition of platy fines in greater percentages reduces the bulk density until finally, it falls below that of the loose rotund sand specimen. Yamamuro et al. (1999) investigated the behaviour of a silty sand and found that an increase in fines (silt) resulted in an increase in relative and bulk density. This discrepancy could be attributed to the difference in particle shape of the fines. Hight et al. (1999) also noted the influence of particle shape on the density of a rotund sand.

An increase in platy fines content above 10% resulted in a decrease in relative density of the rotund particles until finally negative values were obtained at 15% and 20% mica (Table 5.2). A relative density of -114% was obtained for the latter. As mentioned, the aspect ratio of the mica particles is relatively high (in the order of 25[2]) and the addition of 1% mica by weight is equal to 25% by number of grains (Hight et al., 1999). If this argument is followed through, the addition of 20% mica by weight is thus equal to

[2]aspect ratio of mica particles obtained from microscope photographs

500% by number of grains. In the light of this, the negative relative densities obtained for the rotund particles at high mica content seem realistic.

The rate at which the relative density of the rotund particles decreases, reduces as the platy particle (mica) content is increased. In order to establish how this is brought about, the change in fabric of the Soton Soil was investigated. Initially the addition of platy fines partially fills the voids between the rotund particles, thereby increasing the weight of the specimen without altering its volume. The void ratio decreases whilst the bulk density increases. Specimens containing 5% and 10% platy fines satisfy this condition (Table 5.2). The particle shape (i.e. rotund or platy) controlling the mechanical behaviour of the Soton Soil depends on whether or not clean contact between the rotund coarse particles exists. The course rotund particles are in clean contact with each other as the platy fines only partially fill the voids and hence the mechanical behaviour of the Soton Soil at these mica contents are governed by the rotund particles. As the platy fines fill the voids, the rotund grains are pushed apart and the governing particle shape changes from rotund to platy. This transition appears to take place for mica content in excess of 10%. The rotund particles become "suspended" in the mica matrix and the behaviour is controlled by the fines.

In order to validate this mechanism, results were interpreted in terms of an equivalent void ratio (e^*). The equivalent void ratio is defined as the void ratio of the platy fine particles if it were to occupy the same volume as the corresponding Soton Soil (Equation 5.1). A similar definition but with regards to coarse particles was employed by Kuerbis et al. (1988), Mitchell (1993), Thevanayagam (1998), Lade et al. (1998), Bouckovalas, Andrianopoulos and Papadimitriou (2002) and Vermeulen, Rust, Clayton and Powrie (n.d.) to investigated the influence of fines on behaviour of silty sand and gold mine tailings.

$$e^* = \frac{e}{1 - f_c} \tag{5.1}$$

where

$$f_c = \text{proportion of coarse particles by weight}$$
$$e = \text{void ratio of Soton Soil specimen}$$

The influence of platy fines on the equivalent void ratio is illustrated in Figure 5.1. At 5% platy fines the equivalent void ratio is relatively high (11.12) but decreases drastically with the addition of only 5% platy fines (i.e. 10%). The particle arrangement at 5% platy fines is clearly governed by the rotund sand grains. Above 10% platy fines, the rate at which the equivalent void ratio reduces, decreases until it stabilizes around a value of 3.78 for 15% and 20% fines content. The rotund coarse particles are suspended in the platy fine matrix and the fines dominate the mechanical behaviour of the Soton Soil. This illustrates the importance of the amount and location of the platy mica particles in the sand.

Microscope photographs taken of the thin sections were employed to study the fabric of the Soton Soil on a local scale. Figures 5.2 to 5.5 show polarised and cross-polarised photographs of the thin sections in the horizontal plane at 22.5 magnification of the 5% to 20% platy fines specimens. The field of view of the photographs differ slightly as the additional lens for cross polarization changed the lighting and hence focus. The quartz sand particles appear colourless whilst the mica appear pale green to black in the polarized thin sections. In terms of the cross polarized photographs, the colour of the quartz particles varied between white, yellow, light and dark grey whilst that of mica between bright yellow and orange. It can be seen that the mica flakes align themselves parallel against the surface of the rotund quartz particles. In the voids between the quartz particles, mica particle orientation is random. At 10% mica content, the fines are mostly confined to the voids between the quartz although some could be noted between quartz particles. This is highlighted when investigating a cross polarized photograph at 47.5 magnification of the 10% Soton Soil specimen (Figure 5.6). As the mica content increases,

the presence of mica particles between the quartz grains is more pronounced and less clean contacts between the quartz particles exist. Finally, at 20% mica content, the mica particles appear to cover the quartz eliminating almost all of the clean contacts between the rotund particles. A similar trend was noted when investigating thin sections in the vertical plane.

The equivalent void ratios of the Soton Soil in the vertical and horizontal plane were calculated from thin section photographs to investigate specimen uniformity and fabric anisotropy. The equivalent void ratio in this case, refers to the coarse rotund particles present in the specimens. Polarized photographs of the thin sections at 47.5 magnification were employed for this purpose. A computer package named "Image Tool" was used to analyse the specimens. This was done by specifying the scale of the photographs and manually outlining each of the rotund specimens. The area of the photograph as well as the rotund sand particles were then calculated. A "two-dimensional" equivalent void ratio was then calculated and compared with the 'three-dimensional" equivalent void ratio calculated from specimen measurements (Table 5.3). Harr (1977) considered a cross-section through a sample of particulate media and found that the average area porosity is the volume porosity. "Relating the geometric definition of probability, it follows that in concept the porosity of a particulate material is the propability of finding (hitting) a void in a unit of material," (Harr, 1977). Since porosity and void ratio are related to each other ($e = \frac{n}{1+n}$), this implies that the area (two-dimensional) and volume (three-dimensional) void ratio are also equal, which makes them fit for comparison. Good agreement was obtained between the three-dimensional and averaged two-dimensional equivalent void ratios of the specimens.

The vertical and horizontal equivalent void ratios differed with the former being greater, suggesting fabric anisotropy. Anisotropy appeared to increase with mica content. In order to confirm these observations, the average local axial and radial strains of the Soton Soil was compared. Similar to the equivalent void ratio, some anisotropy could be noted that increased with

mica content (Table 5.4). This could be attributed to the compressibility of the mica flakes. Particle arrangement of the mica particles changes during construction of the specimen. Initially mica orientation is random as the voids between the rotund particles are relatively large. As the Soton Soil is spooned into the mould, the voids decrease and the mica flakes progressively arrange themselves parallel to the surface of the rotund particles. An increase in mica content would thus result in an increase in platy particles that orientate themselves parallel to the rotund particle surfaces thereby increasing compressibility. In the horizontal dimension the specimen was confined by the mould while in the vertical dimension by the base pedestal and top-cap. As the diameter of the mould was less than the length of the mould, the compressibility in the horizontal direction was less, resulting in a lower void ratio. The adopted specimen procedure thus did not produce uniform specimens. It was however, doubted that any of the reviewed techniques discussed in Chapter 4 would produce better results.

5.2.2 *Compressibility*

The influence of particle shape on the compressibility of sand was assessed by isotropically consolidating Soton Soil specimens containing various percentages of platy fines (mica) by weight, in a triaxial apparatus. Effective consolidation pressures ranging between 25kPa and 400kPa were employed. The compressibility behaviour of the soton soil and rotund sand are shown in Figure 5.7. The slope of the isotropic consolidation line (C_c) of the specimens are indicated. The loose and dense rotund specimens appear to be incompressible with the dense rotund specimen being more so. This is noticeable from the difference in the slope of the isotropic consolidation line (the slope of the dense rotund sand specimen is one order of magnitude less than that of the loose rotund sand specimen).

Compressibility of the Soton Soil increased with increasing platy fines content. A similar behaviour was noted by Gilboy (1928). Been and Jefferies (1985) illustrated that the compressibility of a uniform quartz sand increased

with silt content although less than observed from the Soton Soil containing platy particles. The increase in compressibility with the addition of 5% platy fines is relatively low. As mentioned before, platy fines in such a low quantity partially fill the void spaces between the rotund particles. The increase in compressibility is thus the result of some of the load being carried by the platy fines. However, the addition of 10% mica fines increased the compressibility of the soil by an order of magnitude. This relatively large change in soil behaviour between 5% and 10% mica content was also noted when investigating the equivalent void ratio, calculated from specimen weight and dimensions.

The increase in compressibility of the Soton Soil could be explained in terms of the change in fabric of the material. Platy particles are more compressible than the rotund grains due to their particle shape i.e. bedding can take place and tend to align themselves perpendicular to the loading direction. As the platy fines content increased, the rotund grains are further removed from each other and the sand becomes progressively more compressible. Ultimately, the rotund grains are suspended in the platy fines matrix and the compressibility of the Soton Soil is that of the fines.

5.2.3 *Small strain stiffness*

The influence of particle shape on the small strain stiffness of Soton Soil was investigated by considering both shear and Young's modulli. The small strain shear modulus (G_{max}) of the specimens was measured using side bender element probes (i.e. a transmitter and two bender receivers). This configuration was adopted on the basis of the conclusions drawn from Chapter 3.

The repeatability of the measured travel time of the Soton Soil containing 10% mica, was evaluated by exciting the transmitter element by a range of input frequencies (10kHz to 30kHz at 5kHz intervals). The measured travel times appeared to be repeatable for input frequencies ranging between 15kHz and 30kHz. The travel time obtained from an input frequency of 10kHz deviated from the rest of the results. Back analysis indicated that the first

receiver was still in the near field. A large scatter preceded the shear wave of the remainings specimens when excited by an input frequency of 30kHz. The scatter took on the form of a "compression wave", although this was unlikely as the receivers were in the far field at this input frequency. This phenomenon was ascribed to the particle shape of the Soton Soil, as such a trend was not observed when investigating rotund sand specimens. It was thought that the difference in particle shape and hence the nature of the contacts between the particles resulted in different interference patterns being set up than those typically found in a specimen of equi-dimensional particles such as rotund sand.

Figure 5.8(a) shows the normalised cross correlation function derived from the two received signals of the Soton Soil specimen containing 20% platy fines for an input frequency and consolidation pressure of 15kHz and 250kPa respectively. Two prominent peaks were observed, with the first having a greater normalised cross correlation value. The travel time obtained from this peak resulted in an unrealistically high shear wave velocity while the shear wave velocity of the second peak was within reasonable bounds. This phenomenon was noted on more that one occasion. Table 5.5 presents the travel times of the 20% Soton Soil specimen obtained from the first and second peaks of the cross correlation function as well as that obtained from characteristic peaks (hand picking) for a range of input frequencies and effective consolidation pressures. It should be noted that not all of the travel times derived from the first peak of the cross correlation function were unrealistic. Unrealistic travel times corresponded to cross correlation functions with two prominent peaks. In the event of two prominent peaks, the travel times obtained from the second peak compared well with those obtained from characteristic peaks. Consequently, the travel time obtained from the second peak was assumed to be correct for two prominent peaks.

In comparison, the cross correlation of the dense sand specimen for a similar input frequency and effective consolidation pressure is shown in Figure 5.8(b). A single clear peak could be seen of which the corresponding travel

time is realistic and compared well with the travel times obtained from other effective consolidation pressures. In order to establish the cause of the two cross correlation peaks of the 20% Soton Soil specimen, the recorded received signals were considered. In terms of characteristic peaks, it could be seen that two possible travel times exist (Figure 5.9) which explains the two peaks in the cross correlation function. The only possible way of telling the "true" travel time is by evaluating the derived shear wave velocity in terms of characteristic shear wave velocity values. It is thus recommended that cross correlation analysis results should not be adopted blindly, but should be checked against those obtained from characteristic peaks and that measurements should be made for at least two input frequencies. This will allow for comparison of results.

The addition of platy fines to rotund coarse particles resulted in reduced specimen stiffness and consequently, reduced received signal quality. This complicated interpretation of the bender element results. The quality of the received signals was assessed by considering the signal-to-noise ratio of the recorded signals. In order to illustrate this point, the change in signal-to-noise ratio with effective consolidation pressure and mica content of the bottom bender receiver was calculated. This was done by dividing the amplitude corresponding to the arrival of the shear wave by the average noise. The noise was taken as the change in amplitude prior to the arrival of the shear wave (Figure 5.10). Figure 5.11 shows the relationship between the signal-to-noise ratio and effective consolidation pressure of a Soton Soil containing 20% fines (mica). A reference input frequency of 20kHz was used. The signal-to-noise ratio was especially low at 25kPa effective consolidation pressure. It then slightly increases up to an effective consolidation pressure of 250kPa after which there is a sharp increase. An increase in signal-to-noise ratio implies an increase in signal quality. Consequently an increase in the repeatability of the travel time with effective consolidation pressure was thus found as shown by Figure 4.13.

Figure 5.12 shows the signal-to-noise ratios of the rotund sand and Soton

Soil specimens. A reference effective consolidation pressure of 250kPa and input frequency of 15kHz were adopted. The influence of specimen density on the quality of the received signals could clearly be noted by the large difference in signal-to-noise ratio of the dense and loose rotund specimens. The addition of only 10% mica reduces the signal-to-noise ratio significantly. As already noted, the voids between the rotund coarse particles are partially filled by the platy fines, which have a lower stiffness. The mechanical behaviour of the Soton Soil however, is still controlled by the rotund particles which explains the relative high signal-to-noise ratio obtained. Beyond this platy fines content, the controlling particle shape progressively changes from rotund to platy as the platy fines fill the voids. At 20% platy fines the behaviour of the Soton Soil is essentially that of the platy fines, confirmed by the low signal-to-noise ratio.

Figure 5.13 shows the small strain shear modulus (G_{max}) results obtained from bender element measurements. The derived G_{max} of the Soton Soil specimens containing 10% to 20% platy particles, were unrealistically high at effective consolidation pressures of 25kPa and 50kPa. This was due to the low signal-to-noise ratio as previously illustrated (Figure 5.11). The measured G_{max} at these pressures should be ignored. Apart from the initial erroneous measurements of the Soton Soil specimens containing 10% to 20% platy fines, G_{max} increased with increasing effective consolidation pressure. As the effective consolidation pressure of the specimens increased, so did the bulk density. Greater particle contacts are thus established which allows for greater propagation of the shear wave and consequently, higher shear stiffness. Fioravante and Capoferri (2001), Jovičič and Coop (1997) and Jovičič and Coop (1998) also noted the influence of effective consolidation pressure on the G_{max} of clay and sand.

The addition of 10% platy fines to the rotund coarse particles reduced the G_{max} considerably. However, the addition of platy fines in this quantity resulted in an increase in bulk density (Table 5.2) which at first glance would lead one to expect the opposite reaction. As discussed, platy fines are

predominantly situated in the voids between the coarse rotund particles. Depending on the fines content, the coarse particles are in clean contact with each other. However, as not all of the fines are located in the voids, rotund sand particles may be separated from each other to some degree. This results in a change in inter-particle contacts and therefore the small strain shear stiffness. It thus seems reasonable to assume that the addition of platy fines would result in a further decrease of G_{max}. Surprisingly however, the G_{max} of the 10% and 15% Soton Soil specimens were similar. The reason for this was not certain and the results will later be compared with small strain Young's modulus results obtained from local strain and pressure measurements. A minimum G_{max} was obtained for the 20% Soton Soil specimen. At this point the coarse rotund particles are suspended in the fines matrix and the small strain stiffness of the specimen is essentially that of the fines.

Degradation of the undrained effective secant Young's modulus (E'_{usec}) of the Soton Soil and rotund sand was measured at effective consolidation pressures of 100kPa, 200kPa and 400kPa (Figures 5.14 to 5.16). In order to establish whether the E'_{usec} of the soton soil was also a function of effective consolidation pressure and platy fines (mica) content, results were compared at an axial strain of 0.01%.

The E'_{usec} increased with effective consolidation pressure as expected. In terms of platy fines content, a reference effective consolidation pressure of 400kPa was adopted (Figure 5.16). Once characteristic behaviour at 400kPa was established, the results were confirmed by comparison of the stiffness at the remaining effective consolidation pressures. As before, a maximum stiffness was obtained for the dense rotund sand specimen. The E'_{usec} of the loose rotund and soton soil specimen containing 5% platy fines, were almost similar. This was not surprising as very little platy fines were present and the mechanical behaviour of the soil was that of the coarse rotund particles. The addition of 10% platy fines however, greatly reduced the E'_{usec} of the Soton Soil as sufficient platy fines were present in the voids between the coarse particles to influence its behaviour to some extent. The rate of decrease in

E'_{usec} with increasing fines content reduced until finally there were hardly any differences between the E'_{usec} of the 15% and 20% platy fines content. As noted, the equivalent void ratio also stabilized at these platy fines content which could be attributed to the platy fines controlling the behaviour of the Soton Soil.

Comparing the small strain Young's modulus behaviour of the Soton Soil and rotund sand at 400kPa effective consolidation pressure with that at 100kPa and 200kPa effective consolidation pressures, it was noted that:

- A maximum E'_{usec} value was obtained for the dense rotund sand specimen.
- Apart from the 200kPa effective consolidation pressure, the E'_{usec} of the loose rotund sand specimen was greater than the 10% platy fines content specimen. It is not clear what the reason for this exception was as this was not noted when investigating the small strain shear stiffness (G_{max}) of the specimens (Figure 5.13).
- The E'_{usec} of the 15% and 20% platy fines content specimens were similar.
- E'_{usec} results of the 10% and 15% Soton Soil specimens thus differed from the small strain shear stiffness results obtained from bender element tests.

Following the above, it can be concluded that the E'_{usec} of the sand decreases with increasing platy fines content.

In a summary given by Matthews, Clayton and Own (2000) regarding the elastic strain limit of certain geomaterials, Leighton Buzzard sand was estimated as 0.002%. Bender elements impose strains of less than 0.001% on soil (Brignoli et al., 1996) which in theory makes them suitable for measuring the stiffness of soil within the linear stress-strain range. If it is assumed that the limit of the linear stress-strain behaviour of the soton soil and Leighton

Buzzards sand is similar, E'_{usec} and G_{max} results would lie within an almost straight line. Small strain shear modulus (G_{max}) results were calibrated against the E'_{usec}. The measured G_{max} values of the specimens are shown as enlarged data points on Figures 5.14 to 5.16. A reasonable correlation exists between the measured small strain shear and Young's modulus. It should however be noted that the shear stiffness and Young's modulus are different stiffness measurements and consequently, a good correlation can not be expected.

5.2.4 *Shear strength*

Triaxial compression tests were conducted on the Soton Soil and rotund sand specimens at effective consolidation pressures of 100kPa, 200kPa and 400kPa.

The shear strength behaviour of the Soton Soil and rotund sand was investigated for a reference effective consolidation pressure of 400kPa to establish whether shear behaviour is characteristic of cohesionless soil. The shear response of cohesionless soil is typically dilative or contractive by nature (Figure 5.17) (Verdugo and Ishihara, 1996). Contractive behaviour (C) is characterised by a monotonic increase in deviator stress to an ultimate state at large strains. It then continues to deform under constant shear and mean effective stress. Such behaviour is characteristic of loose sand (Bishop and Henkel, 1962). The shear response of dense sand on the other hand, is partially contractive followed by dilation (C-D) or dilative from the onset of shear (D). In the case of the former, a minimum strength is reached at some point after which it gradually increases until ultimate failure is reached at large strains. The condition of minimum strength has been referred to as quasi-steady state (C-D) (Alarcon-guzmand, Leonards and Chameau, 1988). The term steady state deformation, defined by Poulos (1981), was adopted as the criterion for continued deformation under constant shear stress, and constant normal stress was satisfied to some extent. Additional criteria such as constant volume and velocity are satisfied by the nature of the test (undrained) and strain controlled loading system.

The change in deviator stress and build up of excess pore pressure with axial strain are shown in Figure 5.18. In terms of shear stress, the dense rotund sand specimen does not reach peak shear strength. Dense sand typically reaches steady state at large strains (Lo Presti, Pallara, Maniscalco and Pedroni, 2000) and since shear behaviour was measured only up to an axial strain of 3.2%, steady state was not be reached. Dilation however, could be noted from the excess pore pressure response of the specimen. The shear behaviour of the loose rotund sand specimen was also not characteristic as it appeared to be slightly dilative. This was due to the difficulty in preparing a loose sand specimen that displays true contractive behaviour.

The addition of 5% platy fines to the rotund sand particles increased the dilative behaviour of the soil to somewhere between that of the dense and loose rotund sand specimens. As can be seen from Table 5.2, the addition of 5% platy fines resulted in an increase in bulk density. An increase in bulk density implies an increase in the number of particles per unit volume and consequently an increase in the number of interparticle contacts. The soil is in a denser state than the loose sand specimen, thus explaining the increase in dilation. As mentioned, the behaviour of the soil at this platy particle percentage is partly controlled by the fines. Some of the platy fines are located between the coarse rotund particles, forming bridges between them. During shear, the bridging is dislodged and a sudden collapse occurs producing quasi-steady state. Once this has happened, the coarse rotund particles are in clean contact and shear behaviour follows that of the rotund sand specimens. Thevanayagam (1998) noted a similar effect when investigating the behaviour of kaolin silt (10%) and host sand. Soton soil specimens containing 15% and 20% platy fines were purely compressive. The rotund particles are suspended in a platy matrix at these fine contents and hence the shear behaviour is that of the fines. An increase in platy fines content thus suppresses dilation thereby reducing the stability of the sand. All of the specimens with the exception of the dense rotund sand specimen, displayed some degree of quasi-steady state. Quasi-steady state is thus a function of the fabric and dilatancy of the

soil (Verdugo and Ishihara, 1996; Wan and Guo, 2001).

In order to asses the influence of effective consolidation pressure on the shear behaviour of the material, the results of the 100kPa and 200kPa effective consolidation pressures were investigated (Figures 5.19 and 5.20). As expected, both the deviatoric stress and excess pore pressure increased with increasing effective consolidation pressure. The shear behaviour of the dense and loose rotund sand as well as the 15% and 20% Soton Soil specimens remained unchanged. The dilative nature of the 10% Soton Soil specimen, however increased with increasing effective consolidation pressure. The reason for this is that the behaviour of the Soton Soil is partly controlled by the platy particles. As the effective consolidation pressure increases, so does the number of clean contacts between the rotund particles.

Figure 5.21 shows the stress paths (p'-q plane) of the rotund sand and Soton Soil specimens for 100kPa, 200kPa and 400kPa effective consolidation pressures. All but the dense rotund sand specimen displayed phase transfer[3]. According to Verdugo and Ishihara (1996), Yamamuro et al. (1999) and Wan and Guo (2001) the point of phase transfer coincides with quasi-steady state. Comparing Figures 5.19 to 5.18 with Figure 5.21, can be seen that this was indeed the case. Lo Presti et al. (2000) noted that these two points do not coincide at low consolidation pressures ($\approx 50kPa$) for very loose specimens. However, as effective consolidation pressures in excess of this value were adopted in this investigation, this was not noted. The degree of phase transfer appeared to increase with increasing fines content.

The effective internal friction angles (ϕ') of the rotund sand and Soton Soil specimens were based on Mohr-Coulomb failure criteria. The principal stresses required to construct the Mohr circles were that at failure state and were derived based on the following:

- the shape of the triaxial paths with regards to the deviator and mean normal effective stress as well as the excess pore pressure response with

[3]defined as a temporary state of transition from contractive to dilative behaviour of sand Ishihara, Tatsuoka and Yasuda (1975)

shear strain and

- the maximum stress ratio $\eta = q/p'$.

The effective internal friction angle of the rotund and Soton Soil specimens are shown in Figure 5.22. The influence of density can clearly be noted from the relatively large difference in effective friction angle between the loose and dense rotund sand specimens. The effective friction angle of the Soton Soil (mica content ranging between 10% and 20%) on the other hand, remained relatively constant around a value of 28.3° with a standard deviation of 0.5°. This average value was achieved regardless of the change in particle size distribution, shape and bulk density (Table 5.2). The effective friction angle of the 5% Soton Soil was not included as it was only sheared at 400kPa effective consolidation pressure. It could however be noted that the effective friction angle changed drastically by the addition of 10% mica particles. Based on the previous analysis, one might expect the effective friction angle of the 5% Soton Soil specimen to be close to that of the loose rotund sand sample. The turning point from changing to constant effective friction angle thus remain uncertain. This might be a good field for future research.

Been and Jefferies (1985) introduced a state parameter (ψ) which incorporates the influence of void ratio and stress. It is defined as the difference in void ratio between the initial sand state and steady state conditions at the same effective stress. Depending on the polarity of the state parameter, sand will dilate or contract at large strains. Been and Jefferies (1985) found that the shear behaviour of Kogyuk sand (containing various percentages of silt) and the polarity of the state parameter are related to each other in the following way:

$$\begin{aligned} \text{small positive or negative state parameter} &= \text{dilative} \\ \text{high positive state parameter} &= \text{contractive} \end{aligned}$$

The state parameter of the Soton Soil and loose rotund sand specimens was determined at the various effective consolidation pressures to establish whether they follow the suggested trend. Not all of the specimens reached steady state and hence only those that did were considered (Table 5.6). The steady state line was calculated from the steady state condition[4] of the respective specimens and their corresponding virgin compression line slope (λ). It could be seen that a good correlation exists between the predicted and observed shear behaviour of the 10% and 15% Soton Soil specimens. This however, were not the case for the 20% Soton Soil, which was surprising as the platy particles was cohesionless and would be expected to fit within the framework. It should be noted that the correlation between the observed shear behaviour and predicted employing the state parameter, was based on sand and silt particles which have low aspect ratios. The mica particles used in this study however, have a high aspect ratio and may thus not behave in a similar manner. The 10% and 15% Soton Soil specimens contained a sufficient amount of rotund particles so that their behaviour is governed by the rotund particles to some extent and thus react in the predicted way. At 20% platy fines, the rotund particles are suspended in the platy fines and shear behaviour follows that of the latter, which as mentioned might not behave as predicted.

The Nor-Sand model (Jefferies, 1993) was employed to analyse the behaviour of the rotund sand and Soton Soil as they were essentially granular. As mentioned, not all of the specimens reached steady state or critical state as referred to by Jefferies (1993) and Andrianopoulos, Bouckovalas and Papadimitriou (2001). Critical state parameters could thus only be determined for those specimens that reached critical state (Table 5.7). The slope of the critical state line (λ) and specific volume at a reference pressure of 10kPa (Γ) increased with increasing mica content. The addition of platy particles thus changed the position of the state boundary surface in the compression plane.

[4]achieved when the pore pressure become constant under continued shear at large strains (Yamamuro et al., 1999)

The slope of the critical state line (M) however, remained constant around a value of 1.19, thus verifying the nearly constant friction angles obtained for the Soton Soil specimens. Bouckovalas et al. (2002) conducted a statistical analysis on published data to assess the influence of fines on the location of the critical state line. Their results confirmed that of the author, namely that M is unaffected by fines content whilst λ and Γ increased.

Taylor (1948) suggested that the strength of dense sands consisted in part of internal rolling and sliding friction between the particles and in part of interlocking. Following on this research, Rowe (1969) proposed a dilatancy rate (D) for granular material given by:

$$D = (1 - \frac{\delta\epsilon_\nu}{\delta\epsilon_a}) \tag{5.2}$$

where

ϵ_ν = volume decrease per unit volume

ϵ_a = major principle strain in compression test

Bolton (1986) proposed the use of a dilatancy index (I_R)

$$I_R = I_D(10 - lnp) - 1 \tag{5.3}$$

where

I_D = relative density

p = mean effective stress (kPa)

The dilatancy index relates the effective critical friction angle and rate of dilatancy in the following fashion:

$$\begin{aligned} \phi' - \phi'_{cs} &= 3\mathrm{IR} \\ -(\delta\epsilon_\nu/\delta\epsilon_a)_{max} &= 0.3I_R \end{aligned}$$

Referring to Table 5.2, it was noted that the relative densities of the 10% to 20% Soton Soil specimens are extremely low with that of 15% and 20% platy fines being negative. The proposed correlation thus does not apply as very low or negative values for the dilatancy index would be obtained. The difference between the effective friction angle obtained from the Mohr-Coulomb failure criteria and that of critical state were none the less calculated (Table 5.8) as it would provide some indication of the dilative nature of the material. It could be seen that the difference between the two effective friction angles reduced with increasing platy fine content. This implied a decrease in the dilative nature of the soil with increasing fines content which confirmed previous results.

5.3 Influence of platy fines on the behaviour of mine tailings

An hypothesis is presented to explain the behaviour of mine tailings, using gold mine tailings as an example, namely that: the mechanical behaviour of mine tailings are governed by the platy fines present in the tailings. A test was designed to validate this hypothesis. An experimental program was conducted (Chapter 4) to establish whether platy fines influence the behaviour of coarse rotund particles. This was found to be the case. The observed behaviour of the Soton Soil (platy fines and coarse rotund particles) and the documented behaviour of mine tailings were compared. The hypothesis would prove to be true if a good correlation between the two was obtained.

In order to confirm that the Soton Soil was fit for comparison with the mine tailings, the particle shape and size of the two were compared.

Hamel and Gunderson (1973), Mittal and Morgenstern (1975), Colin (1980) and Vermeulen (2001) described mine tailings fines as platy or needle shaped (appearing flaky) with the coarse particles being angular (Pettibone and Kealy, 1971; Colin, 1980; Vermeulen, 2001). Photographs taken of the magnified mica and Leighton Buzzard sand particles (Figure 4.7) showed

that they fit the above description.

Considering the particle size distribution of the dispersed gold tailings (Figure 2.8), the ratio of the mean particle diameter (D_{50}) of the coarsest tailings (0.06) to the fine tailings (containing some platy particles) (0.006) is 0.10. In comparison, the diameter ratio of the rotund to platy particles is in the order of 0.09. The relative particle sizes of the Soton Soil are thus a good approximation of the tailings.

Several researchers such as Hamel and Gunderson (1973), Aubertin et al. (1996) and Vermeulen (2001) have noted the presence of muscovite or biotite particles in mine tailings. Aubertin et al. (1996) estimated the mica content in four different hard rocks as 5% to 10% while Vermeulen (2001) estimated that in gold mine tailings as 7% to 9%. The mica content of the Soton Soil varied between 5% and 20%. According to Vick (1990), the percentage fines present in tailings varies between 10% and 20%, but could be as much as 50%. The platy fines contents of the Soton Soil thus fall within the typical range found in mine tailings.

Following the above, it is concluded that based on particle shape and size, the Soton Soil is fit for comparison with mine tailings. A comparison of the behaviour of the two materials now follows.

5.3.1 *Compressibility*

In order to draw a comparison between the compressibility behaviour of mine tailings and Soton Soil, field conditions need to be identified to establish whether similar conditions prevailed during the laboratory testing of Soton Soil.

Tailings are in a normally consolidated state owing to their recent stress history (Vick, 1990). Exceptions to the rule could be found when the tailings are deposited sub-aerially. Tailings appear to be anisotropic due to depositional processes. This is especially evident from the permeability of the material as reported by Matyas et al. (1984), Robertson (1987) and Byrne and Seid-Karbasi (2003). Isotropic normally consolidation tests were conducted

on the Soton Soil and the observed behaviour would thus only be comparable to normally consolidated tailings. Soton soil was not anisotropically consolidated as it was expected that some degree of anisotropy might be brought about by the nature of the particles. Calculation of the equivalent void ratio of the soil from magnified thin sections, confirmed that some degree of anisotropy was present and that it increased with platy fines content.

The adopted effective consolidation pressures (25kPa, 50kPa, 100kPa, 150kPa, 200kPa, 250kPa, 300kPa and 400kPa) were in accordance with vertical effective pressures to which tailings are typically subjected in a tailings dam. Vermeulen (2001) employed a similar stress range (20kPa to 500kPa) during the testing of gold mine tailings.

A quantitative comparison was drawn between the coefficient of compressibility of the Soton Soil (Figure 5.7) and mine tailings as documented in the literature (Table 2.2). It could be seen that the coefficient of compressibility of the Soton Soil is lower than that of the mine tailings. This was ascribed to the coarser grading of the Soton Soil.

Several researchers such as Mittal and Morgenstern (1976) and Aubertin et al. (1996) have noted that the compressibility of mine tailings increased with distance from the discharge point i.e. with increasing fines content, despite the fact that very little colloidal clay minerals are present. The relatively high compressibility of the mine tailings should thus be ascribed to some other mechanism. The fines consist of platy or needle shaped particles. An increase in compressibility with fines content may imply an increase in compressibility with platy fines content. To establish whether this might be the case, the influence of platy fines on the compressibility of Soton Soil was considered (Figure 5.7). The coefficient of compressibility (C_c) of the loose rotund sand specimen was included for comparative purposes as tailings are considered to be in a loose state. The addition of only 5% platy particles, more than doubles the coefficient of compressibility of the sand. A platy fines content of 10% increases the coefficient of compressibility of the material by an order of magnitude, when at 20% it more than doubles again.

The addition of platy fines thus greatly influences the coefficient of compressibility of Soton Soil, and since similar particle size ratio and consolidation conditions prevail, this may also be applicable to mine tailing.

5.3.2 *Small strain stiffness*

Höeg et al. (2000) noted that the small strain shear stiffness (G_{max}) of fine tailings, collected from the Polish Zelazny tailings dam, decreased with distance from the discharge point. This implies a decrease in the G_{max} with platy fines content.

The G_{max} behaviour of the Soton Soil was investigated to establish whether similar behaviour could be noted. Small strain shear stiffness was measured using similar equipment, namely bender elements, to those employed by Höeg et al. (2000). Referring to Figure 5.13, it can be seen that the addition of 10% platy fines decreased the G_{max} of the Soton Soil drastically. The rate of decrease of G_{max}, decreases with increasing platy fines.

Considering the undrained effective secant Young's modulus (E'_{usec}) of the Soton Soil at effective consolidation pressures of 100kPa, 200kPa and 400kPa (Figures 5.14 to 5.16), it can be seen the that influence of 10% platy fines is less pronounced than that of the G_{max}. It should be noted that the strain level at which the G_{max} was measured was at least one order of magnitude less than that of E'_{usec}, which would explain this difference (Brignoli et al., 1996). Similar to the G_{max} behaviour, the rate of decrease of E'_{usec} decreases with increasing platy fines content so that it is unchanged from 15% to 20%.

It appears as though small quantities of platy fines (10%) have the greatest influence on the G_{max} and E'_{usec} of Soton Soil, a fines content typically found in mine tailings.

5.3.3 *Shear strength*

As mentioned in Chapter 2, the effective internal friction angle (ϕ') of sand is governed by density, particle size distribution and shape. Mine tailings on

the other hand, has an almost constant ϕ' that is unaffected by the above. It would thus be fair to expect the Soton Soil specimens shear strength behaviour to follow that of sand, as the addition of mica particles not only affects the particle size distribution and shape, but also its density.

Figure 5.22 shows the ϕ' of the Soton Soil as well as that of the rotund sand specimens. The ϕ' of the Soton Soil were unaffected by platy particle content and consequently density and particle size. An average value of 28.3° and standard deviation of 0.5° were obtained for the soton soil. The depositional nature, mineral composition, particle size distribution and density of the Soton Soil and mine tailings (as reported by among others, Vermeulen (2001)) differ and yet the characteristic feature of a nearly constant ϕ' was noted in both cases. The only common feature of the two materials is the platy particle shape of the fines. It is thus assumed that the nearly constant ϕ' is associated with the platy particle shape of the fines. The effective internal friction angle of the mine tailings is higher than the Soton Soil (Table 2.3). It should be noted that the particle shape of the fine tailings is not only platy which might explain this difference. Both materials have a constant critical state line slope, which confirms the nearly constant effective friction angles.

Traditional soil mechanics has and continues to develop strength models for two types of materials namely clay and sand. In terms of the undrained response of clay, shear is associated with the build-up of excess pore pressure with the available shear strength remaining constant with shear whilst that of loose sand is brittle. Man-made typical mill tailings streams however, produce a unique material that tends to be simulated by the traditional methods (Martin and Roberts, 1998). As noted by several researchers such as Vick (1990), Martin and Roberts (1998) and Vermeulen (2001), the shear response of tailings varies with fines content and is either dilative of contractive.

In order to establish whether the platy fines might be responsible for such behaviour, the shear behaviour of the Soton Soil was investigated. An effective consolidation pressure of 400kPa was adopted for illustrative purposes

(Figure 5.23). Comparing the shear behaviour of the Soton Soil specimens at 1% axial strain, it could be seen that the shear stress is high for the 5% Soton Soil specimen while the remaining specimens relatively low. This difference in behaviour is confirmed by the relatively high excess pore pressures of the 10% to 20% Soton Soil specimens. Platy particles increase the compressibility of the material (as noted before) and hence increase the build up of excess pore pressures. This implies that for a given axial strain, soil having a low platy particle content will exhibit higher mobilised shear strength than those with high platy particle content. On the other hand at 3% axial strain, the 5% Soton Soil specimen has strongly dilated, thus is increasing its mobilized strength with axial strain. Dilation of the 10% Soton Soil specimen reduced, implying a decrease in the stability of the soil with continued axial strain. The 15% and 20% Soton Soil specimens compressed, however, thereby reducing mobilised shear strength considerably.

This means that especially for the tailings slimes, the true stability conditions may drastically differ from those predicted. Hight et al. (1999) investigated the stress anisotropy of micaceous material by conducting undrained triaxial compression and extension tests on model and natural sand. The platy mica particles increased the stability of the sand in compression, but reduced its strength considerably in extension. It was thought that flow slides occurring in such material could be attributed to this phenomenon. As mentioned in Chapter 2, friction angles following failure for this material were much lower than mobilised friction angles at failure, on which stability analysis was based. Although this aspect of the fabric has not been investigated in this research, the effect of platy mica particles has been illustrated in compression and the results are in accordance with those obtained by Hight et al. (1999). It is assumed that a similar mechanism prevails in mine tailings as it has been proved that the behaviour of mine tailings is governed by the particle shape of the fines.

The stability of tailings impoundments is generally assessed by means of effective or undrained limit state equilibrium analysis where some failure

surface is assumed to slide as a rigid body. The effect of internal deformation within this sliding mass is thus ignored. Tailings failure however, often occurs as flow slides which contradicts the assumption of a rigid body (Vick, 1990). Effective stability analysis assumes that the effective stresses during shear remain unchanged from that at the onset of shear (Ladd, 1991; Carrier, 1991). This implies that shear occurs gradually enough and/or that the material is sufficiently free-draining so that no excess pore pressures are induced and are usually applied to frictional material. Undrained stability analysis on the other hand, is employed to cohesive material where it is assumed that undrained conditions prevail during shear (Martin and Roberts, 1998). It is commonly found in South Africa that the stability of upstream tailings dams is normally assessed by means of effective stability analysis since the rock flour is non-plastic and hence frictional. Undrained stability analysis is often ignored irrespective of whether shear response is dilative or contractive.

Ladd (1991) found that the shear stress at failure for effective stability analysis was twice that of undrained stability analysis. This discrepancy in mobilised shear strength at failure was confirmed by Vermeulen (2001) who found the undrained shear strength of the coarse tailings was almost three times that of the drained shear strength of the fine tailings. The use of effective stability analysis for upstream tailings dams does not take into account the true physical behaviour of tailings under shear. This type of analysis is usually applied to compacted embankments that exhibit a different behaviour to that of uncompacted loose tailings slopes. Undrained stability analysis carried out in isolation however, ignores the need for some disturbance to trigger the undrained behaviour. It is thus concluded that both effective and undrained stability analysis should be conducted on tailings slopes.

Table 5.1: Classification of sands according to their relative density (after Terzaghi and Peck (1948))

Classification	Relative density(%)
Very loose	0-15
Loose	15-35
Medium dense	35-65
Dense	65-85
Very dense	85-100

Table 5.2: Initial bulk and relative densities of Soton Soil and rotund sand specimens

Specimen description	Bulk density	Relative density of sand in specimen, without the mica content
	kgm^{-3}	%
Dense rotund sand	2036	75
Loose rotund sand	1904	14
Soton Soil containing 5% mica	2017	36
Soton Soil containing 10% mica	2010	9
Soton Soil containing 15% mica	1989	-3
Soton Soil containing 20% mica	1843	-114

Table 5.3: Calculated and measured equivalent void ratios

	5% mica		10% mica		15% mica		20% mica	
	Horizontal	Vertical	Horizontal	Vertical	Horizontal	Vertical	Horizontal	Vertical
Measured equivalent void ratio	0.52	0.53	0.53	0.55	0.68	0.74	0.77	0.90
Average "two-dimensional" equivalent void ratio	0.52		0.54		0.71		0.84	
"Three-dimensional" equivalent void ratio	0.53		0.57		0.72		0.81	

Table 5.4: Measured radial and average axial strain for an effective consolidation pressure of 400kPa

	5% mica	10% mica	15% mica	20% mica
Radial strain (%)	0.08	0.90	1.25	2.28
Average axial strain (%)	0.18	1.65	2.08	4.56

Table 5.5: Travel time obtained from cross correlation and characteristic peak

Effective consolidation pressure	Input frequency	Travel time obtained from max cross correlation	Travel time obtained from 2^{nd} prominent cross correlation peak	Normalised cross correlation value of 2^{nd} peaks	Travel time obtained from characteristic peak
kPa	kHz	s	s		s
25	15	0.00012			0.00274
	20	0.00012			0.00031
	30	0.00012			0.00007
50	15	0.00037			0.00038
	20	0.00037			0.00038
	30	0.00016			0.00032
100	15	0.00015	0.00028	0.63	0.00028
	20	0.00015	0.00027	0.69	0.00027
	30	0.00016	0.00027	0.70	0.00027
150	15	0.00011	0.00023	0.49	0.00023
	20	0.00011	0.00023	0.50	0.00024
	30	0.00011	0.00023	0.43	0.00022
200	15	0.00010	0.00021	0.63	0.00021
	20	0.00010	0.00021	0.69	0.00021
	30	0.00011	0.00021	0.80	0.00022
250	15	0.00019			0.00018
	20	0.00019			0.00020
	30	0.00019			0.00018
300	15	0.00018			0.00017
	20	0.00018			0.00018
	30	0.00018			0.00018
400	15	0.00017			0.00016
	20	0.00017			0.00017
	30	0.00017			0.00017

Table 5.6: Comparison between predicted and observed shear behaviour at large strains

Mica content	Effective consolidation pressure	Steady state	State parameter	Predicted shear behaviour	Observed shear behaviour
%	kPa				
0% mica	100				
	200				
	400				
10% mica	100	x	-0.011	dilative	dilative
	200				
	400				
15% mica	100	x	-0.012	dilative	contractive
	200	x	0.008	dilative or contractive	contractive
	400	x	0.000	dilative or contractive	contractive
20% mica	100	x	0.024	dilative or contractive	contractive
	200	x	-0.001	dilative	contractive
	400	x	-0.023	dilative	contractive

Table 5.7: Summary of critical state parameters of Soton Soil

Sample description	λ	Γ	M
10% mica	0.0217	1.650	1.19
15% mica	0.0256	1.677	1.19
20% mica	0.0657	1.979	1.15

Table 5.8: Estimate of dilatancy obtained from effective friction angles of Soton Soil

Mica content	ϕ	ϕ_{cs}	$\phi - \phi_{cs}$
%	degrees	degrees	degrees
10% mica	32.1	24.9	7.2
15% mica	29.1	25.1	4.0
20% mica	25.9	25.8	0.1

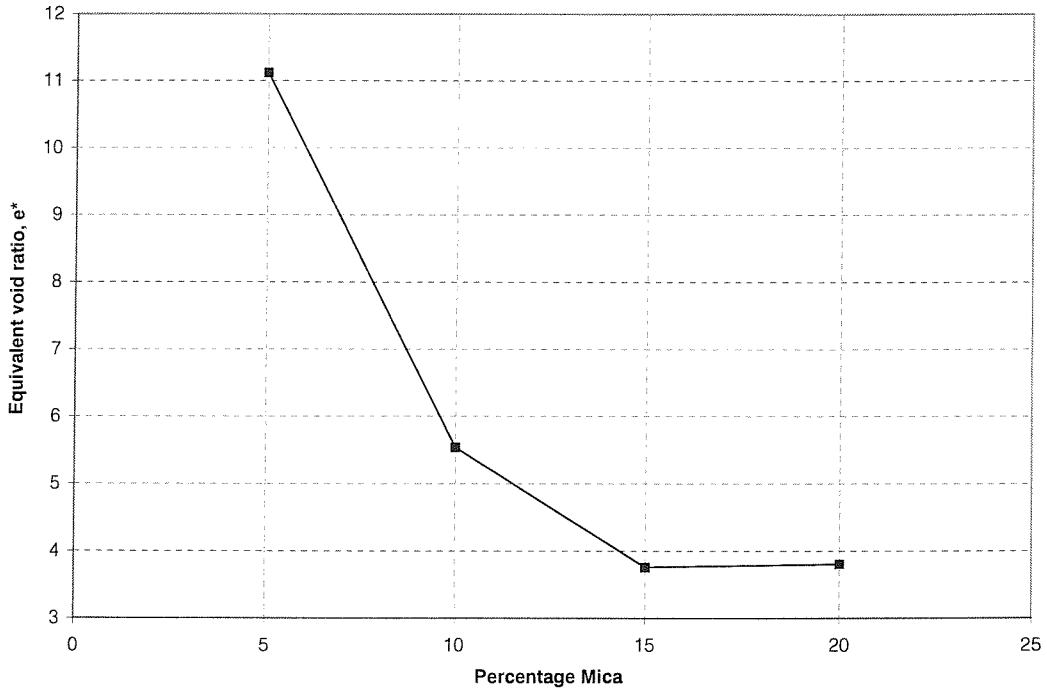

Figure 5.1: Influence of mica content on the equivalent void ratio of Soton Soil

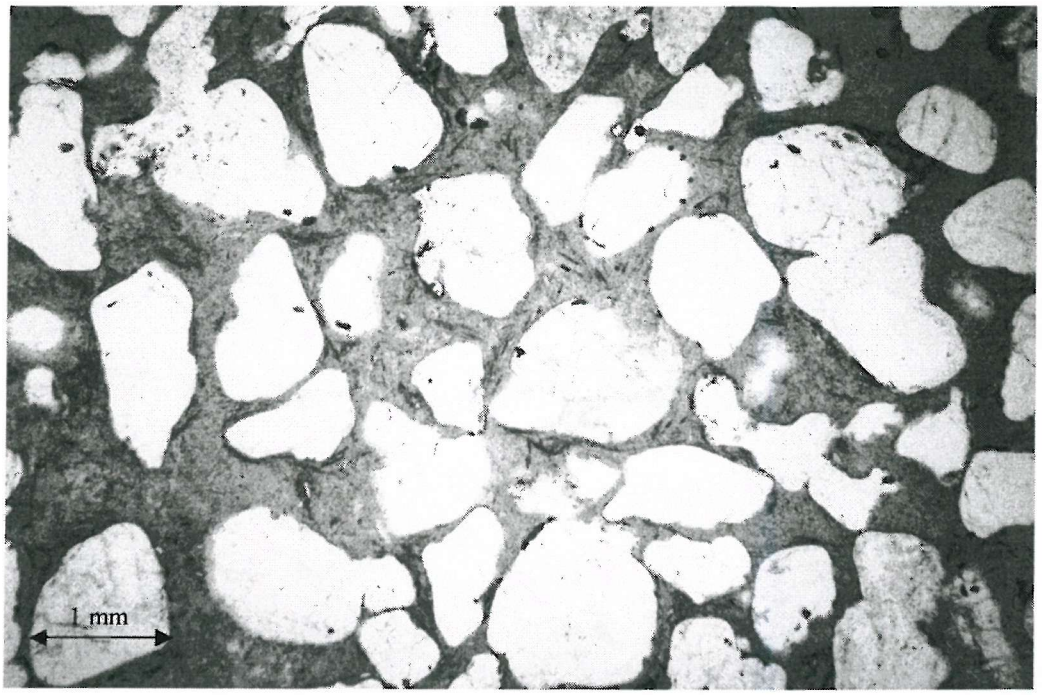

(a)

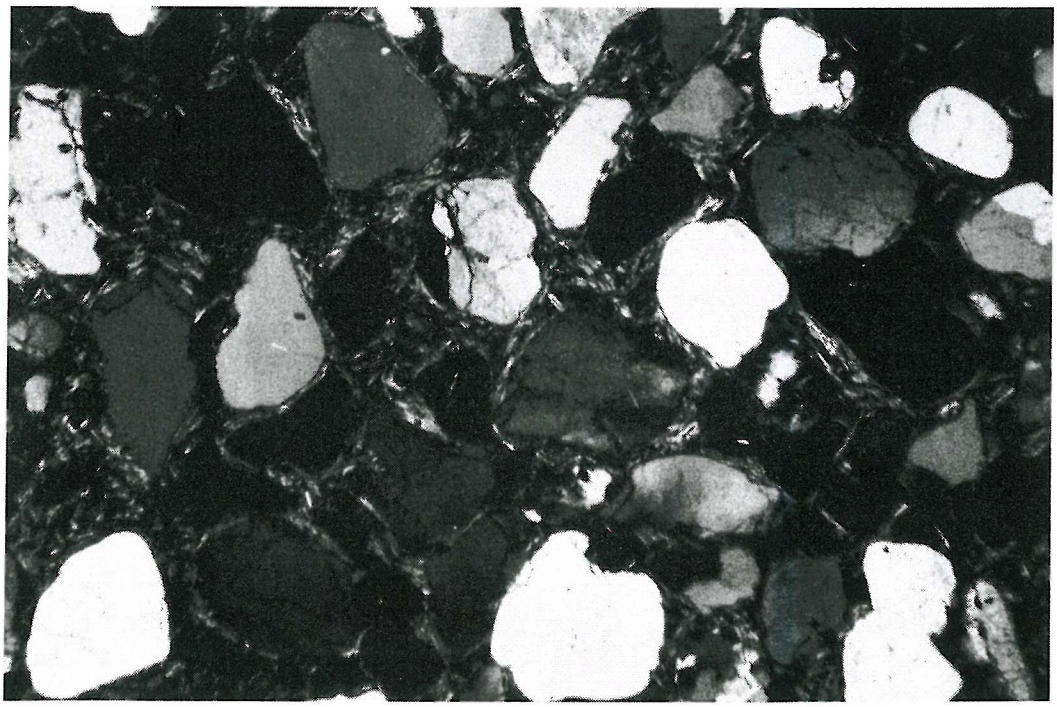

(b)

Figure 5.2: Horizontal section of Soton Soil containing 5% mica at a magnification of 22.5 for (a) polarization and (b) cross polarization

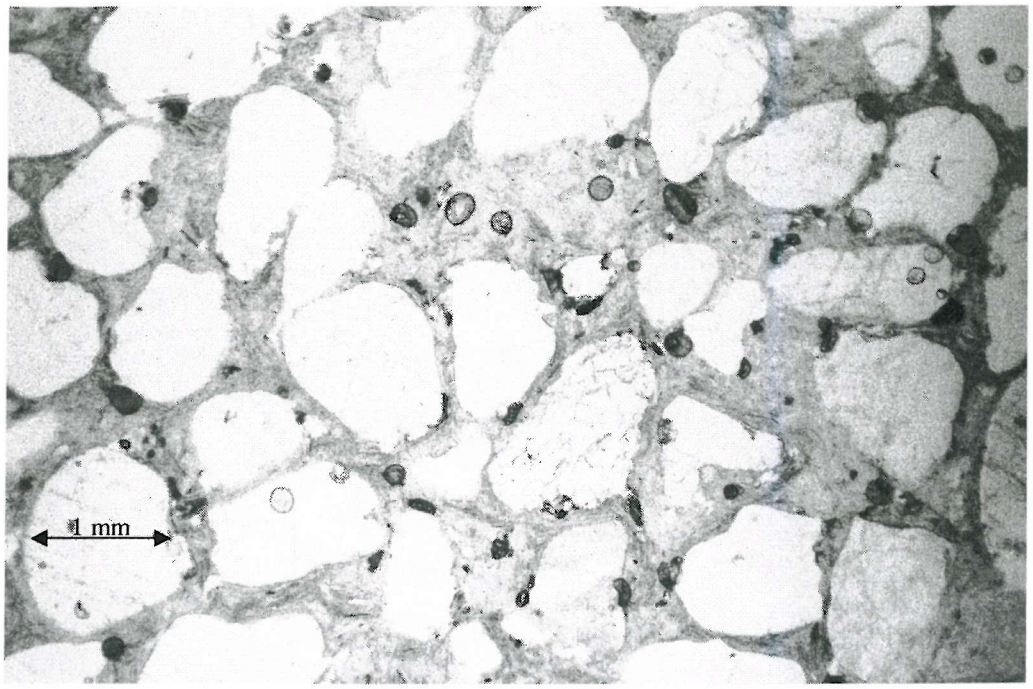

(a)

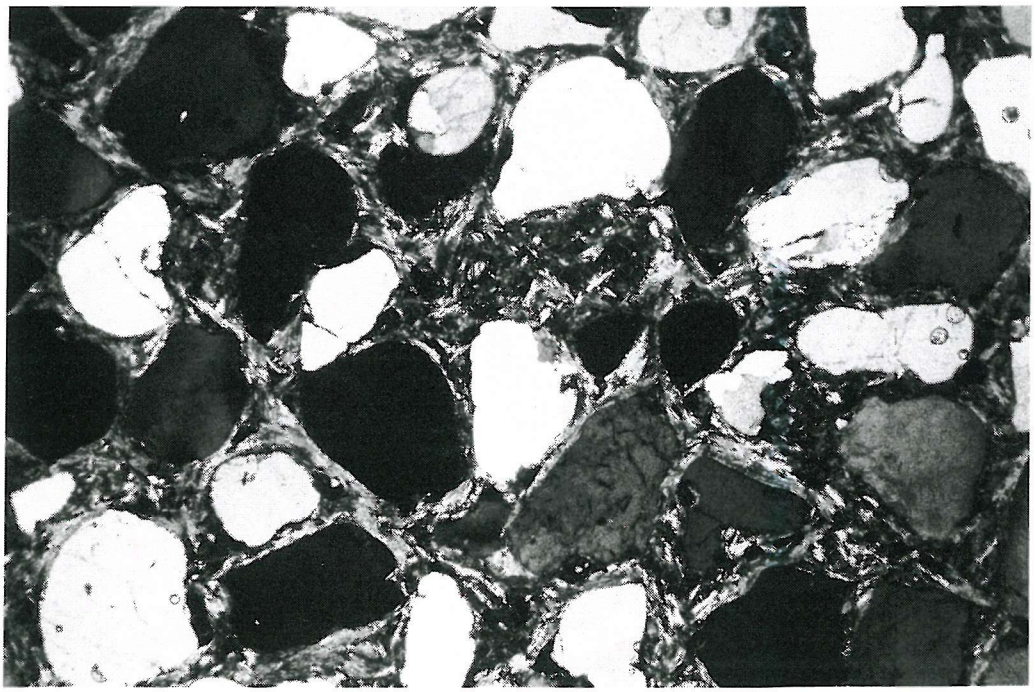

(b)

Figure 5.3: Horizontal section of Soton Soil containing 10% mica at a magnification of 22.5 for (a) polarization and (b) cross polarization

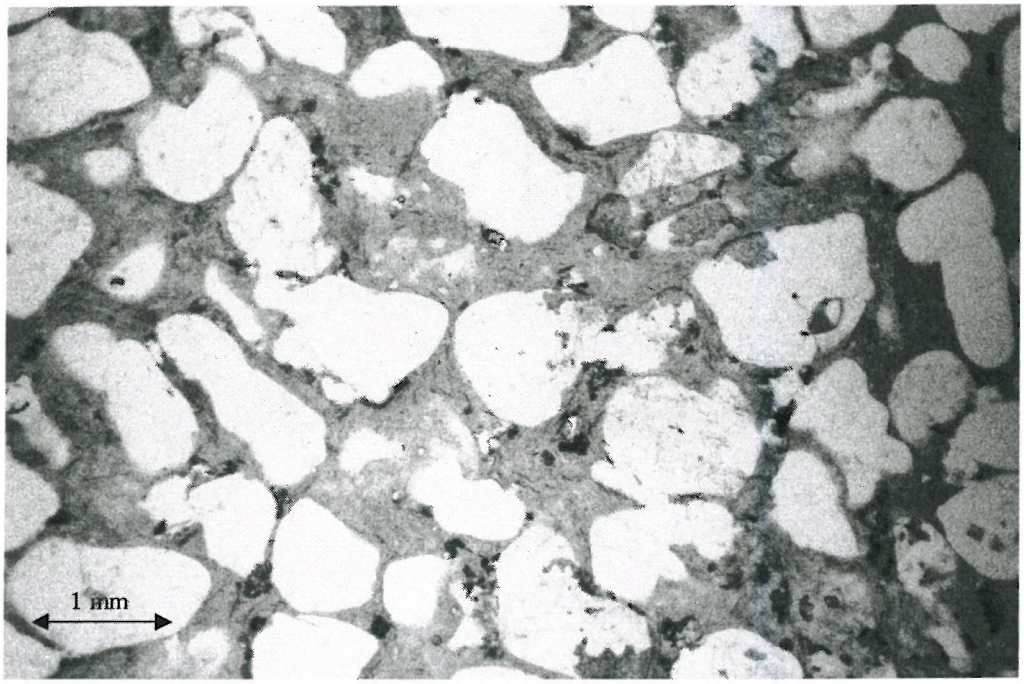

(a)

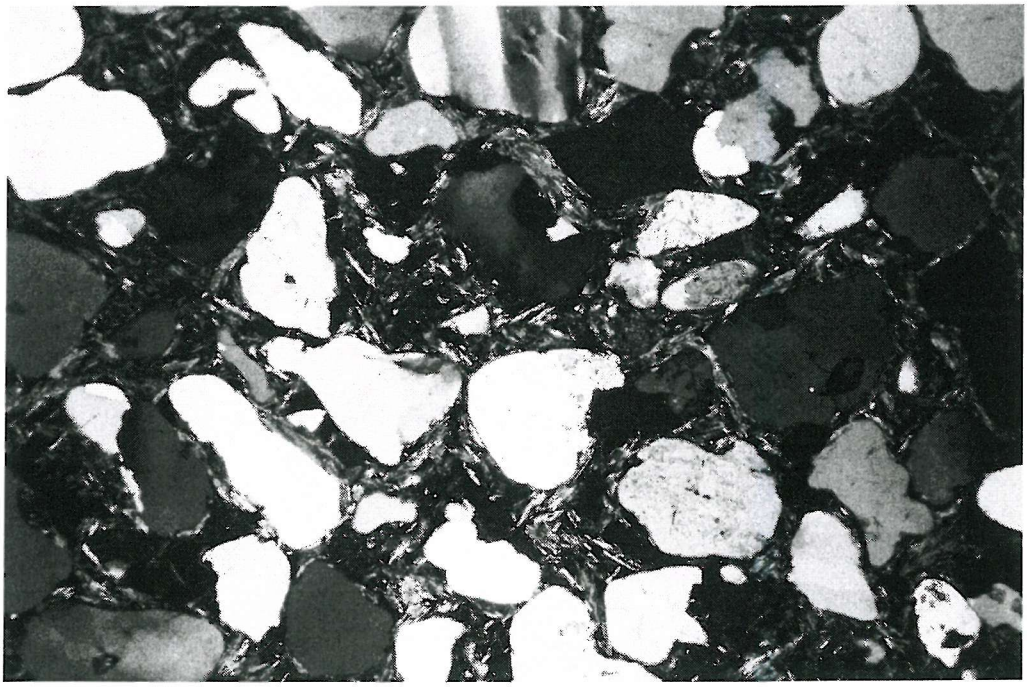

(b)

Figure 5.4: Horizontal section of Soton Soil containing 15% mica at a magnification of 22.5 for (a) polarization and (b) cross polarization

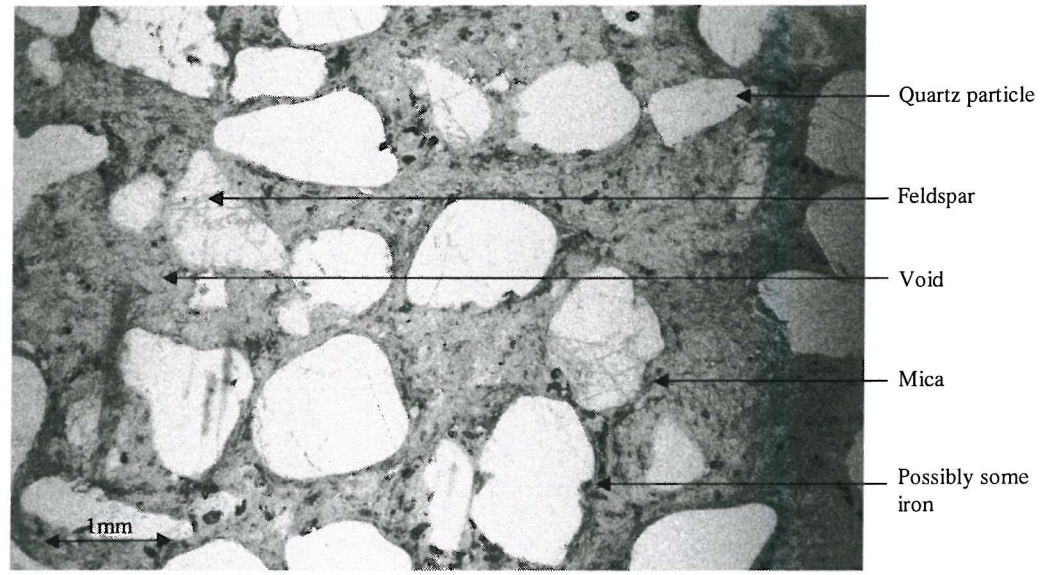

(a)

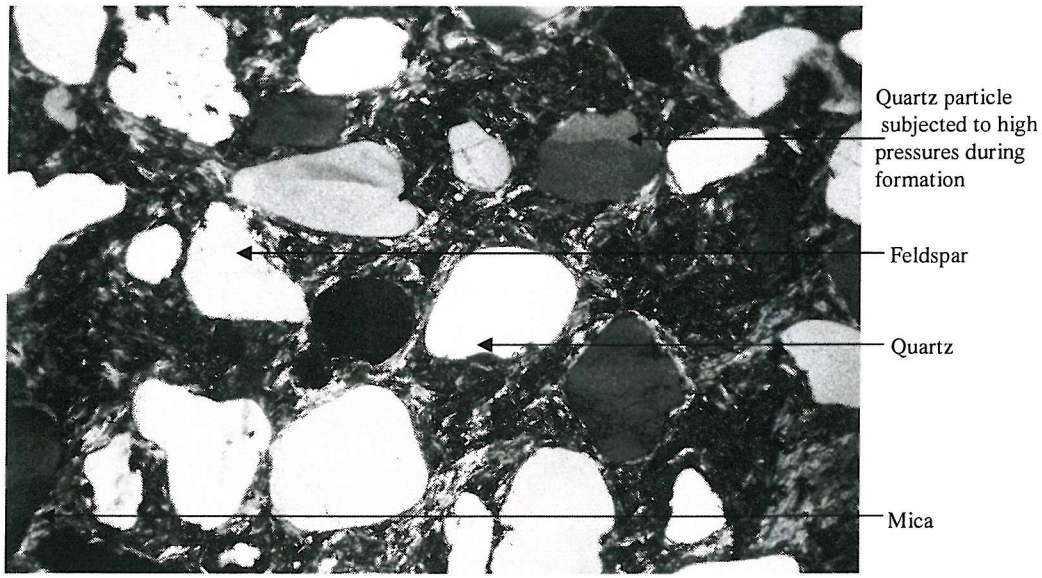

(b)

Figure 5.5: Horizontal section of Soton Soil containing 20% mica at a magnification of 22.5 for (a) polarization and (b) cross polarization

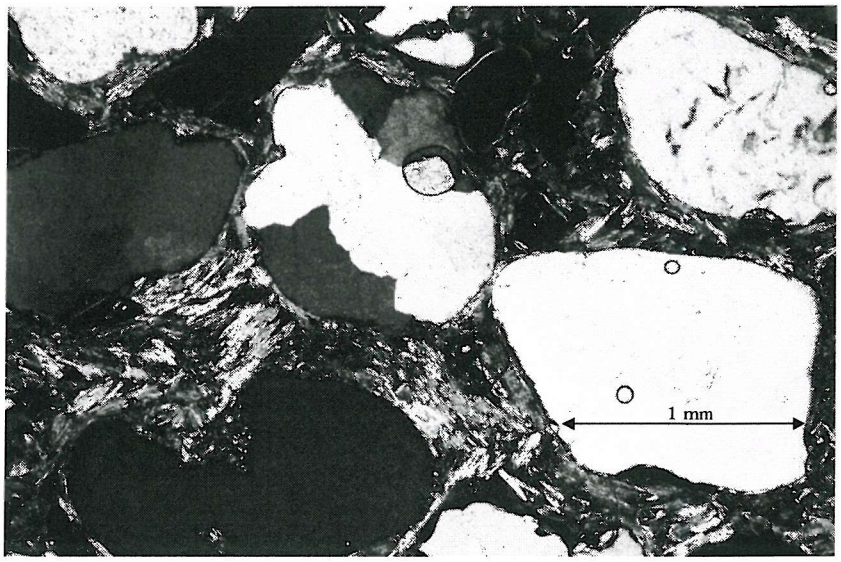

Figure 5.6: Horizontal section cross polarized photograph of Soton Soil containing 10% mica at 47.5 magnification, highlighting location and orientation of mica particles

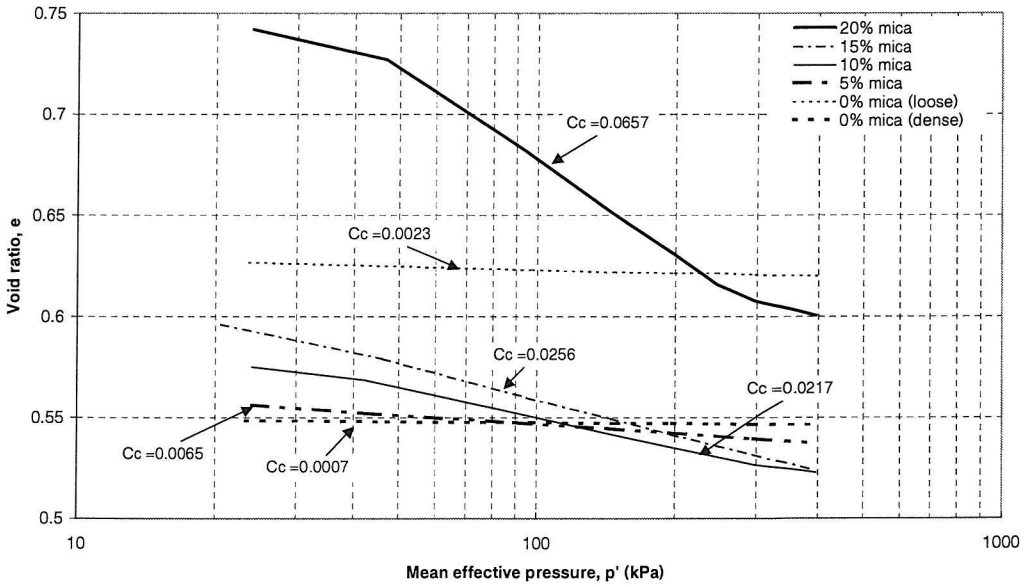

Figure 5.7: Void ratio vs. mean effective stress for isotropically consolidated rotund sand and Soton Soil specimens containing various percentages of mica

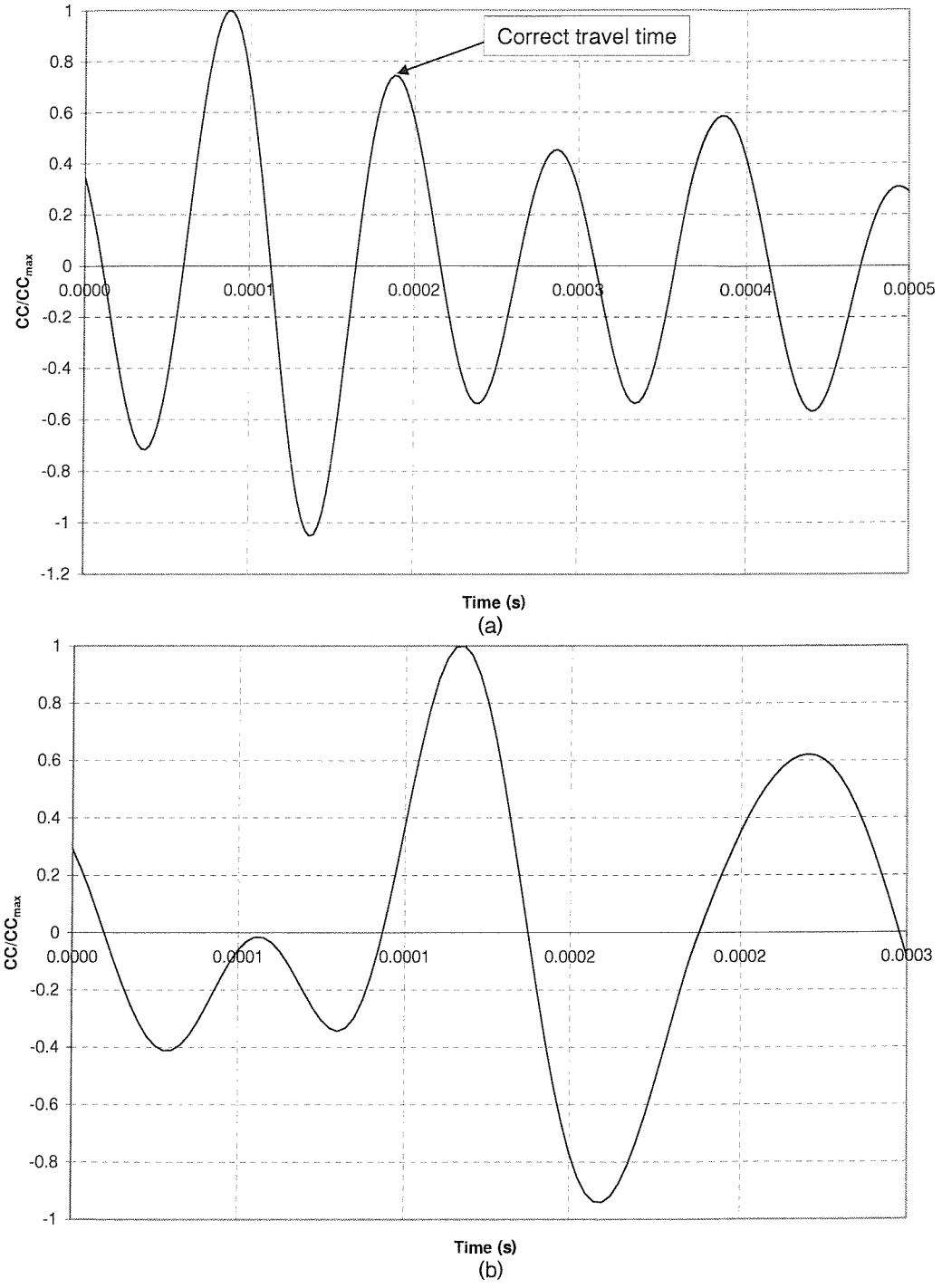

Figure 5.8: Cross correlation of (a) 20% Soton Soil and (b) dense rotund sand specimen at an effective consolidation pressure of 250kPa

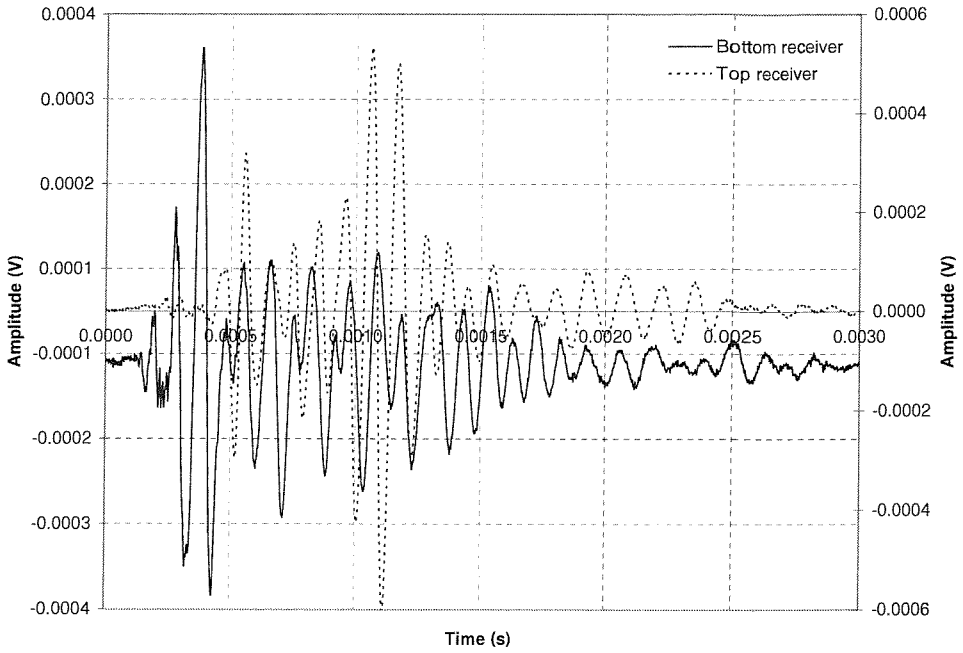

Figure 5.9: Recorded traces of 20% Soton Soil specimen at 250kPa effective consolidation pressure

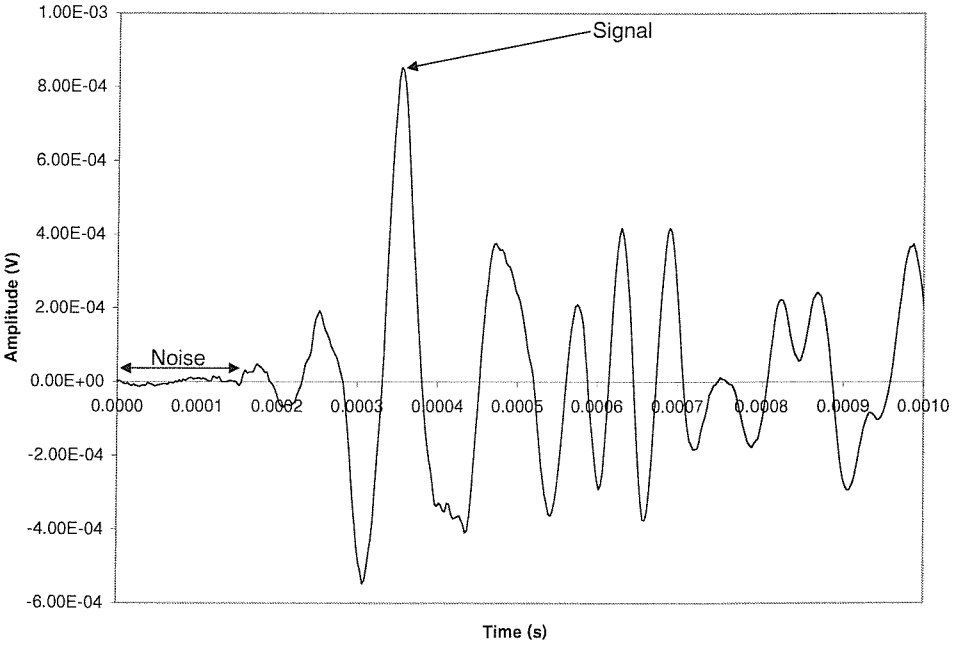

Figure 5.10: Recorded bottom receiver signal and noise amplitudes employed for calculating the signal-to-noise ratio

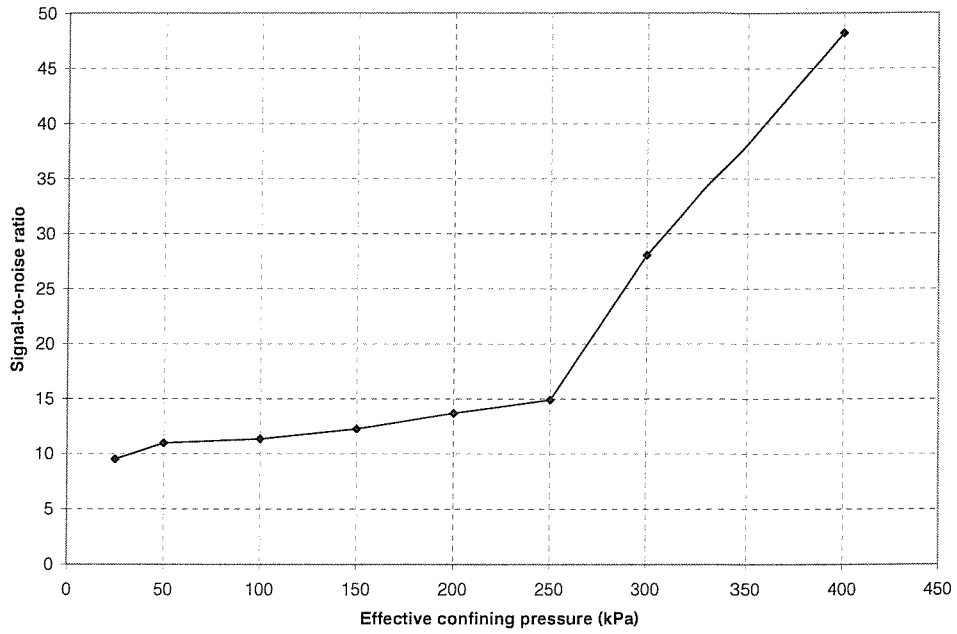

Figure 5.11: Influence of effective consolidation pressure on the signal-to-noise ratio of the recorded bottom receiver for input frequency of 15kHz and 20% mica content

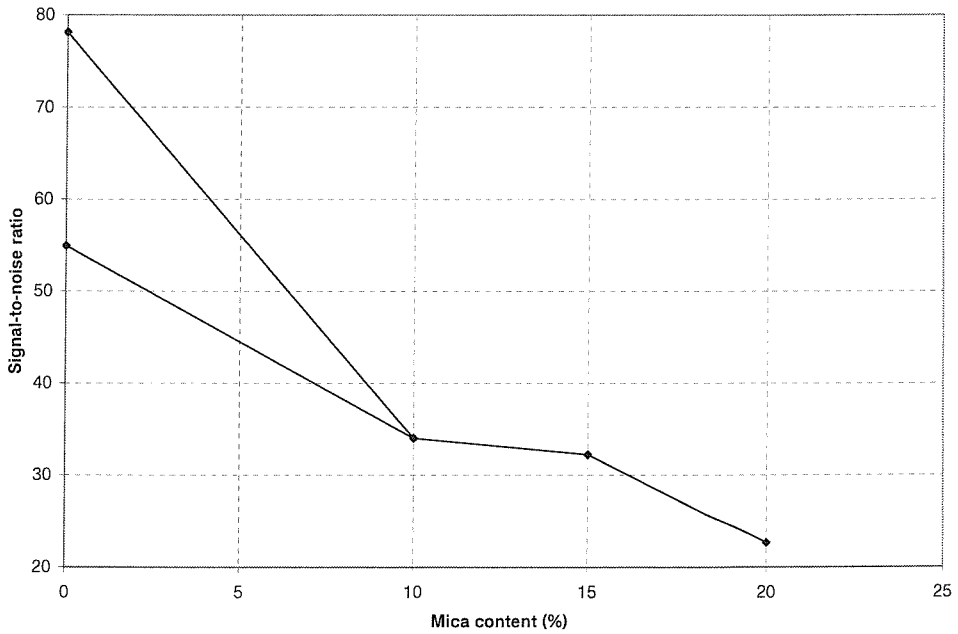

Figure 5.12: Signal-to-noise ratio degradation with mica content of recorded bottom receiver for an effective consolidation pressure of 250kPa and input frequency of 15kHz

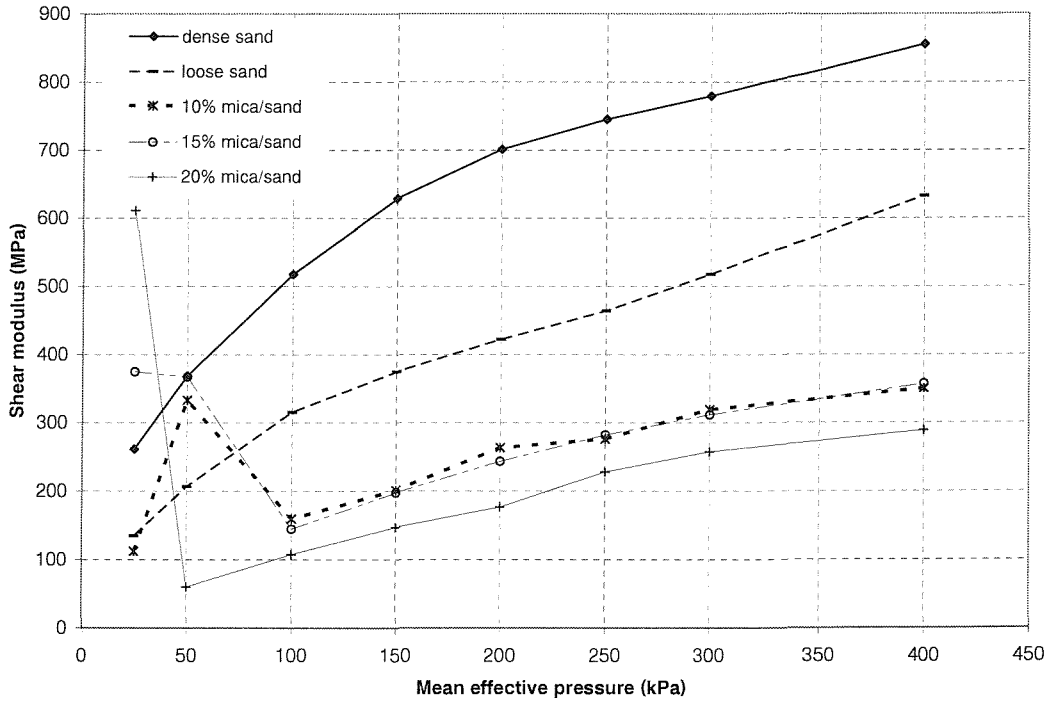

Figure 5.13: Small strain shear stiffness derived from bender element results for Soton Soil and rotund sand specimens

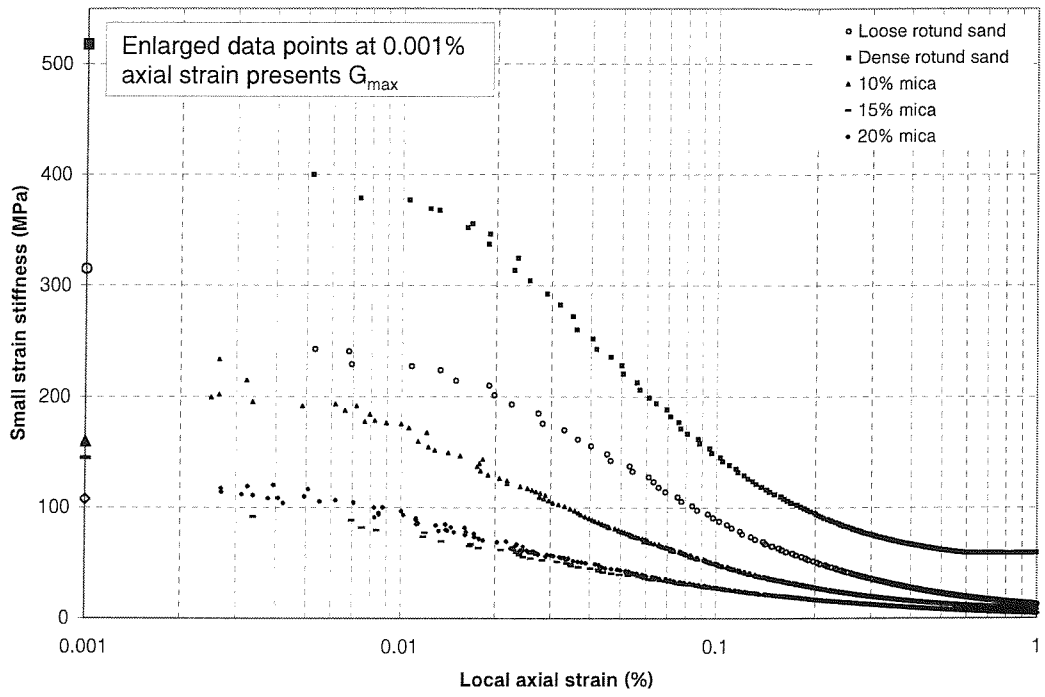

Figure 5.14: Comparison of bender element and local axial strain results for an effective consolidation pressure of 100kPa

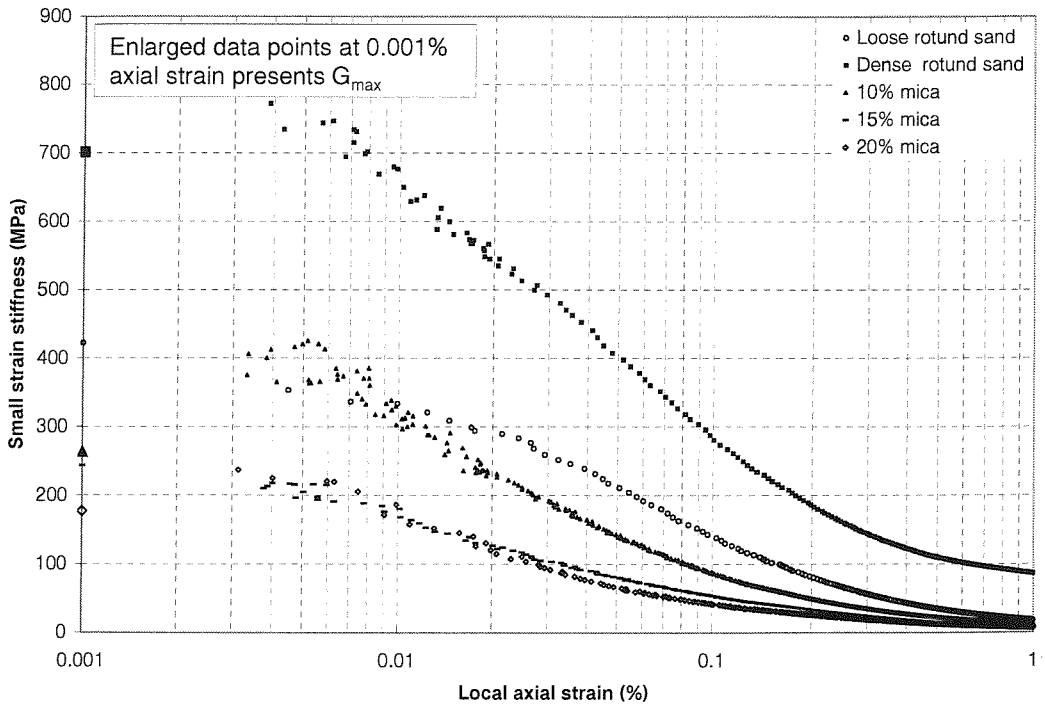

Figure 5.15: Comparison of bender element and local axial strain results for an effective consolidation pressure of 200kPa

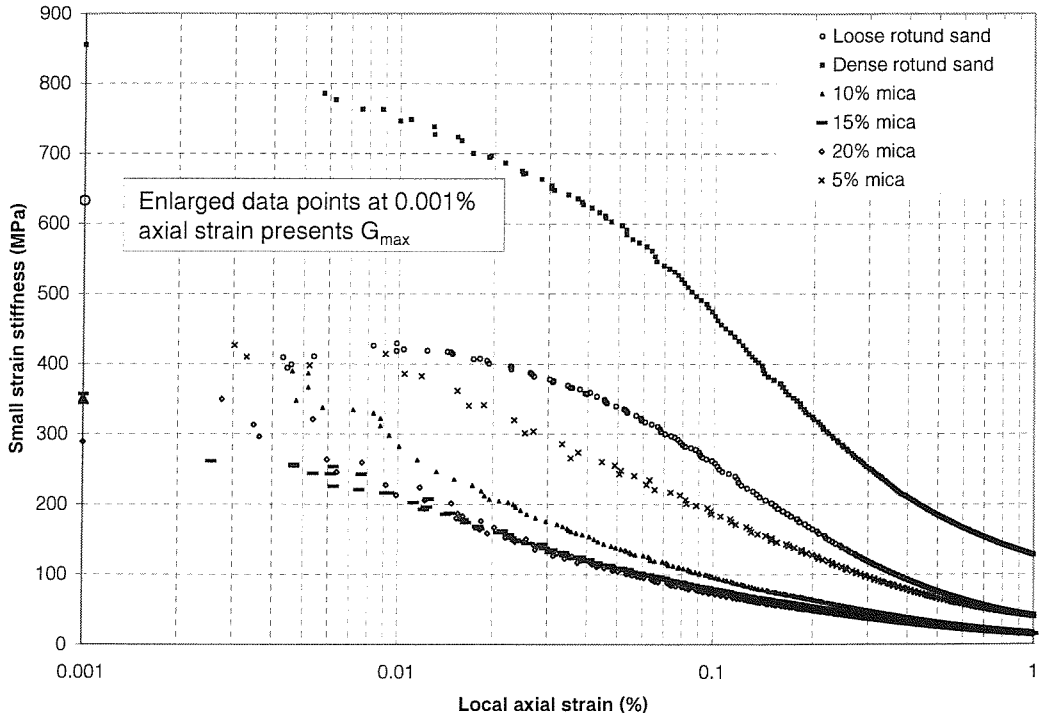

Figure 5.16: Comparison of bender element and local axial strain results for an effective consolidation pressure of 400kPa

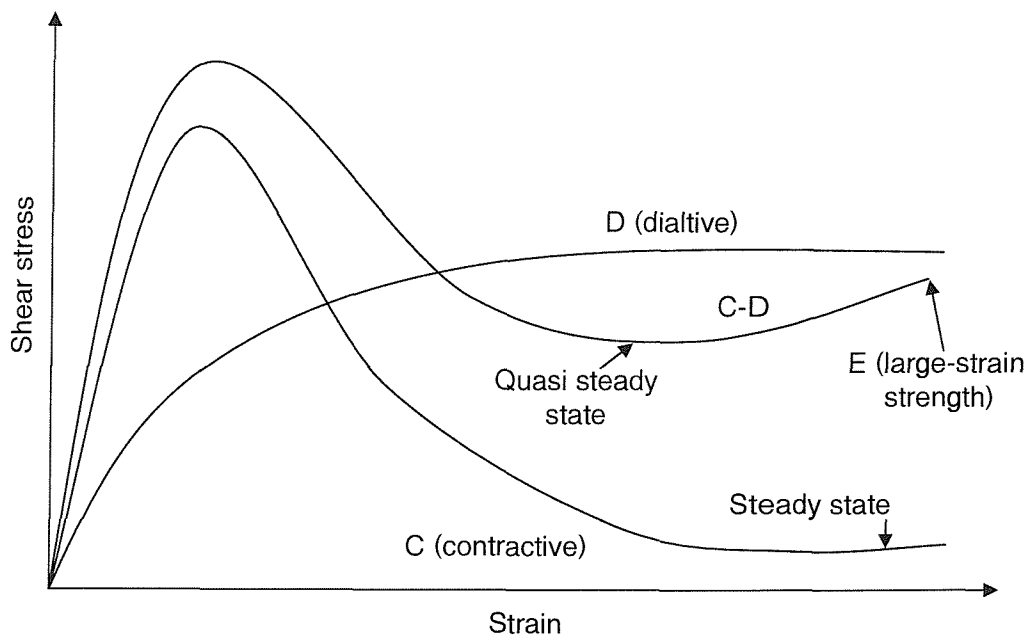

Figure 5.17: Undrained stress-strain behaviour (after Poulos (1981))

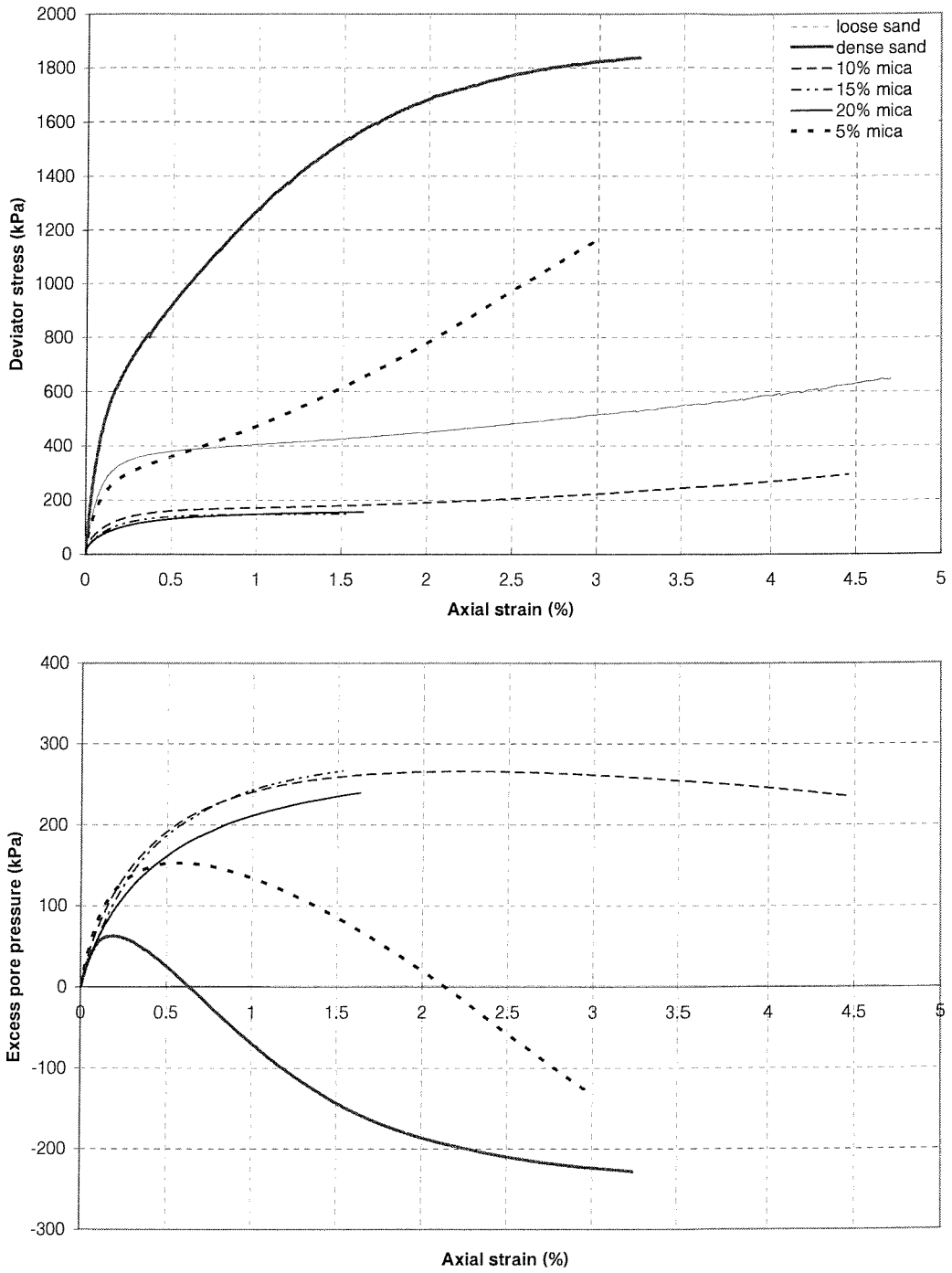

Figure 5.18: Stress-strain and pore water vs strain curve for rotund sand and Soton Soil at 400kPa effective consolidation pressure

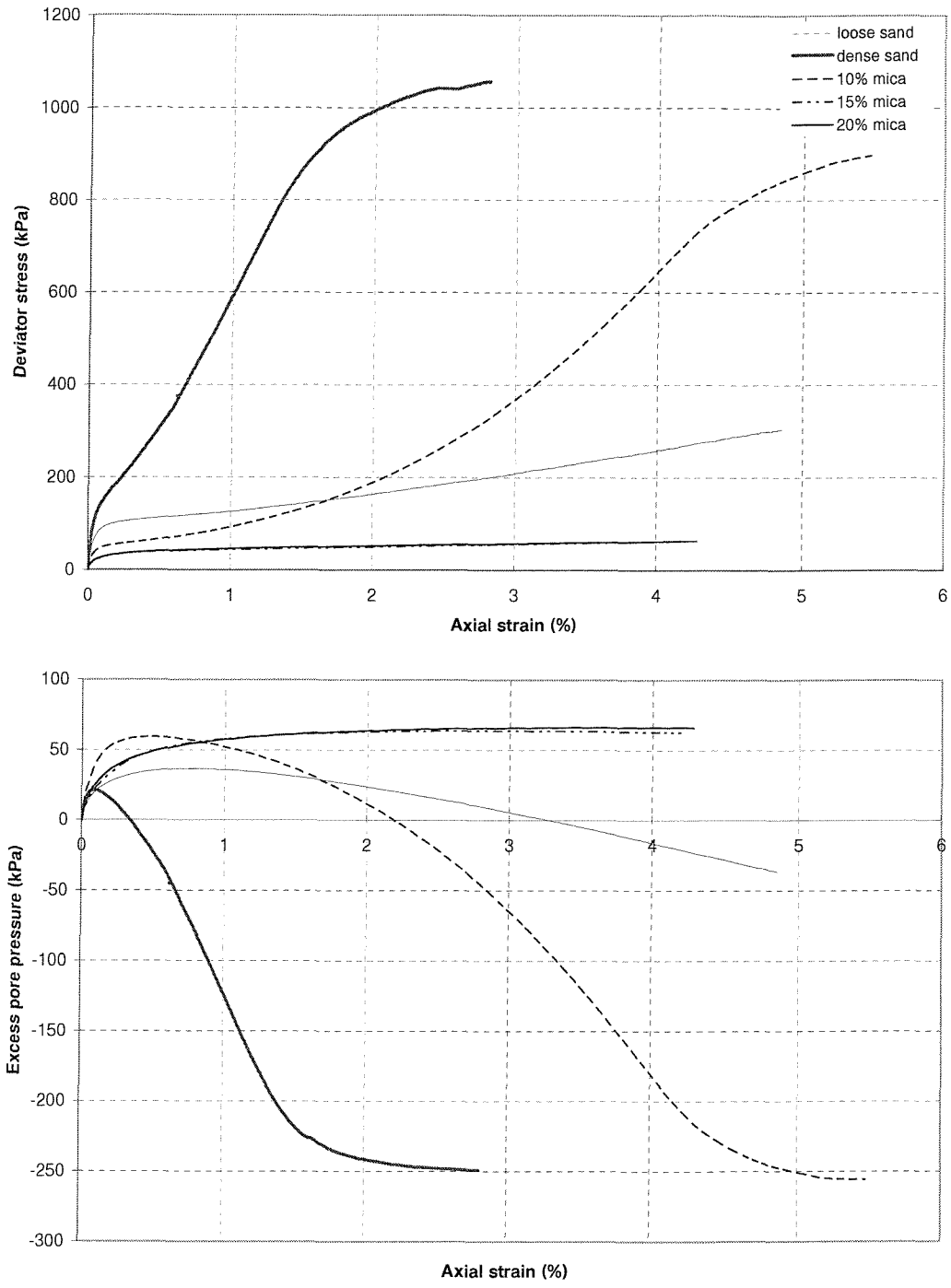

Figure 5.19: Stress-strain and pore water vs strain curve for rotund sand and Soton Soil at 100kPa effective consolidation pressure

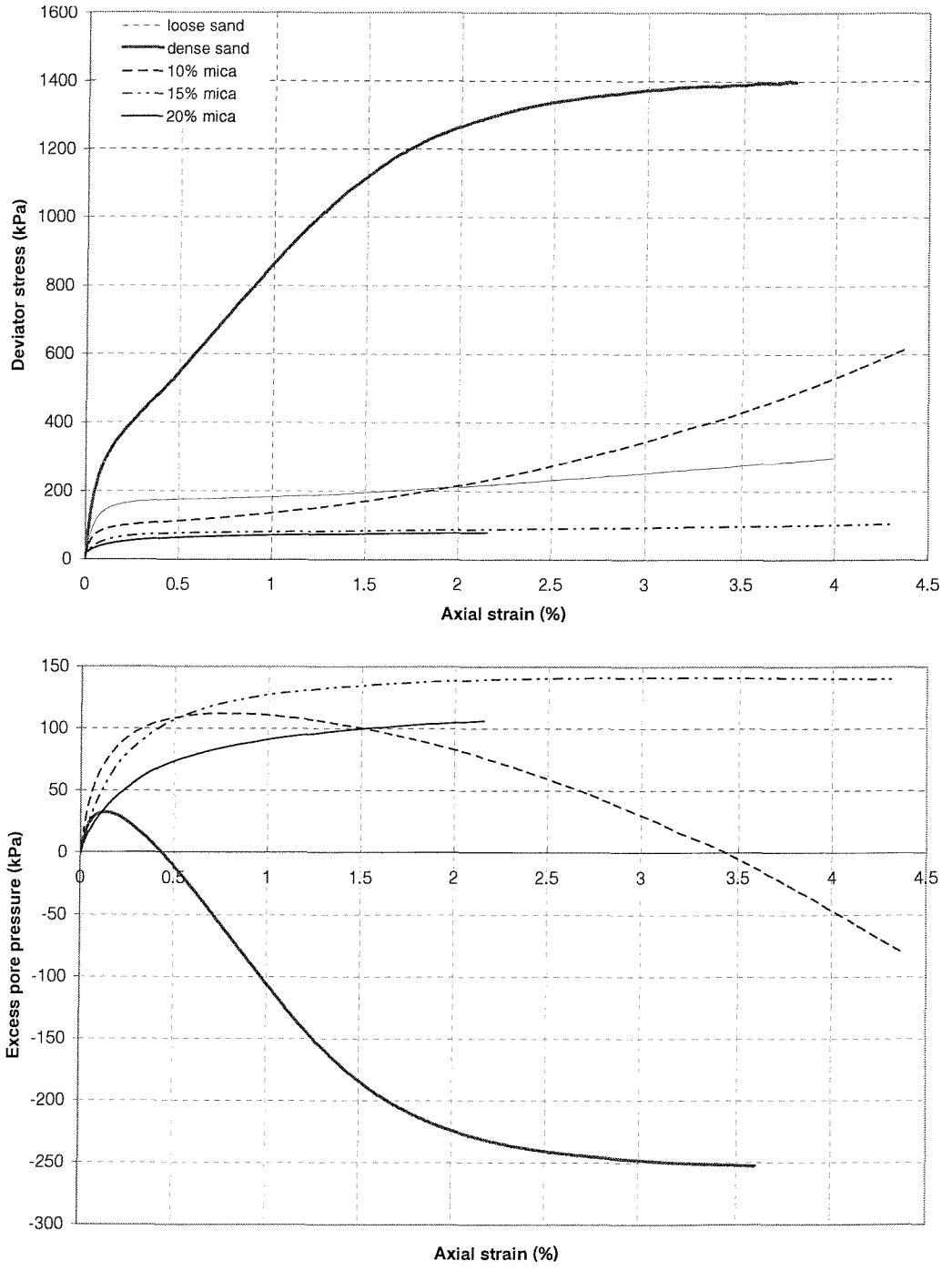

Figure 5.20: Stress-strain and pore water vs strain curve for rotund sand and Soton Soil at 200kPa effective consolidation pressure

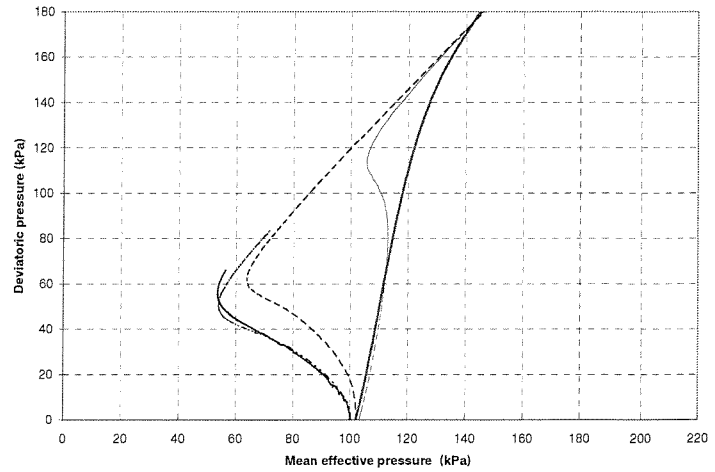

(a)

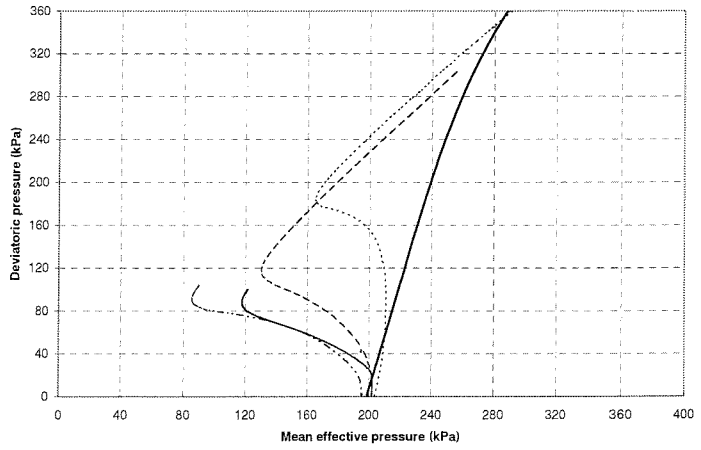

(b)

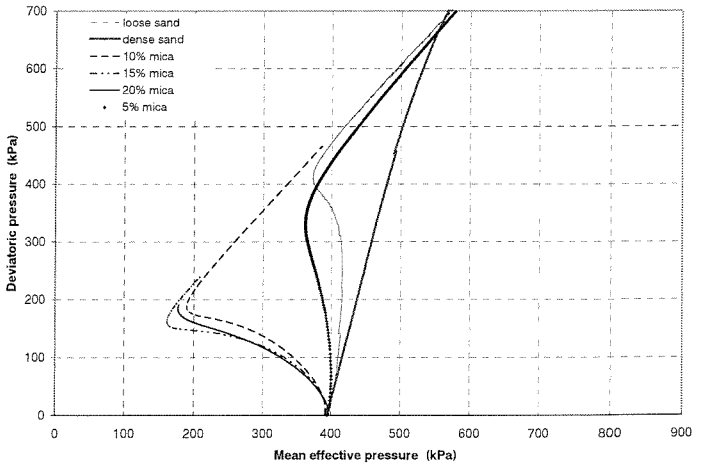

(c)

Figure 5.21: Effect of mica content on stress paths of rotund sand and Soton Soil specimens isotropically consolidated to (a) 100kPa, (b) 200kPa and (c) 400kPa effective consolidation pressure

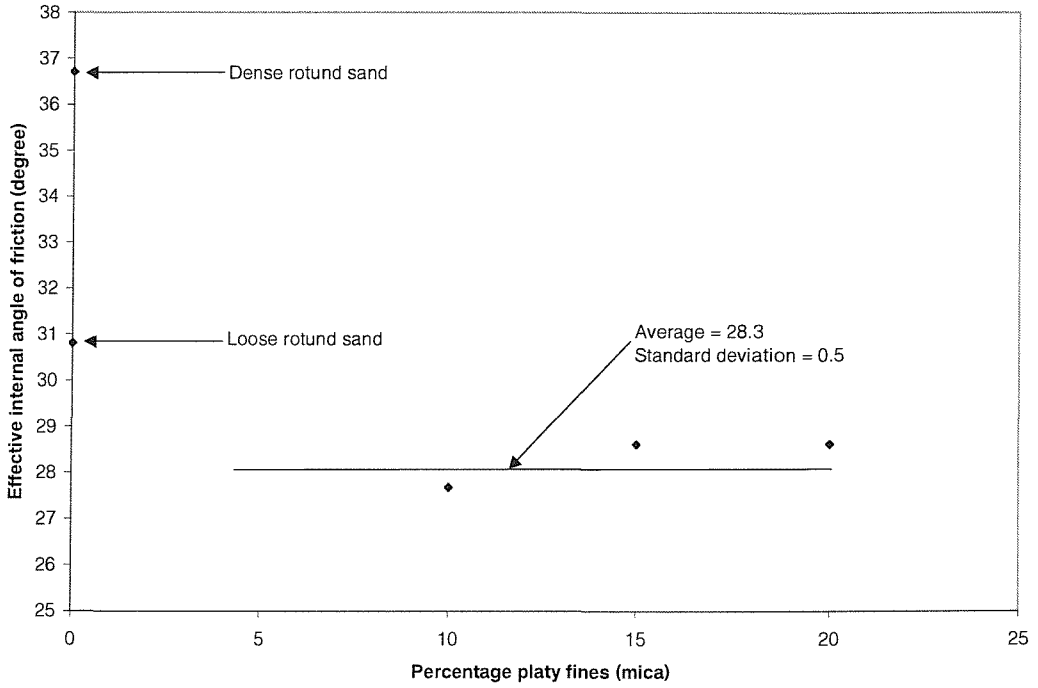

Figure 5.22: Effective internal friction angle of Soton Soil and rotund sand specimens

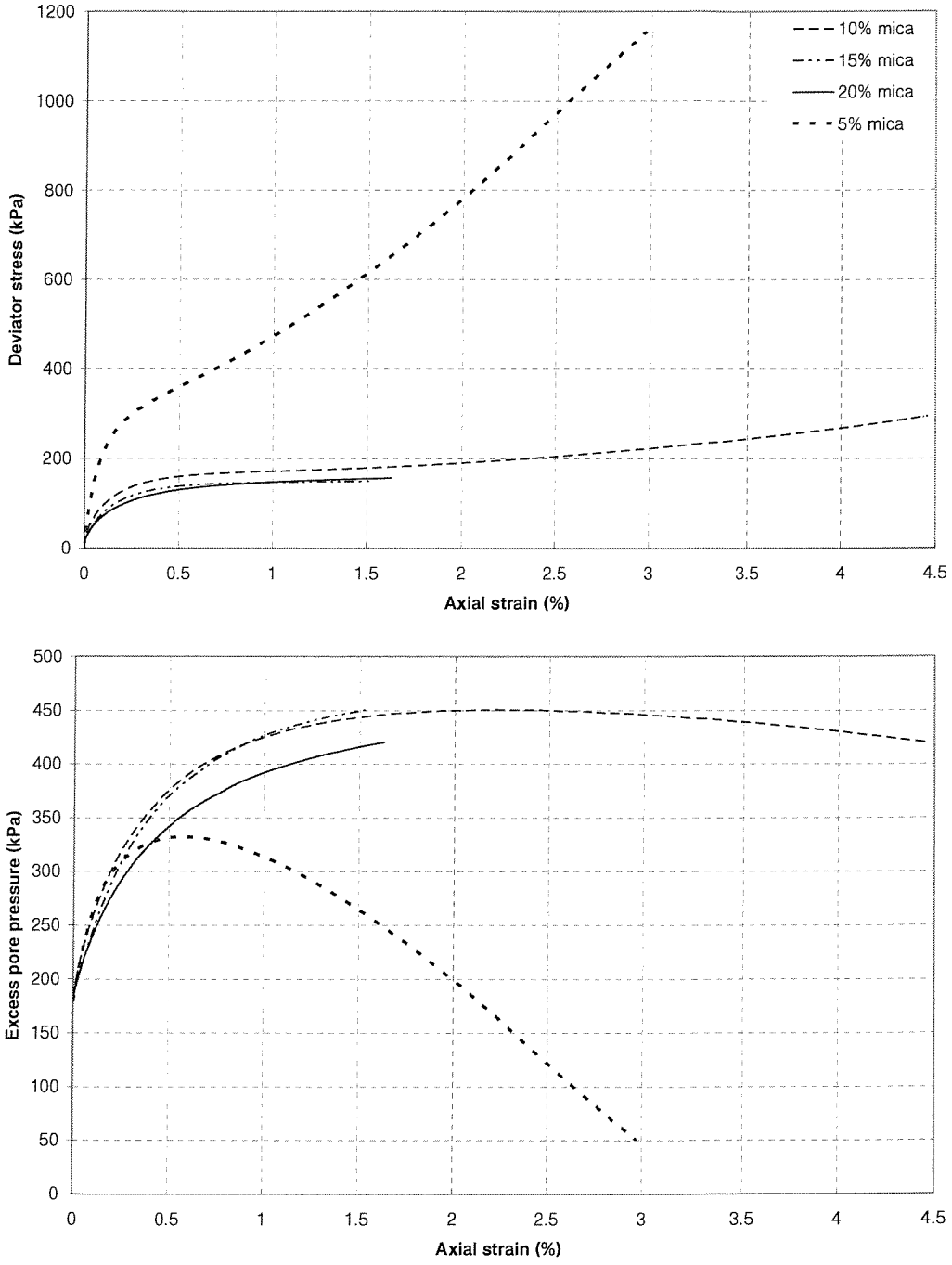

Figure 5.23: Influence of mica content and internal deformation on the shear behaviour of Soton Soil at an effective consolidation pressure of 400kPa

Chapter 6

CONCLUSIONS AND RECOMMENDATIONS

It has been widely recognised that the behaviour of mine tailings are governed by its fines content. Although very few colloidal clay minerals are present, tailings appear to be more compressible than other natural soils of similar type. Vermeulen (2001) noted that the particle shape of gold tailing slimes is predominantly flat and platy. The author postulated that the behaviour of tailings could be attributed to the particle shape of the fines. Similar compressibility and shear behaviour was noted for other geomaterials containing platy particles such as mica, which strengthened this belief. This chapter summarizes the conclusions drawn from the research in terms of the influence of particle shape on the behaviour of a rotund sand as well gold mine tailings.

6.1 Bender elements

6.1.1 *Interpretation of bender element results*

Interpretation of bender element results are complicated by several uncertainties (Chapter 2). As a result of this, several bender element interpretation techniques were developed in an attempt to reduce these uncertainties.

Time-of-flight and phase sensitive techniques were investigated to establish which yield the most reliable results. Results obtained from the phase sensitive technique proved to be frequency-dependent. This was considered to be the result of complex interference patterns being set up within the specimen by the reflected waves.

6.1.2 *Development of a new bender element configuration and novel interpretation technique*

The bender element configuration was altered to measure the shear wave velocity between two side bender receivers, inserted along the side of a triaxial specimen. The two receivers were subjected to similar dispersion and coupling effects and consequently, the recorded traces contained more similarities than those recorded from conventional sender-receiver bender element configuration. The group velocity measured using this configuration proved to be repeatable. It also allowed for the use of cross correlation within the time domain, improving the repeatability of the results.

The use of a side bender transmitter and two receivers allowed for the measurement of the small strain shear modulus of a specimen within a simple triaxial configuration. Results compared well with those obtained from an embedded transmitter and two side mounted bender receivers.

6.2 Influence of platy particles on the behaviour of rotund sand

6.2.1 *Fabric*

Platy fines occupy the voids between coarse rotund particles. Depending on the percentage of platy fines present, the coarse rotund particles are in clean contact with each other and the behaviour of the soil is controlled by the rotund particles. As the clean contacts between the rotund particles

reduce, the behaviour becomes progressively more like that of the fines. A critical mica content of 10% by weight was identified as the transition point where after behaviour was governed by the fines (mica). This was noted when investigating the change in bulk and relative density of the coarse rotund particles as well as the equivalent void ratio, with platy fines content.

Thin section photographs of the soton soil specimens were employed to study the fabric of the soil. Platy fine orientation between two adjacent rotund particles appeared to be parallel to the surface of the rotund particles, while in the voids it was random. Clean contacts between the coarse rotund particles appear to decrease with platy fines content. This implies that the governing particle shape changed from coarse rotund to platy fine. A "two-dimensional" equivalent void ratio in terms of the coarse rotund particles were calculated from thin section photographs. Average two-dimension equivalent void ratios compared well with three-dimensional equivalent void ratios obtained from specimen measurements.

The measured horizontal and vertical two-dimensional equivalent void ratios differed with the former being the lesser. The difference between the two increased with platy fines content. Measured local axial and radial strain also indicated a disparity between horizontal and vertical behaviour, thus confirming thin section measurements. The difference in behaviour was attributed to the compressibility of the mica flakes and specimen preparation technique.

6.2.2 *Compressibility*

The compressibility of the soton soil increased with platy fines content. Ten percent mica content had the greatest influence on the compressibility of the soil. This confirmed results from other researchers such as Gilboy (1928) and Hight and Leroueil (2003), namely that small percentages of mica had the greatest influence on the compressibility of sand, in this case the Soton Soil. The increase in compressibility was attributed to the shape of the platy fines.

6.2.3 *Limitations of the new bender element technique and Soton Soil results*

Travel times of the Soton Soil were repeatable for input frequencies of 15kHz to 25kHz. The first receiver was still in the near field at 10kHz whilst at 30kHz, the shear wave was preceded by a large scatter. The latter was not noted when investigating the small strain shear stiffness of the rotund sand. The scatter was attributed to different interference patterns being set up due to the nature of the particle contacts.

Cross correlation analysis between the two received signals of the Soton Soil resulted in two prominent peaks with the value of the first being greater. However, two prominent peaks were not observed in all of the test scenarios. Travel time obtained from the first peak was unrealistically high while that of the second peak was in good agreement with those at the remaining effective consolidation pressures. Travel times obtained from the second peak compared well with those from characteristic peaks (hand picking). It was assumed that travel time obtained from the second peak is correct. Following the above, it is thus concluded that cross correlation analysis results should not be applied blindly.

Interpretation of the bender element results of the Soton Soil was complicated by low signal-to-noise ratios. This was especially the case at low effective consolidation pressures of 25kPa and 50kPa. As a result, the small strain shear modulus results of the Soton Soil at these pressures were unrealistically high. It was also found that signal-to-noise ratio decreased with increasing platy fine (mica) content.

6.2.4 *Small strain stiffness* (G_{max})

The small strain shear modulus of the Soton Soil was governed by effective consolidation pressure and platy fines content. It was directly proportional to effective consolidation pressure and inversely proportional to platy fines content. The rate of decrease of the small strain shear stiffness decreased

with platy fines content. The undrained effective secant Young's modulus was effected in a similar manner by effective consolidation pressure and platy fines content.

Bender elements impose very small strains (in the order of 0.001%) on soil and are thus able to measure the stiffness of soil in the elastic zone. Consequently, the small strain shear stiffness and effective undrained secant Young's modulus results can be compared. A reasonable correlation between the two was obtained (Figures 5.14 to 5.16). This proved that the bender element results were reliable.

6.2.5 *Shear strength*

The shear behaviour of sand can be classified as contractive or dilative. Neither the dense nor loose rotund sand specimens displayed characteristic shear behaviour. The shear behaviour of the dense rotund specimen was measured only up to an axial strain of 3.2% and thus did not reach steady state. The observed shear behaviour of the loose sand specimen was associated with the difficulty in preparing a loose sand specimen that is truly contractive. The addition of platy fines to the coarse rotund particles, reduced the dilatancy of the soil until finally the Soton Soil appeared to be contractive at 20% platy fines. Platy fines formed bridges between the rotund particles that dislocate with continued shear, thereby displaying quasi-steady state. Phase transfer was noted for all of the specimens with the exception of the dense rotund sand specimen (Figure 5.21). Phase transfer coincided with quasi-steady state, which confirmed results from other researchers such as Verdugo and Ishihara (1996), Yamamuro et al. (1999) and Wan and Guo (2001).

An increase in effective consolidation pressure resulted in an increase in deviatoric and excess pore pressure. Shear behaviour of all of the specimens with the exception of the 10% platy fine specimens, remained unchanged. The dilatancy of the 10% Soton Soil increased with effective consolidation pressure. This was attributed to an increase in clean contacts between the rotund particles with effective consolidation pressure.

The effective internal friction angle of the Soton Soil was unaffected by particle size, shape and density. This was surprising as the literature reports the opposite for granular material.

The state parameter of the Soton Soil was determined to establish whether shear behaviour followed the suggested trend in terms of dilatancy as proposed by Been and Jefferies (1985). Not all of the specimens reached steady state and hence only those that did, were taken into account. A good correlation was obtained between the proposed and observed behaviour of the 10% and 15% Soton Soil. This however was not the case for 20% Soton Soil. The discrepancy was ascribed to differences in the aspect ratio of the Soton Soil (high) and the soil (low) for which the state parameter was developed. The two other percentages did not follow the behaviour of the 20% Soton Soil as sufficient rotund sand particles were present to reduce the infiuence of the platy fines.

Bolton (1986) dilatancy index could not be employed to the Soton Soil as the relative density of the sand was too low. The difference between the effective internal friction angle at failure and critical state was however, calculated as it provided some indication of the dilatancy of the soil. The difference between the two decreased with platy fines content thus confirming previous observed behaviour (Figures 5.19 to 5.21).

The addition of platy fines to the coarse rotund particles changed the location of the critical state line in the compression plane, while it remained unchanged in the stress plane.

6.3 Influence of platy fines on the behaviour of gold mine tailings

6.3.1 *Comparison between gold mine tailings and Soton Soil characteristics*

A good agreement was obtained between the particle size and shape as well as relative percentages of fines present in the Soton Soil and gold mine tailings. The behaviour of the Soton Soil was thus fit for comparison with the gold mine tailings.

Mine tailings are mostly in an anisotropic normally consolidated state. Isotropic normally consolidated tests were conducted on the Soton Soil. Thin section analysis however revealed that the fabric of the Soton Soil was anisotropic. The effective consolidation pressured employed for the consolidation tests were similar to those typically found in tailings dams.

6.3.2 *Compressibility*

The coefficients of consolidation of the Soton Soil were lower than the mine tailings due to the coarser grading of the Soton Soil. The compressibility behaviour of the Soton Soil compared well with that of mine tailings, suggesting that the compressibility behaviour of the tailings could be attributed to the particle shape of the fines.

6.3.3 *Small strain stiffness*

The small strain shear stiffness of mine tailings and Soton Soil decreased with platy fines content. It should be noted that the comparison was limited to a single case scenario (Höeg et al., 2000) for reasons given in Chapter 4. The rate of decrease in stiffness (both shear and Young's modulus) reduced with platy fines content. It appears that small quantities of platy fines (10%) have the greatest influence on the small strain shear stiffness and undrained

secant Young's modulus of Soton Soil. A fines content that is typically found in tailings.

6.3.4 *Shear strength*

The effective friction angle of the Soton Soil remained constant which was also noted for mine tailings with the effective slightly greater than that of Soton Soil. The difference in effective friction angle may be attributed to the particle shape of the tailings not only consisting of platy fines. This was confirmed by the constant slope of the critical state line.

Traditional soil mechanics strength models do not predict the behaviour of mine tailings accurately. Effective stability analysis is usually employed which does not take the compressive shear behaviour of the fines into account. Shear strength tests conducted on the Soton Soil highlighted the importance of taking the platy fines content into account. Undrained stability analysis carried out in isolation ignores the necessity f a trigger mechanism for failure. It was thus recommended that both undrained and effective stability analysis should be conducted on tailing slopes.

The results of this research have indicated that the addition of platy particles in the form of mica greatly influences the behaviour of a rotund sand. This change was noted in terms of compressibility, stiffness and shear behaviour of the sand. A transition from sand to clay-like behaviour was observed with the addition of platy particles.

It was noted that the behaviour of the Soton Soil is similar to that of mine tailings. Furthermore both rotund and platy particle shapes were observed in the mine tailings. Consequently, the unexpected behaviour of mine tailings may well be attributed to the platy particle shape of the fines.

6.4 RECOMMENDATIONS

The minimum and maximum dry densities of the Leighton Buzzard sand and mica was initially determined using commonly adopted techniques (BS1377,

1990; Cresswell et al., 1999). The particle orientation of the mica particles changed whilst falling through the air due to to their particle shape. Standard techniques thus did not yield the expected results and alternative techniques were adopted such as experimenting with funnel apertures, pluvation tube and vibration. It is recommended that the methods should be developed for determining the minimum and maximum dry densities of particles with a high aspect ratio.

The influence of platy fines on the behaviour of Soton Soil was illustrated in Figure 5.22. It could be noted that density greatly influenced the effective friction angle of the dense and loose rotund sand specimens but that the Soton Soil specimens were unaffected by it, despite being granular. The effective friction angle of the 5% Soton Soil specimen however was not included as it was only sheared at 400kPa effective consolidation pressure to illustrate the influence of very little platy fines. Following the conclusions drawn from the comparative equivalent void ratios, compressibility and shear behaviour (at 400kPa effective consolidation pressure), it could be assumed that the effective friction angle of the 5% Soton Soil specimen would be close to that of the loose rotund sand. The mica content where the transition from coarse rotund particles controling the effective friction angle to platy fines takes place, was not determined. It is postulated that this transition point is a function of the relative particle sizes of the rotund and platy particles. Future research determining this transition point as well as the factors that influence it, would provide valuable information towards establishing a framework for the behaviour of mine tailings and micaceous soils.

Bibliography

Abbiss, C. P. (1981). Shear wave measurements of the elasticity of the ground, *Geotechnique* **31**(1): 91–104.

Airey, D. W. (2003). Automating G_{max} measurement in triaxial tests, *Deformation Characteristics of Geomaterials* **1**: 73–80.

Alarcon-guzmand, A., Leonards, G. and Chameau, J. (1988). Undrained monotonic and cyclic strength of sands, *Journal of Geotechnical Engineering, ASCE* **114**(10): 1089–1109.

Andrianopoulos, K. I., Bouckovalas, G. D. and Papadimitriou, A. G. (2001). A critical state evaluation of fines effect on liquifaction potential, *Proc. of the* 4^{th} *Internasional Conference on Recent Advances in Geotechnical Earthquake Engineering and Soil Dynamics* pp. 1–6. San Diego, California.

Arroyo, M., Wood, D. M. and Greening, P. D. (2003). Source near-field effects and pulse tests in soil samples, *Geotechnique* **53**(3): 337–345.

Arulnathan, R., Boulanger, R. W. and Riemer, M. F. (1998). Analysis of bender element tests, *Geotechnical Testing Journal, ASTM* **21**(2): 120–131.

Aubertin, M., Bussière, B. and Chapuis, R. P. (1996). Hydraulic conductivity of homogenized tailings from hard rock mines, *Canadian Geotechncal Journal* **33**: 470–482.

Audibert, J. M. E., Ismael, N. F. and Clough, G. W. (1976). Response footings on micaceous, cohesionless soils, *Numerical Methods in Geomechnics, ASCE* pp. 567–579. C. S. Desai.

Baldi, G., Hight, D. W. and Thomas, G. E. (1988). A re-evaluation of conventional triaxial test methods, *Advanced Triaxial Testing of Soil and Rock, American Society for testing and materials* **STP977**: 219–263.

Barrett, P. J. (1980). The shape of rock particles, a critical review, *Sedimentology* **27**: 291–303.

Been, K. and Jefferies, M. G. (1985). A state parameter for sands, *Geotechnique* **35**(2): 365–381.

Biot, M. A. (1956). Theory of propagation of elastic waves in a fluid-saturated porous solid. II Higher frequency range, *Journal of the Acoustical Society of America* **28**(2): 179–191.

Bishop, A. W. and Henkel, D. J. (1962). *The measurement of soil properties in the triaxial test*, 2^{nd} edn, Edward Arnold Ltd, pp. 640–642.

Blewett, J., Blewett, I. J. and Woodwards, P. K. (1999). Measurement of shear-wave velocity using phase-sensitive detection techniques, *Canadian Geotechnical Journal* **36**: 934–939.

Blewett, J., Blewett, I. J. and Woodwards, P. K. (2000). Phase and amplitude responses associated with the measurement of shear-wave velocity in sand by bender elements, *Canadian Geotechnical Journal* **37**: 1348–1357.

Blight, G. E. (1987). The concept of the master profile for tailings dam beaches, *International Waste Management Conference, Johannesburg* pp. 95–100.

Blight, G. E. and Bentel, G. M. (1983). The behaviour of mine tailings during hydraulic depostition, *Journal of the South African Institute of Mining and Metallurgy* pp. 73–86.

Blight, G. E. and Steffen, K. H. (1979). Geotechnics of gold mining waste disposal, *Current Geotechnical Practise in Mine Waste Disposal, ASCE* pp. 1–53.

Bolton, M. D. (1986). The strenght and dilatancy of sands, *Geotechnique* **36**(1): 65–78.

Bouckovalas, G. D., Andrianopoulos, K. I. and Papadimitriou, A. G. (2002). A critical state interpretation for the cyclic liquifaction resistance of silty sands, *Soil Dynamics and Earthquacke Engineering* **20**: 1–11.

Bowman, E. T., Soga, K. and Drummond, T. W. (2000). Particle shape characterisation using fourier analysis, *Technical report*, CUED/D-Soils/TR, Cambridge.

Brignoli, G. M., Gotti, M. and Stokoe, K. H. (1996). Measurement of shear waves in laboratory specimens of piezoelectric transducers, *Geotechnical Testing Journal* **19**(4): 384–397.

Brocanelli, D. and Rinaldi, V. (1997). Measurement of low-strain material damping and wave velocity with bender elements in the frequency domain, *Canadian Geotechnical Journal* **35**: 1032–1040.

Brocanelli, D. and Rinaldi, V. (1998). Measurement of low-strain material damping and wave velocity with bender elements in the frequency domain, *Canadian Geotechnical Journal* **35**: 1032–1040.

BS1377 (1990). British standard methods of tests for soils of civil engineering, *Technical report*, British Standards Institution, London.

BS812 (1975). British standard methods of tests for soils of civil engineering, *Technical report*, British Standards Institution, London.

Burland, J. B. (1990). On the compressibility and shear strenght of natural clays, *Geotechnique* **40**(3): 329–378.

Byrne, P. M. and Seid-Karbasi, M. (2003). Seismic stability of impoundments, 17^{th} *Annual Symposium, VGS.* www.civil.ubc.ca/liquefaction/VGS12r.pdf.

Capps, C. (2001). Near field or far field?, *EDN magazine* pp. 95–102. www.ednmag.com.

Carrier, W. D. (1991). Stability of tailings dams, *XV Ciclo di Conferenze di Geotecnica di Torino.*

Colin, B. (1980). *Design considerations for earthquake-resistant mine tailings impoundment structures in Northern Ontario*, Msc. thesis, University of Toronto, Toronto.

Craig, R. F. (1997). *Soil Mechanics*, 6^{nd} edn, E and FN Spon, New York.

Cresswell, A. (n.d.). Personal communication.

Cresswell, A., Barton, M. E. and Brown, R. (1999). Determining the maximum density of sands by pluvation, *Geotechnical Testing Journal* **22**(4): 324–328.

Cuccovillo, T. and Coop, M. R. (1997). Yielding and pre-failure deformation of strucutred sands, *Geotechnique* **47**(3): 41–508.

De Alba, P. and Baldwin, K. (1991). Use of bender elements in soil dynamics experiments, *Proc. of ASCE National Convention, Recent Advances in Instrumentation, Data Acquisition and Testing in Soil Dynamics, Geotechnical Special Publication* **12**: 86–101. Florida.

De Alba, P., Baldwin, K., Janoo, V., Roe, G. and Celikkol, B. (1984). Elastic-wave velocities and liquefaction potential, *Geotechnical Testing Journal* **7**(2): 77–87.

Dunnicliff, J. (1988). *Geotechnical Instrumentation for Monitoring Field Performance*, 1^{st} edn, Wiley and Sons, New York.

Dyvik, R. and Madshus, C. (1985). Laboratory measurements of G_{max} using bender elements, *Advances in the Art of Testing Soil under Cyclic Conditions* pp. 186–196. New York :ASCE.

Dyvik, R. and Olsen, T. S. (1989). G_{max} measured in oedometer and DSS tests using bender elements, *Proc. of the* 12^{th} *ISSMFE* pp. 37–42. Rio de Janeiro.

Erricson, P. (n.d.). Personal communication.

Fioravante, V. and Capoferri, R. (2001). On the use of multi-directional piezoelectric transducers in triaxial testing, *Geotechnical Testing Journal* **24**(3): 243–255.

Fourie, A. B. and Papageorgiou, G. (2003). Reply to the discussion by J. Chu, W. K. Leong and W. L. Loke on "Defining an appropiate steady state line for Merriespruit gold tailings", *Canadian Geotechnical Journal* **40**: 487–488.

Fratta, D. and Santamarina, J. C. (1996). Wave propagation in soils: Multimode, wide-band testing in a waveguide device, *Geotechnical Testing Journal* **19**(2): 130–140.

Frost, J. D. and Yang, C. (2002). Image analysis of void distributions in sand during shearing, *US-Japan seminaar on seismic disaster mitigation in urban areas by geotechnical engineering.* Alaska.

Gajo, A., Fedel, A. and Mongiovi, L. (1997). Experimental analysis of the effects of fluid-solid coupling on the velocity of elastic waves in saturated porous media, *Geotechnique* **47**(5): 993–1008.

Gibbs, H. J. and Holtz, W. G. (1957). Research on determining the densit of sands by spoon penetration testing, *Proc of the* 4^{th} *ISSMFE* **1**: 35–39.

Gilboy, G. (1928). The compressibility of sand-mica mixtures, *Proc of the ASCE* **2**: 555–568.

Gohl, W. B. and Finn, W. D. L. (1991). Use of a piezocemraic bender element in soil dynamics testing, *Proc. of ASCE National Convention, Recent Advances in Instrumentation, Data Acquisition and Testing in Soil Dynamics, Geotechnical Special Publication* **12**: 118–133. Florida.

Gordon, M. A. and Clayton, C. R. I. (1997). Measurement of stiffness of soils using small strain triaxial testing and bender elements, *Proc. Conference on Modern Geophysics in Engineering Geology, Geological Society Engineering Group Special Publication* **12**: 365–371. The Geological Society, London.

Hamel, J. V. and Gunderson, J. W. (1973). Shear strength of Homestake slimes tailings, *Journal of the Soil Mechanics and Foundations Division, ASCE* **99**(SM5): 427–432.

Hammond, C. J. and Hardcastle, J. H. (1987). Shear strength and densities of micaceous sands, *VII CPMSIF-PCSMFE, Colombia* pp. 45–56.

Harr, M. E. (1977). *Mechanics of particulate media - A propabilistic approach*, McGraw-Hill.

Hight, D. W. (1982). A simple piezometer probe for the routine measurement of pore pressure in triaxial tests on saturated soils, *Geotechnique* **32**(4): 396–401.

Hight, D. W. and Leroueil, S. (2003). Characterisation of soils for engineering purposes, *Characterisation and Engineering Properties of Natural Soils* pp. 255–314. Swets and Zeitlinger, Lisse.

Hight, D. W., Georgiannou, V. N., Martin, P. L. and Mundegar, A. K. (1999). Flow slides in micaceous sands, *Problematic Soils* pp. 945–958. Balkema, Rotterdam.

Höeg, K., Dyvik, R. and Sandbaekken, G. (2000). Strength of undisturbed versus reconstitute silt and silty sand specimens, *Journal of Geotechnical and Geoenvironmental Engineering* **126**(7): 606–616.

Hope, V. S., Clayton, C. R. I. and Butcher, A. P. (1999). In situ determination of G_{hh} at Bothkennar using a novel seismic method, *Quarterly Journal of Engineering Geology* **32**: 97–105.

Ishihara, K., Tatsuoka, F. and Yasuda, S. (1975). Undrained deformation and liquefaction of sand under cyclic stresses, *Soils and Foundations* **15**(1): 29–44.

Jefferies, M. G. (1993). Nor-Sand: A simple critical state model for sand, *Geotechnique* **43**(1): 91–103.

Jovičič, V. (1997). *The measurement and interpretation of small strain stiffness of soils*, PhD thesis, City University, London.

Jovičič, V. and Coop, M. R. (1997). Stiffness of coarse-grained soils at small strains, *Geotechnique* **47**(3): 545–561.

Jovičič, V. and Coop, M. R. (1998). The measurement of stiffness anisotrophy in clays with bender element tests in the triaxial apparatus, *Geotechnical Testing Journal, American Society for Testing and Materials* **21**(1): 3–10.

Jovičič, V., Coop, M. R. and Simic, M. (1996). Objective criteria for determining G_{max} from bender element tests, *Geotechnique* **46**(2): 357–362.

Karl, L., Haegeman, W., Pyl, L. and Degrande, G. (2003). Measurement of material damping with bender element in triaxial cell, *Deformation Characteristics of Geomaterials* **1**: 3–12.

Krumbein, W. C. (1941). Measurement and geological significance of shape and roundness of sedimentary particles, *Journal of Sediment, Petrol* **11**(2): 64–72.

Kuerbis, R., Negussey, D. and Vaid, Y. P. (1988). Effect of gradation and fines content on the undrained response of sand, *Hydraulic Fill Structures, ASCE Geotechnical Special Publication* **21**: 330–345.

Kuwano, R., Connolly, T. M. and Kuwano, J. (1999). Shear stiffness anisotrophy measured by multi-directional bender elements, *Pre-failure Deformation Characteristics of Geomaterials* pp. 205–212. Balkema, Rotterdam.

Ladd, C. C. (1991). 44^{nd} Karl Terzaghi Lecture: Stability evaluation during staged construction, *Journal of Geotechnical Engineering , ASCE* **117**: 537–615.

Lade, P. V. and Overton, D. D. (1989). Cementation effects in frictional material, *Journal of Geotechnical Engineering Division, ASCE* **115**(10): 1373–1387.

Lade, P. V., Liggio, C. D. and Yamamuro, J. A. (1998). Effects of nonplastic fines on minimum and maximum void ratios of sand, *Geotechnical Testing Journal* **21**(4): 336–347.

Lees, G. (1963). The measurement of particle shape and its influence in engineering materials, *Journal of British Granite and Whinston Federation* pp. 1–22.

Leroueil, S., Guerriero, G., Picarelli, L. and Saihi, F. (1997). Large deformation shear strenght of two types of structured soils, *Deformation and Progressive Failure in Geomechanics* pp. 217–222. Elsevier Science.

Lo Presti, D. C. F., Pallara, O., Maniscalco, R. and Pedroni, S. (2000). Experimental laboratory determinations of the steady state of sands, *Soils and Foundations* **40**(1): 113–122.

Lupini, J. F., Skinner, A. E. and Vaughan, P. R. (1981). The drained residual strength of cohesive soils, *Geotechnique* **31**(2): 181–312.

Mancusco, C., Simonelli, A. L. and Vinale, F. (1989). Numerical analysis of in situ S-wave measurement, *Proc. of the* 12^{th} *ISSMFE* pp. 277–280.

Martin, T. E. and Roberts, E. C. (1998). Some considerations in the stability analysis of upstream tailings dam.

Matthews, M. C., Clayton, C. R. I. and Own, Y. (2000). The use of field geophysical techniques to determine geotechnical stiffness parameters, *Proceedings of the Institute of Civil Engineers, Geotechnical Engineering* **143**: 31–42.

Matyas, E. L., Welch, D. E. and Reades, D. W. (1984). Geotechnical parameters and behviour of uranium tailings, *Canadian Geotechnical Journal* **21**: 489–504.

McPhail, G. I. and Wagner, J. C. (1989). The extractive metallurgy of gold in South Africa, *The Chamber of Mines of South Africa* **2**: 655–707.

Mitchell, J. K. (1976). *Fundamentals of Soil Behaviour*, Wiley, New York.

Mitchell, J. K. (1993). *Fundamentals of Soil Behaviour*, 2^{nd} edn, Wiley.

Mittal, H. K. and Morgenstern, N. R. (1975). Parameters for the design of tailings dams, *Canadian Geotechnical Journal* **12**: 1159–1576.

Mittal, H. K. and Morgenstern, N. R. (1976). Seepage control in tailings dams, *Canadian Geotechnical Journal* **13**: 277–293.

Miura, K., Maeda, K., Furukawa, M. and Toki, S. (1997). Physical characteristics of sands with different primary properties, *Soils and Foundations* **37**(3): 53–64.

Mohsin, A. K. H. and Airey, D. W. (2003). Automating G_{max} measurement in triaxial tests, *Deformation Characteristics of Geomaterials* **1**: 73–80.

Moore, C. A. (1971). Effect of mica on the K_0 compressibility of two soils, *Journal of Soil Mechanics and Foundations Division, ASCE* **97**(SM9): 1275–1291.

Mulilis, J. P., Seed, H. B., Chan, C. K., Mitchell, J. K. and Arulanandan, K. (1977). Effects of sample preparation on sand liquefaction, *Journal of Geotechnical Engineering Division, ASCE* **103**(GT2): 91–108.

Mundegar, A. (1997). *An investigation into the effects of platy mica particles on the behaviour of sand*, MSc. dissertation, Imperial College, London.

Oda, M. (1972a). Initial fabric and their relations to mechanical properties of granular material, *Soils and Foundations*.

Oda, M. (1972b). The mechanism of fabric changes during compressional deformation of sand, *Soils and Foundations*.

Olsen, R. E. and Mesri, G. (1970). Mechanisms controlling compressibility of clays, *Journal of the Soil Mechnics and Foundation Division, ASCE* **SM6**: 1863–1878.

Pettibone, H. C. and Kealy, C. D. (1971). Engineering properties of mine tailings, *Journal of Soil Mechanics and Foundation Division, ASCE* **97**: 97.

Phillips, J. R. (1998). Piezoelectric technology primer. www.ctscorp.com/electro/piezotechprimer.pdf.

Poulos, S. J. (1981). The steady state of deformation, *Journal of Geotechnical Engineering Division, ASCE* **107**(GT5): 553–562.

Qiu, Y. and Sego, D. C. (2001). Laboratory properties of mine tailings, *Canadian Geotechnical Journal* **38**: 183–190.

Rassam, D. W. (2002). Variation of evaporative and shear strength parameters along a tailings delta, *Canadian Geotechnical Journal* **39**: 32–45.

Rio, J., Greening, P. and Medina, L. (2003). Influence of sample geometery on shear wave propagation using bender elements, *Deformation Characteristics of Geomaterials* **1**: 963–974.

Robertson, A. M. (1987). The influence of depositional methods on the engineering properties of tailing deposits, *International Waste Management Conference, Johannesburg.*

Rogers, A. F. and Kerr, P. F. (1942). *Optical Mineralogy*, 2^{nd} edn, McGraw-Hill book company Inc.

Rowe, P. W. (1969). The relation between shear strenght of sands in triaxial compression, plane strain and direct shear, *Geotechnique* **19**(1): 75–86.

Rowe, P. W. (1972). The relevance of soil fabric to site investigation practise, *Geotechnique* **22**(2): 195–300.

Sanches-Salinero, I., Roesset, J. M. and Stokoe, K. H. (1986). Analystic studies of body wave propagation and attenuation, *Technical Report GR86-15*, University of Texas, Austin.

Santamarina, J. C. and Aloufi, M. (1999). Small strain stiffness: A micromechanical experimental study, *Proc. of the Pre-failure Deformation Characteristics of Geomaterials, Torino* pp. 451–458.

Santamarina, J. C., Klein, K. A. and Fam, M. A. (2001). *Soils and Waves, Particulate Materials Behaviour, Characterization and Process Monitoring*, 1^{st} edn, Wiley.

Shirley, D. J. (1978). An improved shear wave transducer, *Journal of the Acoustic Society of America* **63**(5): 1643–1645.

Shirley, D. J. and Hampton, L. D. (1978). Shear-wave measurements in laboratory sediments, *Journal of the Acoustic Society of America* **63**(2): 607–613.

Stokoe, K. H. and Santamarina, J. C. (2000). Seismic-wave-based testing in geotechnical engineering, *Internasional Conference on Geotechnical and Geological Engineering, GeoEng2000* pp. 1048–1055. Melbourne, Australia.

Stone, K. J. L., Randolph, M. F., Toh, S. and Sales, A. A. (1994). Evaluation of consolidation behaviour of mine tailings, *Journal of Geotechnical Engineering. ASCE* **120**(3): 473–490.

Sukumaran, B. and Ashmawy, A. K. (2001). Quantitative characterisation of the geometery of discrete particles, *Geotechnique* **51**(7): 619–627.

Taylor, D. W. (1948). *Fundamentals of Soil Mechanics*, Wiley, New York.

Terzaghi, K. (1925). Zur charakteristik der bausande, *Zeitschrift des Oesterreichischen Ingenieur und Architekten Vereines* pp. 33–34.

Terzaghi, K. and Peck, R. B. (1948). *Soil mechanics in Engineering Practice*, 2^{nd} edn, John Wiley and Sons, Inc.

Terzaghi, K., Peck, R. B. and Mesri, G. (1996). *Soil mechanics in Engineering Practice*, 3^{rd} edn, John Wiley and Sons, Inc.

Thevanayagam, S. (1998). Effect of fines and confining stress on the undrained shear strength of silty sand, *Journal of Geotechnical and Geoenvironmental Enigeering* **124**(6): 479–491.

Thevanayagam, S. (1999). Role of intergrain contacts, friction, and interactions on undrained response of granular mixes, *Physics and Mechnics of Soil Liquifaction* pp. 67–78. Lade and Yamamuro.

Trojcek, J. (2002). Predicting the long term stabilisation of uranium mill tailings, *Survey and Analysis of Selected Geotechnical Data of the Rozana K1 Tailings Pond, Second Progress Report.*

Vaid, Y. P., Sivathayalan, S. and Stedman, D. (1999). Influence of specimen-reconstituting method on the undrained response of sand, *Geotechnical Testing Journal* **22**(3): 187–195.

Verdugo, R. and Ishihara, K. (1996). The steady state of sandy soils, *Soils and Foundations* **36**(2): 81–91.

Vermeulen, N. J. (2001). *The Compression and State of Gold Tailings*, PhD thesis, University of Pretoria.

Vermeulen, N. J., Rust, E., Clayton, C. R. I. and Powrie, W. (n.d.). The compressibility of South African gold tailings.

Vick, S. G. (1990). *Planning, design and analysis of tailings dams*, 2^{nd} edn, John Wiley and sons, New York.

Viggiani, G. and Atkinson, J. H. (1995). Interpretation of bender element tests, *Geotechnique* **45**(1): 149–154.

Wadell, H. (1932). Volume, shape and roundness of rock particles, *Journal of Geology* **40**: 443–451.

Wagener, F., Craig, H. J., Blight, G., McPhail, G., Williams, A. A. B. and Strydom, J. H. (1998). The Merriesprui tailings dam failure-A review, *Proceedings of the* 5^{th} *Internasional Conference on Tailings and Mine Waste, Fort Collins* pp. 925–952.

Wan, R. G. and Guo, P. J. (2001). Effects of microstructure on undrained behaviour of sands, *Canadian Geotechnical Journal* **36**: 16–28.

Wates, J. A., Stevenson, C. and Purchase, A. (1987). The effects of relative densities on the beaching angles and segregation on gold and uranium tailings dams, *International Waste Management Conference, Johannesburg* pp. 89–94.

Wood, F. M. and Yamamuro, J. A. (2000). Quantification of soil fabric of liquafiable silty soils, *Proc. of the* 14^{th} *Engineering Mechanics Conference, ASCE.*

Wright, P. (1955). A method of measuring the surface roughness of aggregate, *Road Research Laboratory, Dept. of Scientific and Industrial Research, Magazine of Concrete Research.*

Yamamuro, J. A. and Lade, P. V. (1997). Static liquifaction of very loose sands, *Canadian Geotechnical Journal* **34**: 905–917.

Yamamuro, J. A., Covert, K. M. and Lade, P. V. (1999). Static and cyclic liquifaction of silty sands, *Physics and Mechanics of Soil Liquifaction* pp. 55–65. Lade and Yamamuro.

Yudhbir and Abedinzadeh, R. (1991). Quantification of particle shape and angularity using the image analyser, *Geotechnical Testing Journal* **14**(3): 296–308.

Zlatovic, S. and Ishihara, K. (1997). Normalized behaviour of very loose non-plastic soils: effective of fabric, *Soils and Foundations* **37**(4): 47–56.

Zywicki, D. J. (1991). *Advanced signal processing methods applied to engineering analysis of seismic surface waves*, Dissertation. Chapter 6.

Appendix A

Cross Correlation program for analysing bender element results

```
Dim   rownr, rownb, rowne, col
Dim   mover As Single
Dim   Currentsheet As String
Dim   topavg, botavg, sum, topvalue, botvalue, topdifference, botdifference, nextcc,
      product, totalproduct, toppower, botpower, sumproduct, sumtoppower

Public Sub crosscorrelation()
'calculate the cross correlation
      mover = 0
      col = 3                          'column
      rowb = 2                         'begin row
      rowe = 1000                      'end row
      sumtop = 0                       'sum of top values
      sumbot = 0                       'sum of bottom values
      sumproduct = 0
      sumtoppower = 0
      sumbotpower = 0

'SLIDE BOTTOM DATA SET RELATIVE TO TOP DATA SET
'calculate the average of top and bottom

For rownr = rowb To rowe
    topvalue = Sheets("cross correlation").Cells(rownr, col).Value
    botvalue = Sheets("cross correlation").Cells(rownr, col + 1).Value
    sumbot = sumbot + botvalue
Next rownr

topavg = sumtop/(rowe - rowb)
botavg = sumbot/(rowe - rowb)
```

```
For mover = 0 To 500
'calculate the difference between current value (top and bottom) and average
For rownr = rowb To rowe - mover
    topvalue = Sheets("cross correlation").Cells(rownr + mover,col).Value
    botvalue = Sheets("cross correlation").Cells(rownr, col + 1).Value
    topdifference = topvalue - topavg
    botdifference = botvalue - botavg
    'calculate the product of topdifference and bottom difference
    product = topdifference * botdifference
    'calculate the power of topdifference and botdifference
    toppower = topdifference^2
    botpower = botdifference^2
    'calculate the sum of product and power calculations
    sumproduct = sumproduct + product
    sumtoppower = sumtoppower + toppower
    sumbotpower = sumbotpower + botpower
    If rownr = rowe - mover Then
            totalproduct = sumproduct
            totaltoppower =sumtoppower
            totalbotpower = sumbotpower
            'calculated crosscorrelation function
            cc = totalproduct/((totaltoppower)^(0.5) * (totalbotpower)^(0.5))
            Sheets("cross correlation").Cells(2 + mover, 8) = cc
    End If
Next rownr
Next mover


Sheets("cross correlation").Cells(1, 8) = "cross correlation"
'write down max cross correlation and time delay
HighestCorr = 0
cc = 0
```

```
sumbotpower = 0
Sheets("cross correlation").Cells(1, 9) = "max cross correlation"
Sheets("cross correlation").Cells(1, 10) = "time delay"


For Row = 2 To 2009
    cc = Sheets("cross correlation").Cells(Row, 8)
    If cc > HighestCorr Then
        HighestCorr = cc
        TimeStep = Sheets("cross correlation").Cells(Row, 2)
    End If
Next Row


Sheets("cross correlation").Cells(2, 9) = HighestCorr
Sheets("cross correlation").Cells(2, 10) = TimeStep
End Sub

Public Sub Engine()
Currentsheet = data(10)
Call crosscorrelation(Currentsheet)
For Frekw = 10 To 30 Step 5
End Sub
```